Specific interactions of Ag$^+$ ions with linear polyacrylate chains and spherical polyacrylate brushes and Ag nanoparticle formation therein

Von der Fakultät für Naturwissenschaften

der Universität Paderborn

genehmigte

Dissertation

zur Erlangung des akademischen Grades

Doktor der Naturwissenschaften

– Dr. rer. Nat. –

von

Anna Ezhova, Dipl.-Chem.

aus Malmysch (Russland)

Mai 2015

Die vorliegende Dissertation entstand im Zeitraum von August 2011 bis Mai 2015 im Fachbereich für Physikalische Chemie (Arbeitskreis Prof. Dr. Klaus Huber) an der Fakultät für Naturwissenschaften der Universität Paderborn.

1. Gutachter: Prof. Dr. Klaus Huber
2. Gutachter: Prof. Dr. Claudia Schmidt

Die Arbeit wurde eingereicht am: 19.05.2015
Tag der mündlichen Prüfung: 22.06.15

Acknowledgments

This thesis would be absolutely impossible without the helping hand of many individuals. I would like to thank them here.

Abstract

The present dissertation investigates two polyacrylate (PA) systems in dilute aqueous solutions, commercially available long linear PA-chains and spherical polyacrylate brushes (SPBs) composed of polystyrene (PS) cores and PA-shells, which were synthesized as part of the thesis. Investigation of these two systems addresses their specific interactions with Ag^+ ions and their potential use in preparing silver nanoparticles (Ag-NPs). Formation of silver acrylate complexes in both linear PA-chains (Ag^+-PA) and SPBs (Ag^+-SPB) were analysed by means of static and dynamic light scattering (SLS/DLS). Based on numerous SLS/DLS experiments made with each PA morphology, phase diagrams which describe the solubility behaviour of Ag^+-PA and Ag^+-SPB solutions were deduced and compared with phase diagrams established for the corresponding PA-systems interacting with alkaline earth cations. The interaction pattern of linear PA-chains with monovalent Ag^+ ions depends on the ratio of $[Ag^+]/[COO^-]$ disclosing a diverse set of Ag^+-PA entities including homogeneous low density aggregates, dense unstable and dense stable aggregates. The solubility behaviour of Ag^+-SPB solutions is less complex and comprises a line where shrinking of the PA-shell reaches the state of a fully collapsed shell and a second line where coagulation of Ag^+-SPBs occurs. Both lines are well separated by a regime of stable Ag^+-SPB with a fully shrunk PA-layer. Based on the investigated properties of both Ag^+-PA and Ag^+-SPB solutions, Ag-NP formation induced by exposure of both systems to UV-light, without application of an additional reducing agent, was analysed. UV-vis spectroscopy, SAXS/ASAXS, SEM and TEM were used as additional methods to characterize Ag-NP formation embedded in PA-matrices. In case of linear PA-chains dense unstable Ag^+-PA aggregates lead to assemblies of Ag-NPs upon exposure to UV-light, whereby the number of Ag-NPs per assembly could be tuned by the size of the dense unstable aggregates achieved by varying the preceding aging time. Dense stable Ag^+-PA aggregates lead to entities with predominantly single Ag-NPs. Ag-NP formation generated in SPB solutions showed that independent of the brush parameters or of the regime of Ag^+ concentration a low amount of Ag-NPs per SPB particle similar in size and amount were generated. The decoration of SPB with Ag-NPs has been enhanced successfully by applying an additional chemical reducing agent ($NaBH_4$).

Zusammenfassung

In der vorliegenden Arbeit wird die spezifische Wechselwirkung von Silberkationen (Ag^+) mit zwei unterschiedlichen Polyacrylat (PA)-Systemen in wässriger Lösung untersucht. Während ein PA-System aus kommerziell erhältlichen langen, linearen PA-Ketten besteht, ist das andere System aus sphärischen Kolloiden gebildet (SPB), die aus einem Polystyrol(PS)-Kern und einer PA-Hülle aus bürstenartig angebrachten kurzen Polymerketten bestehen.

Durch systematische Lichtstreuexperimente an beiden PA-Systemen wurde zunächst deren Löslichkeitsverhalten in Wasser bei Anwesenheit von Silberionen untersucht und in Phasendiagrammen zusammengefasst. In Abhängigkeit des Verhältnisses $[Ag^+]/[COO^-]$ konnten für die linearen PA in Lösung drei verschiedene Bereiche identifiziert werden: neben homogenen Ag^+-PA Aggregaten geringer Dichte (*homogeneous low density aggregates*) ließen sich bei Erhöhung der Ag^+-Konzentrationen instabile (*dense unstable aggregates*) sowie stabile (*dense stable aggregates*) Aggregate mit hoher Dichte nachweisen. Für Ag^+-SPB Systeme wurde ein einfacheres Phaseverhalten als bei den linearen PA-Ketten gefunden. Eine Schwelle bei vergleichsweise niedrigen Ag^+-Konzentrationen entsprach der maximalen Schrumpfung der PA-Schale. Eine zweite Schwelle bei höheren Ag^+-Konzentrationen zeigte die Koagulation der Ag^+-SPB an.

Aufbauend auf dem Phasenverhalten wurde die durch UV-Licht initiierte Reduktion von Ag^+-Ionen zu Silbernanopartikeln (Ag-NPs) in beiden PA-Systemen untersucht, zunächst in Abwesenheit eines zugesetzten Reduktionsmittels. Diese durch PA-Matrices unterstützte Synthese von Ag-NPs wurde neben Lichtstreutechniken auch mittels UV-vis Spektroskopie, SAXS/ASAXS, SEM und TEM charakterisiert. Es konnte zunächst festgestellt werden, dass sich in einer dichten PA-Matrix aus instabilen Ag^+-PA Aggregaten (*dense unstable aggregates*) rasch makroskopische Assemblate aus kleineren Ag-NPs bilden. Die Gesamtgröße dieser Assemblate hing von der Größe der als Matrix verwendeten Ag^+-PA Aggregate ab und ließ sich somit über die Alterungsdauer der instabilen Aggregate (*dense unstable aggregates*) direkt steuern. Demgegenüber führt eine Reduktion von Ag^+ in stabilen, sehr dichten Ag^+-PA Aggregaten (*dense stable aggregates*) hauptsächlich zu kleinen Ag-NPs ohne Assemblatbildung. Für die SPB-Partikel konnte gezeigt werden, dass eine UV-initiierte Reduktion unabhängig von der Beschaffenheit der PA-Hülle oder der Silberkonzentration nur zu wenigen, kleinen Ag-NPs pro SPB-Kolloid führt. Durch Zugabe von $NaBH_4$ als Reduktionsmittel konnte erfolgreich die Anzahl und Größe der Silberpartikel in der PA-Hülle der SPBs unter kontrollierten Bedingungen erhöht werden.

Content

1 Introduction

1.1 State of the Art

1.1.1 Polyelectrolytes in the Presence of Counterions

For neutral polymers in dilute solution the solvent quality is usually modified by a temperature change. With decreasing solvation power (usually decreasing the temperature) the chain conformation undergoes a shrinking. Polyelectrolytes, whose behavior is governed by electrostatic forces, in dilute solution exhibit striking analogies to this behavior if an additional salt is present.

Dominated by electrostatic forces interactions between polyelectrolyte chains and inert salts, such as NaCl or $NaNO_3$, in aqueous solutions are caused by counterion condensation [1, 2]. The counterions screen the electrostatic repulsion between charged groups along the polyelectrolyte chains, inducing a decrease of the coil dimensions and affecting the solubility [2-5]. At very high salt concentration, the coils may even precipitate denoted as "salting-out" effect or H-type precipitation [6, 7]. The term "H-type" originates from the fact that the concentration of inert salt required to cause precipitation is high and independent of the polymer concentration. In some cases if the inert monovalent salt concentration is further increased, polyelectrolyte chains may become redissolved. Consequently, this redissolution is denoted as "salting in" effect [7, 8].

In contrast to this non-specific screening by inert salts, alkaline earth cations or heavy metal cations interact strongly with various polyelectrolytes such as anionic PA chains [7]. The concentration of these specifically interacting cations per monomer unit of the polymer chain (e.g. anionic residue – COO^--group) necessary for reaching the precipitation limit, is much lower than the one required for unspecific "salting out" effects. Therefore, this kind of phase separation is denoted as L-type precipitation [6, 9, 10]. Further increase of the counterion concentration leads to an aggregation process and macroscopic precipitation of the polyacrylate.

This transformation of single chains to aggregates in the presence of specifically interacting cations can be represented by a phase diagram. An important feature of this phase diagram is the aforementioned precipitation threshold [6, 10]. The precipitation of fully dissociated NaPA caused by the addition of specifically interacting cations (M^{n+}), at a molar concentration $[M^{n+}]_c$, obeys the following linear relationship [10]

$$[M^{n+}]_c = m + r_0[NaPA]_c \tag{1.1}$$

where the critical polymer concentration $[NaPA]_c$ is expressed in terms of the molar concentration of COO^--groups. The slope r_0 indicates a stoichiometric amount of M^{n+} per COO^--residues, necessary to precipitate the polyelectrolyte chains. The intercept m corresponds to the lowest critical concentration threshold $[M^{n+}]_c$ necessary to precipitate a polyelectrolyte at infinite dilution. This intercept depends on the ionic strength of the solution induced by an additional inert salt, since the inert salt exerts a certain ion exchange pressure on the specifically interacting cations [11].

Intermediates of the coils can be trapped upon approaching the precipitation threshold by stepwise adjusting the ratio of $[M^{n+}]/[COO^-]$. The shrinking of Ca^{2+}-PA becomes largest at the precipitation threshold, where PA chains adopt the shape of a collapsed sphere [11]. While light [11] and small angle neutron scattering [12, 13] indicated a pearlnecklace-like shape of the shrinking PA coils with Ca^{2+}-COO^- complex nodules, ASAXS experiments for the first time showed in a quantitative manner the extent of decoration of the NaPA coils with Sr^{2+}, being predominantly located in the nodules/pearls [14]. Experiments with Cu^{2+} ions [15] revealed a pattern which partly differs from the one established for the alkaline earth cations. The extent of shrinking achieved at the precipitation threshold is considerably smaller and the aggregates, which precede the actual precipitate, are less dense [15].

A comparison of the precipitation thresholds among Ca^{2+}, Sr^{2+} and Ba^{2+} revealed that the stoichiometric amount of cations required to precipitate NaPA is decreasing with increasing atomic number of the alkaline earth cation [16]. In the case of heavy metal cations such as Cu^{2+} and Pb^{2+}, interaction with PA-coils is even stronger than those exerted by alkaline earth cations [15, 17, 18]. Thus the critical salt concentration was lower compared to the divalent alkaline earth cations and the location of the precipitation threshold was much less sensitive to ion exchange pressure exerted by an inert salt [15]. Although no systematic study was done on the Ag^+-PA system, an investigation of a few Ag^+-PA solutions demonstrated that a strong change of all molecular parameters occurs if a few percent of COO^--groups were decorated by Ag^+ ions [19].

As in H-type precipitation, redissolution of the precipitate in the presence of specifically interacting cations may also occur. Two origins for this redissolution are given in literature. Due to the complexation of multivalent cations some backbone sections of the polymer coil are positively charged and fully dissociated sections are negatively charged. Therefore, one possible reason for redissolution is a screening of attractive interactions between oppositely charged backbone sections while the concentration of multivalent ions is significantly increased [7, 20]. Alternatively, monodentate binding of multivalent cations may surpass the point of electro-neutrality and leads to a charge inversion of the polyelectrolyte chains, which then become redissolvable [7, 21].

1.1.2 The Role of PA in the Photoreduction of Ag⁺ ions

A photochemical decomposition process of Ag^+-PA compounds (Figure 1.1) to Ag-sols had been first reported by Kubal in 1962 [22]. When a hydrophilic alkaline PA solution is added to $AgNO_3$ solution a whitish gelatinous precipitate is formed. Exposed to light it becomes quickly lemon colored. After a longer time in diffused daylight the precipitate turns into red and after some days it changes into dark violet. Direct sunlight and UV-light accelerate the photochemical reduction of Ag^+ ions, whereas Ag^+-PA solution prepared in the absence of actinic light changes color very slow. This visibility study suggested that various colours of the solutions indicate that the photochemical decomposition is accompanied by the formation of colloidal silver at various degrees of polydispersity [22]. Thus one year later Kubal [23] investigated the irradiated aqueous solutions of $AgNO_3$ in the presence of polymethylmethacrylate chains in more detail and concluded that size dispersity of the silver hydrosols can be varied with type and duration of the radiation.
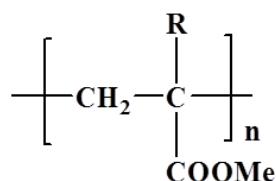
Figure 1.1 General formula of alkaline polyacrylates, where $R = CH_3$, C_2H_5, etc. and $Me = Na^+$, K^+ or other alkaline elements [22].

The research had been extended on the photolysis of Ag^+-PA salts of high molecular carboxylic acids, such as polyacrylic acid, polymethacrylic acid, poly-*L*-glutamic acid, alginic acid, pectic acid, carboxymethylcellulose and cellulose acetate phthalate [24]. Thin silver films on the polymer film were produced in the following way: Polymer coated glass plates were at first immersed into $AgNO_3$ solution for an hour and successively washed with water to eliminate $NaNO_3$ and excess of $AgNO_3$. After irradiating with UV-light under humid atmosphere dried films at first became brown due to the formation of colloidal silver particles. When irradiation was continued, a thin layer of metallic silver on the polymer film was formed [24].

Later, the process of Ag^+ ion reduction in aqueous solutions to Ag atoms, clusters and colloids had been extensively studied by γ-radiolysis or photolysis [25]. Since silver atoms and clusters are highly sensitive to coalescence and corrosion, those studies [25] had been done using fast techniques which generate Ag clusters as transients. Henglein et al. [26] first succeeded to obtain Ag clusters containing polyphosphate with a lifetime of hours. In their next work Henglein et al. [27] showed that radiolytic reduction of $AgClO_4$ solutions containing PA leads to the formation of long-lived oligomeric silver clusters which are stabilized on the PA-chains. The large reactivity of Ag clusters towards nucleophilic reagents was explained by the high coordinative unsaturation of the Ag atoms in the

clusters, which leads to the stabilization of the clusters by the anionic groups of the polymers [27]. Additionally, Coulomb repulsions between the chains prevent the clusters from getting into close contact easily. On the same year 1990 in another work by Belloni et al [28], an ultra-slow aggregation process for Ag clusters in solution was reported. The capability of PA to stabilize Ag clusters even for many days in the presence of air was confirmed [28].

High interest in the production of Ag films was continued by Yonezawa and co-workers [29]. Strong radiation at 253.7 nm (photolysis) of silver alginate films at different temperature and pressure demonstrated formation of colloidal and metallic silver similar to results reported by Konishi et al. [24]. Furthermore, formation of large Ag_n^{m+} clusters stable for many hours was characterized by UV-vis spectroscopy. Registered peaks correspond to the same absorption peaks assigned by Henglein et al [27].

These works [26-29] can be counted as first analytically proven evidences for the efficient stabilization of the primary entities (Ag clusters) by PA and other high molecular carboxylic acids in the silver nanoparticle (Ag-NP) formation induced by UV-illumination. The photochemical reduction of Ag^+ ions in the presence of carboxylate was suggested to occur as one-electron transfer process from the carboxylate ion to the bounded Ag^+ ion giving rise to Ag atoms. In References [29, 30] such an issue was studied using silver alginate where the latter one was proposed to serve as a reagent for photolysis and the matrix to stabilize photolytic silver (Figure 1.2).
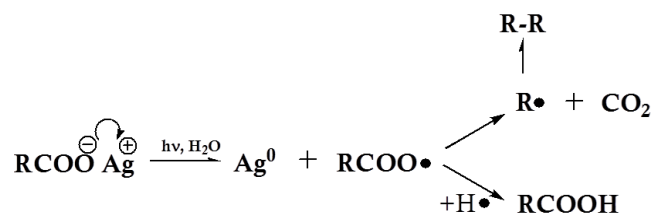
Figure 1.2 Reaction scheme of photochemical reaction [29, 30].

Henglein et al [31, 32] tried to resolve step by step the reduction mechanism of Ag^+ ions on PA towards Ag-NPs in aqueous solution by means of γ-radiolysis where the generated hydrated electrons are the primary reducing agents. Their aim was to characterize the colored $(Ag_n)^{m+}$-PA complexes and compare the radiolytic reduction of Ag^+ ions in the presence of PA to the one in the absence of the polyelectrolyte. These works [31, 32] confirmed the fact that PA strongly retards the growth of silver clusters. Pulse radiolysis study on very early stages of the reduction processes in the presence of polyacrylate qualitatively showed that elementary processes in the growth of small Ag-NPs are affected by a polymer due to inter- and intrachain reactions [32].

The exact structure of the colored complexes remained unknown, however the following hypotheses based on the experimental observations were proposed [31]. Besides using a sodium polyacrylate sample, Henglein et al. [31] used carboxylated polyacrylamide

samples with 10% and 70% carboxylate content. Blue complexes were formed from rose ones when a polyacrylate and 70% carboxylated polyacrylamide samples have been used as the complexing agents. If a polyacrylamide sample with a lower carboxylate content has been used even at a high total amount of COO^--groups, solutions stayed rose [31].

The rose complex was thought to be the Ag_4^{2+}-PA^- species [27], whereas blue complexes, $(Ag_{m+4})^{m+}$, are lager species consisting of a small number of Ag^+ and Ag^0 which are complexed by the COO^--groups of PA [33]. Thus, from these experiments Henglein et al. [31] concluded that a high density of the adjacent carboxyl groups is necessary to form larger blue Ag clusters. They assumed that the latter ones are related to a linear chain of silver atoms and silver ions along the polyacrylate chain, where the number of both Ag^+ and Ag^0 are roughly equal [31].

Further research was focused to study the size and morphology of Ag-NPs formed under UV-illumination of Ag^+-PA solutions. Shiraishi et al. [34] prepared small (ca. 4 nm) Ag-NPs by UV-irradiation of $AgClO_4$ solution in the presence of PA and studied their catalytic activity for the oxidation of ethylene. They used an ethanol-water mixed solution as a solvent, where alcohol acts as radical scavenger and additional reducing agent.

The work by Sergeev et al. [35] demonstrated that depending on the degree of dissociation of PA, i.e, pH of Ag^+-PA solutions, and the ratio between Ag^+ and PA a varying size and shape of Ag-NPs can be obtained. Later, the same author [36] showed that if light sources used in the photoreduction emit over a wide spectral range (without use of cut-off filters) the appearance of nanoparticles can cause photocatalytic reduction of cations on their surface due to plasmon absorption of light. Changes in the spectral composition of the light source revealed the competing photoreduction of Ag^+ ions by PA in the bulk and on the surface of Ag-NPs, which is accompanied by their coalescence [36].

Huber et al. [19] studied the formation of Ag-NPs embedded in long-chain NaPA chains. TR-SLS experiments on Ag^+-PA revealed that the addition of silver ions induces coil shrinking and aggregation of the PA. After exposure to UV-light, small Ag-NPs are formed within the shrunk PA-coils. Like Henglein et al. [31] this work emphasized [19] the fact that no Ag-NPs are formed upon UV-irradiation in the absence of polyelectrolyte or if the molecular weight of the PA-chains is as small as 149 kDa.

The effect of the reduction method in Ag^+-PA systems (UV-exposure or use of the chemical reducing agent $NaBH_4$) on the final size and shape of the Ag-NPs had been compared by Lo Nostro et al. [37] with a few Ag^+-PA solutions. The results obtained by their experimental procedures revealed that Ag-NPs prepared upon both reduction routes exhibit the presence of a population of ultrasmall spherical Ag-NPs (< 2 nm) and of a population of larger Ag-NPs (3-6 nm). If $NaBH_4$ is used, the population of large particles is predominant, while smaller particles dominate under UV-irradiation of Ag^+-PA solutions. Additionally, higher molecular weight PA sample in a combination with $NaBH_4$ lead to a formation of bigger Ag-NPs, while under UV-exposure the opposite effect has been observed. Besides, with UV-illumination method the formation of Ag-NPs is slower

than that with $NaBH_4$. Hence, longer PA-chains can perform their templating effect more efficiently once the reducing agent is the UV irradiation [37].

Due to a high demand of Ag-NPs in catalysis, biotechnology, photonics and electronics, the research was aimed at obtaining a certain particle size, particle size distribution, particle shape, etc. In order to achieve such concrete tasks more complex systems and procedures had been applied, however, in many of them PA remained to act as reducing and stabilising agent. Combinations of PA with further additives are very diverse and in the following paragraph only a few prominent examples are presented.

Thus monodisperse spherical Ag-NPs with a size below 100 nm were prepared by addition of $NaBH_4$ into the inverse micelles of poly(4)-oxyethylene lauryl ether which contain Ag^+-PA solution [38]. Dendritic Ag-NPs (< 500 nm) have been prepared using ascorbic acid as a main reducing agent and PA as a stabilising agent in aqueous solution [39]. Stable colloidal solution of Ag-NPs of ca. 7 nm size were fabricated reducing Ag^+ ions by $NaBH_4$ in aqueous PA solution and successively dispersing PA-protected Ag-NPs into aqueous protein solution (bovine serum albumin) [40]. Spherical Ag-NPs possessing an average diameter of 7 nm were at first synthesised by chemical reduction of $AgNO_3$ with t-BuONa-activated NaH in THF and then dispersed in acrylic formulations composed of tetrahydrofurfuryl acrylate, polyurethane acrylate and polyethylene glycol diacrylate [41]. Ag-NP dispersions with a mean particle diameter of 9-30 nm were synthesized using hydrazine hydrate and sodium citrate as reducing agents and sodium dodecyl sulphate as a stabilizing agent and tested as antibacterial active compounds [42]. Comparably monodisperse spherical Ag-NPs in the size range of 28 nm to 77 nm were prepared by reduction of cationic complexes $[Ag(NH_3)_2]^+$ by D-maltose in the presence of different concentrations of high molecular weight PA [43] and tested as catalysts for redox reactions. In this work it was shown that PA influences both nucleation process and subsequent stage of nanoparticle growth [43].

1.1.3 Spherical Polyelectrolyte Brushes

If long linear polyelectrolyte chains are grafted densely to a solid surface, a polyelectrolyte brush results [44] (Figure 1.3). The term "brush" implicates that the grafting of the chains is sufficiently dense, that is, the average distance between two neighbouring polymer chains (D) is distinctly smaller than two times the radius of gyration (R_g) of the respective free polymer chains. At low grafting density, i.e., if D is greater than R_g, two tethered chains feel no interaction. If polymer chains are poorly soluble in the solvent, it is favourable for them to lie flat on the surfaces. This is the so-called "pancake" conformation (Figure 1.3). If polymer chains are well soluble in the solvent, they form a "mushroom" structure [44].

"pancake"　　　"mushroom"　　　"brush"
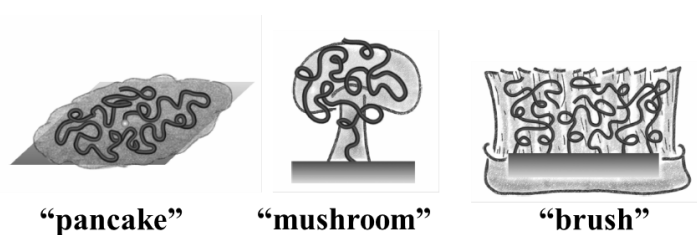
Figure 1.3 Sketch for possible conformations of polymers grafted to a surface [44].

Besides the grafting density and the solvent quality, the curvature of the surface is important. When polyelectrolyte chains are densely grafted on a planar surface, planar polyelectrolyte brushes are formed. Star-polymers consist of polymer chains (arms) of equal length joined at a central "branching point". Grafting linear polyelectrolyte chains densely to colloidal core latex particles leads to spherical polyelectrolyte brushes (SPBs). The grafting density, charge density and particle size can easily be varied by different synthesis conditions.

Polymer brushes are typically synthesized by two different methods, physisorption and chemical bonding. Typically, polymer brushes synthesized using a physisorption approach consist of two-component polymer chains, where one part strongly adheres to the interface and the second part extends to generate the polymer layer [45]. However, the interaction between polymer chains and colloid surface is mostly caused by van der Waals forces or hydrogen bonding. Brush layers are thus unstable and can be thermally or solvolytically desorbed or displaced by other polymers or small molecules.

The chemical bonding of polymer brushes can be classified as "grafting to" and "grafting from" techniques (Figure 1.4). A preformed macromolecule possessing a suitable end-functionality is utilized with a reactive substrate to generate the polymer brush in the "grafting to" technique. The available polymerization methods offer an advantage of synthesizing polymer chains possessing narrow molecular weight distributions, however only moderate molecular weight polymers can be used in this approach. Higher molecular weight of the polymer chains gets, more difficult for the anchor groups to reach the surface of the substrate. The disadvantage of this technique is that it often leads to low grafting densities and low film thicknesses, as the polymer molecules must diffuse through the existing polymer film to reach the reactive sites on the surface.

Steric hindrance for surface attachment increases as the thickness of tethered polymer film increases in the case of "grafting to". To overcome this problem, the "grafting from" approach can be used to prepare dense covalently tethered polymer brushes. The "grafting from" technique involves the immobilization of initiators on the substrate followed by *in situ* surface initiated polymerization to generate the tethered polymers. Using this "grafting

from" technique, the grafting density and molecular weight of the polyelectrolyte brushes can be easily controlled by adjusting the polymerization conditions.
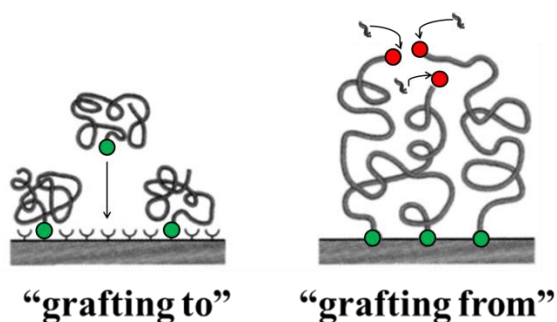
Figure 1.4 Schematic illustration of different processes used for the attachment of polymers to surfaces [44].

Photo-emulsion polymerization is a widely used "grafting-from" technique leading to a dense layer of chemically bound polyelectrolyte chains [46-48]. Figure 1.5 displays schematically the synthetic route of this approach, which is also applied in this thesis [46-48]: First, nearly monodisperse PS cores are synthesized by a conventional emulsion polymerization. Successively a thin layer of a suitable photoinitiator is co-polymerized onto these cores. This second step proceeds as a seeded emulsion polymerization in which the concentration of a new monomer is kept low enough in order to avoid formation of new particles. In a third step a water soluble monomer is added to this core-shell latex and radicals are generated on the surface of the particles by exposure to UV-light. These radicals start a polymerization on the surface and the chains are growing directly from the surface. The fact that the core latex is strongly scattering the incoming light is very helpful in the process of photoemulsion polymerization: light is scattered many times within the turbid latex suspension, which increases considerably the quantum yield of the photoinitiator [46-48].
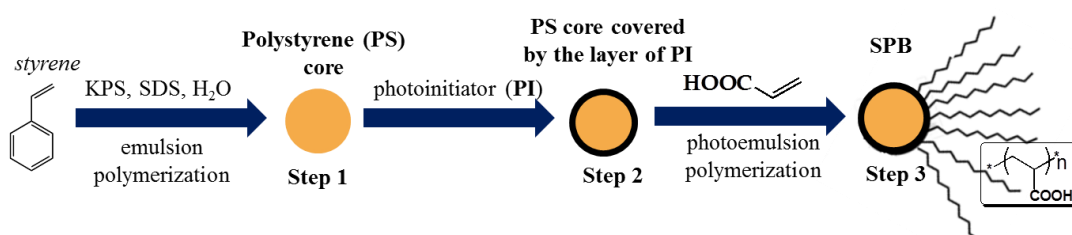
Figure 1.5 Schematic representation of the SPB synthesis: in the first step a polystyrene latex (PS) is generated, which is covered by a thin layer of the photoinitiator in the second step. Photoinitiation in the presence of water soluble monomers as acrylic acid in the third step leads to polyelectrolyte chains grafted onto the surface of the PS-cores.

The SPB are characterized by three parameters: the core radius $R_{h,PS}$, the contour length L_c of the grafted chains and the grafting density σ giving the number of grafted chains per nm^2. All parameters can be determined by the routines described by Ballauff et al. [46, 49].

In SPBs immersed in a solution at low ionic strength the local concentration of ions inside the brush is noticeably different from their bulk values, and screening of the electrostatic repulsion between the polyions is carried out by the counterions trapped inside the brush. Trapping is balanced by the osmotic pressure of the counterions. The regime at low ionic strength is referred to as the "osmotic" regime [50]. In the opposite limit ("salt dominance" regime), in ''salted brush'' the concentration of added salt approaches the concentration of the counterions within the brush. In this limit the electrostatic interaction is strongly screened and the brush layer can be treated as a virtually neutral system [50].
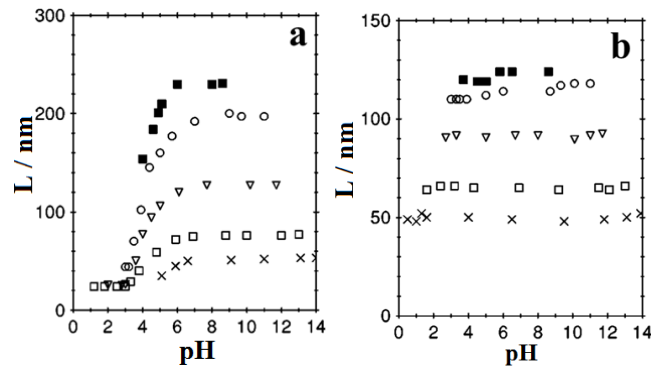
Figure 1.6 Dependence of brush thickness L on pH for an annealed brush (a) and quenched brush (b). The parameter of the data is the ionic strength in the solution, which was adjusted by adding KCl: 1 M ($\times$), 0.1 M ($\square$), 0.01 M ($\triangle$), 0.001 M ($\bigcirc$) and 0.00001 M ($\blacksquare$). The latex samples L23 and LQ4 was used. [51]

By attaching weak polyelectrolytes as polyacrylic acid to solid surfaces an annealed brush is generated [51]. Here the degree of charging of the monomeric units depends on the pH within the brush. Changing the pH from low to high values therefore leads to the transition from a virtually uncharged to a highly charged system. The strong dependence of the brush layer consisting of PA chains on pH is directly seen in Figure 1.6a taken from reference [51], where the thickness L is plotted against the pH adjusted in the system. The thickness can be obtained from the hydrodynamic radius $R_{h,SPB}$ of the brush and the hydrodynamic radius of the practically monodisperse core particles $R_{h,PS}$ via following equation

$$L = R_{h,SPB} - R_{h,PS} \tag{1.2}$$

Figure 1.6a shows that L may increase by nearly one order of magnitude when going from low to high pH. The reason for the strong stretching derives from the fact that the PA

chains become more and more charged if the pH is raised. At low ionic strength the counterions generated in this process, however, cannot leave the brush as discussed above [50]. The enormous osmotic pressure within the brush built up by the counterions in the brush may stretch the chains to nearly full length. At a high ionic strength the effect of stretching is much less pronounced [51].

A brush is denoted as quenched brush if strong polyelectrolyte chains such as, for example, polystyrene sulfonate chains, are grafted to a surface. A similar study of the respective quenched SPB demonstrates that no change takes place upon changing the pH if the ionic strength is kept constant at the same time (Figure 1.6b). In this case the charges along the chains are independent of the pH in the system and the thickness of the brush is determined by the ionic strength only [50, 51].

When a salt comprising multivalent counterions is added to SPB, the shrinking of the brush layer is much more pronounced than in case of monovalent ions. A review of this topic was recently given by Jusufi et al. [52]. There, the process of shrinking and precipitation of SPBs in the presence of divalent or trivalent ions is explained in terms of a model in which coiling of the polymer chains is balanced by the osmotic pressure of the counterions. Due to a decreased number of counterions, multivalent counterions exert a smaller osmotic pressure than monovalent ions do and thus enable chains to further shrink. Ion-specific effects, which were earlier suggested from experiments by Rühe et al. [53, 54] and Ballauff et al. [55], are neglected by this model.

Polymer brushes are widely applied as templates for metallic nanoparticles. Since the latter ones must be stabilised in solution in order to prevent their aggregation, carriers systems such as dendrimers [56], microgels [57] and latex particles [58] are very suitable to immobilize them. A few examples exist where polymer brushes had been applied in Ag-NP production.

"Nano-tree"-type SPB particles were presented by Lu et al. [59] where poly(ethylene glycol) methacrylate macromonomers were densely grafted via photoemulsion polymerisation on PS-cores. The system had a shell consisting of regularly branched chains. These "nano-tree"-like particles were used as nanoreactors for the generation and immobilisation of Ag-NPs with a diameter of ca. 7.5 nm. Ag-NPs were synthesised by means of $NaBH_4$ as reducing agent and scrutinized as catalytic agents in the reduction process of 4-nitrophenol [59].

In situ formation of Ag-NPs in SPB during photoemulsion polymerisation was reported by Ballauff et al. [60] where silver acrylate was used as a functional monomer instead of acrylic acid (Figure 1.5). The catalytic activity of those well-dispersed small Ag-NPs with a diameter of ca. 3 nm was investigated by monitoring the reduction of 4-nitrophenol [60].

Immobilisation of Ag-NPs onto pH-responsive poly(2-vinylpyridine) (P2VP) brushes was reported by Stamm et al. [61]. The process involved chemical grafting of P2VP chains on the underlying substrate in brush topology (Figure 1.3) followed by the chemical

reduction of AgNO$_3$. Here, the effect of Ag$^+$ concentration and the reduction time on the immobilization process was demonstrated [61].

Silver and nickel nanoparticles with an average size of ca. 9 nm and ca. 4 nm, respectively, were prepared by chemical reduction of Ag$^+$ and Ni$^+$ absorbed as counterions inside of the PA-shell grafted to spherical polybutadiene (PB) cores [62]. This work was focused on presenting a novel method to prepare SPBs. The grafting of a PA-shell was performed without having to use an initiator with C=C double bonds. The PA-chains were grown from the PB-core by direct thermo-initiated emulsion polymerisation having made use of abundant double bonds in PB [62].

The catalytic effect of Ag-NPs immobilized in spherical polyacrylate brushes was studied by Guo et al. [63]. Strong catalytic activity of Ag-NPs on the reduction of 4-nitrophenol by NaBH$_4$ was further accelerated by the addition of α-cyclodextrin. Besides this issue the authors reported a slight variation in the size distribution of the Ag-NPs, with an average size of 3 nm, by varying the temperature during the chemical reduction process of AgNO$_3$ by NaBH$_4$ [63].

1.1.4 Raspberry-like Metamolecules

Many familiar optical properties of materials, for example, their colour or refractive index, arise from the interaction of the electric field of light with matter. However, as demonstrated in the field of metamaterials, where artificial media is structured on a scale smaller than the wavelength of an external stimulating wave [64, 65], controlling the interaction of the magnetic field of light with matter can yield unprecedented optical properties [65, 66]. Some of the very exciting applications of metamaterials exhibiting a magnetic response in the regime of visible wavelengths are electromagnetic cloaking devices [67-69] and subwavelengh optical imaging [70]. Materials with magnetic resonance operating in the optical-frequency regime do not exist in nature, therefore such a phenomenon is called artificial magnetism [66, 71].

Using classical top-down nanofabrication technologies, such as electron-beam lithography [72] or focused-ion beam milling [73], structures exhibiting a strong magnetic dipolar response at optical frequencies have been fabricated. However, they suffer from many limitations. For example, it is difficult to achieve bulk materials, required for realistic applications. Moreover, these structures are all geometrically strongly anisotropic. This means, that the strongest magnetic response corresponds to one specific direction of the propagation of electromagnetic waves, and there are directions for which no magnetic response can be observed [74]. Therefore, many theoretical [71, 74-77] and experimental works [78-83] were devoted to design fully three-dimensional structures (situated not in a planar fashion on a substrate) with an isotropic magnetic response in the visible range.

Among them are clusters consisting of dielectric spherical cores decorated by a large number of isolated, nonteaching metallic nanospheres (Figure 1.7) [75, 76, 78].
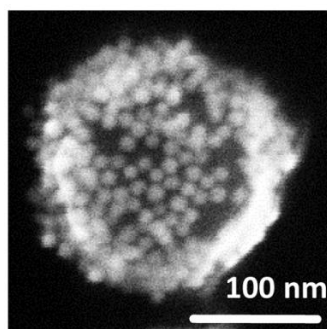
Figure 1.7 Scanning electron micrograph of a core-shell cluster (silica sphere decorated by gold particles fabricated via "thiol assembly") [78].

The optical response of such core-shell clusters is dominated by the arrangement of metallic spheres on the dielectric core [78] and originates from the combination of plasmonic resonances of the individual metal nanoparticle. Surface plasmon resonance of a single metal nanoparticle occurs in the following way: When an electromagnetic wave illuminates nanoparticles, the conduction-band electrons of the metal nanoparticle will be replaced from their equilibrium positions with respect to the center of mass of particles, e.g. nucleus (Figure 1.8). The direction of the displacement depends on the direction of electric field. The direction of the electric field of the electromagnetic wave changes periodically, and the displacement of the electrons also changes periodically like an oscillation of electrons with respect to their "nucleus". Such oscillations in the optical frequency range involve mostly the conduction-band electrons located near the surface of metals due to a skin effect. For example, the "depth" of the involved electrons in case of silver excited in the range of visible light is ca. 6 nm. The energy of the electromagnetic wave will be absorbed when its frequency matches the resonance frequency of metal nanoparticles. The absorbed energy will be used to cause the oscillations of electrons. The resonance frequency depends on the permittivity of the metal, and the size, shape and surrounding medium of the metal nanoparticles [84].
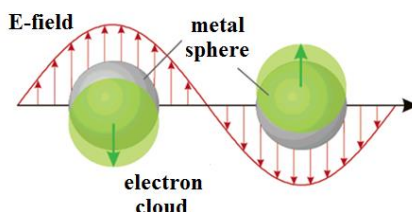
Figure 1.8 Schematic of plasmon oscillation for spherical particles, showing the displacement of the conduction electron charge cloud relative to the nuclei [84].

At a distinct frequency where the excited electric dipoles in metal nanoparticles are oscillating 180° out of phase antisymmetric resonances were forecast [85]. This means that the electric dipole contributions of the metal nanoparticles which establish the shell can be coupled and oscillating around the dielectric core perpendicular to the polarization of the incident magnetic field and therefore result in a magnetic dipole of the entire core-shell cluster parallel to the incident magnetic field. Such magnetic dipole can be identified in Figure 1.9 by looking at the magnetic field distributions reported by Mühlig et al. [78]. The resulting enhancement inside the core sphere of the magnetic field is comparable to the near field distribution of a pure magnetic dipole [78].
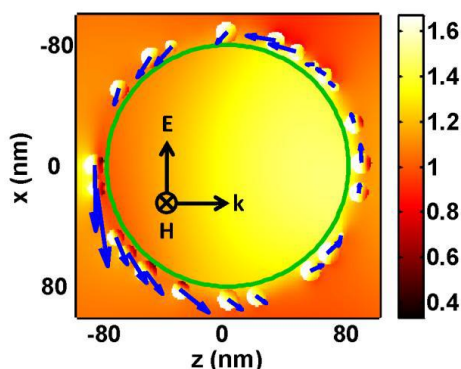
Figure 1.9 Distribution of the magnetic field of core-shell clusters at the magnetic dipole resonance frequency (685 nm). Only the y-component of the magnetic field (normalized to the incident plane wave) is shown in a plane through the center of the core sphere (green circle). The blue arrows depict the excited electric dipole moments in the gold spheres. The direction of the arrows decodes the direction of the excited dipole in the xz-plane and the length decodes the strength of the excited dipoles at the center of each gold nanosphere. The center of each arrow coincides with the center of one gold sphere in the shown plane. [78]

Current progress in colloidal nanochemistry led to many of such core-shell structures. For example, raspberry-like plasmonic nanostructures were synthesized using a surfactant-assisted template seed growth method of gold nanoparticles on the PS-cores [81]. In another example, Urban et al. [82] have fabricated three-dimensional gold nanoparticle clusters by the self-assembly of PS-grafted gold nanospheres and an amphiphilic polymer. Sheikholeslami et al. [80] have prepared a metafluid by assembling Ag-NPs based on protein-directed interactions. Mühlig et al. [78] first compared the measured extinction spectra of core-shell composites (Figure 1.7) with sophisticated simulations thereof and revealed the relation of the optical response to the excitation of an isotropic magnetic dipole resonance by a red-shifted peak on the extinction spectra. Thus, UV-vis spectroscopy can be used as a fast and cheap method to estimate whether the synthesized satellite particles can exhibit artificial magnetism.

1.2 Motivation and Goals of the Present Work

Nobel metal nanoparticles have been the subject of numerous studies due to their unique optical, electronic, mechanical, magnetic and chemical properties that are significantly different from those of bulk materials. These special properties can be attributed to their small size and large specific surface area. Among these particles, silver nanoparticles (Ag-NPs) have been widely studied due to their diverse applications in catalysis [86], biotechnology [87], photonics and optoelectronics [80] and antimicrobial activity [88].

A variety of preparation routes have been reported to control particle shape, particle size and size distribution of Ag-NPs [89-91] and the assembly of Ag-NPs to hierarchical super structures [92]. From the very beginning of these studies, polyacrylic acid and its sodium salts (NaPA) have attracted much interest due to their assistance of the preparation of Ag-NPs via a photoreduction of Ag^+ as well as due to hosting and protecting the growing Ag-NPs [19, 22, 27, 36, 43, 93]. The Ag-NP formation already occurs upon exposing dilute Ag^+-PA solutions to UV-light in the absence of any further reducing agent [19, 22, 36]. If reducing agents have been added to Ag^+-PA solutions [43, 93] or if the latter ones have been combined with surfactant/polymer molecules [38, 40], PA supports the generation of Ag-NPs even more efficiently.

PA are polymers with a negatively charged carboxylate function at every other C-backbone atom and belong to the most frequently applied polyelectrolytes both in household, e.g. scale inhibitors in laundry processes, and industry, e.g. dispersant agents in suspensions of inorganic particles [94]. Aside from their technical significance PA serve as excellent model polyelectrolytes in fundamental research. Highly specific interactions, such as complexation between the polyions and bivalent alkaline earth [6, 10, 11, 95] or transition metal cations [15, 17] (M^{n+}), may cause a coil collapse and a precipitation of PA. The mechanism of collapse/aggregation of single coils along with a shape of formed M^{n+}-PA entities may be relevant for the development of new responsive materials and for a deeper insight into a complex interaction pattern of proteins containing COO^- residues in saline media of living systems.

Hence, investigation of the Ag^+-PA system has a multifold relevance: (i) COO^--groups of PA-coils can form complex bonds with Ag^+ ions, leading to distinct conformational changes of polymer chains and to intermolecular bridges among the PA molecules. Although Ag^+ ions are transition metal cations, they are monovalent, which makes them particularly interesting candidates for a comparative study of its specific interactions with interactions exerted by monovalent inert non-specifically interacting cations like Na^+ ions or bivalent specifically interacting cations, e.g. alkaline earth cations, Cu^{2+} or Pb^{2+}. (ii) Ag-NP formation induced by exposure of Ag^+-PA solutions to UV-light without additional reducing agents can be directly correlated to the intra- and intermolecular organisation within the Ag^+-PA entities. Thus, information from item (i) may help to control the size/shape of Ag-NPs generated in a very simple way.

Aside from linear PA-chains, which are homogeneously distributed in the solution, morphologically different PA particles, such as spherical polyelectrolyte brushes (SPBs) with a shell constituting of PA chains, can be considered as a second type of PA systems analysed with respect to the same issues stated in the previous paragraph. In SPB linear PA-chains are densely grafted to a spherical polystyrene (PS) core via covalent bonds [46, 47]. The local concentration of COO^--groups within the PA-layer is considerably higher than in case of dilute solutions of linear PA-chains and the mobility of single PA-chains therein is drastically restricted. Therefore, the interaction pattern between SPB and Ag^+ ions as well as the photoreduction process of Ag^+ ions may significantly vary from that of linear PA-chains.

SPBs have been widely reported as novel carriers which generate well-defined metal nanoparticles with a narrow-size distribution *in situ* [62, 64, 86, 96-98]. The main purpose of those studies was to substantially decrease aggregation of small metal nanoparticles and thereby retain and increase their catalytic activity. However, aside from catalysis, SPBs can rate as promising candidates also in the field of metamaterials, where the control of the interaction of the magnetic field of light with matter can yield unprecedented optical properties [64-66]. Synthesis of densely packed Ag-NPs localized on the dielectric PS cores may be considered as a novel route to Ag-SPB core-shell/satellite/raspberry-like metamolecules [75, 76]. Additionally, since fabrication of such Ag-SPB particles can be performed using only one solvent (water), another long range perspective is available: formation of a photonic crystal, where aforementioned metamolecules are arranged in a three-dimensional lattice.

This work is intended to investigate two PA systems with respect to the specific interactions with Ag^+ ions: dilute solutions of linear PA chains and highly diluted suspensions of SPBs, where the shell is formed by PA chains. Whereas for the study of linear chains commercial NaPA samples have been used, the SPBs have been synthesized and characterized in the present Thesis using a method introduced by Ballauff et al. [46, 47]. In case of SPBs the molecular weight of PA is by a factor of 10-20 smaller than the one of linear chain PA samples.

The analysis of the Ag^+-PA/Ag^+-SPB systems is suitably carried out by static and dynamic light scattering techniques (SLS and DLS). Combined SLS and DLS methods can not only quantify the size of particles, but also give indications for their shape. Time resolved SLS/DLS experiments are expected to offer insight into the mechanism of the possible aggregation in Ag^+-PA and Ag^+-SPB solutions. Whereas SLS and DLS are highly suitable to analyse conformational changes of PA-coils or the extent of shrinking of PA-layers belonging to SPBs, anomalous small-angle X-ray scattering (ASAXS) may quantify the amount of condensing specifically interacting Ag^+ counterions.

Another goal of this work is to use the investigated properties of Ag^+-PA and Ag^+-SPB systems in order to develop a controlled formation of Ag-NPs under exposure to UV-light thereof. UV-vis spectroscopy and electron microscopy (SEM and TEM) are used as analytical techniques to characterize the resulting Ag-NPs. Besides a photoreduction method, Ag-NPs are prepared using a chemical reducing agent ($NaBH_4$) in Ag^+-SPB solutions in order to substantially increase their number on the surface of PS-cores and hence validate hybrid Ag-SPB systems as potentially candidates in the field of metamaterials.

2 Methods and Instruments

The present Chapter describes the main principles of the characterisation methods as well as the corresponding instruments, which have been used to analyse the investigated systems. Light scattering methods, as techniques used the most frequently in this work, are described in more detail.

2.1 Light Scattering

As an electromagnetic wave light interacts with the charges constituting a molecule. This interaction is defined by the polarizability of the molecule. The electric wave of the incident light induces a periodic modulation of the atomic nuclei and the electrons. Thus the molecule constitutes an oscillating dipole or electric oscillator, which acts as an emitter of an electromagnetic wave of the same wavelength as the incident light, emitted isotropically in all directions perpendicular to the oscillating dipole. (i) The scattering intensity is proportional to the total number of scattering centers one particle/molecule contains, which allows to determine the molecular weight of this particle/molecule. The interference pattern of intraparticular scattered light is called particle form factor ($P(q)$) and characterises the shape and size of the particle. (ii) At the same time particles in solution undergo Brownian motion caused by thermal density fluctuations of the solvent. These temporal changes in interparticle positions and the corresponding temporal concentration fluctuations lead to the changes with time of the interference pattern. The resulting scattered intensity enables to measure the diffusion coefficient of the scattering particles in solution.

Items (i) and (ii) establish the base for static and dynamic light scattering, respectively. The general principles and theories behind these two techniques will be given in the two following Chapters. Detailed information on these methods can be found in the text books by Lindner and Zemb [99], Berne and Pecora [100], Chu [101], Schärtl [102], Teraoka [103], Colby and Rubinstein [104].

2.1.1 Static Light Scattering

We begin to discuss static light scattering (SLS) technique with a schematic representation of an experimental setup used for light scattering measurements (Figure 2.1). A portion of the sample that is illuminated by the incident beam and at the same time being visible for the detector is called scattering volume V_s. It depends on the scattering angle θ. The light source, which is in our case a He-Ne laser operating at 632.8 nm, and the detector are aligned in the horizontal yz plane. Light scattered by an angle θ in the horizontal yz plane at a distance r from the sample is analysed by the detector.
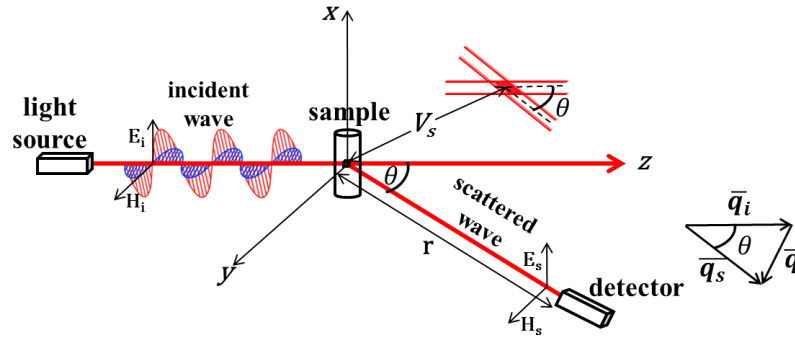
Figure 2.1 Schematic representation of an experimental setup for light scattering measurements.

The direction of propagation of a vertically polarized incident light and scattered light is shown with the initial ($\bar{q}_i$) and scattered ($\bar{q}_s$) wave vectors, respectively. The value of the scattering vector or momentum transfer $\bar{q}$ derived from a given geometry as $\bar{q} = \bar{q}_i - \bar{q}_s$ (Figure 2.1) is related to the scattered angle θ via the following relationship

$$q = \frac{4\pi n}{\lambda_0} sin(\frac{\theta}{2})$$
(2.1)

where n is the refractive index of the solvent and λ_0 is the laser wavelength in vacuum.

In order to describe a measure of the scattered light, which is independent of the apparatus characteristics but only depends on the properties of the system, the Rayleigh ratio ΔR_θ is introduced [105], which in case of polarised light has the following expression [106, 107]

$$\Delta R_\theta = \frac{I_S(\theta)\, r^2}{I_0 V_S(\theta)}$$
(2.2)

where the subscript θ indicates that the Rayleigh ratio is a function of the scattering angle. $I_s(\theta)$ is the intensity of the scattered light measured at the angle of observation θ and I_0 is the intensity of the laser.

A particle or a molecule scatters light isotropically, when the light contributions scattered from the constituent parts (subunits) of the molecule/particle are in phase, i.e., have no phase difference. This will be the case if the molecule/particle is much smaller than the wavelength of the impinging light ($< \lambda_0/20$). If, on the other hand, the scattering particles are big enough, the intensity of the scattered light will decrease with increasing scattering angle (or with increasing q value) [102]. Measuring the intensity of the scattered light for a solution of particles yields the form factor, $P(q)$, as the normalised scattering intensity:

$$P(q) = \frac{I_s(q)}{I_s(0)} \tag{2.3}$$

where $I_s(0)$ is the scattering intensity at zero scattering angle (i.e. zero q value). As this value is not accessible to direct measurement because a detector placed at zero scattering angle would see mainly the direct laser beam, $I_s(0)$ has to be determined by extrapolation of $I_s(q)$ to $q = 0$.

The general expression for the form factor of any molecule consisting of n identical point-like subunits with pair-wise distances r_{jk} is [107]

$$P(q) = \frac{1}{n^2} \sum_{j=1}^{n} \sum_{k=1}^{n} \frac{sin(qr_{jk})}{qr_{jk}} \tag{2.4}$$

If $q \cdot r_{jk} < 1$, the form factor can be approximated by its Taylor series expansion. Keeping the first two terms, one gets the following equation

$$P(q) \approx 1 - \frac{1}{3} q^2 \langle s^2 \rangle \tag{2.5}$$

where $\langle s^2 \rangle$ is the mean square radius of gyration defined as

$$\langle s^2 \rangle = \frac{1}{2n^2} \sum_{j=1}^{n} \sum_{k=1}^{n} r_{jk}^2 = \frac{1}{n} \sum_{j=1}^{n} \langle r_{j,c.m.}^2 \rangle \tag{2.6}$$

where $\langle r_{j,c.m.}^2 \rangle$ denotes the average of the squared distance from the particle's centre of mass to the j'th subunit.

Net scattering intensities can be expressed in terms of the Rayleigh ratio given by

$$\Delta R_\theta = K \cdot c \cdot M \cdot P(q) \cdot B(q) \tag{2.7}$$

where c is the sample concentration in g/L, M is the molar mass and term $B(q)$ in the limit of the spherical particles is directly equal to a structure factor $(S(q))$ and for the particles which are not invariant toward their orientations $B(q)$ is more complex expression. K is the optical contrast constant which is corrected for cylindrical cuvettes (normally applied for light scattering experiments) using the Hermann-Levinson corrections [108] and defined as

$$K = \frac{4\,\pi^2\,n_{Toluene}^{2}}{N_A\lambda^4}\left(\frac{dn}{dc}\right)^2 \tag{2.8}$$

where N_A is Avogadro's number, *dn/dc* is the refractive index increment of the investigated solute in solution and $n_{Toluene}$ is the refractive index of toluene in the goniometer bath.

In practice, the Rayleigh ratio ΔR_θ of the solute particles is determined from the experimentally measured scattered intensities of the solution $I_{Solution}$, of the solvent $I_{Solvent}$ and of the standard $I_{Standard}$ (pure toluene). Renormalizing by absolute scattered intensity of the scattering standard, i.e. $RR_{Toluene}$, the excess Rayleigh ratio ΔR_θ of any solute in solution at a certain scattering angle θ is received as

$$\Delta R_\theta = RR_{Toluene} \cdot \frac{I_{Solution}(\theta) - I_{Solvent}(\theta)}{I_{Standard}(\theta)} \tag{2.9}$$

For very dilute polymer solutions in saline water (Chapters 4.1-4.2) or in very dilute suspension of colloids (Chapter 4.3) the interference pattern between different scattering particles, i.e. the structure factor *S(q)*, can be neglected since the long-range Coulomb interparticle repulsions are screened and the measured scattered intensity $I_s(q)$ is only caused by intraparticular interferences *(P(q))*. Hence, taking into account the effects of solute-solvent interactions on the measured scattering intensity and rearranging eq(2.7) with application of eq(2.5), with use of the approximation that $1/(1-x) \approx 1+x$, we receive the Zimm equation [109] for monodisperse systems

$$\frac{K\,c}{\Delta R_\theta} = \frac{1}{M}\left[1 + \frac{\langle s^2\rangle}{3}q^2\right] + 2A_2 c \tag{2.10}$$

where $\langle s^2\rangle$ is the mean square radius of gyration and A_2 is the second virial coefficient, originating from a series expansion of the osmotic pressure. The term A_2 is a measure of the thermodynamic interactions between two molecules in solution, causing systematic deviations from the ideal gas law.

Usually polymer solutions or suspensions of colloids are not monodisperse. Having a solution of n different types of particles with molecular weights M_1, M_2, …, M_n, mean square radii of gyration $\langle s^2\rangle_1$, $\langle s^2\rangle_2$, …, $\langle s^2\rangle_n$, which are present at weight concentrations c_1, c_2, …, c_n respectively, in the limit of infinite dilution we can rewrite eq(2.7) from the mixture in the following form

$$\Delta R_{\theta,t} = \sum_{i=1}^{n}\Delta R_{\theta,i} = K \cdot \sum_{i=1}^{n} c_i \cdot M_i \cdot P_i(q) \tag{2.11}$$

Via extrapolation of $\Delta R_{\theta,t}$ to zero scattering angle, all form factors $P_i(q)$ approach the value of 1. Thus, via division of the both sides of eq(2.11) by $\sum_{i=1}^{n} c_i$ we get the weight average molecular weight M_w calculated as

$$M_w = \frac{\sum_{i=1}^{n} c_i M_i}{\sum_{i=1}^{n} c_i} \tag{2.12}$$

In a similar way we can determine the z-average squared radius of gyration R_g^2 using eq(2.6) for the molecules/particles in the solution

$$R_g^2 = \frac{\sum_{i=1}^{n} c_i \, M_i \, \langle s^2 \rangle_i}{\sum_{i=1}^{n} c_i \, M_i} \qquad (2.13)$$

By means of eq(2.11-2.13) and considering the total concentration as $c_t = \sum_{i=1}^{n} c_i$, we rewrite eq(2.10) in the following form

$$\frac{K\,c}{\Delta R_{\theta,t}} = \frac{1}{M_w}\left[1 + \frac{R_g^2}{3} q^2\right] + 2A_2 c_t \qquad (2.14)$$

An alternative approach to the Zimm method for the evaluation of static light scattering experiments was developed by Guinier [110]. It showed that the form factor $P(q)$ in the case of compact structures, e.g. spheres, at small q values can be described according to the following equation

$$P(q) \approx e^{-\frac{1}{3}q^2 R_g^2} \qquad (2.15)$$

which leads to the same limiting series given by eq(2.5).

A plot of measured Rayleigh ratios or scattered intensities, $ln(\Delta R_\theta)$ or $ln(I_s(q))$ vs. q^2 is called a Guinier plot. In practice a slope $(-\frac{1}{3}R_g^2)$ is found by linear regression, which will also give $ln(\Delta R_{\theta=0})$ or $ln(I_s(0))$ from which the molecular weight may be calculated. The criterion most frequently used to ensure the validity of the Guinier approximation is that $q \cdot R_g < 1$. The Guinier evaluation was the most suitable for spherical particles.

In order to obtain "true" molecular parameters from the characterisation of the polymer standards (Chapter 3.2) simultaneous extrapolation of the scattering data $(\frac{K\,c}{\Delta R_{\theta,t}})$ from eq(2.14) to $q = 0$ and $c = 0$ is necessary. In case of PA solutions with Ag^+ ions (Chapters 4.1-4.2) or SPBs with Ag^+ or other counterions (Chapter 4.3), where the scattering depends in a complex way on the ratio between counterions ions and COO^- groups, a simple extrapolation procedure to $c = 0$ becomes impossible. Hence, the scattering curves in those cases were approximated with the angular-dependent part of eq(2.14), which renders molecular parameters M_w and R_g to apparent parameters.

2.1.2 Dynamic Light Scattering

Dynamic light scattering (DLS) is also known as quasi elastic light scattering (QELS) or photon correlation spectroscopy (PCS). The scattering geometry of DLS is the same as for SLS (Figure 2.1).

As it was mentioned in Chapter 2.1, fluctuations in the scattered intensity with time are reflecting Brownian motion and are thus carrying information about the diffusion coefficient of the moving particles. Since particles move relatively to the primary beam and the detector, in analogy to Doppler shift of acoustic waves, there is a broadening in a frequency of the scattered waves. In dynamic light scattering time-dependent intensity fluctuations of the detected scattering intensity are considered.
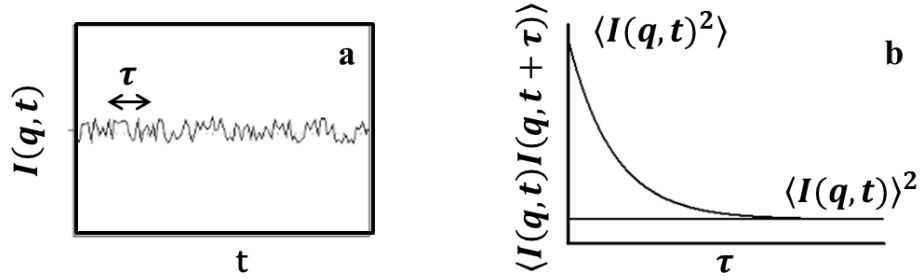
Figure 2.2 Fluctuating scattered intensity with time (a) and the corresponding intensity correlation function (b).

In order to quantitatively analyse the particles mobility by light scattering and derive their diffusion coefficient, an intensity-time correlation function $G^{(2)}$ has to be quantified first. That is achieved by comparing the scattered intensity $I(q, t)$ measured at a certain scattering vector q at time t with the intensity $I(q, t + \tau)$ at a later time $(t + \tau)$. This process is repeated for a large number of values of t starting from 0 to the maximum time T (duration of the intensity data collection). The average of all these multiplication results gives the intensity-time correlation function

$$G^{(2)}(q,\ \tau) = \langle I(q,t) \cdot I(q,t+\tau) \rangle = lim_{T \to \infty} \frac{1}{T} \int_0^T I(q,t) \cdot I(q,t+\tau) dt \qquad (2.16)$$

where τ is the delay time. The quantity $\langle I(q,t) \cdot I(q,t+\tau) \rangle$ is a monotonically decaying function in terms of τ (Figure 2.2b). The reason for that is the following: At $\tau = 0$ the correlation is high because particles did not move very far, thus two signals are almost unchanged and the quantity $\langle I(q,t) \cdot I(q,t) \rangle$ produces maximum correlation equal to $\langle I(q,t)^2 \rangle$. Once the decay time τ is very long, there is no correlation between the scattered intensities of the initial state and the state at τ. Essentially, signals at $I(q,t)$ and $I(q,t+\tau)$ become uncorrelated and $G^{(2)}$ decays to a value of $\langle I(q,t) \rangle^2$. This decay is related to the motion of particles and thus to the diffusion coefficient of the particles.

The normalized time correlation function of the scattered intensity is defined as

$$g^{(2)}(q,\ \tau) = \frac{\langle I(q,t) \cdot I(q,t+\tau) \rangle}{\langle I(q,t)^2 \rangle} \qquad (2.17)$$

Similarly, the normalized time correlation function of the scattered field is

$$g^{(1)}(q, \tau) = \frac{\langle E(q,0) \cdot E^*(q,\tau) \rangle}{\langle |E(q,\tau)^2| \rangle} \tag{2.18}$$

The relevance of the field autocorrelation function $g^{(1)}$ is that it is directly related to the fundamental physical process creating the fluctuations. The relevance of the intensity autocorrelation function $g^{(2)}$ is that it is related to what is directly observable during a light scattering experiment.

Under the assumption that the scattered field obeys Gaussian statistics the two time correlation functions are related via the Siegert relationship [111, 112]

$$g^{(2)}(q, \tau) = 1 + \beta \{ g^{(1)}(q,\tau) \}^2 \tag{2.19}$$

where β is a correction factor that represents the number of coherence area and depends on the detector efficiency. At $\beta \sim 1$ the best signal to noise ratio is obtained.

For monodisperse particles with Brownian motion, the field correlation function is an exponentially decaying function of the correlation time delay τ:

$$g^{(1)}(q, \tau) = e^{-\Gamma(q)\tau} \tag{2.20}$$

where Γ is a decay rate or a mean inverse relaxation time which particles need to cover a mean squared displacement of the order of $1/q^2$. The diffusion coefficient D of the solute particles is related to Γ and q through the following expression

$$\Gamma(q) = D(q) \cdot q^2 \tag{2.21}$$

For polydisperse systems $g^{(1)}(q, \tau)$ is not monoexponential anymore and the interpretation of data from polydisperse samples becomes more complex. Size distribution information now can be obtained from the deconvolution of the sum over all single exponentials contributing to the field autocorrelation function. The general deconvolution of a sum of single exponentials is difficult. The problem may be summarized by eq(2.22) and eq(2.23) which define the normalized time-field correlation function $g^{(1)}(q, \tau)$ as the sum of n exponential functions, with intensity weighted coefficients/contributions $G'(\Gamma_i(q))$ associated with the scattering intensity of particles belonging to the i-th size class $(\Delta R_{\theta,i}(q))$ in a way that $G'(\Gamma_i(q)) = \frac{\Delta R_{\theta,i}(q)}{\Delta R_{\theta,t}(q)}$ and $\sum_{i=1}^{n} G'(\Gamma_i(q)) = 1$ through the following equation

$$g^{(1)}(q, \tau) = G'(\Gamma_1(q))e^{(-\Gamma_1(q)\tau)} + G'(\Gamma_2(q))e^{(-\Gamma_2(q)\tau)} + G'(\Gamma_3(q))e^{(-\Gamma_3(q)\tau)} + \cdots =$$
$$= \sum_{i=1}^{n} G'(\Gamma_i(q))e^{-\Gamma_i(q)\tau} \tag{2.22}$$

where $\Gamma_i(q)$ is defined in eq(2.21). For the limit of $\Gamma_{i+1}(q) - \Gamma_i(q) = \Delta\Gamma \to d\Gamma$, the normalized field autocorrelation function $g^{(1)}(q, \tau)$ is revealed by integrating over the entire range of particle sizes via

$$g^{(1)}(q, \tau) = \int_{\Gamma_{min}}^{\Gamma_{max}} G(\Gamma(q))e^{-\Gamma(q)\tau}d\Gamma \tag{2.23}$$

where $G(\Gamma)$ represents the intensity-weighted distribution of particle sizes in units of [sec] normalized so that $\int_{\Gamma_{min}}^{\Gamma_{max}} G(\Gamma(q))d\Gamma = 1$. Γ_{min} and Γ_{max} define the range of decay constants accessible to the instrument and in principle should be $\Gamma_{min} = 0$ and $\Gamma_{max} = \infty$. In order to extract $G(\Gamma)$ from eq(2.23) one needs to perform the inverse Laplace transformation from $g^{(1)}(q, \tau)$. Provencher [113] has developed an inversion software package, CONTIN, which is a generalized inverse Laplace transform with constraints and parsimony. The result is a distribution function $G(\Gamma)$ according to eq(2.23).

CONTIN analysis has been effectively used in this work as a fast stand-alone program to obtain size distributions in real time during data acquisition and to indicate whether the polymer samples exhibit a single or multi modes. In order to obtain a *z*-average diffusion coefficient D_z the method of cumulants [114, 115] introduced by Koppel was used. According to this method the deviation from the monoexponential decay is accounted for with a cumulant expansion of $g^{(1)}(q, \tau)$ about the mean value $\bar{\Gamma} = \int_0^\infty \Gamma G(\Gamma)d\Gamma$. In this work a quadratic cumulant fit has been applied

$$\ln(g^{(1)}(q, \tau)) = a_0 - \bar{\Gamma}(q)\tau + \frac{\mu_2}{2}\tau^2 \tag{2.24}$$

where a_0 is a constant and the first cumulant $\bar{\Gamma}$ is *z*-average decay rate given by

$$\bar{\Gamma}(q) = D(q){\cdot}q^2 \tag{2.25}$$

In case of the monodisperse sample eq(2.25) turns into eq(2.21). In the limit of $q = 0$ the effect of form factor from polydisperse samples and non-diffusional processes like rotation or polymer segment fluctuation do not any longer contribute to the correlation function. Thus, extrapolation of $D(q)$ values to $q = 0$ gives the *z*-average diffusion coefficient D_z

$$D_z = \frac{\sum n_i M_{w,i}^2 D_i}{\sum n_i M_{w,i}^2} \tag{2.26}$$

In eq(2.24) μ_2 is the so-called second cumulant which corresponds to

$$\mu_2 = \langle D^2(q) \rangle - \langle D(q) \rangle^2 \tag{2.27}$$

where square brackets denote an intensity weighted averaging (i.e. *z*-average values).

An additional measure of polydispersity of particle size as the normalized variance *var*$_z$ can be calculated from first and second cumulants

$$var_z = \frac{\mu_2}{(\bar{\Gamma}(q))^2} \tag{2.28}$$

All diffusion coefficients established in this work were established from the method of cumulants.

In case of the characterization of NaPA standards (Chapter 3.2) the "true" *z*-average diffusion coefficient has been calculated from a procedure analogous to the Zimm evaluation by extrapolation of $D(q)$ not only to $q \to 0$ but also to $c \to 0$ [116]. The dependence of $D(q, c)$ on the scattering vector q and on the concentration of scattering particles c in its linear approximation is

$$D(q, c) = D_z(1 + k_D c + C\, R_g^2 q^2) \hspace{4cm} (2.29)$$

where C is a structure specific dimensionless constant describing the angular dependence of $D(q, c)$ and hence depends both on sample polydispersity, particle topology and internal motion [106, 117, 118]. The parameter k_D describes the concentration dependence of $D(q, c)$. It depends on the frictional coefficient k_f, the second virial coefficient A_2 and the particle specific volume V_p as follows

$$k_D = 2A_2 M_w - k_f - V_p \hspace{4cm} (2.30)$$

Finally, the D_z from eq(2.29) can be transformed into an effective hydrodynamic radius R_h by application of the Stokes-Einstein relationship [119]

$$R_h = \frac{k_B\, T}{6\pi\; \eta}\frac{1}{D_z} \hspace{4cm} (2.31)$$

where k_B, T and η are the Boltzmann constant, the temperature and the solvent viscosity, respectively.

In case of systems characterized by DLS at only one certain concentration (Chapters 3.7, 4.1-4.4) the estimation of the diffusion coefficients was done via eq(2.31) omitting the concentration dependent term of eq(2.29).

2.1.3 Combined Static and Dynamic Light Scattering

When the size of particles gets smaller than 100 nm, the form factor cannot be used any more to characterize the shape of these particles. In this case one can extract the structure-sensitive parameter ρ from combined SLS/DLS experiments which is the ratio of the two radii R_g and R_h:

$$\rho = \frac{R_g}{R_h} \hspace{4cm} (2.32)$$

The structure-sensitive parameter ρ adopts values of $1.3 - 1.8$ for polymer coils [117, 22-24]. For NaPA in 0.1 M NaCl, which corresponds to good solvent conditions, a value of $\rho = 1.84$ was established [123], which is in perfect agreement with the theoretically

predicted value of ρ = 1.86 for neutral polymers [124]. In general, experimental values for neutral polymers tend to be 16-23 % lower than theoretically expected [122]. Polydispersity increases ρ [117]. Hard spheres have ρ = 0.78, which is significantly smaller than the value for linear chains, and which enables distinction between coils and spheres [122]. In case of microgels, which can be in a swollen state or represent a core-shell structure, the ρ value may drop to values as low as 0.3 [125].

Hence, by means of a combination of the radius of gyration obtained from SLS and the hydrodynamic radius gained from DLS one can retrieve information about the shape (coil/sphere) and structure (hard sphere/core-shell) of particles.

2.1.4 Light Scattering Instruments

Combined SLS and DLS experiments were performed with two different instruments from the ALV-Laser Vetriebsgesellschaft (Langen, Germany), a model ALV 5000E Compact Goniometer System (CGS) and a model ALV CGS-3/MD-8 Multidetection Laser Light Scattering. Both instruments are equipped with a He-Ne laser from Soliton with 35 mW (Gilching, Germany), operating at a wavelength of 632.8 nm.

The model 5000E CGS was used to analyze stable systems recording SLS and DLS simultaneously. The scattering intensities were recorded by a photomultiplier mounted on the goniometer. The angular range applied in this work was $30° \leq \theta \leq 150°$.

The model ALV CGS-3/MD-8 was used to analyze static and dynamic light scattering, detected with avalanche photo diodes (APDs), in a time-resolved mode (TR-SLS/DLS) at eight different observation angles simultaneously in an angular regime of $20° \leq \theta \leq 76°$.

The software ALV5000E / Win was used to perform the measurements and CONTIN analysis of the scattering data. The evaluation of the combined SLS and DLS data was done with the software ALV Static & Dynamic FIT AND PLOT 4.31.

TR-SLS measurements were performed with a home-build multi-angle goniometer system [126]. The instrument is equipped with a He-Ne laser from Soliton (Gilching, Germany) operating at 632.8 nm and a power of 35 mW. It enabled simultaneous recording of the scattering intensity at 2×19 scattering angles symmetrically arranged as pairs on both sides of the laser beam. The angular regime covered by the instrument was $25.84° \leq \theta \leq 143.13°$.

Significant turbidity has to be avoided as it causes extinction and multiple scattering. Therefore, a photoreceiver FEMTO OE-200-SI-FS with a lock-in amplifier LIA-MV-150 (Berlin, Germany) was used to follow the evolution of turbidity on-line with the home-built multiangle goniometer system [126] during all performed TR-SLS experiments. Signals based on 100 measurements were recorded every 10 s, in accordance with the frequency of recording scattering curves. The optical signal of a sample which gets turbid

over time was normalized by means of the first transmission value which was still considered to exhibit 100% of transmission. Signals with transmission values larger than 80% were considered still amenable to our TR-SLS analysis and were corrected with the respective transmission factor. Scattering signals which corresponded to smaller values of transmission were discarded, thus predetermining duration for TR-SLS experiment in some cases.

All experiments were performed at a temperature of 25 °C, which was fixed with a precision of 0.01 °C by using a C25 Haake thermostat.

Solution preparation prior to light scattering measurements are given in Chapters 3.2, 3.3 and 3.8.

2.2 Small and Anomalous Small Angle X-ray Scattering

The magnitude of the scattering vector q defines the observation length scale of the scattering experiments. The larger q becomes, the smaller the length scale and the sample details get which can be observed (Figure 2.3). One may consider scattering also as an inverse microscopic technique with the scattering vector as the resolution or magnification of the inverse microscope. The smaller q is, the lower the magnification and the corresponding resolution of the structure of a given scattering particle gets [102].
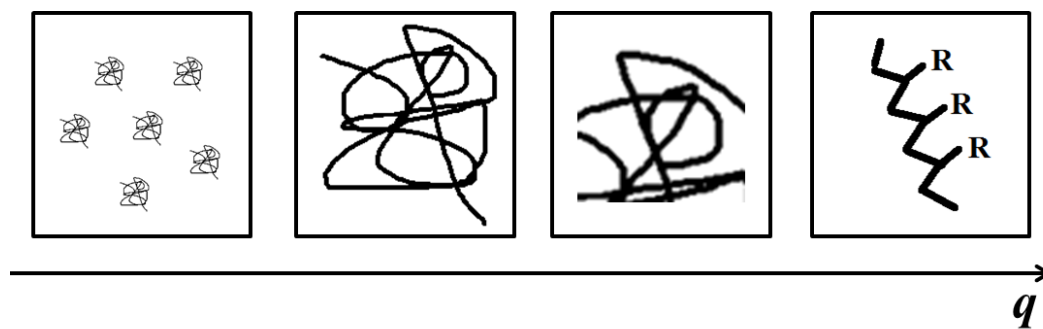
Figure 2.3 Sample details observed in case of a random polymer coil depending on q-scale.

The experimentally accessible q range in light scattering is in between 0.008 nm^{-1} and 0.03 nm^{-1} depending on the solvent and wavelength of the laser (see eq(2.1)). It was already mentioned in Chapter 2.1.3, that in SLS the form factor $P(q)$ is only accessible when the scattering particles exceed a size of about 100 nm and for smaller scatterers allows only the determination of their global dimensions. In small angle X-ray scattering (SAXS) experiments the q range extends approximately from 0.05 nm^{-1} to 5 nm^{-1} depending on the detector-sample distance and the used X-ray energy. Thus, the wider q

range accessible with SAXS experiments makes it possible to scrutinize not only the structural details, but also the form factor *P(q)* of the smaller particles.

The contrast in SAXS experiments is based on the difference in electron density of the constituting components. Therefore, for Ag^+-PA solutions, investigated in this work, the largest contribution to the scattering intensity comes from the monovalent silver cations bound to PA-coils. Due to a low electron density difference between the solvent and the polymer chain, the latter one provides only a small contribution.

Anomalous small angle X-ray scattering (ASAXS) enables the structural characterization of the counterion distribution around the polymer chain and quantitative estimation of the amount of counterions condensed to the chains by tuning the energy in the vicinity of the absorption edge of this counterion. The distribution of the counterions is not accessible by conventional SAXS measurement because the scattering contributions from the polymer and counterions superimpose and cannot be separated. Variation of the wavelength close to an absorption edge of counterions changes the scattering contrast of the counterions at a roughly constant scattering contrast of the anionic chains, which host the cations.

In the following paragraphs the evaluation of the data from ASAXS measurements will be outlined. Mainly, it will be demonstrated how to extract the scattering pattern from the Ag^+ ions and quantify the amount of these counterions bound to the domain of the PA-chains. Detailed information on SAXS and ASAXS methods can be found in the text books [99, 127, 128], a review [129] and selected articles [14, 16, 130].

In case of a dilute solution of PA-chains surrounded by positively charged Ag^+ ions, neglecting interparticle correlations, the scattering amplitude can be subdivided into two terms corresponding to a contribution from the organic polymer backbone, indicated by the index "*Poly*", and the contribution from the counterions, labeled with the index "*Ag*"

$$A(q) = \int_V \Delta\rho_{Poly}(r) \cdot \exp[-iqr]\, d^3r + \int_V \Delta\rho_{Ag}(r) \cdot \exp[-iqr]\, d^3r \qquad (2.33)$$

where q is the magnitude of the scattering vector defined by eq(2.1), $\Delta\rho_{Poly}$ and $\Delta\rho_{Ag}$ are the excess electron densities of the polyelectrolyte chains and Ag^+ ions, respectively

$$\Delta\rho_{Poly}(r) = \Delta f_{poly} \cdot u(r) = (f_{poly} - \rho_s V_{poly}) \cdot u(r) \qquad (2.34a)$$

$$\Delta\rho_{Ag}(r, E) = \Delta f_{Ag}(E) \cdot v(r) = ((f_{0,Ag} - \rho_s V_{Ag}) + f'_{Ag}(E) + if''_{Ag}(E)) \cdot v(r) \quad (2.34b)$$

calculated with respect to the electron density of the solvent ρ_s and with the volume of the chain V_{poly} and the volume of the Ag^+ ions V_{Ag}, while u(r) and v(r) describe the respective number densities of the monomeric units forming the polymer chains and the Ag^+ ions as a function local coordinates. The molecular scattering factor or the excess number of electrons in a monomeric unit $\Delta f_{poly}(E)$ is nearly energy independent, while the atomic scattering factor of the counterions $\Delta f_{Ag}(E) = f_{0,Ag} + f'_{Ag}(E) + if''_{Ag}(E)$ shows a

strong energy dependent variation in the vicinity of the absorption edge of the Ag^+ ions due to the so-called anomalous dispersion corrections $f'_{Ag}(E)$ and $f''_{Ag}(E)$. It should be emphasized that a few percent in energy apart from the value of the energy at the absorption edge contributions from the terms $f'_{Ag}(E)$ and $f''_{Ag}(E)$ decrease to zero and X-ray scattering experiments turn into conventional SAXS experiments.

The scattering intensity I(q), expressed as the differential scattering cross section $\frac{d\Sigma}{d\Omega}$, is calculated by squaring the amplitude in eq(2.33) according to $\frac{d\Sigma}{d\Omega} = I(q) = |A(q)|^2 = A(q) \cdot A^*(q)$ and averaging over all possible spatial distributions accessible to the monomers and counterions, which leads to a sum of three contributions

$$\frac{d\Sigma}{d\Omega}(q) = I(q, E) =$$

$$\left|A_{poly}(q)\right|^2 + 2Re\left\{A_{poly}(q)\right\} \cdot Re\left\{A_{Ag}(q, E)\right\} + \left|A_{Ag}(q, E)\right|^2 \qquad (2.35)$$

where the term Re{Z} express the real part of a complex function Z. The indication of E as variable in eq(2.34b) and eq(2.35) in addition to q emphasizes the extraordinary dependence of $\Delta\rho_{Ag}(r, E)$ on the energy/wavelength. The three terms in eq(2.35) represent the following integrals [131]:

$$\left|A_{poly}\right|^2 = \Delta f_{poly}^2 \int_V \int u(r) \ u(r') \frac{\sin(q|r-r'|)}{q|r-r'|} d^3r d^3r' \qquad (2.36a)$$

$$2Re\left\{A_{poly}(q)\right\} \cdot Re\left\{A_{Ag}(q, E)\right\} =$$

$$= 2\Delta f_{poly}(f_{0,Ag} - \rho_s V_{Ag} + f'_{Ag}(E)) \int_V \int u(r)v(r') \frac{\sin(q|r-r'|)}{q|r-r'|} d^3r d^3r' \qquad (2.36b)$$

$$\left|A_{Ag}(q, E)\right|^2 = \left|\Delta f_{Ag}(E)\right|^2 \int_V \int v(r)v(r') \frac{\sin(q|r-r'|)}{q|r-r'|} d^3r d^3r' \qquad (2.36c)$$

In eq(2.36) the pair combinations of scattering centers separated by a distance r – r' are spatially averaged over all possible orientations [132]

$$\langle \exp[-iq|r-r'|] \rangle = \frac{\sin(q|r-r'|)}{q|r-r'|} \qquad (2.37)$$

The part of the scattering intensity which originates solely from the polymer gives a nonresonant scattering contribution and is defined by eq(2.36a). The product of the scattering amplitudes of the PA-chains and Ag^+ ions is called cross term or mixed-resonant term given by eq(2.36b). It describes the superposition of scattering amplitudes originating from the polymers and Ag^+ ions. The scattering intensity emanating solely from the Ag^+ cations is given by eq(2.36c). It contains the so-called pure-resonant scattering.

By measuring the scattering curves at two energies in the vicinity of the absorption edge of the Ag$^+$ ions and subtracting the two scattering curves $\Delta I(q, E_1, E_2) = I(q,E_1) - I(q,E_2)$ the nonresonant scattering contribution of the polymer and of the Ag$^+$ cations is vanishing

$$\Delta I(q, E_1, E_2) = 2\Delta f_{poly}\left(f'_{Ag}(E_1) - f'_{Ag}(E_2)\right)\int_V \int u(r)v(r')\frac{\sin(q|r-r'|)}{q|r-r'|}d^3rd^3r'$$
$$+ \left(\left|\Delta f_{Ag}(E_1)\right|^2 - \left|\Delta f_{Ag}(E_2)\right|^2\right)\int_V \int v(r)v(r')\frac{\sin(q|r-r'|)}{q|r-r'|}d^3rd^3r' \qquad (2.38)$$

In order to cancel the cross term one additional measurement at a third energy is required in order to receive $\Delta I(q, E_1, E_3) = I(q,E_1) - I(q,E_3)$

$$\Delta I(q, E_1, E_3) = 2\Delta f_{poly}\left(f'_{Ag}(E_1) - f'_{Ag}(E_3)\right)\int_V \int u(r)v(r')\frac{\sin(q|r-r'|)}{q|r-r'|}d^3rd^3r'$$
$$+ \left(\left|\Delta f_{Ag}(E_1)\right|^2 - \left|\Delta f_{Ag}(E_3)\right|^2\right)\int_V \int v(r)v(r')\frac{\sin(q|r-r'|)}{q|r-r'|}d^3rd^3r' \qquad (2.39)$$

Thus, as a last step for isolating the pure resonant scattering contribution, $S_{Ag}(q)$, the difference between $\Delta I(q, E_1, E_2)$ and $\Delta I(q, E_1, E_3)$ is formed and normalized by the energy dependent anomalous dispersion corrections of the atomic scattering factor of the Ag$^+$ at the related energies

$$S_{Ag}(q) = \int_V \int v(r)v(r')\frac{\sin(q|r-r'|)}{q|r-r'|}d^3rd^3r' =$$

$$= \left[\frac{\Delta I(q,E_1,E_2)}{f'_{Ag}(E_1)-f'_{Ag}(E_2)} - \frac{\Delta I(q,E_1,E_3)}{f'_{Ag}(E_1)-f'_{Ag}(E_3)}\right]\frac{1}{F(E_1,E_2,E_3)} \qquad (2.40)$$

The prefactor of the scattering contribution from the pure resonant species is given by

$$F(E_1,E_2,E_3) = \frac{\left|\Delta f_{Ag}(E_1)\right|^2 - \left|\Delta f_{Ag}(E_2)\right|^2}{f'_{Ag}(E_1)-f'_{Ag}(E_2)} - \frac{\left|\Delta f_{Ag}(E_1)\right|^2 - \left|\Delta f_{Ag}(E_3)\right|^2}{f'_{Ag}(E_1)-f'_{Ag}(E_3)} \qquad (2.41)$$

Hence, eq(2.40) provides direct access to the scattering from the Ag$^+$ ions. Subtraction of scattering curves (procedures expressed by eq(2.38-2.40)) has to be performed at identical q values for each contributing component. The structural information of the Ag$^+$ ions surrounding the macroions can be obtained from the analysis of $S_{Ag}(q)$. The only parameters required to calculate $S_{Ag}(q)$ are the two energy dependent correction factors $f'_{Ag}(E)$ and $f''_{Ag}(E)$. Table 2.1 provides the anomalous dispersion corrections for Ag at the three energies used in this work based on the calculations of Cromer and Liberman [133, 134].

Table 2.1 Anomalous dispersion corrections obtained by Cromer-Liberman calculations [133, 134]

Energy	24.637 keV	25.500 keV	25.521 keV
$f'_{Ag}(E)$	-2.999	-6.519	-10.143
$f''_{Ag}(E)$	0.591	0.555	3.619

An important quantitative information can be deduced from the Porod-invariant [130, 135] of the pure resonant scattering contribution from the absorbing species. It is related to the amount of Ag atoms localized in the PA-phase.

For didactic reasons let us start with the full invariant of the Ag^+ ions $Q_{Ag} = \int_q \langle A_{Ag}(q) \cdot A_{Ag}^*(q) \rangle q^2 \mathrm{d}q$ over a wide enough q regime. The respective invariant is determined by the averaged squared fluctuation of the excess electron density of the Ag^+ ions $\langle \Delta\rho_{Ag}^2 \rangle - \langle \Delta\rho_{Ag} \rangle^2$ [135]

$$Q_{Ag} = \int_q \langle A_{Ag}(q) \cdot A_{Ag}^*(q) \rangle q^2 \mathrm{d}q = 2\pi^2 r_0^2 \left[\langle \Delta\rho_{Ag}^2 \rangle - \langle \Delta\rho_{Ag} \rangle^2 \right] \tag{2.42}$$

or with respect to eq(2.36c) and eq(2.40) it can be rewritten as

$$Q_{Ag} = \left| \Delta f_{Ag}(E) \right|^2 \cdot \int_q S_{Ag}(q) q^2 dq \tag{2.43}$$

where r_0 in eq(2.42) corresponds to the absolute scattering length of an electron, which renders the left hand side of this equation into absolute cross sections recorded in a scattering experiment. Application of eq(2.34b) introduces the number density of Ag^+ ions $v(r)$ leading to new expression

$$Q_{Ag} = 2\pi^2 r_0^2 \left| \Delta f_{Ag}(E) \right|^2 [\langle v^2 \rangle - \langle v \rangle^2] \tag{2.44}$$

With the known volume of a single Ag^+ ion (V_{Ag}), the number of Ag^+ ions (N_{Ag}) and the sample volume (V) probed by the X-ray scattering experiment, one can define the average of the squared number density of (absorbing) Ag^+ ions in solution via the following relation

$$\langle v^2 \rangle = \frac{N_{Ag} V_{Ag}}{V} \cdot \frac{1}{V_{Ag}^2} = \frac{\langle v \rangle}{V_{Ag}} \tag{2.45}$$

where $\langle v \rangle$ represents the averaged number density of the absorbing counterions in solution. Inserting eq(2.45) into eq(2.44) results in

$$Q_{Ag} = 2\pi^2 r_0^2 \left| \Delta f_{Ag}(E) \right|^2 \left[\frac{\langle v \rangle}{V_{Ag}} - \langle v \rangle^2 \right] \tag{2.46}$$

In dilute solutions the second term in the brackets of eq(2.46) can be neglected [129]. Thus combination of eq(2.43) with eq(2.46) leads to the following expression

$$\langle v \rangle = \frac{V_{Ag}}{2\pi^2 r_0^2 |\Delta f_{Ag}|^2} Q_{Ag} = \frac{V_{Ag}}{2\pi^2 r_0^2} \int_q S_{Ag} q^2 dq \tag{2.47}$$

where the integral is limited to the experimentally accessible q space. Along this line of thought, i.e. from eq(2.42) until eq(2.47), the nonresonant scattering contribution of the

Ag$^+$ ions is elegantly cancelled out and one can determine exclusively the amount of Ag$^+$ ions/Ag atoms absorbed onto the PA-matrix.

From eq(2.47) one can calculate the molar concentration of [Ag$^+$] related to the resonant invariant by taking into account Avogadro's number N_A and using the radius of a silver ion R_{Ag}[136]

$$\langle v \rangle = \frac{2R_{Ag}^3}{3\pi N_A r_0^2} \int_q S_{Ag}(q)q^2 dq \tag{2.48}$$

In the present work SAXS patterns of the Ag$^+$-PA solutions before and after UV-exposure (Chapter 4.2) were recorded at three different photon energies (Table 2.1) in the vicinity of the silver K-edge (E_{edge} = 25.5155 keV). The measurements have been performed at the B1 beamline (former JUSIFA) of the HASYLAB at DESY (Hamburg, Germany) [137, 138]. The Ag$^+$-PA solutions were prepared according to a procedure described in Chapter 3.3.

Quartz capillaries with an inner diameter of 2 mm and a wall thickness of 0.05 mm were purchased from Hilgenberg (Malsfeld, Germany) and used as scattering cells for the SAXS experiments. After the sample was filled into the capillary with a syringe and thin needle, two-component adhesive glue was used to seal the open end of the tube with a funnel-like piece from a Pasteur pipette [139].

Measurements of glassy carbon at all three energies were used to normalize the scattering curves to absolute scattering cross sections. All scattering patterns have been normalized and corrected for background and transmission. The scattering of the solvent (0.01 M NaNO$_3$) was measured at 24.637 keV and subsequently subtracted from the sample scattering. The scattering intensity is given in units of reciprocal length [cm^{-1}] by use of the JUSIFA calibration standards. The ASAXS sequences covering three energies obeyed the JUSIFA standard procedures, i.e. repeating the whole sequence several times with subsequent averaging [17, 140].

2.3 Ultraviolet-visible Spectroscopy

Ultraviolet-visible (UV-vis) spectroscopy is a technique used to quantify the fraction of light that is absorbed and scattered by a sample. The obtained data are a quantity known as extinction or attenuation, which is defined as the sum of absorbed and scattered light [84, 141]. Also denoted as absorbance we use the symbol **A** for attenuation/absorbance.

In a typical UV-vis spectroscopy measurement, we are measuring the intensity of light passing through a sample (**I**), and comparing it to the intensity of light before it passes through the sample (**I$_0$**). The ratio **I/I$_0$** is called the transmittance (**T**). The absorbance (**A**) of the sample is related to the transmittance by

$$\mathbf{A} = -\log_{10}(\mathbf{T}) \tag{2.49}$$

In its simplest form, a sample is placed between a light source and a photodetector, and the intensity of a beam of light is measured before and after passing through the sample (Figure 2.4). Typically, UV-vis measurements record the wavelength dependent absorbance spectrum of the measured samples. The data is plotted as absorbance **A** versus wavelength λ. Each spectrum is background-corrected using a cuvette filled with only the dispersing medium to guarantee that spectral features from the solvent do not modify the sample absorbance spectrum.
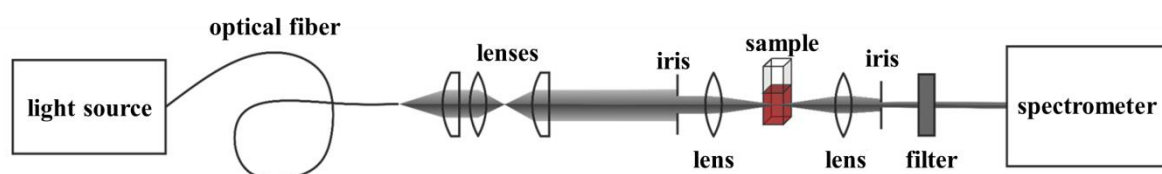
Figure 2.4 Schematic representation of the UV/vis spectrophotometer.

Conduction-band electrons of nanoparticles made of noble metals, particularly as gold and silver, interact strongly with light having specific range of wavelengths. The phenomenon of the surface plasmon resonance of metal nanoparticles is explained in detail in Chapter 1.1.4 (Figure 1.8). Silver nanoparticles have characteristic optical absorption spectra in the UV-vis region and therefore can be studied using UV-vis spectroscopy.

The UV-vis spectra were taken with a Lambda 19 (Perkin-Elmer) in the wavelength range of 350-800 nm. The visible spectrum is generated by a tungsten-halogen-lamp, whereas the UV-range originates from a deuterium lamp. For each measurement the absorption of distilled water was measured and subtracted. Before measurement, the samples were diluted with aqueous 0.01 M $NaNO_3$ solution to ensure the ionic strength to be constant (Chapter 4.2.2). The extent of dilution was indicated along with the presented UV-vis spectra. For UV-vis measurements the solutions were filled into disposable PMMA cuvettes from VWR (Leuven, Belgium) with a volume of 3 mL and a path length of 10 mm. The absorbance data were recorded by the program PerkinElmer WinLab.

2.4 Transmission Electron Microscopy

Transmission electron microscopy (TEM) operates with the same basic principles as light microscopy but uses electrons instead of light as probing waves. The much shorter wavelength of the electrons makes it possible to get a thousand-times better resolution than

with an optical microscope. Therefore, small details down to near atomic levels can be studied by TEM.

The instrument is equipped with a medium accelerating voltage, a high-brightness electron source, digital image recording, a computer-controlled sample goniometer and a geometrically optimized X-ray detector (Figure 2.5). The primary source at the top of the microscope emits the electrons into the vacuum of the column of the microscope. Instead of using glass lenses to focus the light in a light microscope, TEM uses electromagnetic lenses to focus the electrons into a very thin beam. The electron beam then gets through the specimen to be studied. Depending on the density of the investigated material, some of the electrons are scattered and disappear from the beam. At the bottom of the microscope the unscattered electrons hit a fluorescent screen, which gives rise to a "shadow image" of the specimen with its different parts displayed in varied darkness according to their density. The image can be studied directly by the operator or photographed with a camera.
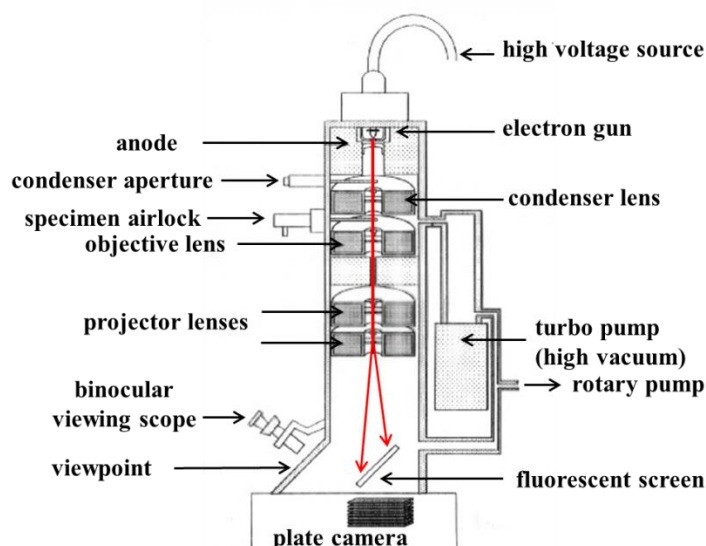
Figure 2.5 Schematic construction of TEM.

In this work three TEM instruments were used in order to identify and characterize Ag-NPs formed under exposure to UV-light in Ag^+-PA (Chapter 4.2) and in Ag^+-SPB solutions (Chapter 4.4).

The TEM-micrographs presented in Figures 4.2.12, 4.2.15, 4.2.19 and 4.2.20 were taken using a CM100 (PW6021) microscope (Philips, Herrsching, Germany). The TEM was operated at an acceleration voltage of 80 kV in a bright-field mode. The specimen were prepared on carbon coated copper grids (200 µm mesh, Science Services, Munich, Germany) at room temperature. For the TEM measurements, 3 µL of Ag^+-PA solutions illuminated with UV-light for $t_{UV} = 4$ min were dropped on the copper-grid and after one minute the residual solvent was blotted off with a filter paper.

The TEM-micrographs shown in Figures 4.2.13 and 6.11 were taken using a JEM-2100 with a LaB_6 cathode (JEOL, Eching, Germany). The TEM was operated at an acceleration voltage of 200 kV in a bright-field mode. TEM specimens were prepared by putting ca. 5 µL of Ag^+-PA solutions UV-exposed for $t_{UV} = 4$ min on a TEM copper grid with carbon support film (200 µm mesh, Science Services, Munich, Germany) at room temperature. The carbon coated copper grids have been pretreated 20 s by glow discharge. The excess of liquid was blotted with a filter paper after 2 min. The remaining liquid film on the TEM grid was dried at room temperature for at least one hour.

TEM-micrographs displayed in Figure 4.4.6 were taken using JEM-2000FX microscope (JEOL, Eching, Germany). The TEM was operated at an acceleration voltage of 200 kV in a bright-field mode. The specimen were prepared on coated copper-grids (200 µm mesh, Plano GmbH, Wetzlar, Germany) at room temperature. For the TEM measurements, ca. 3 µL of Ag^+-SPB solutions illuminated with UV-light for $t_{UV} = 4$ min were dropped on the copper-grid and after one minute the residual solvent was blotted off with a filter paper.

2.5 Scanning Electron Microscopy

Scanning electron microscopy (SEM) is a type of electron microscopy technique that produces images of a sample by scanning over it with a high-energy focused beam of electrons. The electrons interact with electrons in the sample, producing secondary electrons (SE), back-scattered electrons (BSE) and characteristic X-ray signals that contain information about the sample surface topography and composition. The electron beam generally scans the sample with a raster scan pattern and the beam position is combined with the detected signal to produce an image.

In a typical SEM, an electron beam (Figure 2.6a) is thermionically emitted from an electron gun fitted with a tungsten filament cathode. Other types of electron emitters include lanthanum hexaboride (LaB_6) cathodes, field emission guns, which may be of the cold-cathode type using tungsten single crystal emitters or the thermally assisted Schottky type, using emitters of zirconium oxide (ZrO_2). The electron beam is focused by condenser lenses to a spot of about 0.4 nm to 5 nm in diameter. The beam passes through pairs of scanning coils or pairs of deflector plates in the electron column, typically in the final lens, which deflects the beam in the x and y axes so that it scans in a raster fashion over a rectangular area of the sample surface.

When the primary electron beam interacts with the sample, the electrons lose their energy by repeated random scattering and absorption within a teardrop-shaped volume of the specimen known as the interaction volume (Figure 2.6c). Depending on energy of the primary electrons, the atomic number of the specimen and the density of the specimen, the interaction volume may extend from less than 100 nm to approximately 5 µm into the bulk.

The energy exchange between the electron beam and the sample results in the reflection of high-energy electrons by elastic scattering of BSE, emission of SE by inelastic scattering and the emission of electromagnetic radiation, each of which can be detected by specialized detectors.
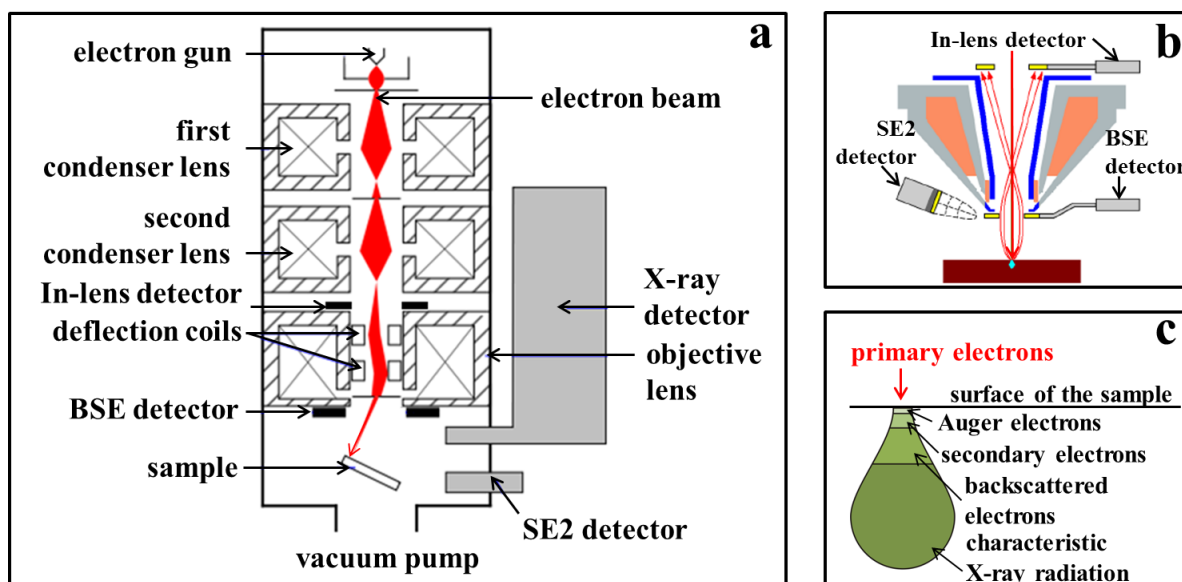
Figure 2.6 Schematic representations of the construction of SEM (a), the distinction between In-lens and SE2 detectors (b) and the interaction volume (c).

The signals from SE result from the interactions of the electron beam with atoms at or near the surface of the sample and are detected by In-lens detectors (Figure 2.7b). The In-lens detector is perpendicular to the sample surface in the electro-optical path. This implies that it can only be used efficiently at low voltages up to 20 kV. In this range the suction of the so called beam booster has a very high yield of electrons. This allows a faster and gentler image generation compared to other detectors, especially at very low voltages. Nearly pure detection of secondary electrons by the In-lens detector allows a very close to the surface image that contains only little information from the bulk phase.

BSE are often used in analytical SEM along with the spectra made from the characteristic X-rays, because the intensity of the BSE signal is strongly related to the atomic number of the specimen. BSE images can provide information about the distribution of different elements in the sample. The SE2 detector captures a combination of secondary and back-scattered electrons. Compared to the In-lens detector the image information originates from a greater average sample depth. The SE2 detector distinguishes itself from other detectors because it is located in the chamber. Due to its side mounting to the chamber wall it gives much better topographical information than other detectors.

A SEM instrument Neon 40 (Zeiss) was used for qualitative characterisation of solutions with SPBs decorated with Ag-NPs on the PS-cores. Technical characteristics used for taking SEM-images are given with the SEM-micrographs presented in this work (see Figures 4.4.6, 4.4.9, 6.13, 6.14). Pure SPBs were characterized by a SEM Pioneer (Raith GmbH) with EHT (extra high tension) voltage level of 5 kV (Figure 3.11).

SEM experiments with all colloids were performed directly on a cleaned aluminium stub as a substrate. Sample preparation was performed by placing a few drops of the solution on a cleaned aluminium stub and by gently evaporating the solvent under ambient (room temperature and pressure) conditions. SEM-images of the SPBs decorated with Ag-NPs were taken by In-lens and SE2 detectors, where the latter one gave more information on the coverage of PS-cores by Ag-NPs.

2.6 Other Methods and Instruments

Nuclear magnetic resonance (NMR) spectra of synthesized photoinitiators (Chapter 3.4) were recorded at room temperature in acetone-d_6 (Cambridge Isotope Laboratories Inc, Andover, USA) using an AC 400 spectrometer (Bruker) operating at 400 MHz (^{1}H-NMR). Tetramethylsilane (TMS) served as an internal standard.

The pH-value of NaPA and SPB aqueous solutions was adjusted to desired values using a small amount (ca. 0.05-0.1 mL) of 0.1 M NaOH and monitored at room temperature using the pH-meter SevenEasy S20 (Mettler-Toledo).

Conductivity of outer water (eluate) during the ultrafiltration of latices (Chapters 3.6) was measured by a handheld conductivity meter Cond 340i (WTW) equipped with a standard conductivity cell TetraCon 325 (WTW). In order to determine the exact concentration of COO^--groups (Chapter 3.7.2) conductivity titrations of SPBs with aqueous NaOH solutions was performed using the same conductivity device.

The viscosity-average molecular weight M_η of the NaPA chains constituting PA-shells of SPBs (Chapter 3.7.2) was determined from the intrinsic viscosity $[\eta]$ in 0.5 M NaCl at 25 °C using an Ubblohde capillary viscometer (Schott, Ubbelohde KPG, Cappilary Size 0, K=$0.001081 \cdot 10^{-2} cm^2 s^{-2}$). Depending on the amount of the polymer, obtained after hydrolysis of SPBs and subsequent purification by ultrafiltration, stock solutions of NaPA with a concentration of 1-1.2 g/L were prepared. The stock solutions of NaPA were gently stirred at ambient temperatures during two days. Based on these stock solutions three additional NaPA solutions with the concentrations of 0.75 g/L, 0.5 g/L and 0.25 g/L were prepared using 0.5 M NaCl as a solvent. Details on the calculation of the molecular parameters from intrinsic viscosity, defined by means of the extrapolation of the specific viscosity to zero NaPA concentration, are given in Chapter 3.7.2.

3 Experimental Procedures

3.1 Materials

Sodium nitrate (NaNO$_3$), magnesium sulphate hexahydrate (MgSO$_4 \cdot$ 6H$_2$O), sodium chloride (NaCl) and calcium chloride hexahydrate (CaCl$_2 \cdot$ 6H$_2$O) from Fluka (Buchs, Switzerland), silver nitrate (AgNO$_3$) from Sigma-Aldrich (St. Louis, USA), potassium persulfate (KPS) from Sigma-Aldrich (Taufkirchen, Germany), sodium borohydride (NaBH$_4$) (Taufkirchen, Germany), sodium dodecyl sulfate (SDS) from Sigma-Aldrich (Tokyo, Japan), 4-hydroxybenzophenone from Sigma-Aldrich (Shanghai, China), triethylamine from Sigma-Aldrich (Diegem, Belgium), benzoin from Sigma-Aldrich (Taufkirchen, Germany), dimethylaniline from Sigma-Aldrich (Bangalore, India), 2-hydroxy-4´-hydroxyethoxy-2-methylpropiophenone from Sigma-Aldrich (St. Louis, USA) with a purity > 99% were used as received.

Styrene from Sigma-Aldrich (Taufkirchen, Germany), acrylic acid from Sigma-Aldrich (Zwijndrecht, Netherlands), acryloyl chloride from Fluka (Buchs, Switzerland) and methacryloyl chloride from Fluka (Buchs, Switzerland) were used as received. These liquids were destabilized by a flush column charged with basic aluminium oxide Woelm B-Super I from Woelm Pharma (Bad Honnef, Germany) before use.

Acetone, chloroform, diethyl ether, ethanol, toluene, *tert*-butanol, pyridine, dimethylaniline, triethylamine from Sigma-Aldrich (Taufkirchen, Germany) with a purity > 99% were used as received.

Silica gel 60 from Fluka (Buchs, Switzerland) was used for column chromatography.

The NaPA standards NaPA800 and NaPA1300 were purchased from Polysciences (Eppelheim, Germany) and were used as received. Characterization of both samples in dilute solution was performed by combined SLS/DLS (see Chapter 3.2).

Bidistilled water with a conductivity < 0.1 μS/cm was purified by reverse osmosis (Millipore) and used for the preparation of all aqueous solutions.

3.2 Characterisation of NaPA Standards by Light Scattering

The NaPA standards NaPA800 and NaPA1300 were characterized by combined SLS/DLS with the Model ALV-CGS 5000E in aqueous solution of 0.1 M NaCl which represents a thermodynamically good solvent [5] at pH = 9 at 25 °C. The NaPA800 standard was also characterized in aqueous solution of 0.01 M NaNO$_3$ at pH = 9 at 25 °C. All NaPA stock solutions were prepared and gently stirred at room temperature for 2 days.

All solvents and solutions were filtered through 0.22 μm cellulose mixed ester syringe filters from Millipore (Eschborn, Germany) prior to the scattering experiments to remove dust. Cylindrical quartz cuvettes from Hellma (Müllheim, Germany) with an outer diameter of 25 mm were used for all light scattering experiments. Prior to any measurements scattering cuvettes were cleaned from dust by continuously injecting distilled acetone for 15 min.

In the evaluation of the light scattering data values of a refractive index $n = 1.3363$ and a viscosity $\eta = 0.956$ mPa×s for aqueous solution of 0.1 M NaCl and of a refractive index $n = 1.3357$ and a viscosity $\eta = 0.948$ mPa×s for aqueous solution of 0.01 M $NaNO_3$ were used. Refractive index increments $dn/dc = 0.174$ mL/g and $dn/dc = 0.167$ mL/g were used in the evaluation of the static light scattering data for standards NaPA800 and for NaPA1300, respectively [5]. Dynamic data (lower graphs of Figures 3.1, 3.3-3.5) was treated via eq(2.29) and eq(2.31). The particle size distribution of the NaPA solutions in terms of var_z were characterized by means of DLS: ten intensity-correlation functions were evaluated with a decay of $g^{(2)}(q, \tau) - 1$ (see eq.(2.19)) to 31% by the second order cumulant method at a scattering angle of $\theta = 30°$.

3.2.1 Characterisation of NaPA800

Five concentrations of the sample NaPA800 in aqueous solution of 0.1 M NaCl had been used based on a stock solution with a concentration of 2 g/L. The SLS/DLS analyses was carried out in the regime of the scattering vector q of $47 < q^2 < 657$ μm^2.

Figure 3.1 shows the Zimm's diagrams from the SLS/DLS analysis. Static light scattering data were evaluated by Berry analysis [144], which is more appropriate because the width of the concentration regime induces an upward-bending of the extrapolated (blue) data points. Thus a mixed data evaluation is needed: In a first step we linearly extrapolate $Kc/\Delta R_\Theta$ to $q^2 = 0$, where $126 < q^2 < 554$ μm^2. In the second step we plotted the square root of each intercept as a function of the concentration according to Berry's method eq(3.1) (Figure 3.2). The results of the evaluation from both SLS and DLS are summarized in the Table 3.1.

$$\sqrt{\frac{Kc}{\Delta R_{\theta=0}}} = 1/\sqrt{M_w} + A_2\sqrt{M_w}c \tag{3.1}$$

Table 3.1 Characteristic parameters of sample NaPA800 in 0.1 M NaCl from the combined SLS/DLS analysis (Figure 3.1).

M_w / gmol^{-1}	R_g / nm	R_h / nm	ρ	A_2 / 10^{-6} molLg^{-2}	k_D / Lg^{-1}	var_z*
503 000	72	48	1.5	1.1	0.47	0.25

*The polydispersity index was indicated by a supplier as $M_w/M_n = 1.3$, where M_w and M_n is the weight average and number average of the molar mass respectively.

Figure 3.1 Zimm diagram from static and dynamic light scattering of sample NaPA800 characterized in aqueous 0.1 M NaCl solution: k = 3000, $47 < q^2 < 657 \ \mu m^2$. The blue data points correspond to the linear extrapolation of $Kc/\Delta R_\Theta$ to $q^2 = 0$. The dashed line is a guide for the eye indicating the extrapolation of $Kc/\Delta R_{\Theta=0}$ to $c = 0$.
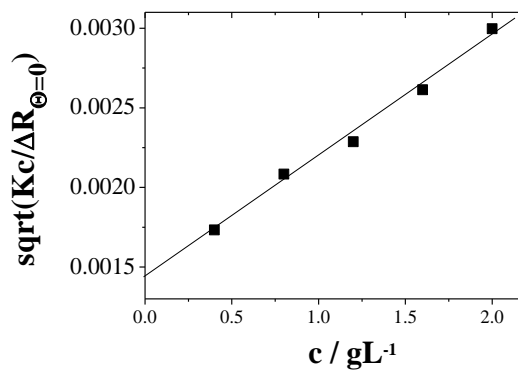
Figure 3.2 Extrapolated values of the $Kc/\Delta R_{\Theta=0}$ plotted verses c according to Berry's method (eq(3.1)).

In order to verify the results from the previous characterization, polyacrylate sample NaPA800 was characterized in 0.1 M NaCl at pH = 9 at 25 °C a second time in a different concentration range: $0.1 < c < 0.4$ g/L (Figure 3.3). The SLS/DLS analyses was carried out in the regime of the scattering vector q of $47 < q^2 < 470$ µm². The static data presented in Figure 3.3 were treated via Zimm's approximation [109] using eq(2.14), since in this concentration range the extrapolation of $Kc/\Delta R_{\Theta=0}$ to $c = 0$ is possible via linear regression. The established molecular parameters from both SLS and DLS are summarized in Table 3.2.
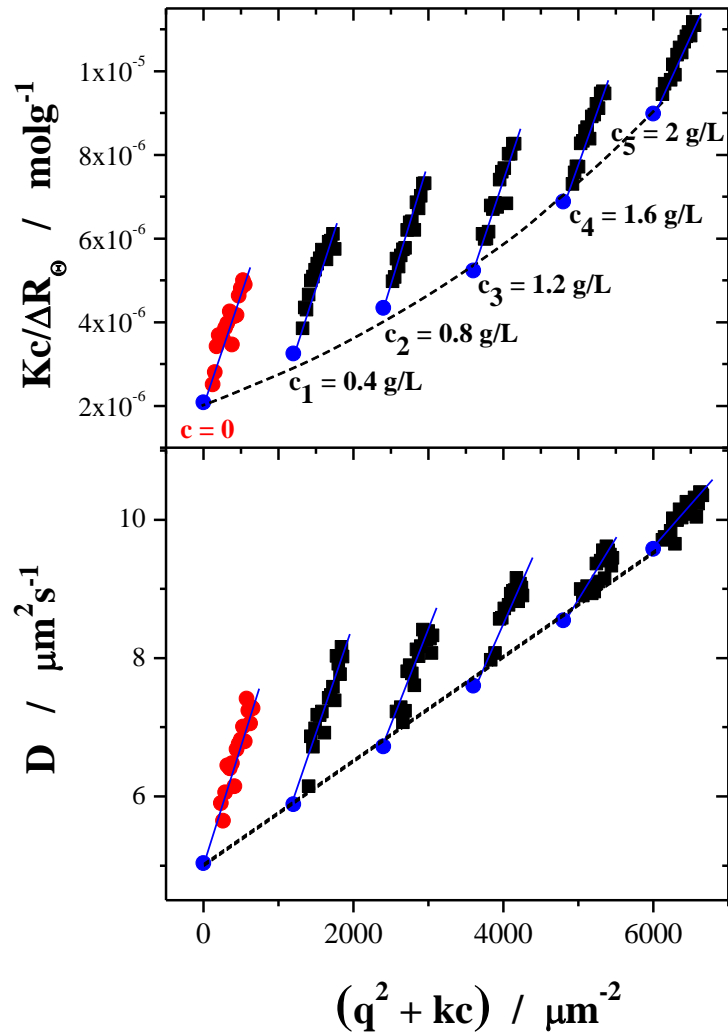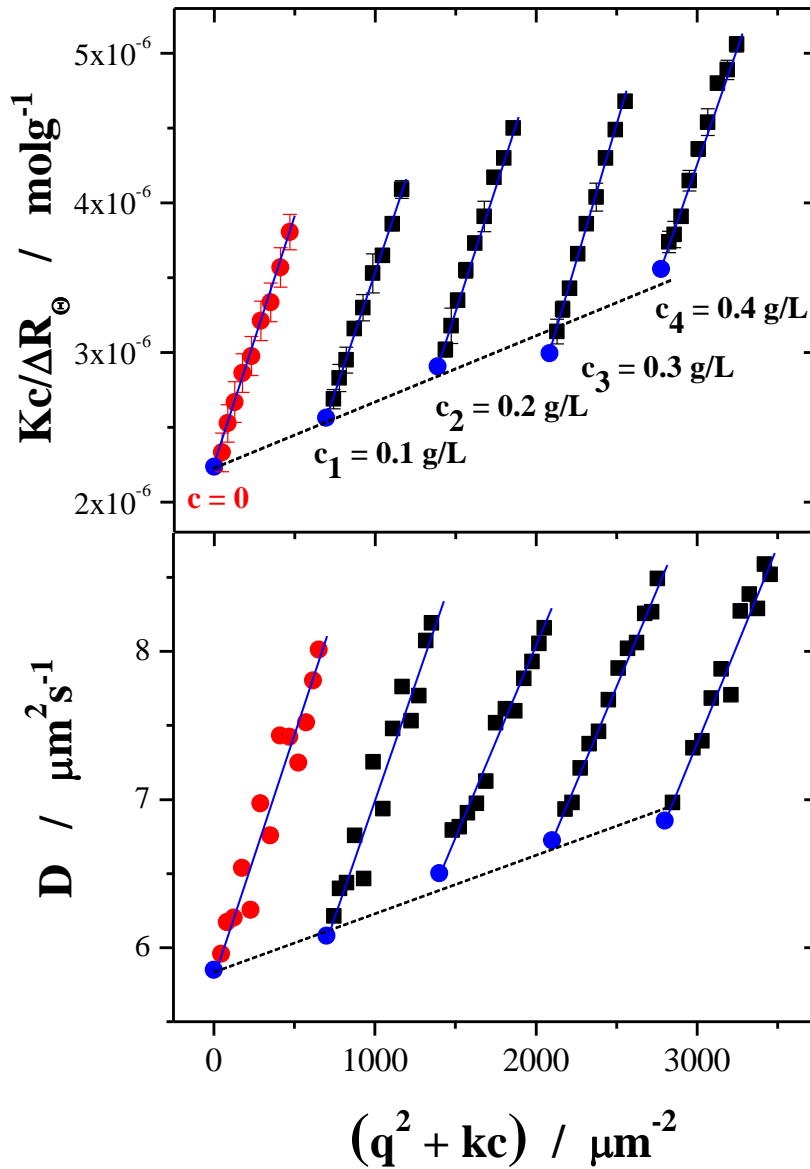

Figure 3.3 Zimm diagram from static and dynamic light scattering of sample NaPA800 characterized in aqueous 0.1 M NaCl solution: k = 7000, $47 < q^2 < 470$ µm². The blue data points correspond to the linear extrapolation of $Kc/\Delta R_{\Theta}$ to $q^2 = 0$. The dashed line is a guide for the eye indicating the extrapolation of $Kc/\Delta R_{\Theta=0}$ to $c = 0$.

Table 3.2 Characteristic parameters of sample NaPA800 in 0.1 M NaCl from the combined SLS/DLS analysis.

M_w / gmol^{-1}	R_g / nm	R_h / nm	ρ	A_2 / 10^{-6} molLg^{-2}	k_D / Lg^{-1}	var_z
447 200	67	41.6	1.58	1.5	0.39	0.25

Both SLS/DLS characterisations in good solvent (0.1 M NaCl) gave values of the molecular parameters close to each other and are considered as a satisfactory reproduction.

Since there are a lot of experiments on NaPA with Ag$^+$ ions in 0.01 M NaNO$_3$, the NaPA800 standard was characterized in that solvent too. A concentration range of $0.1 < c < 0.4$ g/L had been applied. The SLS/DLS analyses was carried out in the regime of the scattering vector q of $47 < q^2 < 470$ μm^2. The static data presented in Figure 3.4 were treated via Zimm's approximation [109] using eq(2.14). The established molecular parameters from both SLS and DLS are summarized in Table 3.3.

Table 3.3 Characteristic parameters of sample NaPA800 in 0.01 M NaNO$_3$ from the combined SLS/DLS analysis.

M_w / gmol^{-1}	R_g / nm	R_h / nm	ρ	A_2 / 10^{-6} molLg^{-2}	k_D / Lg^{-1}	var_z
449 800	89.1	52.8	1.69	4.28	1.096	0.25

As it can be expected the molar mass of NaPA800 established in 0.01 M NaNO$_3$ (Table 3.3) is in a close agreement with results of NaPA800 characterisation in 0.1 M NaCl (Tables 3.1-3.2). The values of the second virial coefficient A_2 as well as the radius of gyration R_g are bigger in 0.01 M NaNO$_3$. As it is known an increase of the inert salt concentration in dilute solutions of polyacrylate results in a decrease of a solvent quality [5], therefore the impact of excluded volume effect (A_2) is supposed to be smaller in 0.1 M NaCl. The small discrepancies in R_g, M_w and R_h (Tables 3.1-3.3) can be explained by the fact that polymer was used from different vials received from the producer (Polysciences, Eppelheim, Germany) therefore the actual polymer parameters can slightly deviate.

Figure 3.4 Zimm diagram from static and dynamic light scattering of NaPA800 in aqueous 0.01 M NaNO$_3$ solution: k = 7000, 47 < q^2 < 470 µm^2. The blue data points correspond to the linear extrapolation of $Kc/\Delta R_\Theta$ to $q^2 = 0$. The dashed line is a guide for the eye indicating the extrapolation of $Kc/\Delta R_{\Theta=0}$ to c = 0.

## 3.2.2 Characterisation of NaPA1300

Five concentrations of the sample NaPA1300 in aqueous solution of 0.1 M NaCl have been used based on a stock solution with a concentration of 0.4 g/L. The SLS/DLS analyses was carried out in the regime of the scattering vector q of $47 < q^2 < 350$ µm^2.
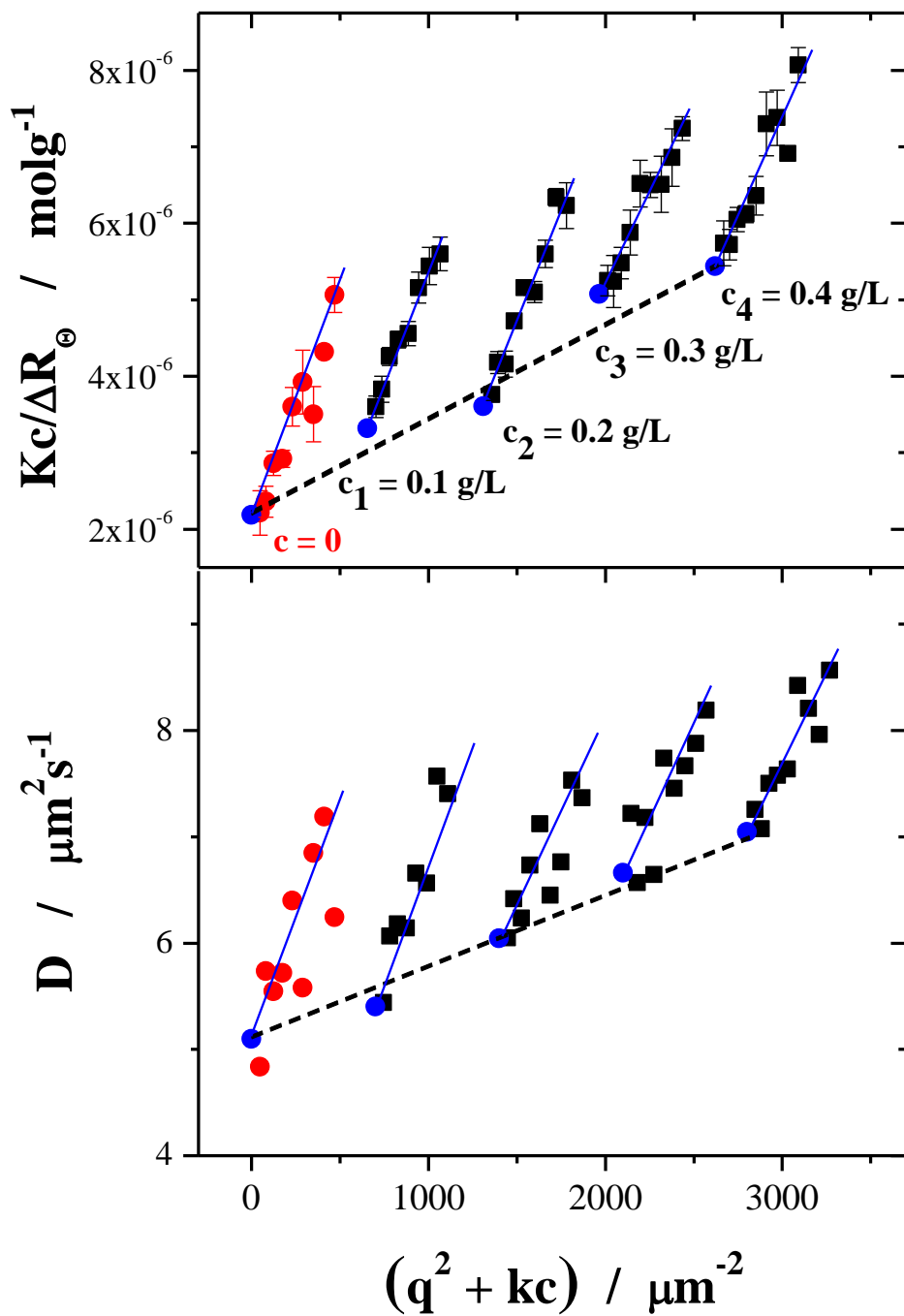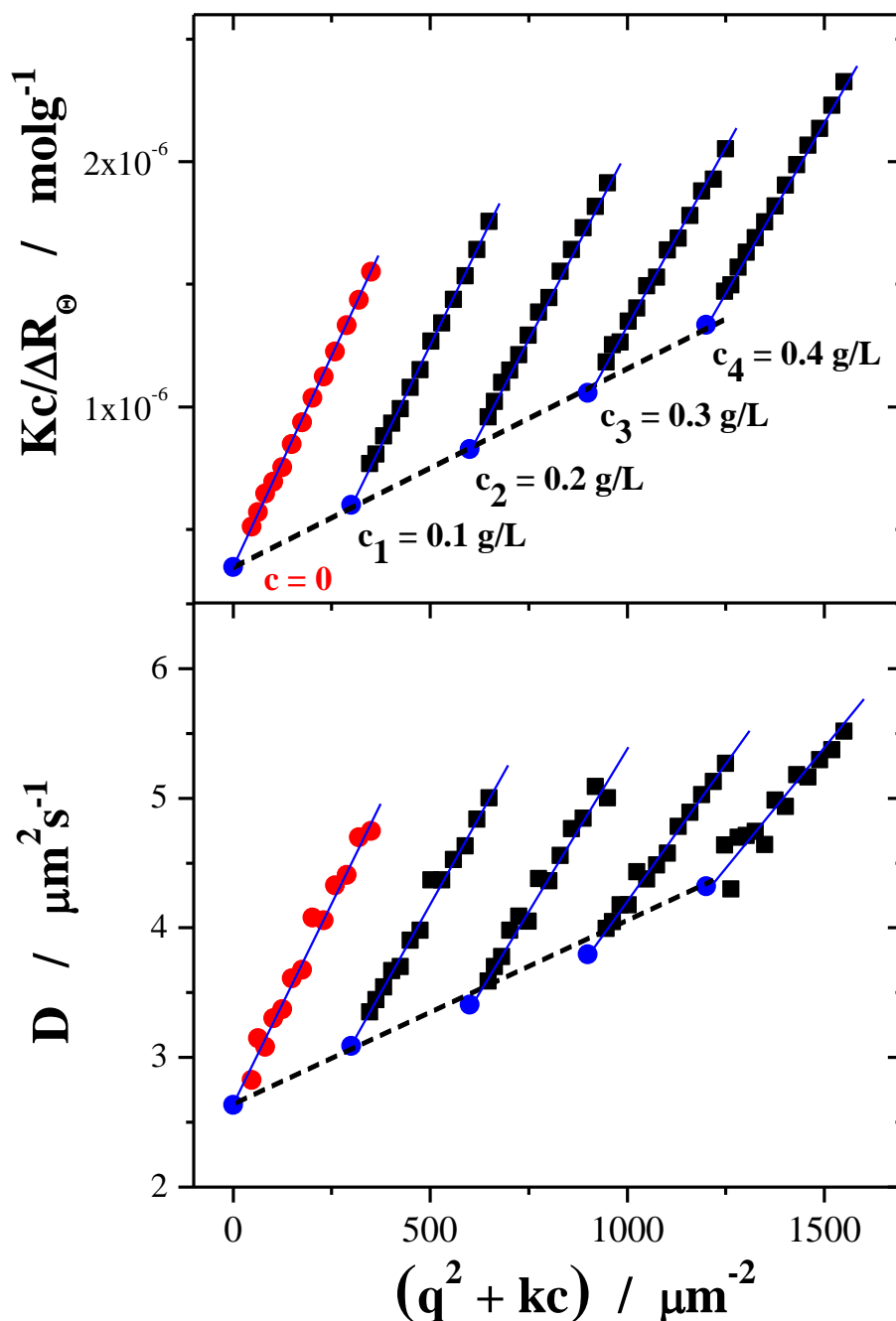

Figure 3.5 Zimm diagram from static and dynamic light scattering of NaPA1300 in aqueous 0.1 M NaCl solution: k = 3000, $47 < q^2 < 350$ µm^2. The blue data points correspond to the linear extrapolation of $Kc/\Delta R_\Theta$ to $q^2 = 0$. The dashed line is a guide for the eye indicating the extrapolation of $Kc/\Delta R_{\Theta=0}$ to $c = 0$.

The static data presented in Figure 3.5 were treated via Zimm's approximation [109] using eq(2.14). The established molecular parameters from both SLS and DLS are summarized in Table 3.4.

Table 3.4 Characteristic parameters of sample NaPA1300 in 0.1 M NaCl from the combined SLS/DLS analysis.

M_w / gmol^{-1}	R_g / nm	R_h / nm	ρ	A_2 / 10^{-6} molLg^{-2}	k_D / Lg^{-1}	var_z^*
2 890 000	156	92	1.7	1.1	1.55	0.33

*The polydispersity index was indicated by a supplier as $M_w/M_n = 1.5$, where M_w and M_n is the weight average and number average of the molar mass respectively.

3.2.3 Comparison and Conclusion

The established molecular parameters as R_g, R_h, ρ-ratio and A_2 from the SLS/DLS characterisation of the NaPA800 and NaPA1300 samples in 0.1 M NaCl solution are compared with calculated ones via equations 3.2-3.4 [5]:

$$R_g = 0.0214 * M_w^{0.6} \tag{3.2}$$

$$R_h = 0.0112 * M_w^{0.6} \tag{3.3}$$

$$A_2 = 0.107 * M_w^{-0.34} \tag{3.4}$$

Table 3.5 The calculated and established molecular parameters of NaPA800 and NaPA1300 samples from SLS/DLS characterisation in 0.1 M NaCl.

NaPA sample	M_w / gmol^{-1}	R_g / nm		R_h / nm		ρ		A_2 / 10^{-6} molLg^{-2}	
	(exp.)	exp.	calc.	exp.	calc.	exp.	calc.	exp.	calc.
NaPA800	503 000	72	**56.4**	48	**30**	1.5	**1.88**	1.1	**1.23**
NaPA800	447 200	67	**52.6**	41.6	**27.5**	1.58	**1.91**	1.5	**1.28**
NaPA1300	2 890 000	156	**161**	92	**84.3**	1.7	**1.91**	1.1	**0.68**

Table 3.5 summarises the R_g, R_h, ρ-ratio and A_2 values from Tables 3.1-3.2 and 3.4 and the calculated ones by means of eq(3.2-3.4) with molar mass values M_w used from the experiment. The size of the PA-coils in terms of R_g and R_h of the NaPA800 sample from the experimental data are higher than the theoretically expected ones for 22-35%, whereas values of the structure-sensitive factor ρ are 10-20% smaller than the calculated ones. For the NaPA1300 sample the deviations of the experimental parameters from the theoretical ones are smaller than in case of the sample NaPA800 and are within ±10%. The reasoning

for the observed discrepancies in this work and in reference [5] can be the connected with the differences in the concentration ranges of NaPA solutions used for the SLS/DLS analysis as well as in the q ranges and the methods (Zimm, Berry of Guinier) used during the evaluation of the SLS/DLS data. The experimental ρ-ratio for chains with a high polydispersity can be lower than theoretically expected value of 1.86, therefore the observed variance in this parameter (Table 3.5) can be considered as acceptable. Moreover, the data presented in Chapters 3.2.1-3.2.2 are within the uncertainties of the established values in Table 4 presented in reference [5] and can be regarded as an adequate analysis for further discussions.

3.3 Sample Preparation for Light Scattering – Linear PA

All stock solutions were prepared with bidistilled water, which was degassed by exposing it to ultrasound for 2 h and subsequently to a gentle stream of argon for 2 h. A stock solution of the NaPA in 0.01 M aqueous $NaNO_3$ at a pH of 9 was prepared and gently stirred at room temperature for 2 days. Solutions of Ag^+ ions were prepared as aqueous solutions of $AgNO_3$ in 0.01 M aqueous $NaNO_3$ at a constant overall concentration of positive charges of $[Ag^+] + [Na^+] = 0.01$ M. This was achieved by replacing a selected small amount of Na^+ ions by an equivalent amount of Ag^+ ions. All solutions were kept under an atmosphere of argon in the dark until they were used [19].

All solvents and solutions were filtered through 0.22 μm cellulose mixed ester syringe filters from Millipore (Eschborn, Germany) prior to the scattering experiments to remove dust. Cylindrical quartz cuvettes from Hellma (Müllheim, Germany) with an outer diameter of 25 mm were used for all light scattering experiments. Prior to any measurements scattering cuvettes were cleaned from dust by continuously injecting distilled acetone for 15 min.

An aggregation threshold of Ag^+-PA solutions (Chapters 4.1.1) was established using combined SLS/DLS instrument Model 5000E Compact Goniometer System (CGS) from ALV-Laser Vetriebsgesellschaft (Langen, Germany) in an angular regime of $30° \leq \theta \leq 60°$.

TR-SLS experiments on Ag^+-PA solutions (Chapters 4.1.2) were performed with a home-build multi-angle goniometer system [126] in an angular regime of $25.84° \leq \theta \leq 143.13°$.

TR-SLS/DLS experiments of Ag^+-PA solutions (Chapters 4.1.2-4.1.4) were done using model ALV CGS-3 Compact Goniometer System from ALV-Laser Vetriebsgesellschaft (Langen, Germany) in an angular regime of $20° \leq \theta \leq 76°$.

All light scattering experiments were performed at 25° C. In the evaluation of the light scattering data values of a refractive index $n = 1.3363$ and a viscosity $\eta = 0.956$ mPa×s for aqueous solution of 0.1 M NaCl and of a refractive index $n = 1.3357$ and a viscosity $\eta = 0.948$ mPa×s for aqueous solution of 0.01 M $NaNO_3$ were used. Refractive index

increments $dn/dc = 0.174$ mL/g and $dn/dc = 0.167$ mL/g were used in the evaluation of the static light scattering data for standards NaPA800 and for NaPA1300, respectively [5].

The scattering from NaPA solutions in the presence of AgNO$_3$ depends in a complex way on the ratio of Ag$^+$ ions and COO$^-$-groups, and a simple extrapolation procedure to $c = 0$ becomes impossible. Hence, the static and dynamic scattering curves in those cases were approximated with the angular-dependent parts of eq(2.14) and eq(2.29), which render molecular parameters M_w, R_g and R_h to apparent parameters. Hydrodynamic radius R_h was treated via eq(2.31). Zimm's approximation [109] was used for comparatively small particles in the range of $qR_g < 1$. Data for the aggregation experiments with Ag$^+$ ions turned out to be in most cases suitably analyzed according to Guinier's approximation [110].

3.4 Synthesis of Photoinitiators

3.4.1 Synthesis of HMEM

The procedure of the synthesis of 2-[p-(2-hydroxy-2-methylpropiophenone)]-ethyleneglycol-methacrylate (HMEM) was reported earlier in references [46-48]. HMEM was prepared by a Schotten-Baumann reaction (Figure 3.6). In a typical run 11.9 g of 2-hydroxy-4´-hydroxyethoxy-2-methylpropiophenone and 5.4 g of destabilized methacryloyl chloride were added into a 250 mL flat-bottomed flask charged with 100 mL of acetone. Reactants were dissolved at 30 °C under vigorous stirring (ca. 500 rpm). The mixture was then cooled down to 0 °C using an ice bath and 10 mL of pyridine was added dropwise to the cooled mixture. The reaction lasts for 8 h. The reaction mixture was put into the fridge during the successive night. On the next day the resulting product was carefully washed for five times with water and dried over anhydrous Na$_2$SO$_4$. Further purification was achieved through column chromatography on silica gel using a mixture of acetone : toluene = 1:1 as an eluent. The overall yield was ca. 40%.

^{1}H NMR (CD$_3$COCD$_3$, δ in ppm): 1.50 (*s*, 3 H, -C(CH$_3$)-), 2.09 (*s*, 3 H, =C(CH$_3$)), 2.89 (*s*, 1 H, OH), 4.40, 4.52 (*t*, 4 H, CH$_2$CH$_2$), 5.63, 6.08 (*d*, 2 H, CH$_2$), 7.01, 8.24 (*m*, 4 H, C$_6$H$_4$).
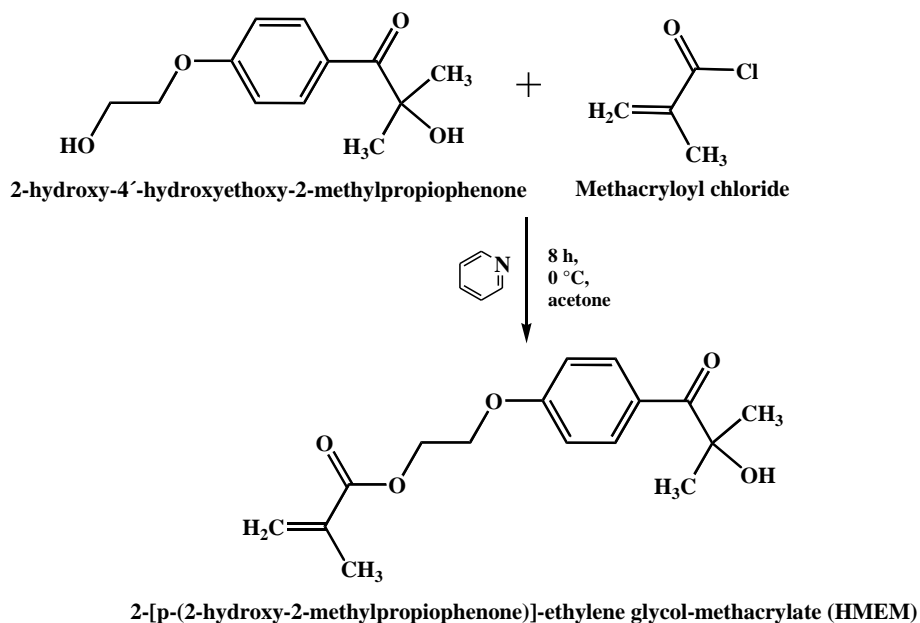
Figure 3.6 Scheme of the synthesis of HMEM.

3.4.2 Synthesis of BA

The procedure of the synthesis of benzoin acrylate (BA) was reported earlier in references [47, 48]. BA was prepared by a Schotten-Baumann reaction (Figure 3.7). Under vigorous stirring (ca. 500 rpm), 28.5 g of destabilized acryloyl chloride was dropped into a mixture of 11.1 g benzoin, 28.5 mL of dimethylaniline and 50 mL of chloroform at 10 °C. After the addition of acryloyl chloride, the reaction was gently stirred for 2 h at 0 °C. Chloroform and the remaining acryloyl chloride were removed under vacuum. The solid residue was hydrolysed with 6 M H_2SO_4 and washed with water for eight times until a pH = 7 was reached for the organic layer. The final product was recrystallized from ethanol twice. The overall yield was ca. 75%.

^{1}H NMR (CD_3COCD_3, δ in ppm): 5.97, 5.99 (*d*, 2H, =CH_2), 6.27-6.32 (*q*, 2H, =CH_2), 6.42, 6.46 (*s*, 1H, CH), 7.09 (*s*, 1H, C_6H_5), 7.40 (*m*, 2H, C_6H_5), 7.49 (*t*, 2H, C_6H_5), 7.60 (*m*, 2H, C_6H_5), 8.06 (*d*, 1H, C_6H_5).

51
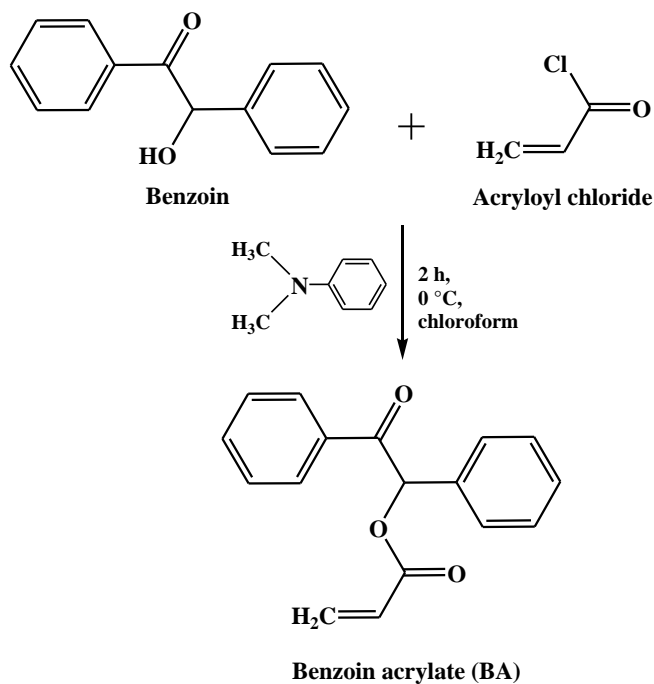
Figure 3.7 Synthesis of BA.

3.4.4 Synthesis of ABP

The procedure of the synthesis of 4-acryloxybenzophenone (ABP) was reported earlier in references [47, 48]. ABP was synthesized by a Schotten-Baumann reaction (Figure 3.8). In a typical run, 5.9 g of destabilized acryloyl chloride was added dropwise to the mixture of 7.5 g of 4-hydroxybenzophenone and 7.3 g triethylamine in 100 mL of anhydrous diethyl ether solution. The reaction mixture was refluxed for 2 h at 0 °C and then hydrolysed with 0.1 M aqueous HCl. The organic layer was washed at first with 5% aqueous NaOH solution to remove the impurities and successively for 7 times with water until a pH of 7 was reached. After being dried by anhydrous Na_2SO_4, the solvent was removed under vacuum. The raw product, a yellow oil, was dissolved in boiling ethanol and then filtered after treatment with activated charcoal. A white powder of ABP was obtained by recrystallizing the solution from ethanol at 0 °C twice. The total yield was 60%.

^{1}H NMR (CD_3COCD_3, δ in ppm): 6.14 (*m*, 2H, =CH_2), 6.41 (*m*, 2H, =CH_2), 6.61 (*m*, 1H, CH), 7.38 (*m*, 2H, C_6H_5), 7.57 (*m*, 2H, C_6H_5), 7.67 (*m*, 1H, C_6H_5), 7.80 (*m*, 2H, C_6H_5), 7.88 (*m*, 2H, C_6H_5).
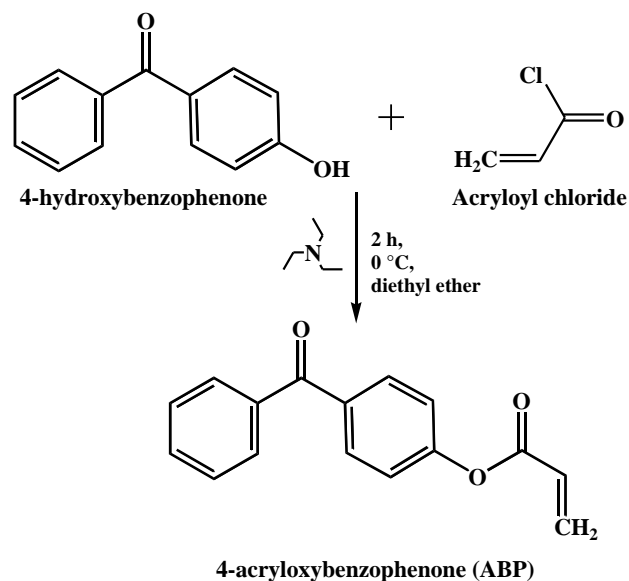
Figure 3.8 Synthesis of ABP.

3.5 Preparation of Spherical Polyelectrolyte Brushes

3.5.1 Synthesis of Polystyrene Cores

The polystyrene (PS) core latices were synthesized using a conventional emulsion polymerisation according to a procedure reported in references [46-48]. In a 500 mL three-neck round-bottom flask equipped with a thermometer, a reflux condenser, a stirrer and thermostatic system (IKA RCT classic) 40 mL of styrene was polymerized in 150 mL of bidistilled H_2O using 0.382 g of SDS as surfactant and 0.086 g of KPS as initiator. SDS was dissolved first in bidistilled water while stirring and then freshly destabilised styrene was added into the flask. Successively, the solution was degassed in vacuum and filled with N_2 by means of four freeze-pump-thaw cycles using liquid nitrogen. The emulsion polymerisation was started by adding KPS at the temperature of 80 °C. The reaction lasted for 1.5 h at 80 °C. At the end of the reaction the temperature was lowered to 70 °C. The next step followed immediately after the styrene polymerisation.

3.5.2 Grafting of Photoinitiator Layers

In order to achieve a well-distributed layer of the photoinitiator on the PS-core, the photoinitiator HMEM, BA or ABP (2-3% mole percent of styrene) was dissolved in acetone and added with a syringe under starved conditions manually: 0.1 mL of a 30 wt. % solution of photoinitiator was injected into the reaction mixture every 2 min [46-48]. After

the last addition, the latex was cooled down to room temperature and purified by serum replacement (see Chapter 3.6) against pure water until the conductivity of the outer water became stable.

3.5.3 Synthesis of Spherical Polyacrylate Brushes

The purified core latex equipped with a thin layer of photoinitiator was added to a homemade UV-reactor (UV-lamp Heraeus TQ 150, range of wavelengths: 250-600 nm) and diluted to 2 wt. % with bidistilled water. Destabilised acrylic acid (50 % mole percent of styrene) was added and afterwards the solution was degassed in vacuum and filled with N_2 by means of four freeze-pump-thaw cycles using liquid nitrogen. Photopolymerization was performed with the use of UV-vis radiation at room temperature for 3 h. This time period of UV-vis illumination insures the complete formation of the PA-shell [47]. Vigorous stirring ensured homogeneous conditions during the photopolymerization. To remove possible coagulum the latex was filtrated through a folded filter (Machery-Nagel, Düren, Germany) after the polymerisation was completed.

Photoinitiators HMEM, BA and ABP follow two different mechanisms of the photoinitiation. Figure 3.9a illustrates the cleavage mechanism of HMEM and BA, where these molecules split into two radicals under UV-irradiation. The ABP molecule gives rise to free radical species by a hydrogen abstraction mechanism (Figure 3.9b), which provides the formation of a ketone singlet excited state (S1), its evolution by an intersystem crossing process (ISC) to triplet state (T1), and finally its photoreduction by a hydrogen donor (RH). Without the use of a hydrogen donor, no brush can be formed [47, 48]. Hence, 7 mL of *tert*-butanol has been used as a hydrogen donor to initiate the mechanism of photoinitiation.

$$ Ar-\overset{\overset{O}{\parallel}}{C}-R \quad \xrightarrow{h\nu} \quad Ar-\overset{\overset{O}{\parallel}}{C}\bullet \;+\; \bullet R \tag{a} $$

$$ Ar-\overset{\overset{O}{\parallel}}{C}-Ar \xrightarrow{h\nu} \left[Ar-\overset{\overset{O}{\parallel}}{C}-Ar \right]_{S1} \xrightarrow{ISC} \left[Ar-\overset{\overset{O}{\parallel}}{C}-Ar \right]_{T1} \xrightarrow{RH} Ar-\overset{\overset{OH}{|}}{\underset{\bullet}{C}}-Ar \;+\; \bullet R \tag{b} $$
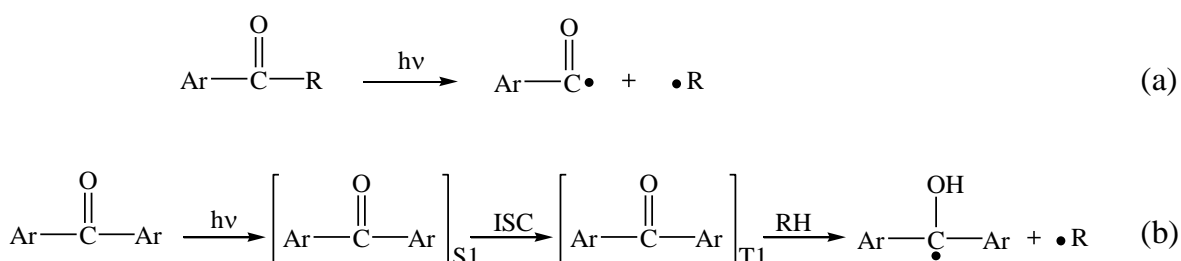
Figure 3.9 Mechanism for photoinitiation. (a) Cleavage mechanism for the photoinitiators HMEM and BA. (b) Hydrogen abstraction mechanism for the photoinitiators ABP.

3.6 Purification of Latices

The latices must be cleaned from impurities incorporated in the latex prior to the characterization and further application in order to avoid potential problems. It is particularly important for polyelectrolytes since their behaviour is very sensitive to the ionic strength in solution. The serum replacement method (also denoted as ultrafiltration) was used in order to clean both PS-cores equipped with a layer of the photoinitiator and SPBs.

The serum replacement applies pressure to force the solvent and small impurities across a membrane while the larger latex particles are retained. The equipment was made in our university (Figure 3.10) in accordance with literature [145]. Latices with a concentration of 5 wt. % were cleaned by serum replacement with nitrocellulose membrane filters from Millipore. In case of purification of solutions with PS-cores decorated with the photoinitiator the membrane pore size of 50 nm was used, in case of solutions with SPBs the membrane pore size was 100 nm. The applied pressure was 1.8 bars. The cleaning process in the ultrafiltration cell was performed against bidistilled water until the conductivity of the eluate did not change anymore.

Figure 3.10 Schematic sketch and photo of the serum replacement cell.

3.7 Characterisation of Spherical Polyacrylate Brushes

3.7.1 Determination of Sizes and Size Distributions

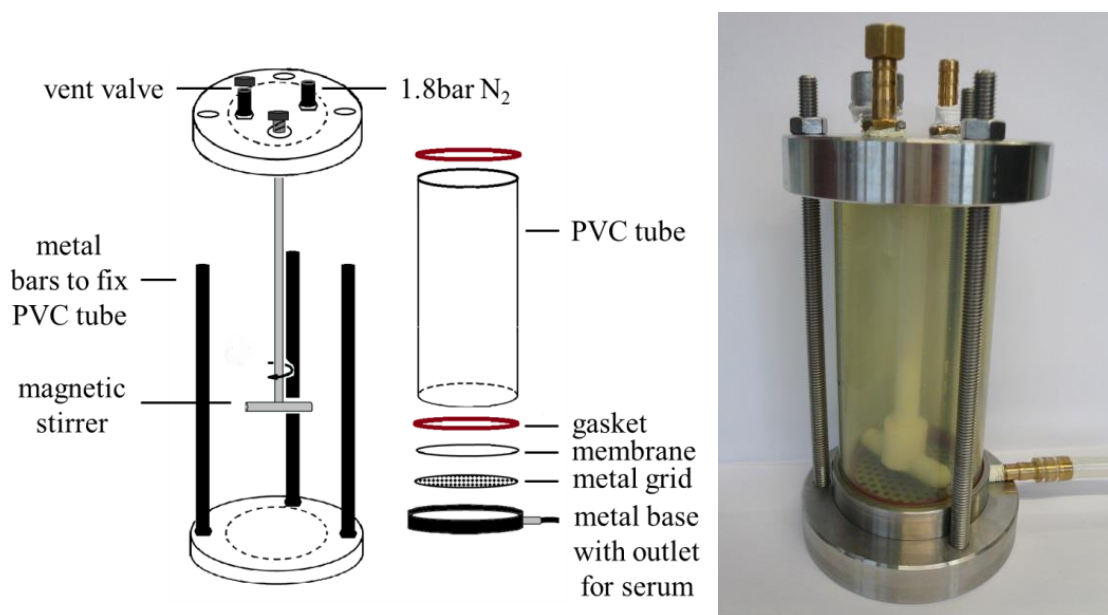A drop of latices was diluted with deionized water to a final concentration of ca. 10 ppm for the DLS analysis performed with the Model ALV-CGS 5000E at 25 °C in the range of the scattering angles $30° < \theta < 150°$. All solutions were filtered through 0.45 μm cellulose mixed ester syringe filters from Millipore (Eschborn, Germany) prior to the scattering experiments to remove dust. A refractive index $n = 1.3357$ and a viscosity $\eta = 0.948$ mPa×s for aqueous solution of 0.01 M NaNO$_3$/NaCl were used. Dynamic data was treated via eq(2.29) omitting the concentration dependent term, hydrodynamic radius R_h was calculated by means of eq(2.31).

Such a low concentration of polyacrylate brushes in pure water did not lead to any aggregation process which is expected in polyelectrolyte salt free solutions. The pH value of salt free solutions was adjusted to the value of ca. 10 prior to the DLS analysis, which enables to assume that the PA-chains of SPBs are fully stretched. The particle size distributions were characterized in terms of var_z. Ten intensity-correlation functions were evaluated with a decay of $g^{(2)}(q, t)$ - 1 to 31% by the second order cumulant method at a scattering angle of $\theta = 30°$. The averaged var_z values are summarised in Table 3.6 together with the R_h of PS-cores and SPBs.

Table 3.6 Values of hydrodynamic radii R_h and var_z of the PS-cores and of the SPBs measured by DLS.

Grafted photoinitiator	$R_{h,PS}$ / nm	var_z of PS-cores	pH of solutions with SPBs	$R_{h,SPB}$ / nm	var_z of SPBs	L / nm
HMEM	59.2	0.058	10.3	218.9	0.064	159.7
ABP	71.7	0.053	9.6	163.1	0.069	91.4
BA	70.0	0.070	10.1	220.0	0.071	150

Since the time of emulsion polymerisation of styrene was fixed to ca. 60 min before the photoinitiator had been chemically bonded to, the final size of all PS-cores in three types of SPBs is similar. Figure 3.11 shows SEM micrographs of SPBs, which exhibit a well-defined spherical structure and also demonstrate a narrow size distribution, in accordance with the DLS data (Table 3.6). The diameters of latices are all around 110-130 nm, which is close to the PS-core size $R_{h,PS}$ determined by DLS. Apparently, the PA-chains fold back onto the PS-core surface during drying of the sample and hardly contribute to the visible size in this case.
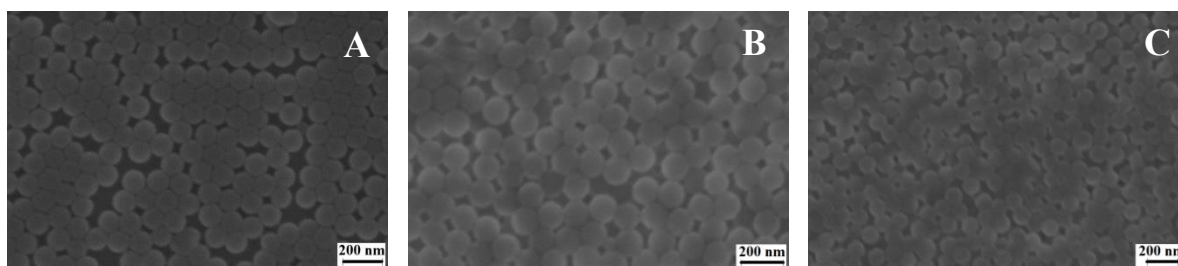
Figure 3.11 SEM micrographs of SPBs prepared by photoemulsion polymerisation using photoinitiator ABP (A), BA (B) and HMEM (C).

A polydispersity as low as ca. $var_z = 0.07$ allows to derive the thickness L of the surface layer as [46-48]

$$L = R_{h,SPB} - R_{h,PS} \tag{3.5}$$

Accordingly to Guo et al. [47, 48] the thickness of the PA-shell L is expected to depend on the grafted photoinitiator in the following order: $L(\text{ABP}) < L(\text{HMEM}) < L(\text{BA})$. However, in Table 3.6 the maximal L value was obtained for SPBs based on the PS-cores grafted with photoinitiator HMEM. This slight incompatibility may stem from experimental conditions during the two-step polymerisation, of the shell such as a variation of the exact rate of adding the solution with photoinitiator to the polystyrene solution or a variation of the exact amount of destabilized acrylic acid leaving the flush column. The results are still in agreement with works published earlier and suitable for further experiments [46-48].

3.7.2 Determination of Brush Parameters

The initiators ABP, HMEM and BA used in this work contain an ester bond (Figures 3.6-3.8) which connects the initiating group to the PS-core. Since the ester bond can be cleaved by a strong aqueous base, the polyelectrolyte chains can be removed from the surface of latex particles and analysed separately. Hence, 70 mL of latices which contain about 0.1-0.3 g of polyacrylate were hydrolysed with 2 M NaOH solution in a 250 mL round-bottom PFA flask at 120 °C for 10 days. During the hydrolysis the latices became unstable and coagulated. After hydrolysis, the coagulum was separated from the suspension by centrifugation with 20000 rpm/min for 3 h. After neutralisation the PA-chains remained in the supernatant liquid. They were purified by means of serum replacement with regenerated cellulose membrane (Millipore, molecular exclusion size: 5 kDa) against deionized water.

The amount of purified NaPA was determined by gravimetry after freeze-drying. Measurements of the intrinsic viscosity $[\eta]$ in 0.5 M NaCl at 25 °C using an Ubblohde capillary viscometer allowed to determine the viscosity-average molecular weight M_η of the NaPA by means of Mark-Houwink relation

$$[\eta] = \mathrm{K} M_\eta^\alpha \tag{3.6}$$

where K and α are Mark-Houwink constants characteristic for the type of polymer, solvent and temperature of the viscosity experiment (for NaPA in 0.5 M NaCl solution at 25 °C: K = 0.0186 mL/g, $\alpha = 0.72$ [146]).

The hydrodynamic radius of free PA-chains was estimated by

$$R_{h,PA\text{-}chain} = \left(\frac{3M_\eta[\eta]}{10\pi N_A}\right)^{1/3} \tag{3.7}$$

The determination of the grafting density σ follows from the measurement of the grafted amount of PA-chains on the PS-surface, determined by direct conductivity titration of latices after serum replacement with aqueous NaOH solution:

$$\sigma = \frac{\frac{wt\%_{PA-shell}}{wt\%_{PS-core}} \rho_{PS} {}^4/_3 \pi R_{h,PS}^3 N_A}{M_{[\eta]} 4\pi R_{h,PS}^2} \tag{3.8}$$

where ρ_{PS} is the density of bulk PS equal to 1 g/cm^3, N_A is Avogadro's constant, $R_{h,PS}$ is the hydrodynamic radius of the PS-core determined by DLS (Table 3.6), wt. % $_{PA\text{-}shell}$ = $\frac{C_{PA-shell}}{C_{SPB}}$ is the mass percent of the PA-shell (calculated from the conductivity titration of latices) to the overall mass of the brush (found from gravimetric measurements) and wt. % $_{PS\text{-}core}$ = $\frac{C_{SPB}-C_{PA-shell}}{C_{SPB}}$ is the mass present of the PS-core to the overall mass of the brush.

The average distance D between two neighbouring grafted points can be derived from the grafting density σ via relation [48]

$$D = \frac{4}{\sqrt{\sigma\pi}} \tag{3.9}$$

Only once D gets distinctly smaller than two times of R_g of the PA-chains, the polymer chains stretch away from the surface into the solution, forming a brush, otherwise the configurations of the grafted chains resemble either "pancake" or "mushroom" [44].

Table 3.7 summarizes the analytical results of three solutions with SPBs prepared by means of photo-emulsion polymerisation.

Table 3.7 Parameters of SPBs synthesised by photoemulsion polymerisation.

SPB	$R_{h,PS}$ / nm	M_{η} / gmol^{-1}	σ / nm^{-2}	$R_{h,PA\text{-}chain}$ / nm	D / nm	L_c / nm
SPB(HMEM)	59.2	61642	0.055	8.0	4.9	163.5
SPB(ABP)	71.7	34837	0.044	5.8	5.4	93.6
SPB(BA)	70.0	56946	0.046	7.8	5.3	153.6

The average distances D are all much smaller than two times the hydrodynamic radius $R_{h,PA\text{-}chain}$ of free PA-chains, which confirms the fact that the PA-chains form a brush structure on the PS-cores. The values of the viscosity-average molecular weight M_{η} and grafting density σ are in a close agreement with the literature data where the same synthetic route in the preparation of the SPBs was applied [46-48]. As it can be seen from Tables 3.6-3.7 the averaged contour length of the PA-chains L_c, estimated from M_{η}, and the thickness of the PA-shell L, measured by DLS of the salt free solution at high pH, agree also well.

3.7.3 Effects of pH and ionic Strength on the PA-shell

It is well known from literature that the behaviour of SPBs consisting of PA-chains must depend on the pH value and ionic strength [51]. To check the influence of these parameters on the synthesized SPBs in our work, a drop of latices SPB(HMEM) was diluted by 50 mL aqueous NaNO$_3$ solution at different NaNO$_3$ concentrations: 0.001 M, 0.01 M and 0.1 M to a final concentration of ca. 10 ppm. Successively, the pH-values were adjusted to ca. 10 and to ca. 5 by adding a small amount of 0.1 M NaOH (0.05-0.1 mL). Solutions were mixed with a magnetic stirrer for 2 h before being monitored by DLS. The DLS analysis performed with the Model ALV-CGS 5000E at 25 °C in the range of the scattering angles $30° < \theta < 150°$. All solutions were filtered through 0.45 μm cellulose mixed ester syringe filters from Millipore (Eschborn, Germany) prior to the scattering experiments to remove dust. A refractive index $n = 1.3357$ and a viscosity $\eta = 0.948$ mPa×s for aqueous solution of 0.01 M NaNO$_3$/NaCl were used. Dynamic data was treated via eq(2.29) omitting the concentration dependent term, hydrodynamic radius R_h was calculated by means of eq(2.31).
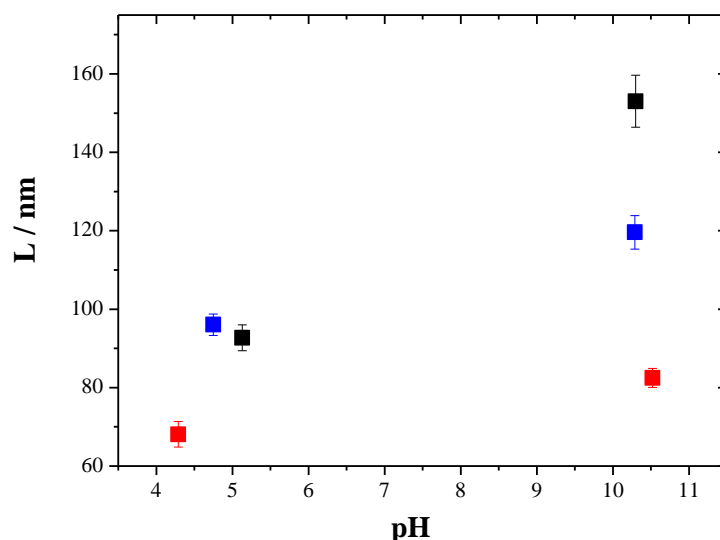
Figure 3.12 Thickness *L* of the PA-layer of SPB(HMEM) as a function of pH at different ionic strengths: 0.001 M NaNO$_3$ (■), 0.01 M NaNO$_3$ (■) and 0.1 M NaNO$_3$ (■).

Figure 3.12 demonstrates the change in brush size measured by DLS at two significantly different pH and three NaNO$_3$ concentrations. At low pH the PA-chains are slightly charged and due to low electrostatic repulsions the PA-chains a hardly stretched. Upon increasing pH a marked stretching of the PA-chains with increasing electrostatic repulsions occurs due to the increased dissociation of COO$^-$-groups. With increasing the salt concentration the SPB shrinks due to the screening of charged carboxyl groups by counter ions. At high pH this screening effect is more pronounced because of the higher degree of dissociation of carboxylic groups.

The dependence of the thickness *L* of the PA-layer, calculated from DLS measurements (eq. 3.5), on the salt concentration is also depicted in Figure 3.13 where a broader range of salt concentration has been applied: $0.001 < [NaNO_3] < 1$ M. Particles were transformed into the fully dissociated form by addition of small amounts of 0.1 M NaOH until a pH of ca. 11 was reached. Subsequently, the salt concentration was adjusted by diluting the SPB solution with NaNO$_3$ solutions of the respective concentrations.

It has been predicted and first shown experimentally by Hariharan et al. [147] that in solutions of monovalent salt with a concentration of C_a, the brush thickness scales as $L \sim C_a^{-m}$, with an exponent $m = -\frac{1}{10}$. However, combined effects of curvature and rafting density may vary value *m*. Our experimental data results in $m = -\frac{1}{7}$ which is in a good agreement to reported values [46, 62, 148].

These results allow us to finally conclude that the synthetic route applied in this work gave adequate brush parameters and resulted in proper spherical polyelectrolyte brushes.
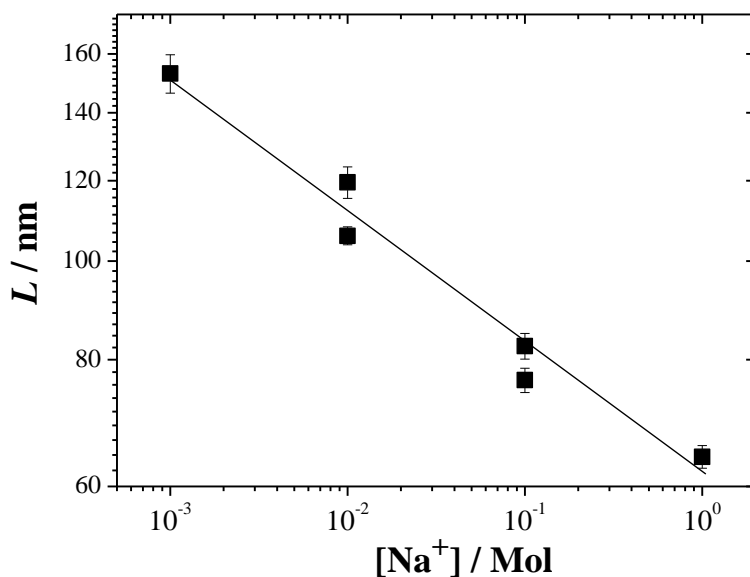
Figure 3.13 Thickness L of the PA-layer of SPB(HMEM) as a function of salt concentration C_a in terms of [NaNO$_3$] at a pH of ca.11. The line indicates the resulting scaling law with $m = -\frac{1}{7}$.

3.8 Sample Preparation for Light Scattering - SPB

Ag$^+$-, Ca^{2+}- and Mg^{2+}-SPB solutions were characterized by combined SLS/DLS with the Model ALV-CGS 5000E in the regime of the scattering vector q of $47 < q^2 < 350 \; \mu m^2$ at 25 °C. Cylindrical quartz cuvettes from Hellma (Müllheim, Germany) with an outer diameter of 25 mm were used for all light scattering experiments. Prior to any measurements scattering cuvettes were cleaned from dust by continuously injecting distilled acetone for 15 min. All solutions were filtered through 0.45 μm cellulose mixed ester syringe filters from Millipore (Eschborn, Germany) prior to the scattering experiments to remove dust. A refractive index $n = 1.3357$ and a viscosity $\eta = 0.948$ mPa×s for aqueous solution of 0.01 M NaNO$_3$/NaCl were used. Dynamic data was treated via eq(2.29) omitting the concentration dependent term, hydrodynamic radius R_h was calculated by means of eq(2.31). The thickness of the PA-shell L was calculated by means of eq. 3.5 using $R_{h,PS}$ from Table 3.6.

In order to consider the effect of Ag$^+$ ions on the shrinking of the PA-layer at variable ionic strength (Chapter 4.3.1), two stock solutions of SPB(HMEM) with [COO$^-$] = 0.2 mM were prepared. One SPB stock solution was prepared using 0.01 M NaNO$_3$ as a solvent and the other one was based on salt free water. In both SPB stock solutions the pH was adjusted to 6.5 by adding ca. 0.05 mL of 0.1 M NaOH. Using aqueous solutions of 0.01 M AgNO$_3$, 0.01 M NaNO$_3$ and salt free water, two series of experiments were established. In one series equal amounts of SPB salt free solution and AgNO$_3$ solutions at variable

concentrations were mixed in the scattering cuvettes and immediately monitored by DLS. In the other series of experiments the overall ionic strength was set to 0.01 M thus the desired [Ag^+] was reached by dilution of 0.01 M $AgNO_3$ solution with required 0.01 M $NaNO_3$ solution. Subsequently the solution of two salts was mixed with an equal amount of SBP solution in 0.01 M $NaNO_3$ in the scattering cuvette and immediately analysed by DLS.

The effect of Ca^{2+} ions on the shrinking of the PA-shell at variable ionic strength (Chapter 4.3.4) was analysed in a way analogous to the one used to analyse the impact of Ag^+ ions. $CaCl_2$ salt was used as a source of Ca^{2+} ions. In order to keep the overall concentration of the positive charges at 0.01 M, NaCl was used instead of $NaNO_3$.

The effects of monovalent Ag^+ ions and of divalent Ca^{2+} or Mg^{2+} ions on the shrinking of the PA-layer were compared via the DLS characterisations of Ag^+-, Ca^{2+}- and Mg^{2+}-SBP solutions at variable [COO^-] and metal ion concentration (Chapters 4.3.3-4.3.5). At first small amounts of SBP latices were diluted with 0.01 M $NaNO_3$ (for the experiments with Ag^+) or with 0.01 M NaCl (for the experiments with Mg^{2+} and Ca^{2+}) resulting in [COO^-] concentration of 0.5 mM, 0.4 mM and 0.3 mM for experiments with Ag^+, Ca^{2+} and Mg^{2+} respectively. Afterwards the pH of SPB stock solutions was carefully adjusted to 6.5 by addition of ca. 0.05 mL of 0.1 M NaOH. Solutions of $AgNO_3$/$CaCl_2$/$MgCl_2$ with 0.01 M concentration were used as sources of Ag^+, Mg^{2+} and Ca^{2+} ions and 0.01 M $NaNO_3$/NaCl as solvents. The concentration of positive charges had been set to 0.01 M. Equal amounts of latices SPB and $AgNO_3$/$CaCl_2$/$MgCl_2$ solutions of variable concentration were mixed in the scattering cuvette, thus the analysed [COO^-] and [M^{n+}] with respect to concentration thereof in stock solutions were decreased by a factor of two. Ag^+-, Ca^{2+}- and Mg^{2+}-SBP solutions have been monitored by DLS immediately after their preparation. The concentrations of COO^--groups was varied between 0.05 mM and 0.25 mM. The analysed range of counterion concentrations was $0.01 \leq [Ag^+] \leq 10$ mM, $0.05 \leq [Ca^{2+}] \leq 1.5$ mM and $0.1 \leq [Mg^{2+}] \leq 3$ mM.

3.9 Synthesis of Ag-NPs in Ag^+-SPB Solutions by means of Chemical Reducing Agent ($NaBH_4$)

The pH of the SPB(HMEM) stock solution in 0.01 M $NaNO_3$ with a concentration of [COO^-] = 1 mM was adjusted to 6.3 by addition of a small amount (ca. 0.05 mL) of 0.1 M NaOH. The stock solutions of $AgNO_3$ were prepared in water with a concentration of 0.01 M and 0.015 M. Four solutions of $NaBH_4$ with a concentration of 15 mM, 35 mM, 22.5 mM and 37.5 mM were prepared using cooled water and stored at ca. 4 °C. All solutions were stored for 1 h in ice baths to ensure low enough temperatures therein. 3 mL aliquots of SPB(HMEM) and $AgNO_3$ solutions each were mixed for 5 min and added to a doubled volume (6 mL) of $NaBH_4$ solution stirred at 500 rpm drop by drop (ca. 0.05 mM

per 2 sec) during ca. 5-7 min. After addition of the last portion of Ag^+-SPB solution, stirring of the final reactive mixture was stopped. Solutions were washed with purified water in a serum replacement cell using a cellulose nitrate membrane with a pore size of 100 nm from Millipore. The compositions of solutions are given in Table 4.4.3.

4 Results and Discussion

4.1 Specific Interactions of Ag^+ Ions with PA-chains

Although Ag^+ is a transition metal cation, it is monovalent. Its monovalency makes Ag^+ particular suitable for comparison of its specific interactions with those exerted by monovalent ions like Na^+ ions, which are considered to act as inert salts where mere electrostatic interactions are dominant (see Chapter 1.1.2).

Ikegami and Imai [6] have stated already in 1962 that a critical salt concentration of Ag^+ ions required for precipitation of the polyanion is $[Ag^+]_c = [NaPA]_c$, with m and r_0 in eq(1.1) equal to 0 and 1 respectively. Preceding experiments beyond our own group [19] suggested that the specific binding of Ag^+-cations onto PA chains is even stronger than of Cu^{2+} and Pb^{2+} cations [15, 17]. The concentration of Ag^+ ions required therein to cause an instability of the dissolved NaPA chains was orders of magnitude smaller than in the case of alkaline earth cations. Resolution of these contradictory results requires a detailed analysis of the phase behavior of aqueous solutions of Ag^+-PA complexes.

The present Chapter reveals a systematic characterization of Ag^+-PA solutions. The impact of silver ions on the size and shape of NaPA was analysed by combined SLS/DLS. We studied dilute aqueous solutions of two NaPA samples with a molecular weight of M_w = 503 000 gmol^{-1} and 2 890 000 gmol^{-1} respectively, at a pH of 9 (Chapter 3.2). All experiments were performed at an inert salt level of 0.01 M $NaNO_3$, in order to screen intermolecular electrostatic repulsions among NaPA chains and thus suppressing a structure factor of chains or aggregates. The resulting data were used to identify and locate morphological transitions of Ag^+-PA complexes. TR-SLS and time-resolved combined SLS/DLS (TR-SLS/DLS) provided information about the aggregation processes and structural organization of Ag^+-PA complexes. Hence, these results can offer a new and systematic insight into the shape of the PA-chains and their aggregates in the presence of Ag^+-ions and enable to relate these data to an extended phase diagram.

Moreover, Ag^+-PA complexes are also interesting with respect to Ag-NP formation, which is possible without additional reducing agents in the presence of sufficiently long PA-chains (Chapter 1.1.2) [19, 22]. Hence, these results are a base for the further investigations with respect to generation of Ag-NPs (Chapter 5.2).

4.1.1 Aggregation Threshold

The goal of this Chapter 5.1.1 is to provide a detailed analysis of the NaPA solutions at very low silver concentrations, which causes the aggregation therein. This is done by increasing the $[Ag^+]/[COO^-]$ ratio at constant Ag^+ ion concentration in the Ag^+-PA solution, initially located in the regime where the polymer is expected to be molecularly dispersed. An aggregation process is expected to be induced in the Ag^+-PA solutions by traversing a certain threshold.

Accordingly, two NaPA samples were investigated by means of several dilution series, each at a constant Ag^+ ion concentration. Five dilution series have been performed with sample NaPA1300 (M_w = 2 890 000 gmol^{-1}) and contribute to the evolution of a threshold in the same way as six experimental series performed with sample NaPA800 (M_w = 503 000 gmol^{-1}). The approach to the aggregation threshold and its determination procedure are given in the following Chapters 4.1.1.1 and 4.1.1.2.

4.1.1.1 Approach to the Aggregation Threshold

The procedure to establish the aggregation threshold for NaPA800 and NaPA1300 samples is based on several series of combined SLS/DLS experiments at variable NaPA concentration but constant Ag^+ content. The results of one series at an Ag^+ concentration of 0.0015 mM are outlined in Figures 4.1.1 and 4.1.2. Preparation of analysed solutions is performed as follows. Two starting solutions were prepared first. Both starting solutions had 0.01 M of cationic charges. One starting solution contained 0.01 M of Na^+ ions and a concentration of NaPA of 6 mM and the other starting solution contained a concentration of 0.003 mM of Ag^+ ions and 9.997 mM of Na^+ ions. After mixing equal amounts of both starting solutions, a stock solution resulted with 0.0015 mM of Ag^+ ions and 3 mM of NaPA. By stepwise dilution of this stock solution with the corresponding solvent containing 0.0015 mM of Ag^+, the polymer concentration decreased, while the Ag^+ ion concentration kept constant. After every dilution step the Ag^+-PA solution was characterized by combined SLS/DLS with the instrument model ALV-CGS 5000E over an angular regime of $30° \leq \theta \leq 60°$, which corresponds to a q range of $0.47 \times 10^{-4} < q^2 < 1.75 \times 10^{-4}$ nm^{-2}. The resulting scattering curves were evaluated by means of Zimm's approximation and apparent values of R_g and M_w were calculated. The diffusion coefficient $D_{z,\Theta=0}$ extracted via eq(2.24-2.26) was transformed into an effective hydrodynamic radius R_h via the Stokes-Einstein relationship (eq(2.31)).

Figure 4.1.1 shows the scattering curves in terms of $Kc/\Delta R_\Theta$ vs q^2 as well as D vs q^2 after every dilution step of the series at an Ag^+ concentration of 0.0015 mM. It can be seen that the intercept of $Kc/\Delta R_\Theta$ is getting smaller with decreasing NaPA concentration from 3 mM to 2.0032 mM. Hence, M_w is slightly increasing (Figure 4.1.2). The slopes of the corresponding static light scattering curves and along with it the values of R_g remain

unchanged. The diffusion coefficient $D_{z, \Theta=0}$ also remains the same for the NaPA concentration range of 2.1088 < [NaPA] < 3 mM and significantly drops after the dilution step to [NaPA] = 2.0032 mM.
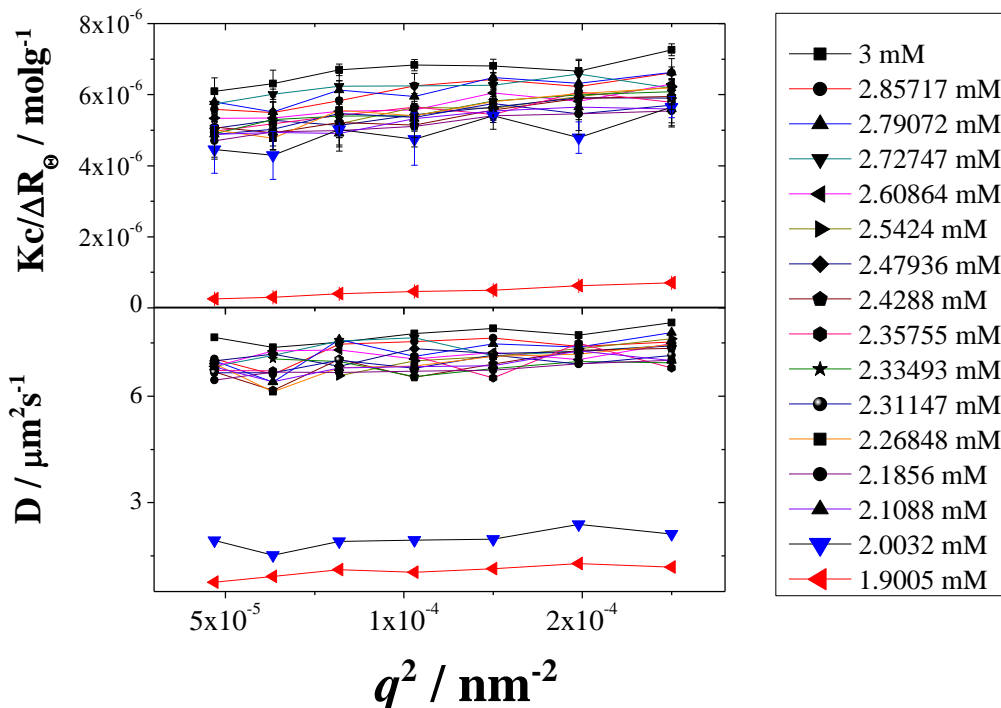

Figure 4.1.1 Plot $Kc/\Delta R_\Theta$ versus q^2 (upper graph) and D versus q^2 (lower graph) for the NaPA concentration range of 1.9005 < [NaPA] < 3 mM at [Ag$^+$] = 0.0015 mM. Each curve represents a dilution step at 0.0015 mM of [Ag$^+$], made from the Ag$^+$-PA stock solution containing 3 mM of NaPA800 and 0.0015 mM of Ag$^+$ ions. Measurement at [NaPA] = 1.9005 mM (◄) led to significant aggregation was made after 1 h of the last dilution step.

Whereas the diffusion coefficient (and along with it the ρ ratio) exhibits a sharp drop at [NaPA] = 2.0032 mM, the M_w value only starts to increase at this [NaPA] value (Figures 4.1.1 and 4.1.2). However, measurements below the corresponding value of [NaPA] reveals a drastic (and time-resolved) increase of the aggregate mass M_w (Figure 4.1.2) and thus proves that the increase of M_w at [NaPA] = 2.0032 mM, which is already more pronounced than for the preceding increment, indicates the onset of aggregation. The Model ALV-CGS 5000E does not enable to make time-resolved SLS/DLS measurements. Thus the measurement at [NaPA] = 1.9005 mM (Symbols ◄ in Figure 4.1.1; symbols in the red frames in Figure 4.1.2) was made ca. 1 h after the dilution from [NaPA] = 2.0032 mM, where the aggregation process stopped and the system got stable. As a consequence, the drop of the ρ ratio from 1.8 to 0.55, which was first observed at the range of 2.0032 < [NaPA] < 2.1088 mM, is considered to unambiguously indicate the onset of aggregation.

Expanded coils exhibit values of 1.5-1.8 [122], therefore, the constancy of $\rho \approx 1.7$ while approaching the onset of aggregation indicates that the PA-coils do not undergo any significant coil shrinking. A structure sensitive factor of $\rho \approx 0.8$ is characteristic for hard spheres, hence the observed drop of ρ suggests a change in particle shape. This significant drop of ρ ratio occurs at [NaPA] when the aggregation is about to start. Hence it is used as the crucial parameter in the determination of the aggregation threshold, discussed in the following Chapter 4.1.1.2.
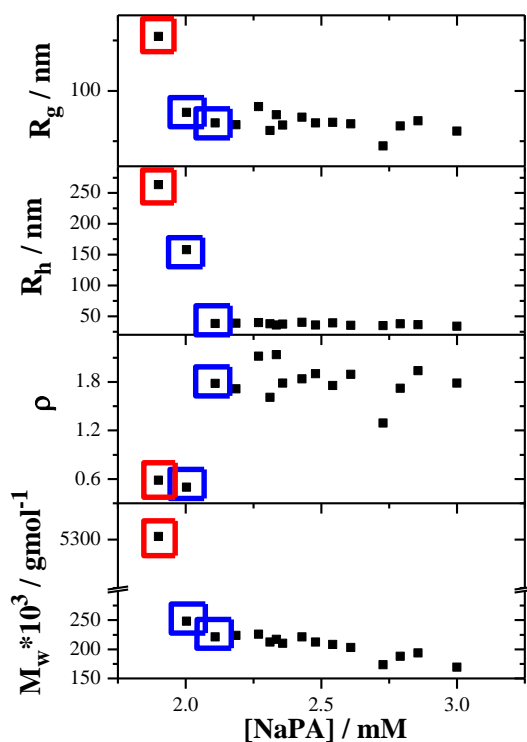
Figure 4.1.2 Radii of gyration R_g, hydrodynamic radii R_h, $\rho = R_g/R_h$ and molar mass M_w plotted versus [NaPA] for sample NaPA800 at [Ag$^+$] = 0.0015 mM. Symbols in the blue frame correspond to two adjoining NaPA concentrations at the aggregation threshold. Symbols in the red frame correspond to molecular parameters of an Ag$^+$-PA concentration which could only be recorded after aggregation has come to a standstill.

4.1.1.2 Determination of the Aggregation Threshold

Systematic analysis of all six dilution series, according to the procedure outlined in Chapter 4.1.1.1, reveals that the aggregation process is always induced at a certain dilution. Figure 4.1.3 represents the results of the dilution series at [Ag$^+$] = 0.0015 mM depicted in Figure 4.1.2 including a reproduction thereof (distinguished by the green colour of symbols). The range of NaPA in this Figure 4.1.3 is determined by the stability of the

solution, therefore the molecular parameters of the solutions with significant aggregation are not included. Data of all dilution series treated accordingly to Chapter 4.1.1.1 are displayed in Figures 6.1 – 6.5 of the Appendix, where changes in coil dimensions performed with sample NaPA800 (M_w = 503 000 gmol^{-1}) covering a [Ag$^+$] concentration range of 0.001 < [Ag$^+$] < 0.003 mM (including the reproductions of dilution pathways for [Ag$^+$] = 0.001 and for [Ag$^+$] = 0.0015 mM).

The aggregation threshold which respect to a drop of ρ ratio was determined in the following way. Averaged values of the ρ ratio before its drop can be found in Table 4.1.1 as ρ_1 before the drop and as ρ_2 after the drop. On Figure 4.1.3 and Figures 6.1– 6.5 values ρ_1 and ρ_2 are indicated as upper and lower black/green lines, respectively. The two NaPA concentrations enclosing this drop of the ρ ratio are named as [NaPA]$_1$ and [NaPA]$_2$ (Table 4.1.1). The way to estimate [NaPA]$_{agg}$ corresponding to the onset of aggregation (Table 4.1.1) proceeds as follows: take the mean value of [NaPA]$_1$ and [NaPA]$_2$ as [NaPA]$_{agg}$ and use the corresponding difference of these two values to estimate the uncertainty of the aggregation threshold at the respective [Ag$^+$] concentration (Table 4.1.1 – Estimated uncertainty of [NaPA]$_{agg}$). Blue symbols on Figure 4.1.3 and Figures 6.1– 6.5 correspond to the [NaPA]$_{agg}$, where the blue bars indicate the estimated uncertainties of the [NaPA]$_{agg}$.

Table 4.1.1 Parameters defining the aggregation threshold of Ag$^+$-PA for sample NaPA800 in 0.01 M NaNO$_3$ at a pH of 9.

[Ag$^+$] / mM	ρ_1	ρ_2	[NaPA]$_1$ / mM	[NaPA]$_2$ / mM	[NaPA]$_{agg}$ / mM	Estimated uncertainty of [NaPA]$_{agg}$
0.001	1.390	0.97	1.46	1.41	1.435	0.05
0.001	1.56	0.87	1.58	1.43	1.505	0.15
0.00125	1.74	0.61	1.43	1.33	1.380	0.10
0.0015	1.80	0.50	2.11	2.00	2.055	0.11
0.0015	1.50	0.54	2.00	1.85	1.925	0.15
0.002	1.75	1.01	2.76	2.35	2.555	0.41
0.0025	1.65	0.75	2.76	2.67	2.715	0.09
0.003	1.56	0.91	2.86	2.71	2.785	0.15

Considering characterization of the sample NaPA800 in 0.01 M NaNO$_3$ aqueous solution by combined SLS/DLS analysis (Figure 3.4, Table 3.3) we can deduce following in the establishing the nature of the entities occurring in the regime of NaPA concentration of [NaPA] > [NaPA]$_{agg}$. Based on the value of A_2 we could interpolate M_w data for the [NaPA] regime under consideration in Figure 4.1.3 and Figures 6.1– 6.5. Accordingly red lines indicate the trend of the apparent values of molar mass in the absence of Ag$^+$ ions and red arrows point to the true value of the molar mass based on the extrapolation to zero-

concentration ($M_{w,c=0}$). As can be seen from these figures, M_w data recorded in the presence of Ag$^+$ ions are close to trends predicted by the impact of the second virial coefficient. Hence, the increase of apparent M_w with decreasing [NaPA] observed in Figure 4.1.3 and Figures 6.1– 6.5 can entirely be attributed to the impact of interparticular excluded volume effect. Only in the immediate vicinity at the threshold a stronger upturn is observed. Regime upon approaching [NaPA]$_{agg}$ can be considered to be dominated by single chain behavior. Yet in none of the investigated samples did the M_w values cross the limit of the value $M_{w,c=0}$ as long as [NaPA] > [NaPA]$_{agg}$.
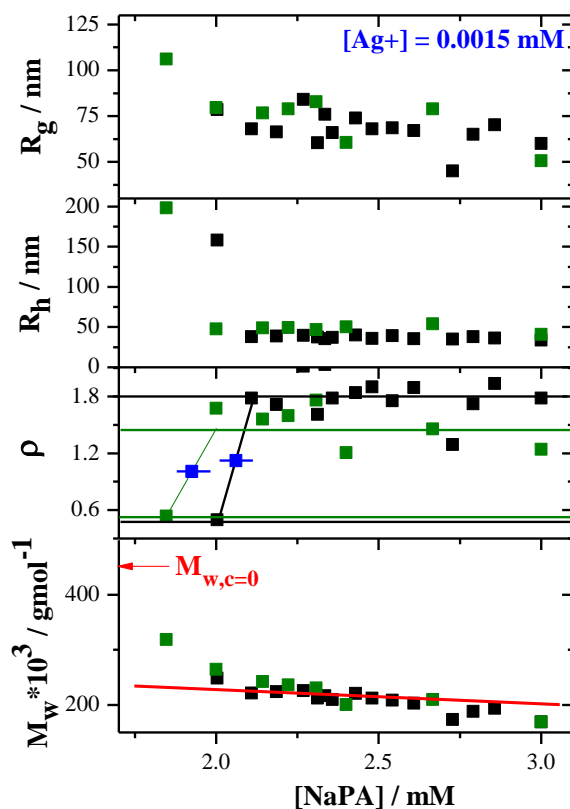
Figure 4.1.3 Radii of gyration R_g, hydrodynamic radii R_h, $\rho = R_g/R_h$ and apparent molar mass values M_w plotted versus [NaPA] for sample NaPA800 at [Ag$^+$] = 0.0015 mM. Symbols (■) and (■) denote two dilution series to prove the reproducibility of the aggregation threshold. Upper black/green and lower black/green lines correspond to ρ_1 and ρ_2, respectively. Inclined vertical black/green line depicts the drop of the ρ ratio from ρ_1 to ρ_2. Blue squares and blue bars represent the [NaPA]$_{agg}$ with the respective estimated uncertainty of [NaPA]$_{agg}$. Red line indicates the trend of M_w calculated with Zimm's approximation using established $A_2 = 4.55*10^6$ molLg^{-2}, whereas the red arrow indicates $M_{w,c=0}$ (Table 3.3).

In the same manner an aggregation threshold was established for sample NaPA1300 with a molecular weight $M_w = 2\,890\,000$ gmol^{-1}. Figures 6.6 – 6.10 of the Appendix show changes in coil dimensions for all five dilution series, which have been performed in an Ag$^+$ concentration range of $0.003 < [Ag^+] < 0.005$ mM. The evaluation of aggregation thresholds was made in the same way as described above for sample NaPA800. Results are summarized in Table 4.1.2. As in Figures 4.1.3, 6.1 – 6.5, in Figures 6.6 – 6.10 the red arrow indicates the molecular weight of single coils (Table 3.4), which are included in order to illustrate that the apparent M_w data established in the presence of Ag$^+$ ions only cross this limit toward larger values once the threshold has been approached, i. e. once $[NaPA] < [NaPA]_{agg}$.

Table 4.1.2 Parameters defining an aggregation threshold of Ag$^+$-PA for sample NaPA1300 in 0.01 M NaNO$_3$ at a pH of 9.

$[Ag^+]$ / mM	ρ_1	ρ_2	$[NaPA]_1$ / mM	$[NaPA]_2$ / mM	$[NaPA]_{agg}$ / mM	Estimated uncertainty of $[NaPA]_{agg}$
0.003125	1.82	0.87	0.62	0.57	0.595	0.05
0.0035	1.61	0.81	1.15	1.05	1.100	0.10
0.0035	1.88	1.02	1.01	0.96	0.985	0.05
0.004	1.70	0.80	1.37	1.31	1.340	0.06
0.0045	1.66	0.85	1.59	1.48	1.535	0.11
0.0045	1.80	0.90	1.44	1.39	1.415	0.05
0.005	1.70	1.09	2.06	1.88	1.970	0.18

We can summarize the reasons to consider the regime upon approaching $[NaPA]_{agg}$ to be dominated by single chain behavior as follows: (i) the slight increase of apparent mass values M_w can at least in part be attributed to a weakening of the impact of the second virial coefficient A_2 on $Kc/\Delta R_\Theta$ while approaching the threshold; (ii) the apparent values for M_w in all cases only exceed the value of the molar mass of the polymer given in Tables 3.3 – 3.4 as long as $[NaPA]$ is larger than $[NaPA]_{agg}$; (iii) the size parameter R_g and R_h remain constant for $[NaPA] > [NaPA]_{agg}$. The drop of ρ to a value of ca. 0.6-0.8 beyond the threshold indicates the formation of homogeneous, sphere-like aggregates, probably with a similarly low density as the one in the constituting coils, but with complete loss of drainage by solvent, therefore we call them **homogeneous low density aggregates**. This can be suggested as the initial stage of the aggregation and defined as aggregation threshold, which occurs at an extremely low Ag$^+$ concentration.

The threshold values $[NaPA]_{agg}$ of dilution series from the two NaPA samples are displayed in Figure 4.1.4 as a phase diagram. The interpretation of the resulting threshold lines by means of eq(1.1) provides additional insight into the onset of aggregation. The

intercept m, corresponding to the minimum concentration $[Ag^+]$ necessary to initiate the aggregation at infinite dilution of NaPA, is negligibly small for both samples and shall not be discussed further. The slope r_0 is close to 0.001 for both lines, indicating that only one bound silver ion is required per 1000 carboxylic functions in order to form primary aggregates. This r_0 value is significantly lower than observed in the case of alkaline earth cations [16] or of Cu^{2+} and Pb^{2+} ions [15, 17] and demonstrates that Ag^+ ions are extremely strong intermolecular cross-linkers for PA-chains. The fact that interconnection among coils in the aggregates is achieved by the formation of only a few COO^- - Ag^+ - ^-OOC bridges, where $[Ag^+]/[COO^-] \approx 1/1000$, supports formation of a loose network of coils without a significant change of the monomer density in the aggregating coils. The aggregation process, which sets in once this threshold line is crossed, will be addressed in the following Chapter 4.1.2.
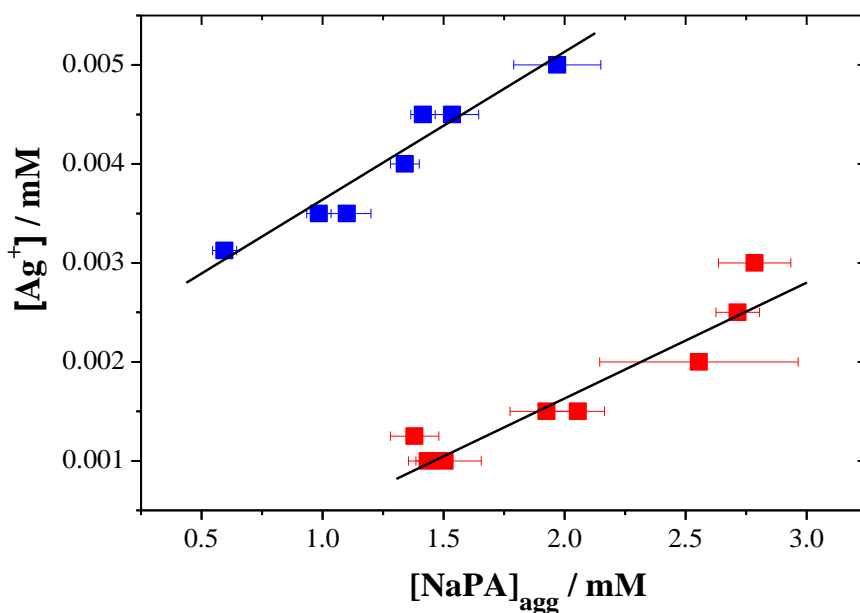

Figure 4.1.4 Phase diagram with aggregation thresholds of Ag^+-PA dilution series in 0.01 M $NaNO_3$ at a pH of 9 for two different molecular weight samples of NaPA: 503 000 gmol^{-1} (NaPA800 – ■) and 2 890 000 gmol^{-1} (NaPA1300 – ■). The two lines indicate a fit with eq(1.1).

4.1.2 Aggregation

We performed various series of light scattering experiments in the range of NaPA concentration of $0.64 \leq [\text{NaPA}] \leq 5.12$ mM and in the range of Ag^+ ion concentration of $0.0005 \leq [Ag^+] \leq 15$ mM and found distinct trends. The ratio $[Ag^+]/[COO^-]$ is a crucial variable, which predestines the aggregation mechanism, the shape of particles and the stability of solutions. Table 4.1.3 summarizes nine representative experimental series, discussed in Chapters 4.1.2 – 4.1.4 in order to cover the entire relevant regime in the phase diagram.

Table 4.1.3 Overview on experimental series of Ag^+-PA solutions in 0.01 M $NaNO_3$, discussed in Chapters 4.1.2 – 4.1.4.

Exp. series	NaPA sample	[NaPA] / mM	$[Ag^+]/[COO^-]$	Regime in the phase diagram
ES-1	NaPA800	2.0	0.001 – 0.01	homogeneous low density aggregates
ES-2	NaPA800	2.0	0.05 – 0.32	dense unstable aggregates and dense stable aggregates
ES-3	NaPA800	2.0	0.10; 0.16	dense unstable aggregates
ES-4	NaPA1300	2.0	0.05 – 0.50	dense unstable aggregates and dense stable aggregates
ES-5	NaPA800	0.64	0.02 – 0.08	dense unstable aggregates
		1.28	0.02 – 0.05	
		2.56	0.0125; 0.05	
		5.12	0.05	
ES-6	NaPA800	1.0	0.16 – 0.40	dense unstable aggregates and dense stable aggregates
		3.0	0.16 – 0.40	
		4.0	0.08 – 0.40	
ES-7	NaPA800	2.0	0.36 – 0.80	dense stable aggregates
ES-8	NaPA800	2.0	0.20	dense unstable aggregates – X1
			0.40	dense stable aggregates – Y1
			0.20	dense unstable aggregates – X2
ES-9	NaPA800	2.0	1.0 – 4.0	dense stable aggregates and macroscopic precipitation

Experimental series ES-1 comprises the Ag^+-PA solutions with the ratios $[Ag^+]/[COO^-]$ close to the aggregation threshold: 0.001, 0.005 and 0.01. Figure 4.1.5 illustrates the results of TR-SLS measurements of this series. The solution with 0.002 mM of Ag^+ ions, corresponding to a ratio of Ag^+ ion per COO^--group of 0.001, is very close to the aggregation threshold, but is still located in the regime of single coil behavior. This can be inferred from the fact that the apparent mass M_w and size R_g remain constant and

comparable to the molecular parameters obtained from the characterization of the NaPA sample without silver ions.

An increase of the ratio $[Ag^+]/[COO^-]$ to 0.005 drastically increases the particle size and enlarges the particle mass by a factor of 100. Part of this increase may stem from light absorption by the Ag^+ ions, which modifies the refractivity of the particles and hence the scattering contrast of the system. At both ratios 0.005 and 0.01 of $[Ag^+]/[COO^-]$ the aggregation stops after ca. 5 min. TR-SLS revealed a particle size of 140 nm and 200 nm at the end of the experiments for $[Ag^+]/[COO^-] = 0.005$ and 0.01 respectively (Figure 4.1.5).
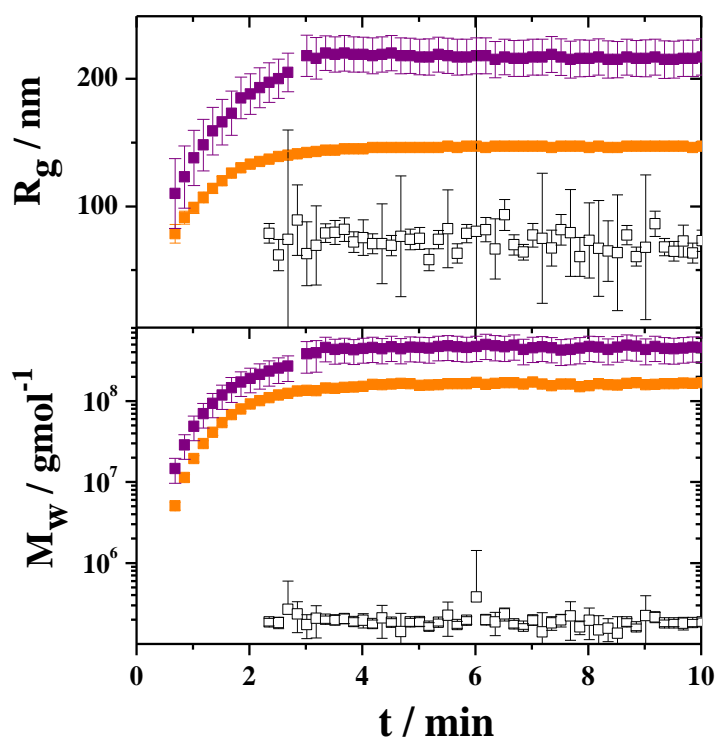
Figure 4.1.5 The evolution of the particle size R_g with time t (upper graph) and of the particle mass M_w with time t (lower graph) for experimental series ES-1. The NaPA concentration in all cases is 2.0 mM applied at the following $[Ag^+]/[COO^-]$ ratios: 0.001 (□); 0.005 (■); 0.01 (■). The error bars for $[Ag^+]/[COO^-] = 0.005$ are omitted since the size of symbols exceeds the experimental uncertainty.

In order to learn more about the structure of these aggregates, the square root of the z-average mean square radius of gyration R_g of the growing particles was correlated with the corresponding weight-averaged particle mass M_w by means of a power law of the following form:

$$R_g \propto M_w^{\alpha} \tag{4.1}$$

The resulting exponent α may indicate the shape of growing particles and their density. Here we have to emphasize that the particle mass values are only apparent values as A_2 has been neglected and the refractive index increment of the Ag^+-PA species has been approximated by using the value determined for NaPA in 0.1 M NaCl [5].

Based on a purely topological reasoning homogeneous spheres or cubes result in $\alpha = 1/3$ and for ideal polymer coils and rods this value is 1/2 and 1, respectively [149]. These exponents can in fact be recovered directly with light scattering data if aggregates grow via particle-particle coalescence. In the case of a monomer addition mechanism, where monomers add to aggregates, monomers and aggregates form a bimodal system, and the exponent α is half of the respective topological value [149], i. e. 1/6 for homogeneous spheres, 1/4 for ideal polymer coils and 1/2 for rods.

The correlation of M_w vs. R_g of the two samples from series ES-1 shows a power law with an exponent of 0.2 ± 0.02 (Figure 5.1.8). Such a value suggests the formation of homogeneous spherical particles obeying a monomer addition mechanism [149]. In the studied case, the "monomer" species corresponds to a single Ag^+-PA coil and the growing particles are aggregates thereof. The form factors of the intermediate aggregates, represented in Figure 4.1.6, confirm the presence of homogeneous sphere-like structures. The Kratky plot exhibits a maximum in close agreement with the theoretically calculated form factor for spheres [105]. Star-like or non-randomly branched polymer chains would also exhibit a maximum in the Kratky plot. However, formation of such structures can be excluded since the respective growing entities would neither be of homogeneous density with an exponent α close to 1/6 nor would the ρ ratio lie close to 0.8 as has been reported in Chapter 4.1.1.
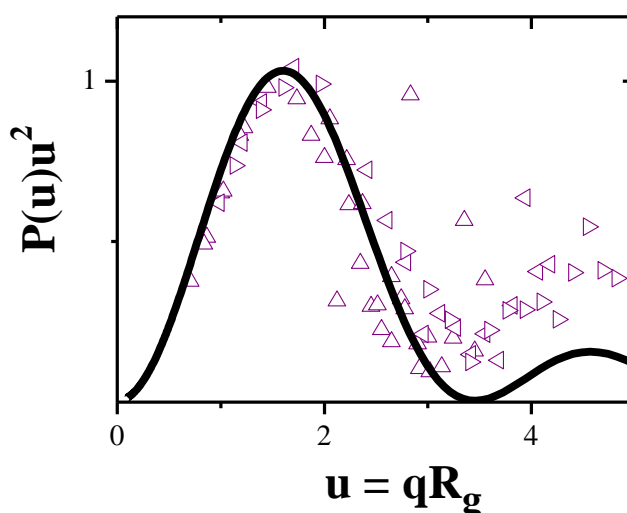
Figure 4.1.6. Selected scattering curves from the aggregation run, shown in Figure 4.1.5 of series ES-1 at [NaPA] = 2.0 mM and $[Ag^+]/[COO^-]$ = 0.01, represented as normalized Kratky plot based on the normalized variable $u = qR_g$. The symbols denote an age of 51 ($\triangle$), 90 ($\triangledown$), 131 ($\triangleleft$) and 191 ($\triangleright$) min. The solid line corresponds to the form factor of a monodisperse sphere [105].

Series ES-2 extends further into the regime of unstable aggregates. It was also performed at [NaPA] = 2.0 mM covering a regime of [Ag$^+$]/[COO$^-$] ratio from 0.05 to 0.32. Figure 4.1.7 shows a representative selection of TR-SLS experiments thereof. It is evident that an increase of the [Ag$^+$]/[COO$^-$] ratio in the Ag$^+$-PA system from 0.05 to 0.16 accelerates the process of aggregation. The first detectable values of apparent molar mass M_w of these systems are already larger by a factor of 10-100 compared to single coils (Table 3.3). These drastic differences in the values of initial particle mass can be attributed to a very fast aggregation, which takes place during the first 40 s. A period of 40 s is close to the time required for mixing the NaPA and AgNO$_3$ solutions in the scattering cell, placing it into the goniometer and beginning to operate the SLS-measurement. The corresponding initial size at all experiments with the ratio of [Ag$^+$]/[COO$^-$] > 0.1 is 25 nm, which is smaller than the apparent size of NaPA coils of 75 nm in the solutions without silver ions (Table 3.3). This drop of R_g accompanied with an increase in M_w becomes strikingly visible in the initial part of Figure 4.1.7 and indicates a significant condensation. The condensation results from a shrinking of the aggregates, which is accompanied by the fast aggregation occurring during the initial 40 s.
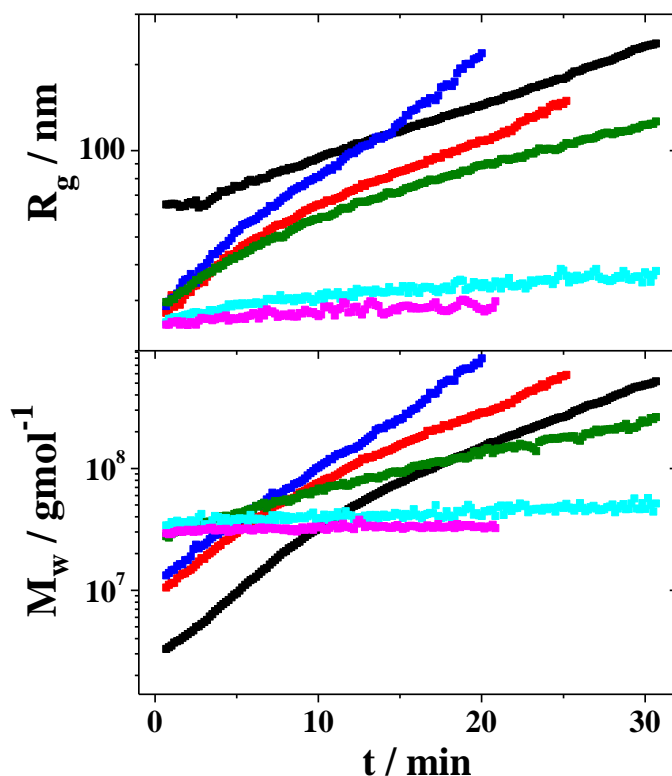

Figure 4.1.7 The evolution of the particle size R_g with time t (upper graph) and the evolution of the particle mass M_w with time t (lower graph) of the experimental series ES-2. The NaPA concentration in all cases is 2.0 mM applied at the following ratios of [Ag$^+$]/[COO$^-$]: 0.05 (■); 0.14 (■); 0.16 (■); 0.24 (■); 0.30 (■); 0.32 (■).
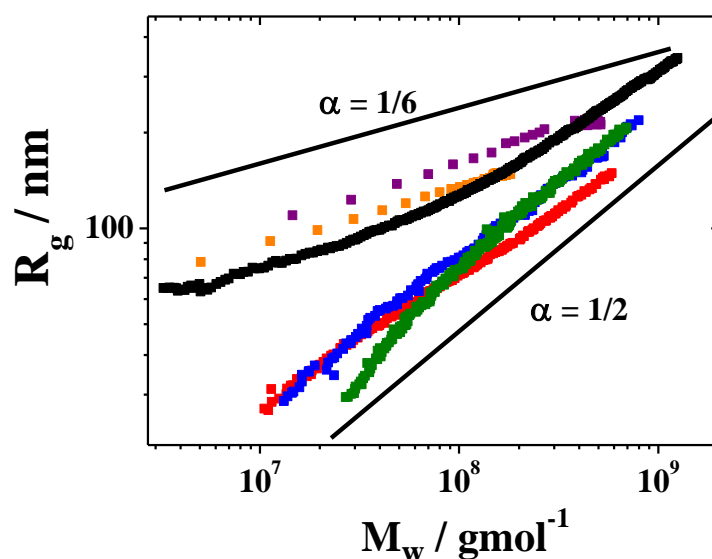
Figure 4.1.8 Correlation between particle size R_g and particle weight M_w for the experiments at [NaPA] = 2.0 mM of series ES-1 and ES-2 at variable $[Ag^+]/[COO^-]$ ratios with symbols having the same meaning as in Figures 4.1.5 and 4.1.7. For the sample with $[Ag^+]/[COO^-]$ = 0.05 (■) the exponent α is 0.21 ($t < 14$ min) and 0.41 ($t > 14$ min). Straight lines with α = 1/6 and 1/2 are used as guides for the eye.

The corresponding relationships between R_g and M_w result in exponents α which increase from 0.18 to 0.58 for the regime $0.01 \leq [Ag^+]/[COO^-] \leq 0.24$ (Figure 4.1.8), whereas at $[Ag^+]/[COO^-]$ = 0.05, this correlation shows two trends: during the first 14 min of aggregation ($R_g \leq 130$ nm) the exponent is 0.2 and at later times it gradually turns toward 0.4. From these observations two questions arise: (i) Do the regular trends in the aggregation process of Ag^+-PA complexes refer to a general phenomenon or are they molecular weight specific? (ii) Is the ratio $[Ag^+]/[COO^-] \approx 0.05$ a threshold where the formation of Ag^+-PA aggregates changes its aggregation mechanism?

Additional TR-SLS/DLS measurements with NaPA samples NaPA800 and NaPA13000 representing experimental series ES-3 and ES-4 in the range of an Ag-content of $0.05 \leq [Ag^+]/[COO^-] \leq 0.5$ were performed both with respect to the first question and in order to provide additional data on the hydrodynamics of the aggregates. Results shown in Figure 4.1.9 for sample NaPA800 and in Figure 4.1.10 for sample NaPA1300 nicely confirm that correlations of R_g versus M_w at the studied Ag-contents yield exponents close to 0.4-0.6.

The radii of gyration R_g for the Ag^+-PA system at $[Ag^+]/[COO^-]$ = 0.20 of sample NaPA1300 is around 20 nm. The SLS analysis does not allow to detect such a small size with a good precision, therefore on the Figure 4.1.10 it is not indicated. However, the hydrodynamic radii R_h for this system is about 40 nm and stable over the whole period of observation. The Ag^+-PA solution based on NaPA1300 sample with $[Ag^+]/[COO^-]$ = 0.5 also did not show any aggregation process and in Figure 4.1.10 the indicated molecular

parameters recorded at two time increments with an interval of ca. 3.5 h remain constant. We will return to these stable Ag$^+$-PA solutions and make a detailed analyses thereof in Chapter 4.1.3. In the current Chapter 4.1.3 we will continue to consider only aggregating samples.

Combined SLS/DLS experiments presented in Figures 4.1.9 and 4.1.10 yield ρ-ratios which fall in between 0.6-0.8. These values suggest spherical or core-shell aggregates in disagreement with the regime of the exponents α. Values of $0.4 < \alpha < 0.6$ are favour of more fractal-like entities. Results shown in Figures 4.1.9 and 4.1.10 for two NaPA samples differing in their molecular weight also nicely demonstrate the reproducibility of light scattering results, even if it is performed with different experimental setups.

Figure 4.1.9 Left: the evolution of the radius of gyration R_g, hydrodynamic radius R_h, molar mass M_w and $\rho = R_g/R_h$ with time t for series ES-3 performed with sample NaPA800. The concentration of [NaPA] is 2.0 mM at the following [Ag$^+$]/[COO$^-$] ratios: 0.10 (■); 0.16 (●).
Right: correlations between particle sizes R_g (■, ●) and R_h (□, ○) particle weight M_w with α indicating the exponent in eq(4.1): 0.364 (■); 0.385 (●).
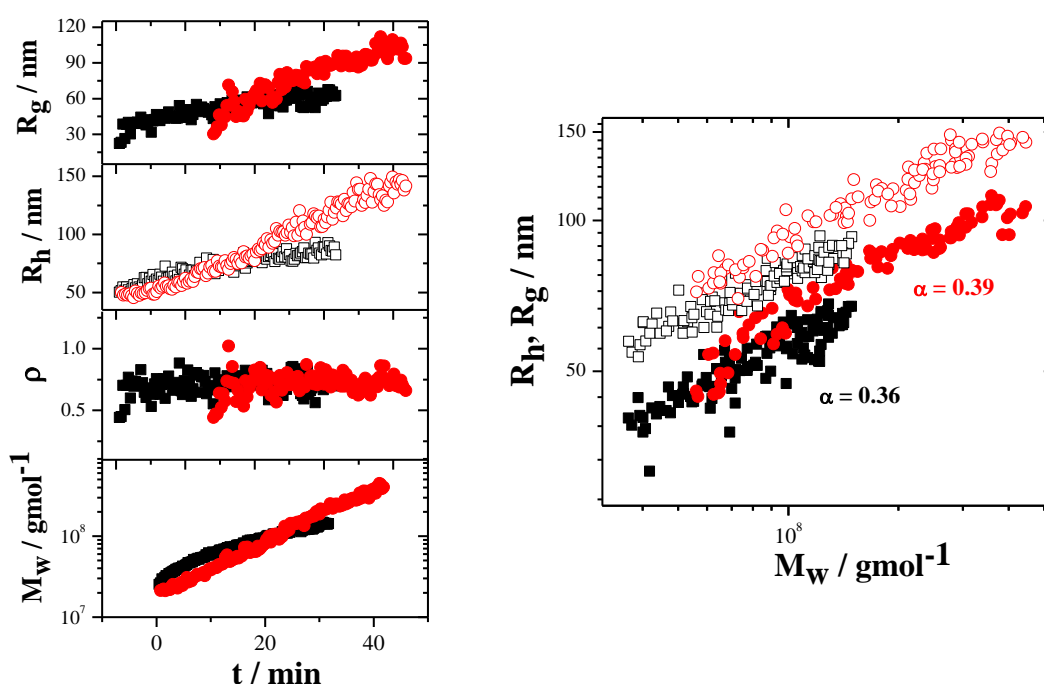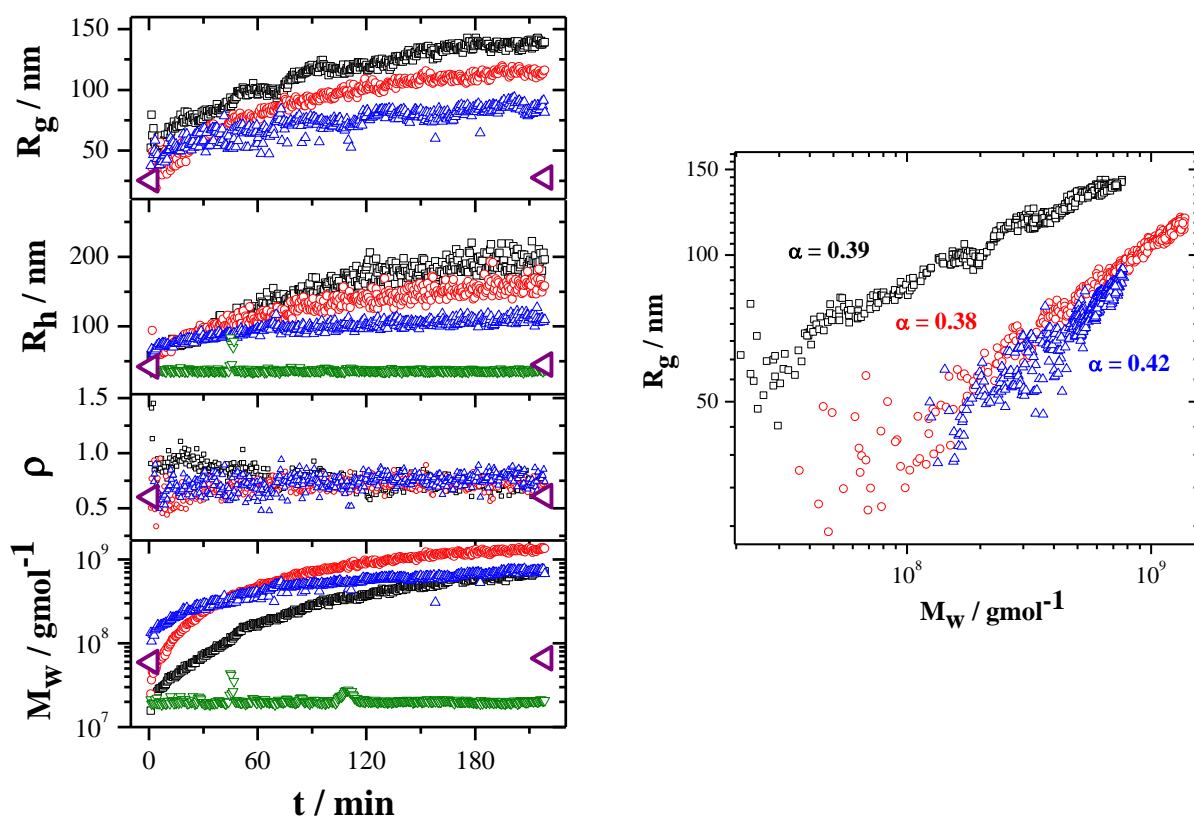
Figure 4.1.10 Left: the evolution of the radius of gyration R_g, hydrodynamic radii R_h, molar mass M_w and $\rho = R_g/R_h$ with time t for series ES-4 performed with sample NaPA1300. The concentration of [NaPA] is 2.0 mM at the following [Ag$^+$]/[COO$^-$] ratios: 0.05 ($\square$); 0.10 (O); 0.15 ($\triangle$); 0.20 (∇); 0.50 ($\triangleleft$).
Right: correlations between particle size R_g and particle mass M_w with α indicating the exponent in eq(4.1): 0.385 ($\square$); 0.384 (O); 0.421 ($\triangle$).

Experimental series ES-5 was performed in the range of polyacrylate concentration of $0.64 \leq$ [NaPA] ≤ 5.12 mM at very low ratios of $0.0125 \leq$ [Ag$^+$]/[COO$^-$] ≤ 0.08 in order to complement data at the [Ag$^+$]/[COO$^-$] ratio of 0.05 of experimental series ES-2 (Figure 4.1.11). TR-SLS experiments at variable NaPA concentration show that the correlation between size and mass by means of the exponent α proves that in this range of [Ag$^+$]/[COO$^-$] ratios there is a change from the formation of homogeneous low density aggregates toward fractal-like entities based on constituting dense aggregates, which are characterized by higher exponents α (Figures 4.1.9-4.1.10).
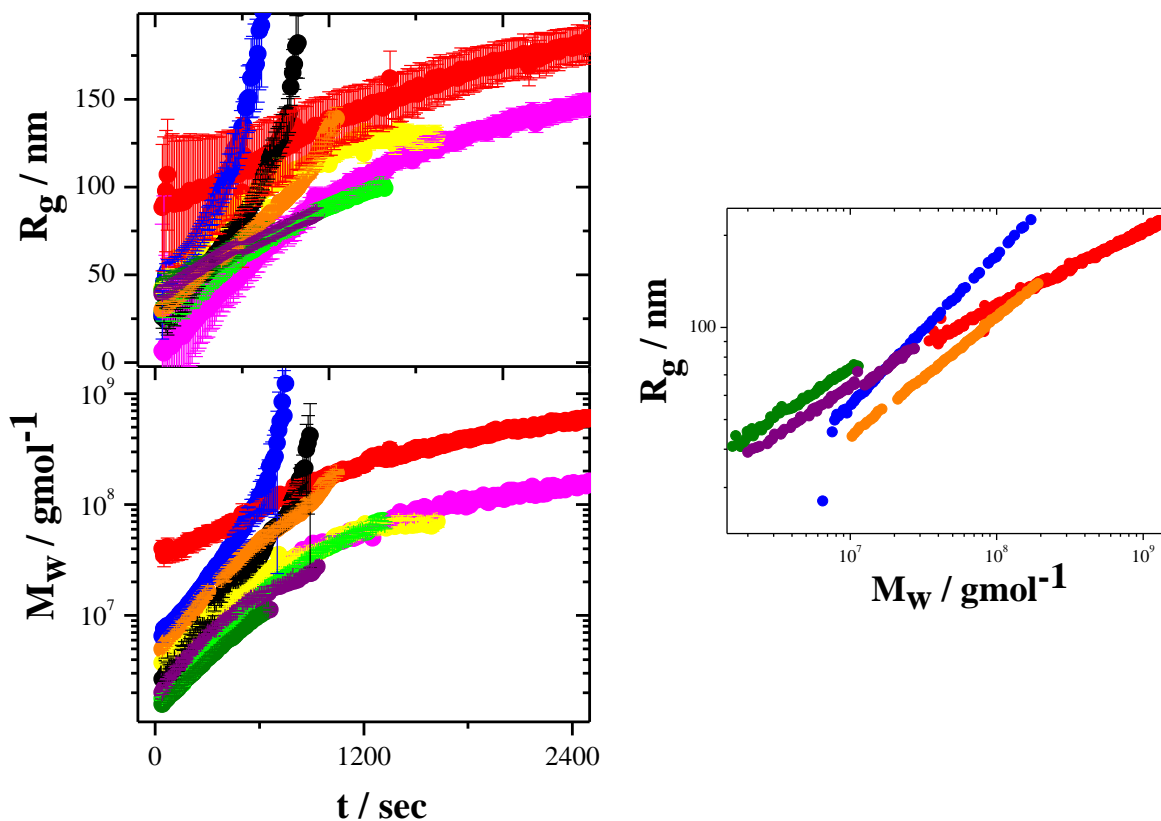
Figure 4.1.11 Left: the evolution of the radii of gyration R_g with time t (upper graph) and the evolution of the molar mass M_w with time t (lower graph) of the experimental series ES-5 performed with sample NaPA800 with [NaPA] = 0.64 mM at the following $[Ag^+]/[COO^-]$ ratios: 0.02 (○), 0.04 (●), 0.08 (●); with [NaPA] = 1.28 mM at the following $[Ag^+]/[COO^-]$ ratios: 0.02 (●), 0.03 (●), 0.05 (●); with [NaPA] = 2.56 mM at the following $[Ag^+]/[COO^-]$ ratios: 0.0125 (●), 0.05 (●); with [NaPA] = 5.12 mM applied at the ratio of $[Ag^+]/[COO^-]$ = 0.05 (●).

Right: correlations between particle sizes R_g and particle mass M_w with α indicating the exponent in eq(4.1): 0.25 (●), 0.5 (●), 0.31 (●), 0.39 (●), 0.3 (●).

Hence the solution with a ratio $[Ag^+]/[COO^-]$ = 0.05 represents a transition regime where the aggregation mechanism changes, emphasizing the important role of the Ag-content in the aggregation process. As already mentioned, transition from the regime with α ≤ 0.2 to the regime with α ≥ 0.4 is accompanied by a collapse of the initially appearing aggregates from R_g > 75 nm to R_g < 30 nm, whereas the corresponding values of M_w get larger. Thus we can call the aggregates formed at $[Ag^+]/[COO^-]$ > 0.05 **dense unstable aggregates**, and distinguish them from the homogeneous low density aggregates forming at $[Ag^+]/[COO^-]$ < 0.05.

It has to be stressed here, that the exact location of the transition of aggregation mechanism, which has been established to be at $[Ag^+]/[COO^-] = 0.05$ for sample NaPA800 at $[NaPA] = 2$ mM, may slightly vary with the polyelectrolyte molar mass and polyelectrolyte concentration. In Figure 4.1.12 we summarize a large set of reliable exponents α from five experimental series performed with two different NaPA samples, which cover a broad range of polymer and Ag^+ concentration. Figure 4.1.12 shows that with increasing the $[Ag^+]/[COO^-]$ ratio the exponent α is increasing. Homogeneous low density aggregates are formed via monomer addition with characteristic value of $\alpha \leq 0.2$ and dense unstable aggregates are characterized by a higher exponent. The threshold between these entities lies close to the ratio of $[Ag^+]/[COO^-] = 0.05$. Accordingly, the largest amount of experiments have been performed close to that threshold and depending on the exact value of $[NaPA]$ and $[Ag^+]$ either homogeneous low density aggregates or dense unstable aggregates are formed. This explains the large variations in α close to the threshold regime of $[Ag^+]/[COO^-] = 0.05$.
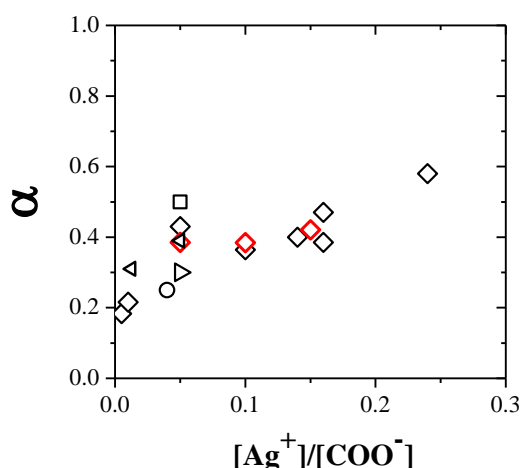
Figure 4.1.12 Selected exponents α from eq(4.1) plotted vs. the $[Ag^+]/[COO^-]$ ratio performed with sample NaPA800 from experimental series ES-1, ES-2 and ES-3 at $[NaPA] = 2$ mM ($\diamond$) and from ES-5 at NaPA concentrations of: 0.64 mM ($\bigcirc$), 1.28 mM ($\square$), 2.56 mM ($\triangleleft$), 5.12 mM ($\triangleright$); performed with sample NaPA1300 for experimental series ES-4 ($\diamond$).

In the following paragraphs we will analyze the shape of dense unstable aggregates. In general, the spherical shape of the homogeneous low density aggregates could be consistently inferred from a set of three parameters including an exponent $\alpha < 0.2$, a distinct peak in the Kratky-plot of the form factor and a ratio of $\rho \sim 0.8$. However, it turned out to be much more difficult to establish a structural model for the dense unstable aggregates with that same set of parameters.
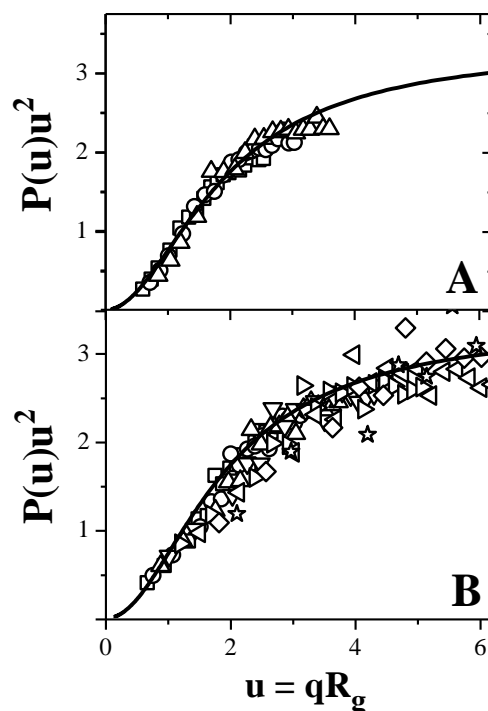
Figure 4.1.13 Selected scattering curves from aggregation runs, shown in Figure 4.1.7 of series ES-2 at [NaPA] = 2.0 mM and at $[Ag^+]/[COO^-]$ ratios of 0.16 (**A**) and 0.05 (**B**), represented as normalized Kratky plot based on the normalized variable $u = qR_g$. The symbols of graph **A** denote an age of 15 (△), 17 (□) and 20 (○) min. The symbols of graph **B** denote an age of 14 (□), 17 (○) and 21 (△), 24 (▽), 27 (▷), 32 (◁), 37 (◇), 41 (☆) min. The solid lines correspond to the form factor of a polydisperse coil with PDI = 2 [109, 150, 151].

The form factor of the intermediates shown in Figure 4.1.13 for the Ag^+-PA aggregates with a ratio of $[Ag^+]/[COO^-] = 0.05$ and 0.16 can be described by the Debye formula [150], which fits well to the experimental data assuming a polydispersity index of PDI = 2 [109, 150, 151]. Polydispersity was taken into account by a Schulz-Zimm distribution [109, 151] of the particle mass with a polydispersity parameter z = 1. This parameter is related to the polydispersity index PDI according to

$$z = 1 / (PDI - 1) = M_n / (M_w - M_n) \qquad (4.2)$$

with PDI = M_w/M_n the ratio of the weight-averaged particle mass to the number-averaged particle mass.

The scattering curves measured at different times overlay, which proves that the respective intermediates being formed during growth of unstable dense aggregates are self-similar. The curves approach a plateau in the Kratky plot, which is characteristic for such structures [151]. The experimental form factors of the dense unstable aggregates are thus compatible with an entity, which has a similar density-density correlation as Gaussian polymer coils.

Entities with a structure obeying the Debye formula have fractal dimensions close to $1/\alpha \sim 2$ (Figure 4.1.13). Such dimensions are compatible with an exponent close to $\alpha \sim 0.25$ for a monomer addition mechanism and $\alpha \sim 0.5$ for particle-particle coalescence. Although, the experimentally found exponents of $0.4 \leq \alpha \leq 0.6$ point to a process where fractals with $1/\alpha \sim 2$ coalesce to ever larger aggregates, this feature cannot be reconciled with the ρ values from TR-SLS/DLS data recorded during formation of dense unstable aggregates for sample NaPA800 and NaPA1300 (Figures 4.1.9 and 4.1.10). Although the ratio changes throughout aggregation for neither of the samples suggesting self-similarity, the average value of $\rho \sim 0.6\text{-}0.8$ points to homogeneous non-draining particles rather than to an entity with a Gaussian coil-like structure as it has been inferred from the experimental form factors. Therefore, we presently cannot establish a structural model for the dense unstable aggregates, which simultaneously agrees with the respective exponent, the form factor and the ρ ratio.

4.1.3 Stable Aggregates

Figure 4.1.7 shows that the aggregation process in Ag^+-PA solutions based on NaPA800 stock solution becomes slower at $[Ag^+][/COO^-] = 0.24$ and even stops for the systems with ratios of $[Ag^+][/COO^-] \geq 0.3$. As it was already mentioned in the previous Chapter 4.1.2 the Ag^+-PA solutions based on higher molecular weight NaPA sample (NaPA1300) with $[Ag^+][/COO^-]$ ratios of 0.2 and 0.5 also demonstrated stability in molecular parameters over a long period of time (Figure 4.1.10). In order to further analyze this behavior, which may represent a new phase state, experimental series ES-6 and ES-7 (Table 4.1.3) using NaPA800 have been prepared.

In order to identify whether the ratio $[Ag^+]/[COO^-] = 0.3$ corresponds to a threshold value between aggregating and stable Ag^+-PA solutions, series of TR-SLS experiments of series ES-6 were performed over a broad regime of NaPA concentrations, in the range of $0.08 \leq [Ag^+][/COO^-] \leq 0.4$. Indeed, results of these experiments shown in Figures 4.1.14 indicate that the growth of dense unstable aggregates ceases once ca. $[Ag^+]/[COO^-] > 0.3$. TR-SLS experiments establishing series ES-7 performed at $[NaPA] = 2$ mM with ratios of silver ions per carboxylic group from 0.36 to 0.8 indicate stability of solutions over two days (Figure 4.1.15). Molecular parameters were changing only within the experimental uncertainty and thus considered to be constant. Looking ahead to Chapter 4.1.4, we can also point that this phenomena was proven by the additional series ES-9 (with $[Ag^+]/[COO^-] = 1$, 1.25 and 2).
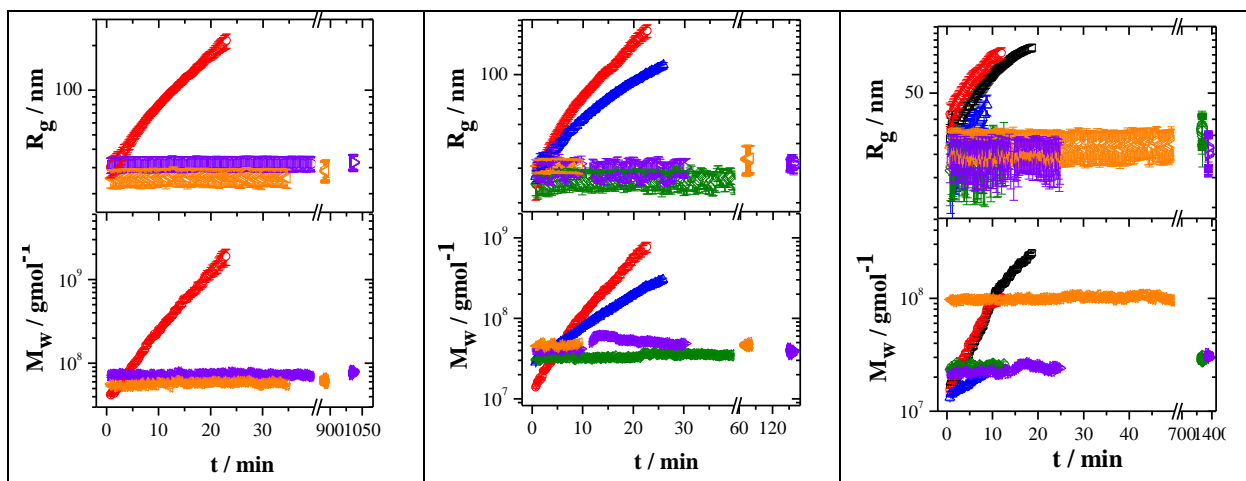
Figure 4.1.14 The evolution of the radii of gyration R_g with time t (upper graph) and the evolution of the molar mass M_w with time t (lower graph) of the experimental series ES-6 performed with sample NaPA800.

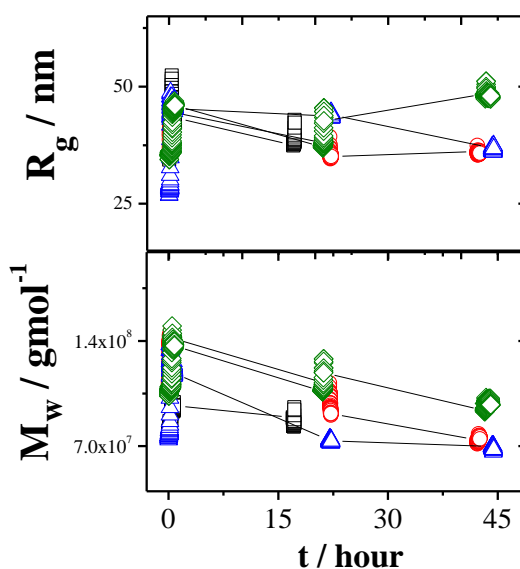|		
The NaPA concentration is 1.0 mM applied at the following ratios of [Ag⁺]/[COO⁻]: 0.16 (O); 0.32 (▷); 0.40 (◁).	The NaPA concentration is 3.0 mM applied at the following ratios of [Ag⁺]/[COO⁻]: 0.16 (O); 0.21 (△); 0.26 (◇); 0.32 (▷); 0.40 (◁).	The NaPA concentration is 4.0 mM applied at the following ratios of [Ag⁺]/[COO⁻]: 0.08 (□); 0.16 (O); 0.24 (△); 0.28 (◇); 0.32 (▷); 0.40 (◁).

Figure 4.1.15 The evolution of particle size R_g with time t (upper graph) and the evolution of the particle mass M_w with time t (lower graph) of experimental series ES-7 performed with sample NaPA800. The NaPA content in all cases is 2.0 mM at variable [Ag⁺]/[COO⁻] ratios: 0.36 (□); 0.45 (O); 0.60 (△); 0.80 (◇).

The size values of these stable aggregates observed in series ES-2, ES-6 and ES-7 are in the range of 25-50 nm. This particle size is comparable to the size of dense unstable aggregates observed for the series ES-2 in the beginning of the aggregation (Figure 4.1.7). In accordance with this observation, the molar mass values observed in ES-7 are also close to the initially detected molar mass values of dense unstable aggregates in the series ES-2, which is much larger than the mass of single coils. Apparently, the primarily formed aggregates observed at $[Ag^+]/[COO^-] < 0.3$ stopped from further growing once $[Ag^+]/[COO^-] > 0.3$. We call them **dense stable aggregates** since their molecular parameters are constant over a long time. The aggregation leading to such small and dense particles is very fast and hence could not be followed by light scattering. Since these stable aggregates were observed at $[Ag^+]/[COO^-] > 0.3$ over the range $1 \leq [NaPA] \leq 4$, a second line can be added to the phase diagram, separating super aggregates from stable aggregates (Figure 4.1.16).
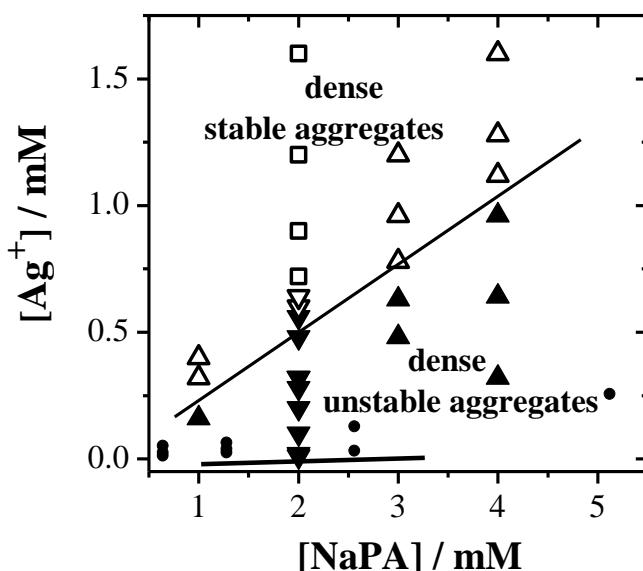
Figure 4.1.16 The location of $[Ag^+]/[COO^-]$ ratios from series ES-1, ES-2 and ES-3 ($\triangledown$, $\blacktriangledown$), ES-5 ($\bullet$), ES-6 ($\triangle$, $\blacktriangle$), ES-7 ($\square$), where full symbols refer to states which showed aggregation (dense unstable aggregates) and open symbols refer to stable states (dense stable aggregates), relative to the aggregation threshold of Figure 4.1.4 (line on the bottom of the graph).

In order to gain further information regarding the nature of stable aggregates the following experiments were performed establishing series ES-8 (Table 4.1.3). The Ag^+-PA solutions with a ratio of $[Ag^+]/[COO^-] = 0.2$ (solution X1), corresponding to the regime of dense unstable aggregates, and $[Ag^+]/[COO^-] = 0.4$ (solution Y), corresponding to dense stable aggregates, were analyzed separately by combined TR-SLS/DLS. The Solution Y was successively diluted by a NaPA solution to a ratio of $[Ag^+]/[COO^-] = 0.2$, giving

solution X2, which was again analyzed by TR-SLS/DLS. Solution X2 had the same composition as solution X1 and only differed from X1 by their sample history. Whereas X1 was prepared in the usual way by mixing the component solutions selected to achieve final concentrations at the start of the experiment, sample X2 is derived from sample Y by adding a solution of NaPA (without Ag^+ ions) after the later one had been characterized by DLS/SLS as a representative of stable aggregates.

Solutions X1 and X2 showed aggregation with molecular parameters comparable to each other (Figure 4.1.17). A structure-sensitive parameter ρ close to 0.5 was observed for Y during the whole period of observation. Values of ρ close to 0.5 indicate dense clusters of PA-coils interconnected by Ag^+ ions. These spherical clusters have to be surrounded by less dense PA-shells, which include a large amount of immobilized solvent molecules, thus keeping R_h high. Yet, the polymer segment density of the shells is too low to significantly contribute to R_g. The values of ρ thus reveal a core-corona structure for stable aggregates as generated in series ES-4, ES-6, ES-7 and of ES-8. The aggregating X1 and X2 resulted in an increase of ρ to values of 0.7-0.8 within the first 30 min in agreement with the ρ values observed for the unstable aggregates of both NaPA samples (Figures 4.1.9 and 4.1.10).
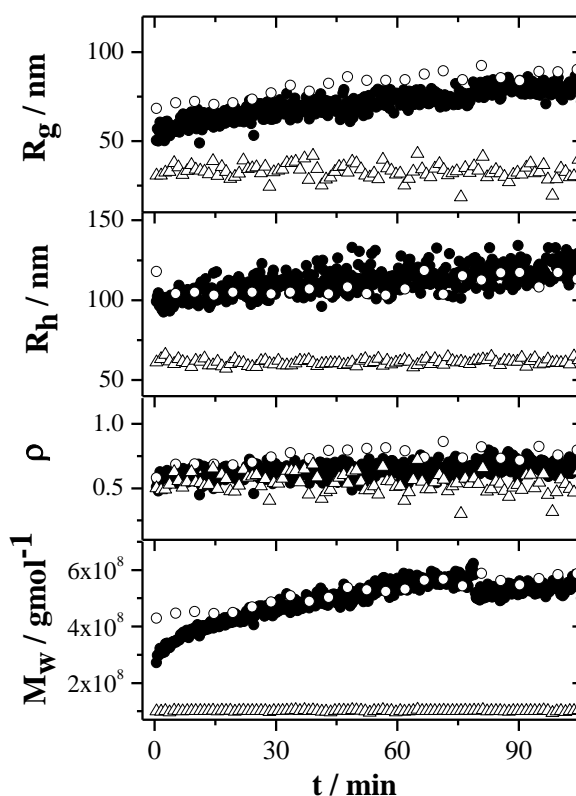

Figure 4.1.17 The evolution of the radius of gyration R_g, hydrodynamic radius R_h, molar mass M_w and $\rho = R_g/R_h$ values with time t for series ES-8. The concentration of [NaPA] is 2.0 mM at the following $[Ag^+]/[COO^-]$ ratios: 0.20 (●) - solution **X1**; 0.40 (△) - solution **Y**; 0.20 (○) - solution **X2**.

These observations indicate two mechanistic aspects: (i) at silver ion concentrations where $0.05 <$ [Ag$^+$]/[COO$^-$] < 0.3 dense unstable aggregates are formed whereby the first observable intermediates are much smaller and denser than the homogeneous low density aggregates formed at [Ag$^+$]/[COO$^-$] < 0.05. The initially observed intermediates at $0.05 <$ [Ag$^+$]/[COO$^-$] < 0.3 are formed from the low density aggregates by a fast aggregation probably combined with shrinking; (ii) at a sufficiently high concentration of silver ions the initially formed dense intermediates adopt a core-shell structure with a loose PA-corona enveloping a dense core, which do not further grow. These core-shell particles, which establish the regime of dense stable aggregates, are stabilized for a reason not yet fully understood. However, an addition of a solution with PA-chains free of Ag$^+$ ions inevitably leads to a reorganization and formation of dense unstable aggregates in close agreement to a process where the two components would have been mixed to their final composition at time zero (series ES-2, ES-3, ES-5, ES-6 and X1 of ES-8).

4.1.4 Precipitation Threshold

The increase of the Ag-content up to [Ag$^+$]/[COO$^-$] ≈ 1.5 does not affect the molecular parameters of the stable aggregates and solutions remain transparent. Only beyond ratios [Ag$^+$]/[COO$^-$] ≈ 2.5, with the exact value of [Ag$^+$]/[COO$^-$] depending on the NaPA concentrations, the Ag$^+$-PA solutions become turbid and precipitate. Visually analysed series of Ag$^+$-PA solutions in the range of $1 \leq$ [NaPA] ≤ 4 mM and $2 \leq$ [Ag$^+$] ≤ 12 mM showed either transparent or turbid solutions, thus separating again the phase diagram for NaPA800 sample into two regimes: dense stable aggregates and precipitates (Figure 4.1.18).

Aggregation is expected to precede the precipitation. Therefore we performed several TR-SLS/DLS experiments to establish the morphology of the formed particles close to the precipitation threshold indicated in Figure 4.1.18. Figure 4.1.19 illustrates the evolution of the particle mass M_w, size R_g and structure-sensitive ratio ρ of the experimental series ES-9. All molecular parameters in the beginning of aggregation adopt comparable values, which indicates the same starting state for all aggregates. The increase of the Ag-content in the system accelerates the aggregation process. The parameter ρ drastically increases from 0.5 to 1.5 within 20 min and 5 min in case of [Ag$^+$]/[COO$^-$] $= 3.5$ and 4 respectively. In case of [Ag$^+$]/[COO$^-$] $= 3$, the aggregation is much slower and ρ value is kept in the range of 0.5 - 0.9 (Figure 4.1.19). This increase of the structure sensitive factor shows changes in the morphology of growing units, which excludes to correlate M_w with R_g and extract a structure sensitive exponent based on self similarities.
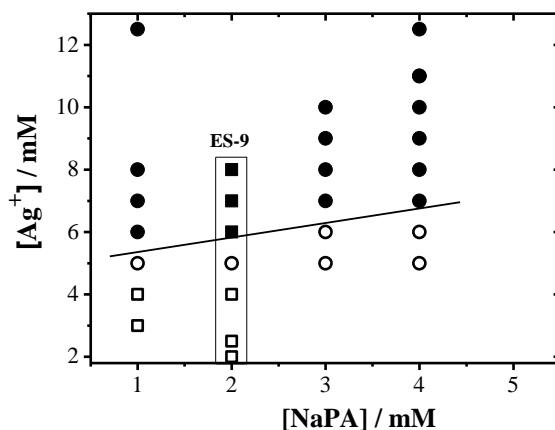
Figure 4.1.18 Representation of the data points indicating two regimes: dense stable aggregates ($\square$; $\bigcirc$) and precipitated samples ($\blacksquare$; $\bullet$). Squares represent results from TR-SLS/DLS, circles represent results from visual observation. The empty symbols correspond to stable and transparent solutions. The full symbols indicate precipitation observed by visual inspection or aggregation detected by TR-SLS/DLS and successive precipitation. The frame at [NaPA] = 2 mM indicates the experimental series ES-9. The black line denotes the precipitation threshold.
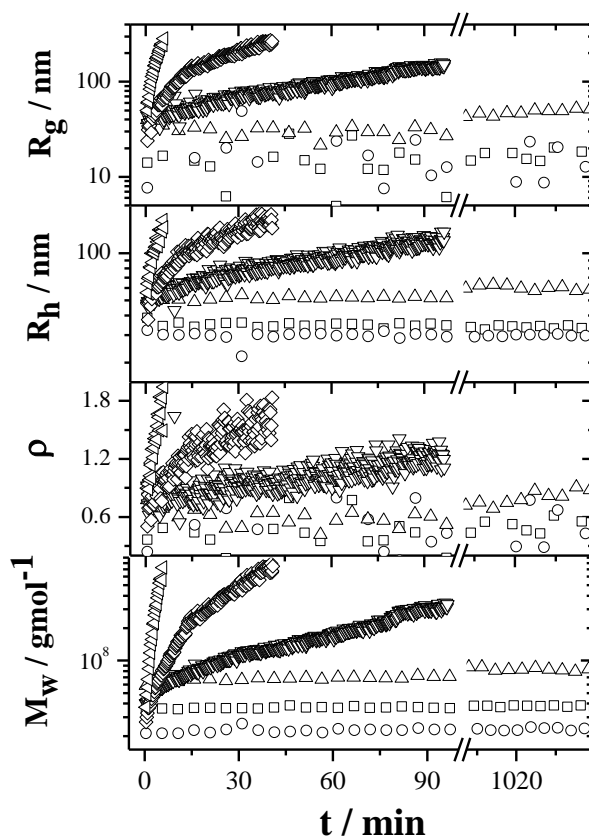
Figure 4.1.19 The evolution of the radius of gyration R_g, hydrodynamic radius R_h, molar mass M_w and $\rho = R_g/R_h$ values with time t for series ES-9. The concentration of [NaPA] is 2.0 mM at the [Ag$^+$]/[COO$^-$] ratios: 1.0 ($\square$), 1.25 ($\bigcirc$), 2.0 ($\triangle$), 3.0 ($\triangledown$); 3.5 ($\diamondsuit$); 4.0 ($\triangleleft$).

The underlying aggregation mechanism of entities may be a coalescence leading to ever larger fractal-like structures. This disordered structure is supported by experimental form factors for the intermediates at $[Ag^+]/[COO^-] = 3$ and $[NaPA] = 2$ mM measured by TR-SLS instrument with sample NaPA800 as representative example of the aggregation process at the precipitation threshold (Figure 4.1.20). Form factor recorded at the earlier stages where $R_g < 200$ nm matches fairly well with the form factor of polydisperse coil. Thus the aggregates at the precipitation threshold resemble high density unstable aggregates.
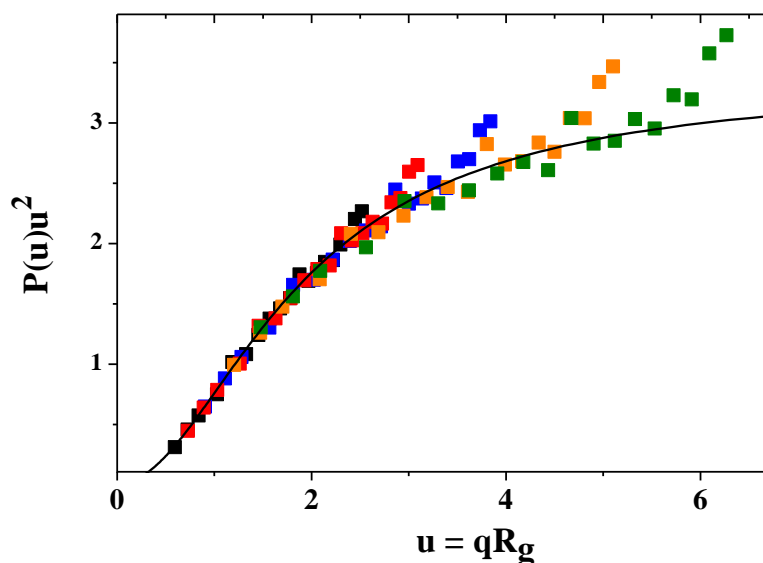
Figure 4.1.20 Selected scattering curves from aggregation run of series ES-9 performed with sample NaPA800 at $[NaPA] = 2.0$ mM and at $[Ag^+]/[COO^-] = 3$, represented as normalized Kratky plot based on the normalized variable $u = qR_g$. The symbols denote an age of 60 (■), 76 (■), 96 (■), 131 (■) and 166 (■) min. The solid lines correspond to the form factor of a polydisperse coil with PDI = 2 [109, 150, 151].

4.1.5 Conclusion

Addition of Ag^+ ions to dilute solutions of high molecular weight NaPA chains induces an aggregation of the NaPA chains. Unlike to alkaline earth cations, Ag^+-PA chains do not undergo a considerable coil-shrinking while approaching the aggregation threshold [11-14, 16]. After crossing the aggregation threshold (indicated as line 1 in Figures 4.1.21 and 4.1.22) by an increase of the $[Ag^+]/[COO^-]$ ratio from 0.001 to 0.3, the PA-coils begin to aggregate. Formation of homogeneous sphere-like networks of coils is observed at a few Ag^+ ions per one thousand of carboxylic groups. At $0.05 < [Ag^+]/[COO^-] < 0.3$ these homogeneous low density aggregates collapse and establish initial intermediates, which further grow as dense unstable aggregates with a much higher density and size. Beyond $[Ag^+]/[COO^-] \approx 0.3$, indicated as line 2 in Figures 4.1.21 and 4.1.22, the initially formed

dense 25-50 nm aggregates remain stable over time and solutions remain clear. We call this Ag$^+$-PA species dense stable aggregates. The structure sensitive factor ρ is in the range of to 0.5-0.7 in this regime, which indicates the existence of a low density corona of dangling PA-coils establishing a draining shell surrounding a non-draining dense core. From this state there are two routes to switch on the aggregation: (i) addition of PA-coils will lead to the formation of dense unstable aggregates; (ii) addition of Ag$^+$ ions will ultimately lead to macroscopic precipitation. The latter boundary is named as precipitation threshold and corresponds to line 3 in Figures 4.1.21 and 4.1.22. This line may essentially represent the same pattern observed by Ikegami and Imai [6] where $[Ag^+]_c$ = $[NaPA]_c$. In both cases, a stoichiometric number of Ag$^+$ ions with respect to the number of negative monomer units is required to precipitate the PA-coils. The difference in the molecular weight of NaPA samples used in the present work and in the work of Ikegami and Imai [6] as well as the corresponding degrees of neutralization achieved by Ag$^+$ ions (e.g. different pH in PA solutions) may have caused the discrepancy in r_0 of eq(1.1) by a factor of 3.
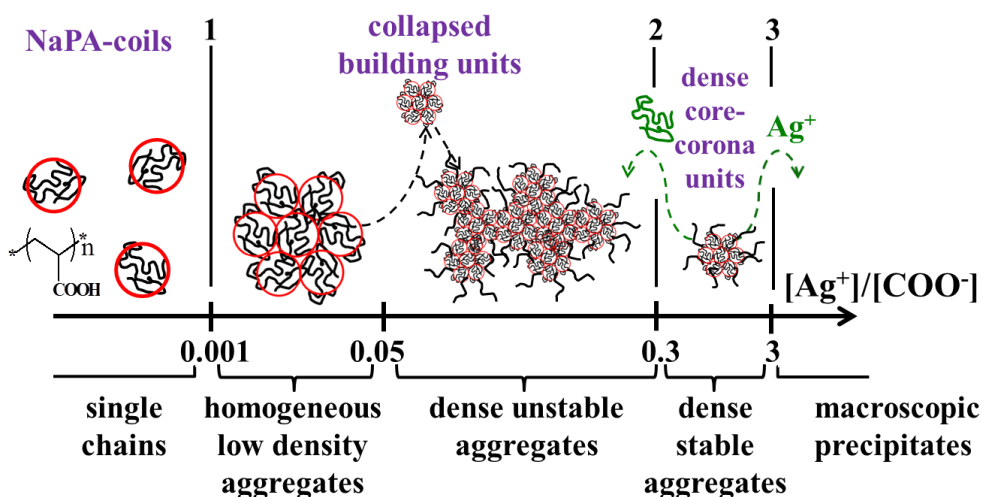
Figure 4.1.21 Illustration of the morphological changes of PA-coils and aggregation thereof in the presence of Ag$^+$ ions expressed in terms of $[Ag^+]/[COO^-]$ ratio: aggregation threshold (line 1), evolution of aggregates and separation between dense unstable aggregates from dense stable aggregates (line 2), precipitation threshold (line 3). The threshold values of the lines refer to sample NaPA800 at [NaPA] = 2.0 mM.
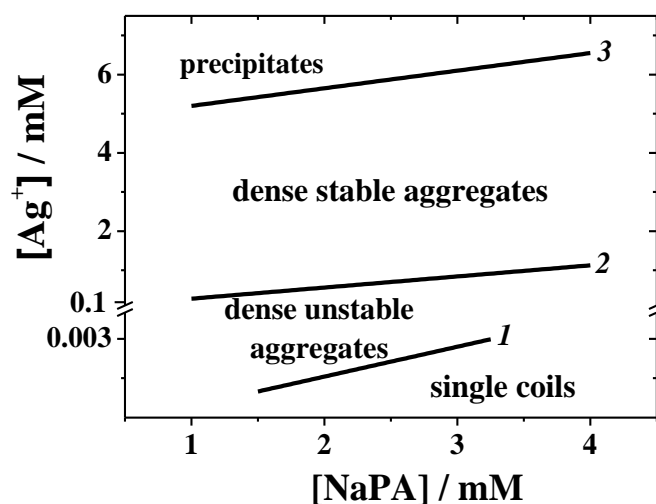
Figure 4.1.22 The phase diagram based on NaPA800 sample with M_w = 503 kDa established for the Ag⁺-PA systems in 0.01 M NaNO₃ at a pH of 9. Line 1 is the aggregation threshold, line 2 separates dense unstable aggregates from dense stable aggregates and line 3 is the precipitation threshold.

The present findings suggest the application of specifically interacting Ag⁺ ions as a new tool to control the formation and morphology of polyacrylate chains in aqueous solution. The next Chapter 4.2 is considering the specific feature of the present Ag⁺-PA phase diagram with respect to Ag-NP formation induced under exposure to UV-light.

4.2 Ag-NP Formation in Ag$^+$-PA Solutions

As mentioned in Chapters 1.1.2 and 4.1.5, formation of Ag-NPs is possible by means of exposure of Ag$^+$-PA solutions to UV-light without additional reducing agent. In the present Chapter 4.2 properties of such Ag-NPs formed under exposure to UV-light shall be correlated with the location of the precursor Ag$^+$-PA solutions in the phase diagram (Figure 4.1.22, used NaPA sample is NaPA800).

We begin the discussions of our results on Ag-NP formation with time-resolved static light scattering experiments, which reveal that Ag$^+$-PA systems undergoing aggregation become stable upon exposing it to UV-light, while Ag$^+$-PA systems, corresponding to dense stable aggregates, do not show significant changes in terms of the particle size after UV-exposure. As a representative example of this phenomena Figure 4.2.1 shows the evolution of R_g with time t for three samples before and after UV-exposure, two corresponding to dense unstable aggregates with [Ag$^+$]/[COO$^-$] = 0.05 and 0.16 (Figure 4.2.1a) and one corresponding to dense stable aggregates with [Ag$^+$]/[COO$^-$] = 0.40 (Figure 4.2.1b). Accordingly, for all three samples (Figure 4.2.1) UV-exposure of solutions was applied after two different aging times t_{AG}, which corresponds to the time periods between the preparation of the solution and UV-illumination: (i) In one experiment UV-exposure had been applied immediately after the preparation of the solution containing both Ag$^+$ ions and NaPA coils in aqueous 0.01 M NaNO$_3$. The samples prepared in such a manner correspond to aging time $t_{AG} = 0$ and will be called **without aging/non-aged**. (ii) In the other experiment the solution was aged for $t_{AG} \approx 30$ min before illumination with UV-light and these samples will be called **aged**. Time until UV-exposure of the aged solution was also used for TR-SLS analysis.

The particle size in case of the silver percentage of [Ag$^+$]/[COO$^-$] = 0.40, which lies in the regime of dense stable aggregates, is the same before and after UV-illumination and corresponds to an averaged value of $R_g = 25$ nm (Figure 4.2.1b). Contrary to this, the aggregating samples at [Ag$^+$]/[COO$^-$] = 0.05 and 0.16 become stable only after UV-exposure and the R_g value drops from 135 nm to 80 nm in case of [Ag$^+$]/[COO$^-$] = 0.05 and to 55 nm in case of [Ag$^+$]/[COO$^-$] = 0.16 (Figure 4.2.1a).

Remarkably, R_g of the non-aged systems with the ratio of [Ag$^+$]/[COO$^-$] = 0.05 and 0.16, exposed to UV-light, are 35 nm and 25 nm, respectively, which is close to the particle size of the system with [Ag$^+$]/[COO$^-$] = 0.40 before and after UV-exposure. This matching of particle size in the solutions from the regime of dense unstable aggregates before and after exposure to UV-light at $t_{AG} = 0$ min with the particle size in solutions from the regime of dense stable aggregates before and after exposure to UV-light at any t_{AG} suggests that the hybrid entities (Ag-NPs in the PA-matrix) in both cases are of the same nature and size. As described in our preceding Chapter 4.1 dense stable aggregates are formed almost instantaneously at ratios of [Ag$^+$]/[COO$^-$] > 0.3. The present findings

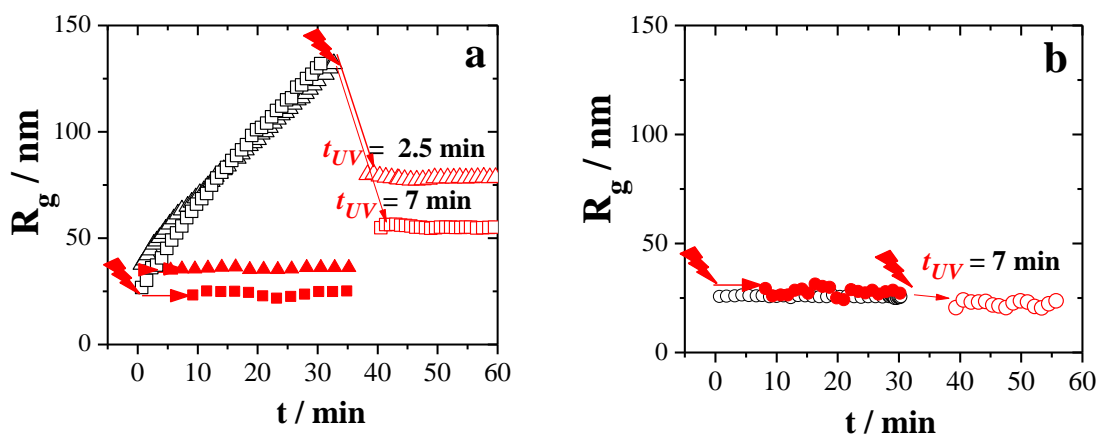reconfirm that they establish the building units for dense unstable aggregates formed at $[Ag^+]/[COO^-] < 0.3$.

Figure 4.2.1 The evolution of the radius of gyration R_g versus time t. Full and hollow red symbols denote the trend of R_g from samples exposed to UV-light at $t_{AG} = 0$ and $t_{AG} = 30\text{-}35$ min, respectively. Black symbols indicate trends of R_g from samples as they are aged prior to UV-exposure. Figure 4.2.1a describes the response of dense unstable aggregates and Figure 4.2.1b the response of dense stable aggregates to UV-light. The symbols denote: $[NaPA] = 2$ mM with $[Ag^+]/[COO^-] = 0.16$, $t_{UV} = 7$ min, (squares); $[NaPA] = 5.12$ mM with $[Ag^+]/[COO^-] = 0.05$, $t_{UV} = 2.5$ min (triangles); $[NaPA] = 2$ mM with $[Ag^+]/[COO^-] = 0.40$, $t_{UV} = 7$ min (circles). Solutions exposed to UV-light for $t_{UV} = 7$ min prior to the TR-SLS analysis were diluted with aqueous 0.01 M NaNO$_3$ to $[NaPA] = 1$ mM.

Ag^+-PA solutions exposed to UV-light may become turbid, due to formation of Ag-NPs. The turbidity is increasing with an increase of the used Ag^+ concentration and duration of the UV-exposure, therefore most part of solutions had to be diluted prior to the light scattering analysis. Dilution was carried out with 0.01 M NaNO$_3$ solution to ensure that the ratio between silver ions and carboxylate functions remained constant. However, since the dense unstable aggregates with the lower concentration of Ag^+ ($[Ag^+]/[COO^-] = 0.05$) remained clear and thus did not require dilution prior to the DLS/SLS-analysis, we can exclude the dilution step as the cause of the halt of aggregation and unambiguously attribute it to the UV-exposure. Moreover, Figure 4.2.2 compares UV-spectra of two solutions with the same ratio of $[Ag^+]/[COO^-] = 0.05$ exposed to UV-light at $t_{AG} = 0$ with the spectrum recorded from the solution, which has been exposed to UV light after $t_{AG} \sim 35$ min. The analysis by the UV-vis spectroscopy is designed to represent plasmonic properties Ag-NPs, where the position and shape of the surface plasmon resonance peak (SPR) thereof depends on several factors including size, shape, surrounding media, polydispersity and tendency of the particles to aggregate [84, 152, 153]. The SPR bands for the non-aged solution ($t_{AG} = 0$) and for the solution aged for $t_{AG} \sim 35$ min appear at the

same wavelength of $\lambda_{max} \sim 412$ nm, indicating that the properties of individual Ag-NPs are similar. Strikingly, the absorption of the SPR for the solution aged for ca. 35 min prior to exposure to UV-light decreased drastically, and in addition a broad shoulder appeared in the infrared region. This broad absorbance at $\lambda > 550$ nm can be regarded as a collective plasmon band of Ag-NPs randomly arranged in Ag-NP assemblies [154, 155].
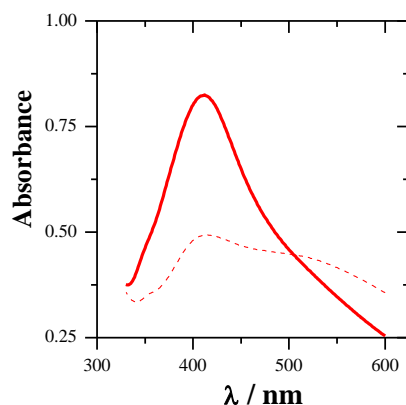
Figure 4.2.2 UV-vis spectra of two Ag^+-PA solutions after exposure to UV-light. The NaPA concentration is 5.12 mM at the ratio of $[Ag^+]/[COO^-]$ = 0.05. The exposure to UV-light for $t_{UV} = 2.5$ min is applied to the aged Ag^+-PA solution, i.e. at $t_{AG} \sim 35$ min (dash line), and to the non-aged Ag^+-PA solution, i.e. at $t_{AG} = 0$ min (solid line). Solutions were characterised without its dilution.

Thus, these results suggest to look at the effect of UV-light on the dense unstable and dense stable Ag^+-PA aggregates in more detail and to clarify the following questions: (i) Does the nature of Ag-NPs depend on the aggregation process in the regime of unstable dense aggregates and, if it does, can we control the size of Ag-NPs via the aggregation process? (ii) Does the nature of Ag-NPs depend only on the regime of the phase diagram? (iii) What is the spatial distribution of the Ag^+ ions / Ag-NPs in the polymer matrix? (iv) Why does the size of aged unstable particles get smaller after UV-illumination? (v) Does the duration of UV-light exposure change the size / properties of Ag-NPs and can it also be used as a tool to control Ag-NP formation?

Before investigating these issues, the effect of UV-light on pure polyacrylate solutions (Chapter 4.2.1) and the effect of dilution of solutions exposed to UV-light prior to SLS/DLS characterisation (Chapter 4.2.2) will be discussed.

4.2.1 Effect of UV-exposure on PA-chains

It is known from literature that NaPA molecules can undergo a random scission and crosslinking of the polymer chain by photolysis under UV-illumination due to free-radical reactions [156-159]. The effect of chain degradation dependents on the wavelength of UV-lamps [160, 161], usage of cutoff filters and the power of the light source. Increase of UV-radiation time enhances the effect of degradation [158] and thus affects the molecular weight of the polyacrylate samples.

In order to better analyse a possible net effect of UV-light on NaPA chains during the Ag-NP formation, induced by the exposure of Ag^+-PA solutions to UV-light, the impact of UV-radiation on pure solutions of NaPA is highly desirable. We performed combined SLS/DLS experiments in order to compare the molecular parameters of an aqueous solution of polyacrylate sample NaPA800 in 0.01 M $NaNO_3$ prior to and after exposure to UV-light. The time of exposure t_{UV} was 7 min, which corresponds to the maximal applied UV-illumination time of Ag^+-PA solutions discussed in the Chapter 4.2.
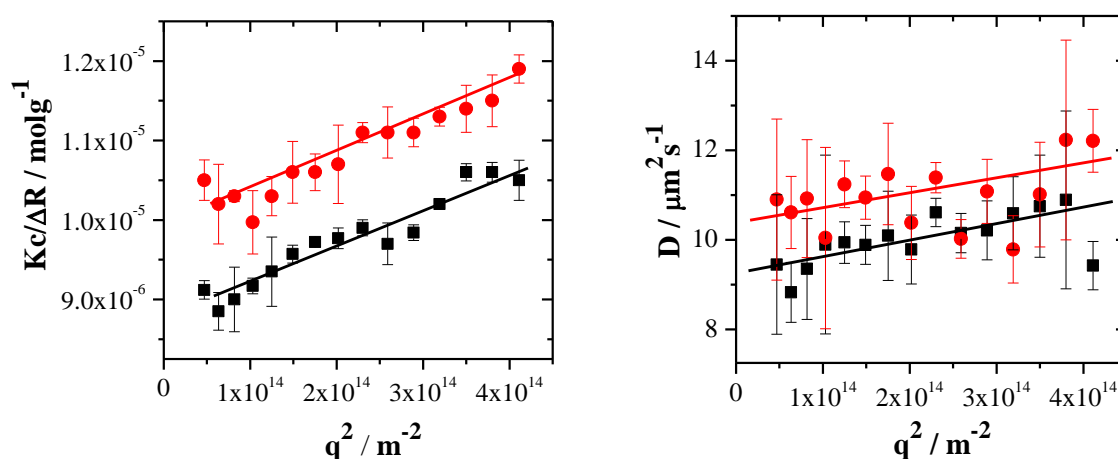
Figure 4.2.3 $Kc/\Delta R$ versus q^2 (left graph) and D versus q^2 (right graph) for the NaPA800 solution at [NaPA] = 2 mM: (■) before UV-exposure, (●) after UV-exposure for t_{UV} = 7 min. Lines indicate the extrapolation to q^2 = 0.

Figure 4.2.3 shows the scattering curves in terms of $Kc/\Delta R$ vs q^2 (left graph) and D vs q^2 (right graph) from SLS/DLS characterisation of the same NaPA solution before and after exposure to UV-light. The intercept of $Kc/\Delta R$ slightly increases after UV-illumination, which gives smaller values of M_w (Table 4.2.1). The slope of the corresponding static light scattering curves are parallel within experimental uncertainty. The extrapolated value of the diffusion coefficient D to q^2 = 0 undergoes a slight increase after UV-exposure. A close look at the CONTIN analysis [113] at θ = 30° shows that the main fraction has a minor shift toward smaller particle size with a broadening of the size distribution (Figure 4.2.4). Table 4.2.1 summarizes the evaluated values of M_w, R_g, and R_h from SLS/DLS measurements.

Table 4.2.1 Characteristic parameters of the NaPA sample analysed by combined SLS/DLS before and after exposure to UV-light.

Condition of analysis	$M_w * 10^3$ / gmol^{-1}	R_g / nm	R_h / nm	$\rho = R_g/R_h$
Before UV-exposure	114.2 ($\pm$1.11)	39.4 ($\pm$1.5)	26.4 ($\pm$2.7)	1.49
After UV-exposure (t_{UV} = 7 min)	101 ($\pm$0.99)	36.3 ($\pm$1.7)	23.5 ($\pm$3.8)	1.54

All molecular parameters indicate that the polymer chains become slightly smaller whereas the structure sensitive factor ρ remains at a value of ca. 1.5, which is characteristic for a coil-like structure in both cases [122]. These variations are considered to be insignificant and within experimental uncertainty. This is particularly true since 2 mM aqueous solution of NaPA800 scattered just 5 times stronger than pure water. Hence, we can conclude from these light scattering results that the polyacrylate chains do not undergo substantial chain scission during the exposure to UV-light.
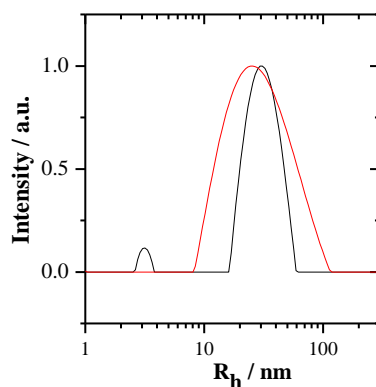
Figure 4.2.4 Size distribution of NaPA800 sample at [NaPA] = 2 mM before exposure to UV-light (black line) and after exposure to UV-light for t_{UV} = 7 min (red line). The distributions have been calculated by means of the CONTIN analysis [122] of the corresponding intensity correlation functions obtained by DLS at θ = 30°.

4.2.2 Effect of Dilution on the UV-exposed Ag$^+$-PA Solutions

It should be emphasised that Ag$^+$-PA solutions exposed to UV-light are becoming brown and turbid thus preventing a useful light scattering study. In order to increase the transmission of the laser light and avoid multiple scattering, these solutions have to be diluted. Dilution is carried out by use of aqueous 0.01 M NaNO$_3$ keeping the ionic strength as well as the ratio [Ag$^+$]/[COO$^-$] constant. Usually the concentration of PA-coils and Ag$^+$

ions is decreased by a factor of two. In the following paragraphs we will analyse to which extent such a dilution of solutions containing Ag-NPs may affect the light scattering data or the results from UV-vis spectroscopy.

In Figure 4.2.5 and Figure 4.2.6 results from SLS/DLS characterisation illustrate the dilution effect. The non-aged Ag^+-PA solution containing 2 mM of NaPA-coils and 0.32 mM of Ag^+ ions was exposed to UV-light and analysed by SLS/DLS at this composition. Since the time of UV-exposure was as short as $t_{UV} = 2$ min, exposure did not lead to a considerable turbidity of the sample and the UV-illuminated solution could be directly analysed by light scattering. Characterisation was carried out by combined SLS/DLS analysis with the Model ALV-CGS 5000E in the regime of the scattering vector q of $47 < q^2 < 350$ μm^2.
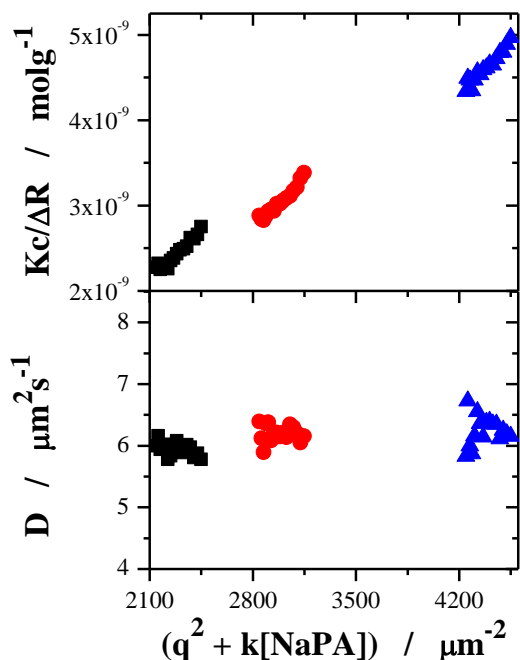
Figure 4.2.5 Zimm diagrams from static and dynamic light scattering of the Ag^+-PA stock solution with k = 22390, $47 < q^2 < 350$ μm^2. The symbols indicate [NaPA] = 2.0 mM and $[Ag^+]/[COO^-]$ = 0.16 exposed to UV-light for $t_{UV} = 2$ min (▲) and two diluted solutions thereof with [NaPA] = 1.333 mM (●), and 1 mM (■) in aqueous 0.01 M $NaNO_3$ solution.

After the SLS/DLS characterisation of the stock solution, it was diluted by a factor of 1.5 and 2 with aqueous 0.01 M $NaNO_3$. Dilution resulted in concentrations of PA-coils of 1.333 mM and 1 mM, respectively. As it is expected, the impact of the second virial coefficient A_2 lowers $Kc/\Delta R_{\Theta=0}$ (see static and dynamic Zimm diagrams of the analysed samples in Figure 4.2.5) and increases the apparent radius of gyration R_g (Figure 4.2.6). This behaviour is typical for a species in good solvent which remains its identity upon

dilution. Only the apparent hydrodynamic radius R_h remained constant for all NaPA concentrations. The results thus demonstrate that integrity of the hybrid particles (PA-chains and embedded Ag-NPs therein) is not affected by dilution of the solution. Clearly, the apparent R_g was more affected by excluded volume effects than the apparent R_h was. Therefore, in further discussions (Chapters 4.2.2-4.2.8) R_h will be considered as the more reliable parameter from SLS/DLS characterisations and values of R_g will be used for qualitative evaluation of the systems.
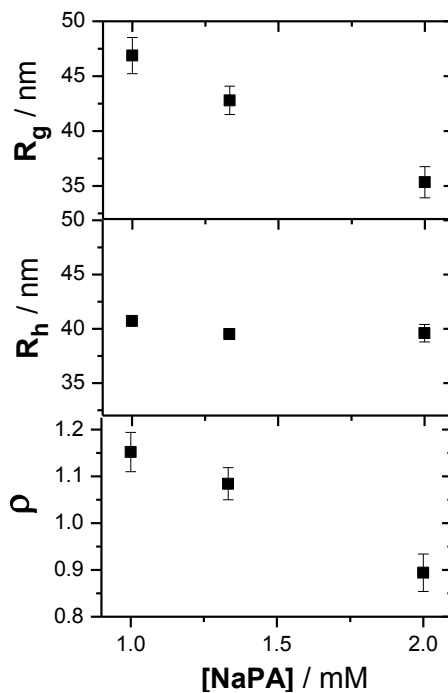
Figure 4.2.6 Radius of gyration R_g, hydrodynamic radius R_h and $\rho = R_g/R_h$ of the Ag$^+$-PA stock solution without aging ([NaPA] = 2.0 mM and [Ag$^+$]/[COO$^-$] = 0.16) exposed to UV-light for t_{UV} = 2 min and of two diluted solutions thereof evaluated from the data in Figure 4.2.5.

In order to further clarify the stability of the formed Ag-NPs, UV-vis spectroscopy was used to analyse a dilution series of UV-illuminated solutions in addition to the SLS/DLS characterisation. Figure 4.2.7 reveals UV-vis spectra of non-aged Ag$^+$-PA solutions exposed to UV-light for 2 min. The composition of the respective stock solution was identical to the stock solution used for the SLS/DLS analysis in Figures 4.2.5-4.2.6. Successively, the original NaPA concentration was decreased via dilution with 0.01 M NaNO$_3$ by a factor of 2 and 4.5, i.g. from 2 mM to 1 mM and from 2 mM to 0.444 mM. Since the cuvettes used for UV-vis spectroscopy were identical, Beer–Lambert–Bouguer law can be applied without a thickness correction. The absorbance values of the UV-spectra from the stock solution were divided by a factor of 2 and 4.5 in order to compare them with the experimentally obtained UV-vis spectra from respective dilutions. As can be seen in

Figure 4.2.7 the experimental spectra almost overlay with Beer-Lambert-Bouguer predictions. The calculated curves are slightly higher, which can be explained by experimental inaccuracy upon dilution of the stock solution. The most crucial and important fact is that no additional peaks or shoulders and no shift of the SPR band are observed. Clearly, dilution does not affect the optical properties of Ag-NPs and can thus be used to facilitate further experiments.
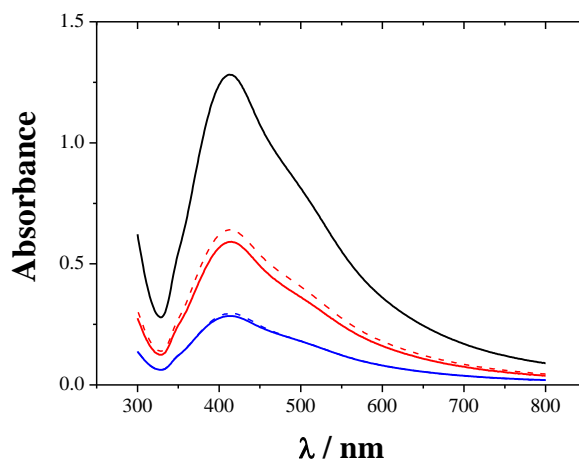
Figure 4.2.7 UV-vis spectra of Ag^+-PA solutions with [NaPA] = 2.0 mM and $[Ag^+]/[COO^-]$ = 0.16 after their exposure to UV-light for t_{UV} = 2 min without aging. Solutions were diluted with aqueous 0.01 M $NaNO_3$ to [NaPA] = 1 mM (—) and 0.444 mM (—) while the $[Ag^+]/[COO^-]$ ratio was kept unchanged. Dashed lines indicate the calculated spectra via Beer–Lambert–Bouguer law from the spectrum with [NaPA] = 2 mM (—).

4.2.3 Effect of Aging of Dense Unstable Ag^+-PA Aggregates on Ag-NP Formation

As it was outlined in Figures 4.2.1-4.2.2 the formation of Ag-NPs is accompanied by a halt of the aggregation in case of Ag^+-PA systems located in the regime of dense unstable aggregates of the phase diagram (Figure 4.1.22). The aggregation stops under the effect of the UV-exposure and not due to the dilution of the illuminated solution before light scattering characterisation (Figures 4.2.1-4.2.2). Apparently, the reduction of Ag^+ to Ag^0 deprives the Ag^+-PA aggregates of the bridging (i.e. cross-linking) Ag^+ ions and the growth of Ag^+-PA aggregates stops once Ag-NPs are formed and embedded within the "arrested" PA-aggregates. Since the aggregation can be stopped at any aging time t_{AG}, the variation of the latter one may enable to control the formation of Ag-NPs.

In order to reveal the correlation between the size of Ag^+-PA aggregates and the resulting Ag-NPs at a specific t_{AG} the following experiment was established. Two stock solutions, both with a total amount of $[Na^+] = 0.01$ M were prepared first: one is a solution of NaPA coils with $[NaPA] = 4$ mM and the other one is a solution of $AgNO_3$ with $[Ag^+] = 0.64$ mM. After filtrating equal amounts of both stock solutions into five scattering cuvettes, each cuvette contained $[NaPA] = 2$ mM and $[Ag^+] = 0.32$ mM corresponding to $[Ag^+]/[COO^-] = 0.16$. This ratio of silver ions per carboxylic groups of the anionic PA-chains generates dense unstable aggregates via aggregation. One of the cuvettes was immediately placed into the goniometer of the combined SLS/DLS instrument and analysed over the next 3 h in a time resolved mode. The other four cuvettes were kept in the dark and exposed to UV-light for 4 min at different t_{AG}. In the same manner as in the previously described experiment (Figure 4.2.1), the aging time t_{AG} corresponds to the time period between the preparation of the solution and UV-illumination.

In Figure 4.2.8 the radius of gyration R_g, hydrodynamic radius R_h and ρ-ratio are plotted versus time t. Although, the Ag^+-PA solution has the same value of [NaPA] and $[Ag^+]/[COO^-]$ as the system in Figure 4.2.1, the aggregation shown in Figure 4.2.8 is slower than in Figure 4.2.1 indicating poor reproducibility of the actual growth rate of the aggregates.

Figure 4.2.8 Radius of gyration R_g, hydrodynamic radius R_h and $\rho = R_g/R_h$ values versus aging time t of five Ag^+-PA solutions containing $[NaPA] = 2$ mM and $[Ag^+]/[COO^-] = 0.16$. Black symbols indicate TR-SLS/DLS measurement of the Ag^+-PA solution prior to the UV-exposure, red symbols indicate molecular parameters of the aged Ag^+-PA solutions after exposure to UV-light for $t_{UV} = 4$ min. The aging time t_{AG} of the Ag^+-PA solutions matches time t. Prior to the SLS/DLS analyses, solutions exposed to UV-light were diluted with aqueous 0.01 M $NaNO_3$ to $[NaPA] = 1$ mM while the $[Ag^+]/[COO^-]$ ratio remained unchanged.

Results from the SLS/DLS experiments obtained from the illuminated samples are compared with the TR-SLS/DLS data of the non-illuminated sample. The aging time t_{AG} of samples illuminated with UV-light is used as time t for proper comparison with the TR-SLS/DLS experiment of non-exposed sample. Figure 4.2.8 shows that R_g values of entities with Ag-NPs at any specific time $t = t_{AG}$ adopt the same values as the system which was not exposed to UV-light. This matching can be considered as accident, since the exposed Ag^+-PA solutions had to be diluted prior to the light scattering analysis, which imposes an additional source of uncertainty in accordance with the discussion in the previous Chapter 4.2.2. Hydrodynamic radii R_h of solutions illuminated with UV-light follow the same trend as of the non-illuminated solution but were lower by 25 nm (Figure 4.2.5). The structure sensitive factor ρ remains almost unchanged over the aggregation process and corresponds to the value of the spherical shape of Ag^+-PA aggregates, whereas after the UV-illumination it increases to $\rho = 1.3$ (Figure 4.2.8). This increase may indicate a change in shape toward fractal-like particles, however this cannot be unambiguously established because of the dilution prior to the light scattering characterisation of illuminated samples (Chapter 4.2.2, Figure 4.2.5).

In order to gain further knowledge about the particle size after UV-exposure three additional solutions with [NaPA] = 2 mM and $[Ag^+]/[COO^-] = 0.16$ were prepared: one was exposed to UV-light without aging ($t_{AG} = 0$), two others were aged for $t_{AG} = 1$ h and 2 h before exposing it to UV-light for 4 min. The respective exposed solutions were diluted twofold with 0.01 M $NaNO_3$ before light scattering characterisation. The extent of dilution applied in this experiment is the same as in the experiment outlined in Figure 4.2.8, therefore we can adequately compare molecular parameters from the two SLS/DLS characterisations in one graph (Figure 4.2.9).
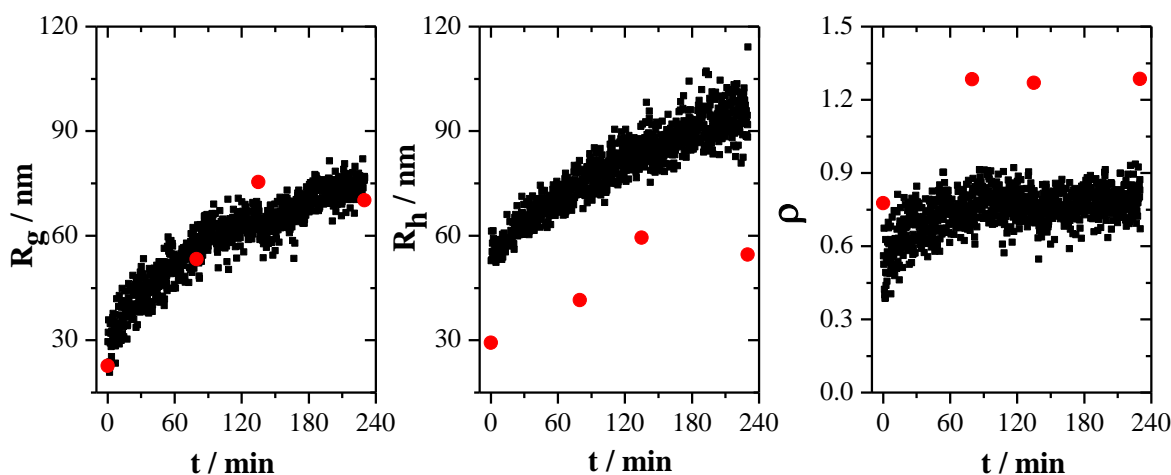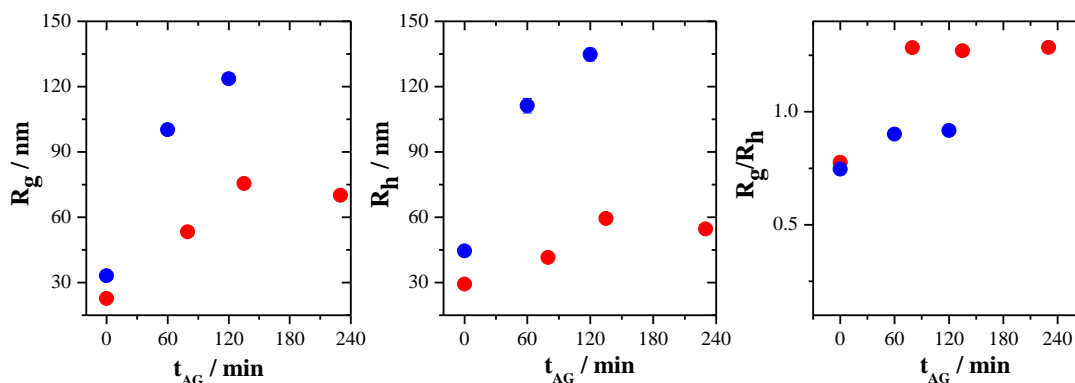

Figure 4.2.9 Radius of gyration R_g, hydrodynamic radius R_h and $\rho = R_g/R_h$ values versus aging time t_{AG} of Ag^+-PA solutions containing [NaPA] = 2 mM and $[Ag^+]/[COO^-] = 0.16$ after exposure to UV-light for $t_{UV} = 4$ min. Red symbols refer to the data from Figure 4.2.8. Prior to the SLS/DLS analysis all solutions were diluted with aqueous 0.01 M $NaNO_3$ to [NaPA] = 1 mM while the $[Ag^+]/[COO^-]$ ratio remained unchanged.

In the present experiment values of R_g and R_h are shifted toward higher values and do not coincide with the data from Figure 4.2.8. This effect is connected with the lack of exact reproducibility of the aggregation rate of Ag$^+$-PA solutions before UV-illumination. However in general, both results show the same trend: the size of entities with Ag-NPs formed under UV-irradiation is increasing with increasing aging time t_{AG}.

The particle size distribution in terms of var_z of the three solutions corresponding to the blue data points in Figure 4.2.9 were characterized by means of DLS. Ten field-correlation functions were evaluated with a decay of $[g^{(2)}(q, \tau) - 1]$ to 31% by the second order cumulant method at a scattering angle of $\theta = 30°$. The averaged var_z values are summarised in Table 4.2.2. These results reveal that Ag$^+$-PA solutions exposed to UV-light at longer aging time t_{AG} are less polydisperse. Figure 4.2.10 displays CONTIN analysis of the corresponding intensity correlation functions for better visualisation of the particle size distribution. It is necessary to emphasise that results from DLS characterisation cannot be directly interpreted as a characterisation of Ag-NPs, because they refer to hybrid particles including both Ag-NPs and "arrested" PA-coils, where the latter ones act as a hosting matrix for the reduction of Ag$^+$ ions.

Table 4.2.2 Estimation of polydispersity by means of var_z of Ag$^+$-PA samples with [NaPA] = 2 mM and [Ag$^+$]/[COO$^-$] = 0.16 at various aging time t_{AG} illuminated with UV-light for t_{UV} = 4 min. Prior to the DLS analysis solutions were diluted with aqueous 0.01 M NaNO$_3$ to [NaPA] = 1 mM while the [Ag$^+$]/[COO$^-$] ratio remained unchanged.

Aging time t_{AG}	$t_{AG} = 0$ h	$t_{AG} = 1$ h	$t_{AG} = 2$ h
var_z	0.47	0.38	0.30
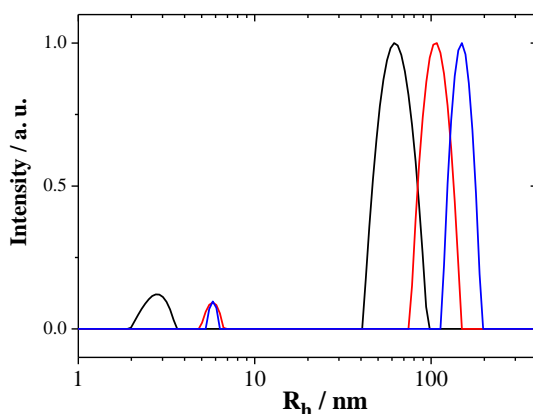
Figure 4.2.10 Size distributions of solutions containing [NaPA] = 2 mM and [Ag$^+$]/ [COO$^-$] = 0.16 exposed to UV-light at various aging time t_{AG}: 0 h (━), 1 h (━) and 2 h (━). Prior to the DLS analysis solutions were diluted with aqueous 0.01 M NaNO$_3$ to [NaPA] = 1 mM while the [Ag$^+$]/[COO$^-$] ratio was kept unchanged. The distributions have been calculated by means of a CONTIN analysis of the corresponding intensity correlation functions measured at a scattering angle of $\theta = 30°$.

In order to characterize the Ag-NPs in solution UV-vis spectroscopy was used. Figure 4.2.11 shows UV-vis spectra of four Ag^+-PA solutions containing 2 mM of NaPA with $[Ag^+]/[COO^-] = 0.16$ exposed to UV-light at four aging times $t_{AG} = 0$ min, 30 min, 60 min and 90 min. UV-vis absorption spectra demonstrate that the position of SPR bands does not show any noticeable shift with increasing the aging time t_{AG} of the Ag^+-PA solutions applied before UV-exposure ($\lambda_{max} \approx 413$ nm for $t_{AG} = 0$ min, $\lambda_{max} \approx 410$ nm for $t_{AG} = 30$, 60 and 90 min). The SPR absorption band of silver at 410-413 nm in the aqueous media can be related to the size of Ag-NPs of ca. 20-30 nm [153].

The absorption efficiency of SPR is decreasing with increasing aging time of the samples while the intensity in the infrared region undergoes an increase. The increasing absorbance in the wavelength regime of $\lambda > 550$ nm indicates a decrease in the interparticle spacing, which is induced by Ag-NP accumulation [154, 155]. At zero aging time an appearance of a shoulder at 500 nm may characterize the assemblies of Ag-NPs as oligomers [162], whereas a broad extinction band at $\lambda > 550$ nm can be regarded as a collective plasmon band of Ag-NP assemblies without a distinct spacing, thereby indicating formation of randomly arranged Ag-NPs in large assemblies [154, 155].
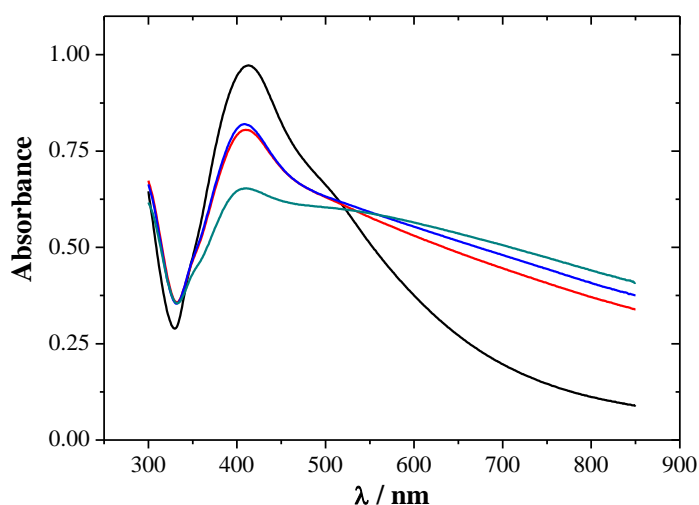
Figure 4.2.11 UV-vis absorption spectra of solutions containing $[NaPA] = 2$ mM and $[Ag^+]/[COO^-] = 0.16$ exposed to UV-light for $t_{UV} = 4$ min. The samples were illuminated with UV-light after different aging times t_{AG}. Color of the line indicates t_{AG}: 0 min (━), 30 min (━), 60 min (━) and 90 min (━). Prior to the UV-vis measurements the solutions were diluted with aqueous 0.01 M $NaNO_3$ to $[NaPA] = 1$ mM while the $[Ag^+]/[COO^-]$ ratio remained unchanged.

Combination of the results from DLS and UV-vis spectroscopy of the system with $[Ag^+]/[COO^-] = 0.16$, as a representative example of dense unstable Ag^+-PA aggregates, suggests that individual Ag-NPs with an averaged size of ca. 20-30 nm can be formed by means of UV-illumination of non-aged Ag^+-PA solutions (Figures 4.2.8 – 4.2.11). Exposure to UV-light of aged dense unstable Ag^+-PA aggregates indicates the formation of Ag-NP assemblies, whose size depends on the size of Ag^+-PA aggregates at the corresponding aging time t_{AG}. The constituting Ag-NPs in such assemblies exhibit an average size of ca. 20-30 nm. Figures 4.2.1-4.2.2 show results from the system with $[Ag^+]/[COO^-] = 0.05$ examined at similar conditions, which support our observations.

Variation of the aging time t_{AG} may enable to control the size of the final Ag-NP assemblies. In order to clarify this issue three Ag^+-PA solutions with $[Ag^+]/[COO^-] = 0.16$ and $[NaPA] = 2$ mM were exposed to UV-light for 4 min after different aging times ($t_{AG} = 0$, 1 and 2 h) and characterized by means of TEM directly afterwards (Figure 4.2.12). The same stock solutions of NaPA and $AgNO_3$ were used as for the experiments depicted in Figure 4.2.9 (blue symbols).

Individual Ag-NPs with an average size of ca. 20-30 nm are seen in the TEM images of the sample exposed to UV-light without aging (Figure 4.2.12a). In this case UV-illumination was reducing Ag^+ ions in the solution containing primary dense Ag^+-PA aggregates of the size ca. 25 nm. Figure 4.2.13 shows additional TEM results performed with a higher resolution TEM-microscope of the solution of the same composition ($[NaPA] = 2$ mM and $[Ag^+]/[COO^-] = 0.16$). This TEM experiment was made on a different day with different stock solutions, but with the same sample history as applied for the series presented in Figure 4.2.12a. Results from Figure 4.2.13 are in agreement with the results of Figure 4.2.12a, with UV-vis spectroscopy (Figure 4.2.11) and DLS measurements (Figure 4.2.9): individual Ag-NPs with an average size of ca. 25 nm prevail and coexist with a small fraction of bigger particles. The latter can be identified as assemblies of Ag-NPs by a slight shoulder at $\lambda > 500$ nm in the UV-vis spectra (Figure 4.2.11). The individual Ag-NPs can be regarded to mono- and polycrystalline Ag-NPs by the well-recognised stripes at a high magnification (Figures 6.11 of the Appendix).
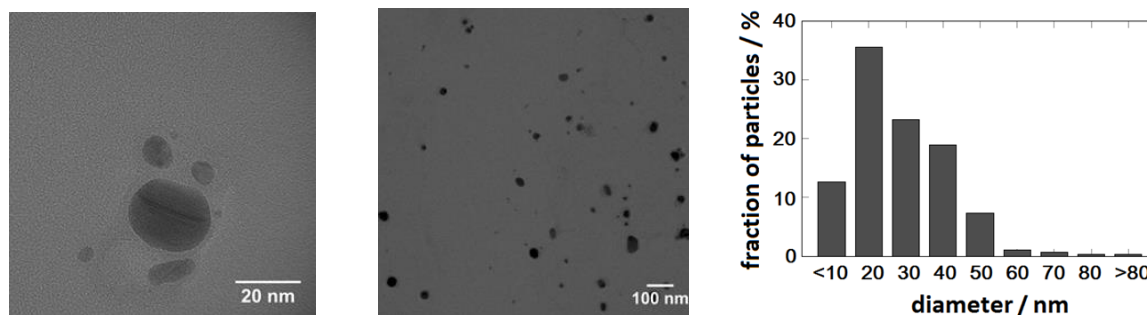
Figure 4.2.13 TEM images from Ag^+-PA solution containing $[NaPA] = 2$ mM and $[Ag^+]/[COO^-] = 0.16$ exposed to UV-light for $t_{UV} = 4$ min without aging.
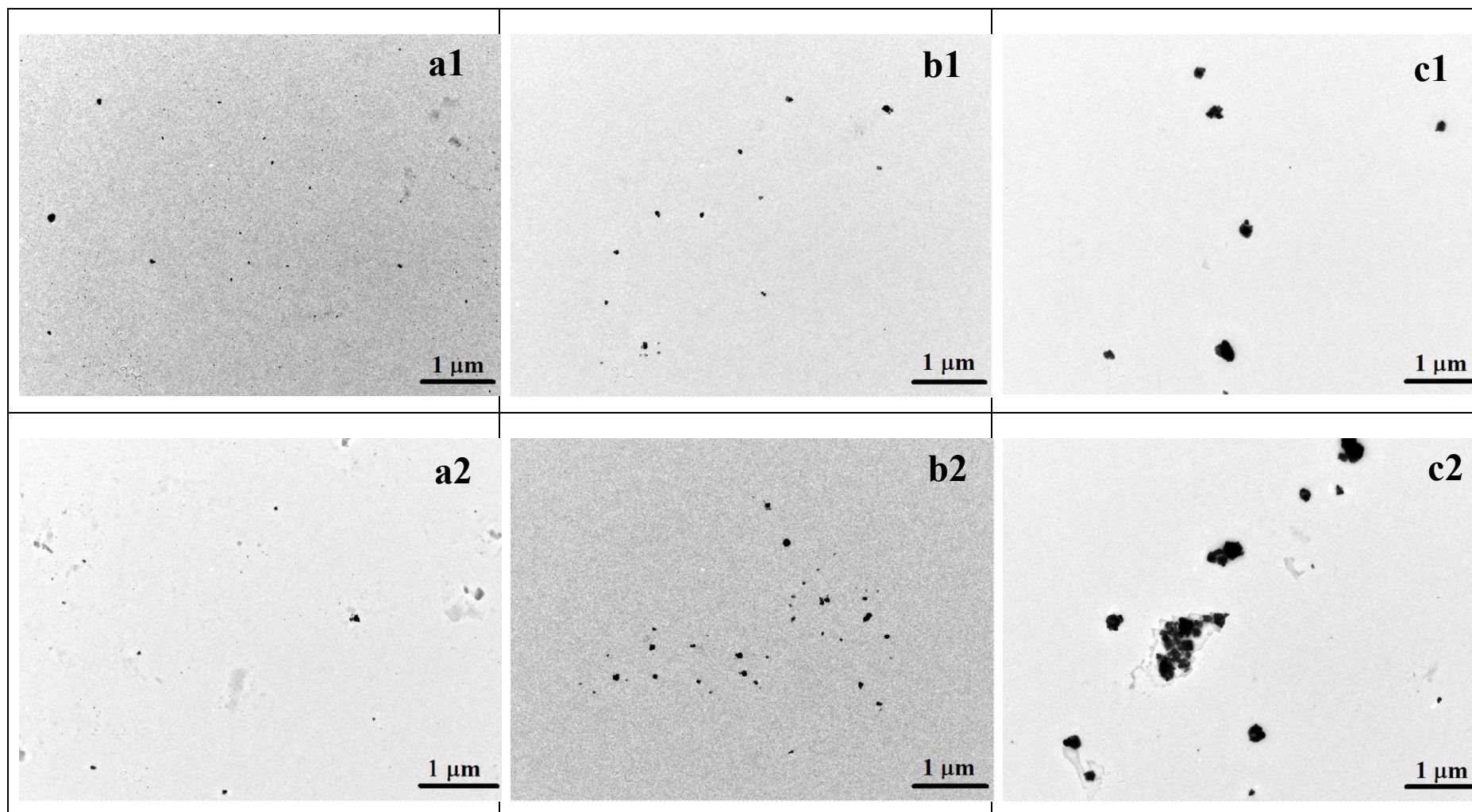
Figure 4.2.12 TEM micrographs of Ag$^+$-PA solutions containing [NaPA] = 2 mM and [Ag$^+$]/[COO$^-$] = 0.16 irradiated with UV-light for t_{UV} = 4 min at different aging times: t_{AG} = 0 h (a), 1 h (b), 2 h (c).
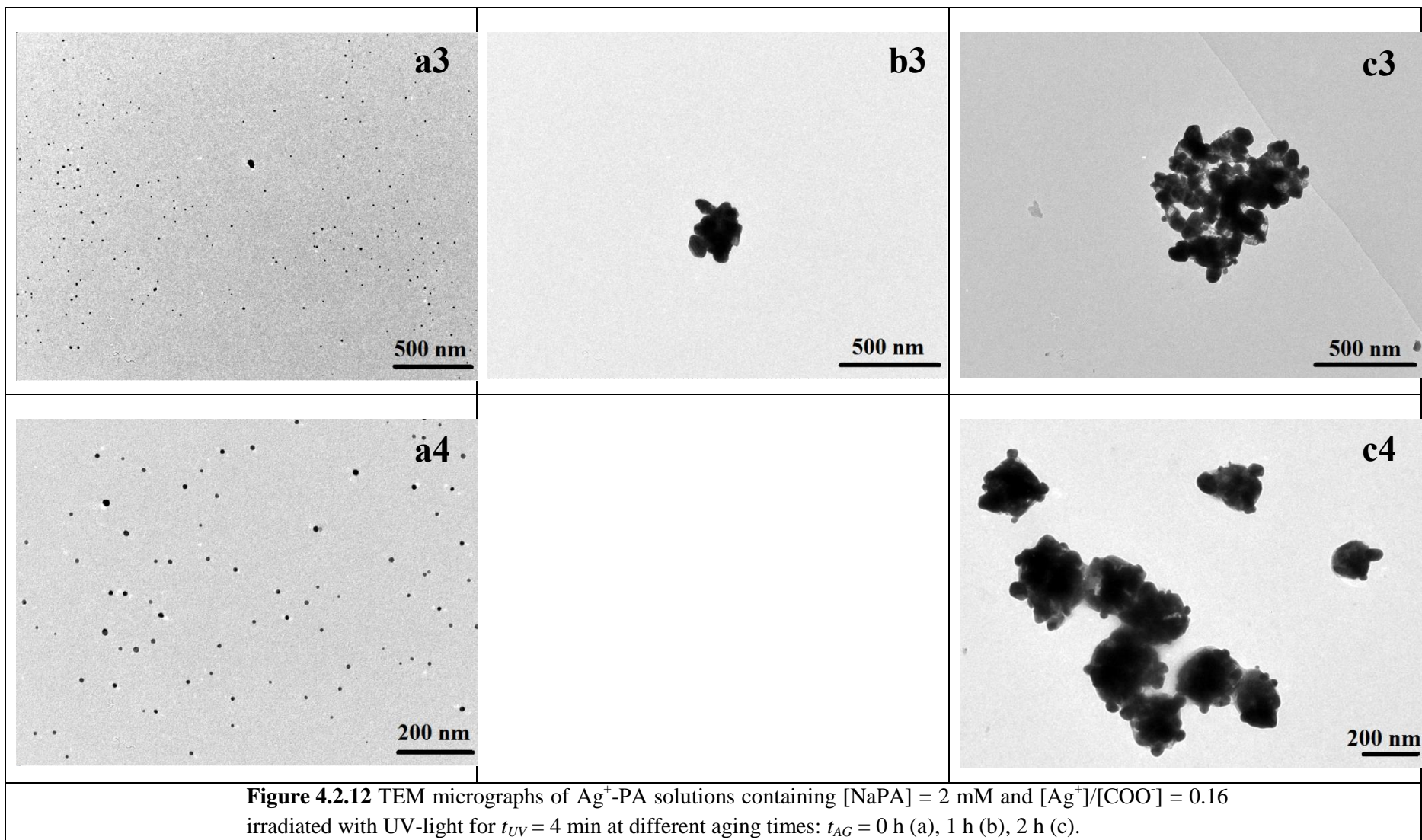
Figure 4.2.12 TEM micrographs of Ag$^+$-PA solutions containing [NaPA] = 2 mM and [Ag$^+$]/[COO$^-$] = 0.16 irradiated with UV-light for t_{UV} = 4 min at different aging times: t_{AG} = 0 h (a), 1 h (b), 2 h (c).

TEM images of the two aged samples (Figures 4.2.12b, c) demonstrate spherically shaped Ag-NP assemblies consisting of numerous individual Ag-NPs sticking together. These TEM micrographs clearly show that the sample aged for 2 h has Ag-NP assemblies of 200-250 nm, which are bigger by 50-100 nm than the Ag-NP assemblies of the sample aged for 1 h. This tendency was also inferred from the UV-spectra, where the absorbance at $\lambda > 550$ nm is higher for longer aged samples (Figure 4.2.11). Apparently, dense Ag^+-PA aggregates, which presumably act as building blocks in the aggregation process of dense unstable Ag^+-PA aggregates, may act as nanoreactors/containers in the reduction of Ag^+ ions induced by UV-exposure. The size of Ag^+-PA aggregates correlates with the size of Ag-NP assemblies, which are formed under exposure to UV-light of the Ag^+-PA aggregates. Individual Ag-NPs in these Ag-NP assemblies are of the same size as Ag-NPs generated from corresponding non-aged solutions. Figures 5.2.12 (a4, c4) support this assumption in particular.

4.2.4 Effect of Ag^+ Concentration of Dense Unstable Ag^+-PA Aggregates on Ag-NP formation

The range of dense unstable Ag^+-PA aggregates is determined by a particularly broad regime of $[Ag^+]/[COO^-]$ ratios in the phase diagram established in Chapter 4.1 (Figure 4.1.22). In order to learn whether systems belonging to the same phase regime but significantly differing in the $[Ag^+]/[COO^-]$ ratio behave in the same or different way with respect to UV-exposure, the following experiments were performed. Three Ag^+-PA solutions containing 2 mM of NaPA and with the ratios of $[Ag^+]/[COO^-] = 0.04, 0.16$ and 0.30 were prepared. Each of the three solutions was subdivided by filtrating it into two scattering cuvettes, respectively, resulting in a total of six samples. Two sample histories were applied: one solution of each $[Ag^+]/[COO^-]$ ratio was exposed to UV-light without aging and the other one was stored in the dark for $t_{AG} = 1$ h and exposed to UV-light for 2-4 min. Since all three samples lie in the regime of dense unstable aggregates, they are supposed to aggregate within $t_{AG} = 1$ h.
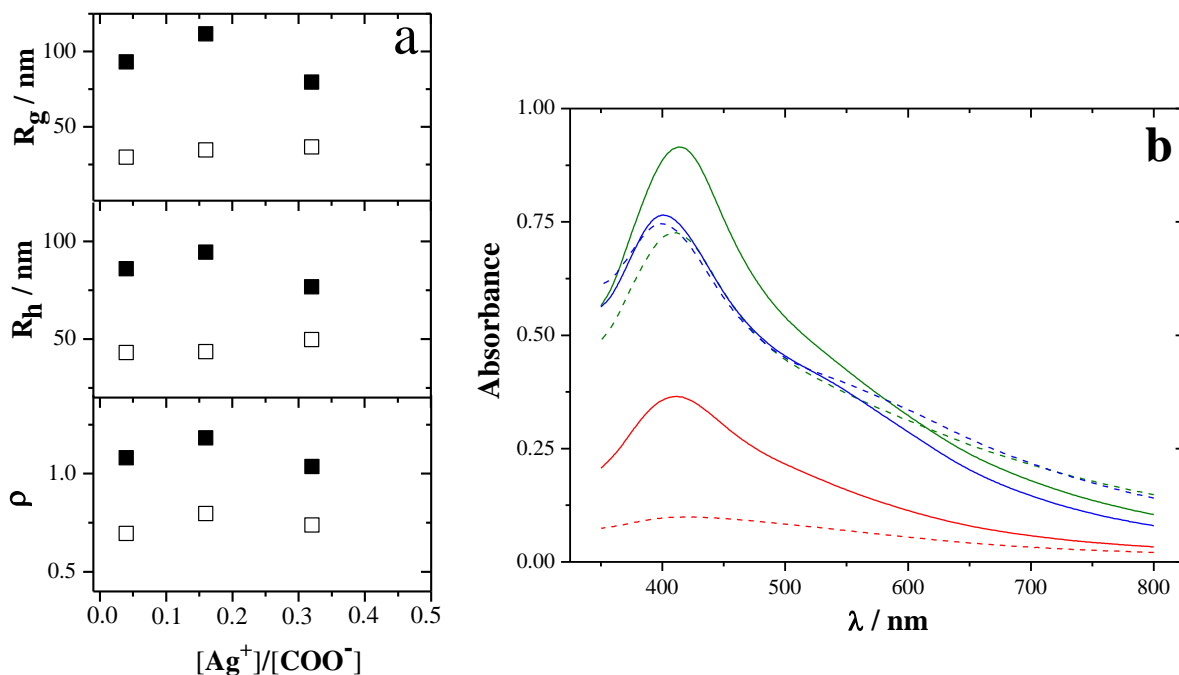
Figure 4.2.14a Radius of gyration R_g, hydrodynamic radius R_h and $\rho = R_g/R_h$ of Ag$^+$-PA solutions with [NaPA] = 2 mM after UV-exposure for t_{UV} = 4 min at [Ag$^+$]/[COO$^-$] = 0.04 and 0.16 and for t_{UV} = 2 min at [Ag$^+$]/[COO$^-$] = 0.30. Full squares correspond to aged solutions ($t_{AG} \sim$ 2 h), hollow squares to solutions exposed to UV-light without aging.

Figure 4.2.14b UV-vis absorption spectra of the Ag$^+$-PA solutions exposed to UV light for t_{UV} = 4 min at the following [Ag$^+$]/[COO$^-$] ratios: 0.04 (—); 0.16 (—); 0.30 (—). Continuous lines represent freshly prepared solutions; dashed lines represent aged solutions.

Prior to the SLS/DLS analysis solutions were diluted with aqueous 0.01 M NaNO$_3$ to [NaPA] = 1 mM and prior to the UV-vis spectroscopy to [NaPA] = 0.5 mM. In each case the [Ag$^+$]/[COO$^-$] ratios remained unchanged.

Figures 4.2.14 reveals results from SLS/DLS and the corresponding UV-vis characterization. There is a unique trend in all parameters from the SLS/DLS measurements independent of the percentage of Ag$^+$ ions in the solutions: aged samples show higher values of the radius of gyration R_g and of the hydrodynamic radius R_h after UV-exposure than the corresponding values of non-aged samples. Evidently, assemblies of Ag-NPs were generated upon UV-exposure after Ag$^+$-PA solutions were aggregating. The structure sensitive factor ρ of UV-exposed solutions without aging is close to the values of a homogeneous sphere. Corresponding values from aged samples are larger, supporting the transition from individual (compact) Ag-NPs to assemblies of Ag-NPs.

UV-vis spectra (Figure 4.2.14a) demonstrate that the maximum of the SPR bands (400 – 412 nm) do not show a significant blue or red shift with varying Ag^+ content and therefore correspond approximately to the same size of individual Ag-NPs. More prominent shoulders at $\lambda \sim 520$ and higher absorbances at $\lambda > 550$ nm for aged samples indicate an accumulation of Ag-NPs to assemblies in agreement with UV-vis spectra displayed in Figure 4.2.11. The spectra of aged samples with $[Ag^+]/[COO^-]$ ratios of 0.16 and 0.30 almost overlap (with the same extinction of SPR band) thus showing only an insignificant increase in the number of Ag-NPs per assembly with increasing the silver ion concentration.

In case of the non-aged solution with $[Ag^+]/[COO^-] = 0.04$ exposed to UV-light, a SPR peak at 400 nm is seen, which turns into a weak absorption with a barely noticeable peak at the same wavelength if the sample has been aged for 1 h before the UV-irradiation (Figure 4.2.14b). The system has a very low Ag-content which may lead to a very small number of formed Ag-NP assemblies. Therefore the SPR of the individual particles at $\lambda \approx 410$ nm overlay with the absorbance at $\lambda > 520$ nm, which may lead to such a flat spectrum.

Figure 4.2.15 shows two representative TEM micrographs from Ag^+-PA solutions exposed to UV-light without aging at $[Ag^+]/[COO^-] = 0.04$ and at 0.16, respectively. The same exposure time to UV-light of $t_{UV} = 4$ min had been applied as in the SLS/DLS and UV-vis experiments presented in Figure 4.2.14. On both TEM images there are individual Ag-NPs with a size of ca. 20-30 nm. Due to a low magnification and a small amount of images it is problematic to estimate the averaged size and the size distribution. However, Figure 4.2.15 clearly illustrates that the increase in Ag^+ concentration only influences the total number of individual Ag-NPs. Since solutions were exposed to UV-light without aging, predominantly individual Ag-NPs are observed in both experiments. In conclusion, variation of $[Ag^+]/[COO^-]$ has no significant effect on the nature of formed Ag-NPs within regime of dense unstable aggregates.
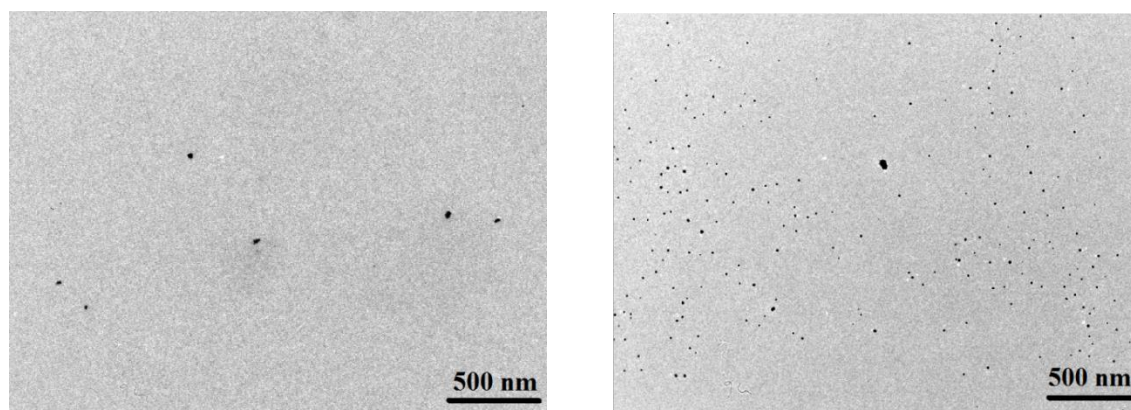
Figure 4.2.15 TEM micrographs of non-aged Ag^+-PA solutions illuminated with UV-light for $t_{UV} = 4$min. Samples contain [NaPA] = 2 mM and $[Ag^+]/[COO^-] = 0.04$ (left image), $[Ag^+]/[COO^-] = 0.16$ (right image).

4.2.5 Effect of Ag$^+$ Concentration of Dense Stable Ag$^+$-PA Aggregates on Ag-NP Formation

In the range of ratios $0.3 < [Ag^+]/[COO^-] < 2.5$ of the Ag$^+$-PA phase diagram (Figure 4.1.22) there is a regime of dense stable aggregates with a corona of dangling chains enclosing dense Ag$^+$-PA aggregates. The radius of gyration of these entities is about 25-50 nm depending on the exact NaPA concentration and the ratio of $[Ag^+]/[COO^-]$. The stability of solutions was proven by TR-SLS experiments, which showed the constancy of all molecular parameters over 45 h (Figure 4.1.15). As it has already been demonstrated in Figure 4.2.1 with a system at $[Ag^+]/[COO^-] = 0.4$ the size of entities aged before UV-exposure did not differ from the size of entities exposed to UV-light without aging thereof. However, due to a large range of $[Ag^+]/[COO^-]$ ratios of the phase regime with stable dense aggregates this issue should further be substantiated experimentally.

Figure 4.2.16 reveals results from UV-vis spectroscopy of two series of experiments after exposure to UV-light. The spectra were recorded with Ag$^+$-PA solutions at [NaPA] = 2 mM in the range of $0.4 < [Ag^+]/[COO^-] < 2.5$. The corresponding Ag$^+$-PA solutions were prepared and divided into two parts: one aliquot was illuminated with UV-light without aging of the Ag$^+$-PA solution (Figure 4.2.16a) and the other one was aged for 2 h and then illuminated with UV-light for the same t_{UV} (Figure 4.2.16b). With increasing the $[Ag^+]/[COO^-]$ ratio from 0.4 to 2.5 the SPR band shifts from 408 nm to 454 nm in case of non-aged samples and from 413 nm to 466 nm for aged samples, respectively (see inlets in Figure 4.2.16), whereas the absorbance seem to exhibit a shallow maximum at λ_{max}.
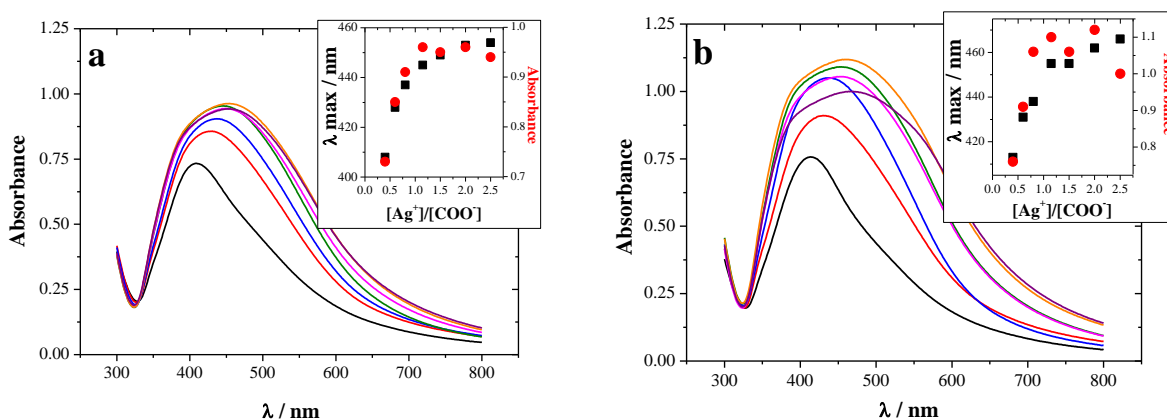
Figure 4.2.16 UV-vis absorption spectra of Ag$^+$-PA solutions after exposure to UV-light for $t_{UV} = 4$ min without aging (graph **a**) and aged for 2 h (graph **b**) prior to the UV-illumination. Ag$^+$-PA solutions contain [NaPA] = 2 mM at the following ratios $[Ag^+]/[COO^-] = 0.4$ (━), 0.6 (━), 0.8 (━), 1.15 (━), 1.5 (━), 2.0 (━), 2.5 (━). The inlets show the change in the position of the SPR band (■) and the corresponding absorbance values (●) at variable $[Ag^+]/[COO^-]$ ratios. Prior to the UV-vis spectroscopy solutions were diluted with aqueous 0.01 M NaNO$_3$ to [NaPA] = 0.5 mM while the $[Ag^+]/[COO^-]$ ratio remained unchanged.

Both series show comparable UV-spectra. The trend of λ_{max} versus $[Ag^+]/[COO^-]$ in the inlets of Figure 4.2.16 can be explained by an observation made by Henglein [163], who studied the effect of excess Ag^+ ions on Ag-NPs. He reported a decrease in absorbance and a red shift of the SPR band of Ag-NPs, if Ag^+ ions were added to solutions with Ag-NPs. He explained these variations in terms of a decrease of the electron density on the Ag-NPs surface upon chemisorption of Ag^+ ions which makes plasmonic oscillations weaker. The wavelength of the absorption maximum is proportional to the reciprocal square root of the density of free electrons in the metal particles [163]. In our systems, the source of electrons for reduction of Ag^+ ions is equal throughout all samples (Figure 4.2.16), since the concentration of PA-coils is the same in all samples. Yet the amount of Ag^+ ions available to photoreduction increases with increasing $[Ag^+]/[COO^-]$ ratio.

Combined SLS/DLS experiments on three systems with $[Ag^+]/[COO^-] = 0.8$, 1.5 and 2.5 were performed to compare properties of the solutions with dense stable Ag^+-PA aggregates exposed to UV-light without aging and after being aged for 2 h (Figure 4.2.17). The results are in agreement with UV-vis spectroscopy (Figure 4.2.16): aging of samples prior to exposure to UV-light increases R_g and R_h only slightly while the shape remains spherical ($0.5 < \rho < 0.85$), thereby excluding significant changes due to aging.
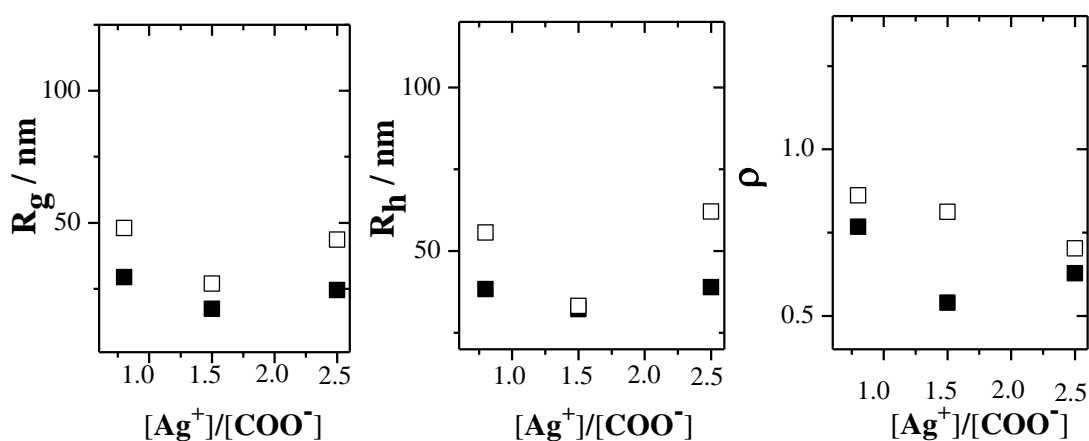
Figure 4.2.17 Radius of gyration R_g, hydrodynamic radius R_h and $\rho = R_g/R_h$ values versus the $[Ag^+]/[COO^-]$ ratio for solutions containing [NaPA] = 2 mM exposed to UV-light for $t_{UV} = 4$ min without aging (■) and aged for $t_{AG} = 2$ h (□). Prior to the SLS/DLS analysis, solutions were diluted with aqueous 0.01 M $NaNO_3$ to [NaPA] = 0.7 mM while the $[Ag^+]/[COO^-]$ ratio was kept unchanged.

Figure 4.2.16 showed a significant change of the UV-vis spectra of solutions containing Ag-NPs formed under UV-irradiation in the regime of $0.4 < [Ag^+]/[COO^-] < 0.6$. In order to reproduce this feature and further verify how the increase of Ag^+ concentration in solutions of these dense stable Ag^+-PA aggregates influences the properties of Ag-NPs, two systems with a significant difference in the ratios $[Ag^+]/[COO^-] = 0.4$ and 0.8 were chosen. Non-aged Ag^+-PA solutions were exposed to UV-light for 4 min and analysed by

SLS/DLS, UV-vis spectroscopy and TEM. Since the aging of dense stable Ag^+-PA aggregates does not show substantial changes, this effect was not considered any further.

Table 4.2.3 Size parameters from SLS/DLS characterisation of non-aged dense stable Ag^+-PA aggregates after being exposed to UV-light for $t_{UV} = 4$ min.

$[Ag^+]/[COO^-]$	R_g / nm	R_h / nm	$\rho = R_g/R_h$	var_z
0.4	33.8	35.5	0.95	0.467
0.8	31.6	29.1	1.09	0.535

As can be seen from Table 4.2.3 all size parameters are very close to each other. The polydispersity (var_z) determined at a scattering angle of $\theta = 30°$ is very high for both samples and bigger for the higher ratio of $[Ag^+]/[COO^-] = 0.8$. Figure 4.2.18a illustrates two size distribution functions calculated by means of the CONTIN analysis [113] from the field-time correlation functions at a scattering angle of $\theta = 30°$ for both samples. In case of $[Ag^+]/[COO^-] = 0.8$ the main fraction has a broader size distribution as well as a higher amount of small particles than the sample with $[Ag^+]/[COO^-] = 0.4$.

UV-vis spectra depicted in Figure 4.2.18b are satisfactory reproductions of the corresponding spectra shown in Figure 4.2.16. The SPR band for a system with $[Ag^+]/[COO^-] = 0.8$ is much broader. However, from additional DLS data (Figure 4.2.18a) we can assume that not only the excess of free Ag^+ ions on the surface of Ag-NPs can modify the SPR peak, but also a high polydispersity of hybrid entities, which size should be correlated with a size of only Ag-NPs, may influence it.
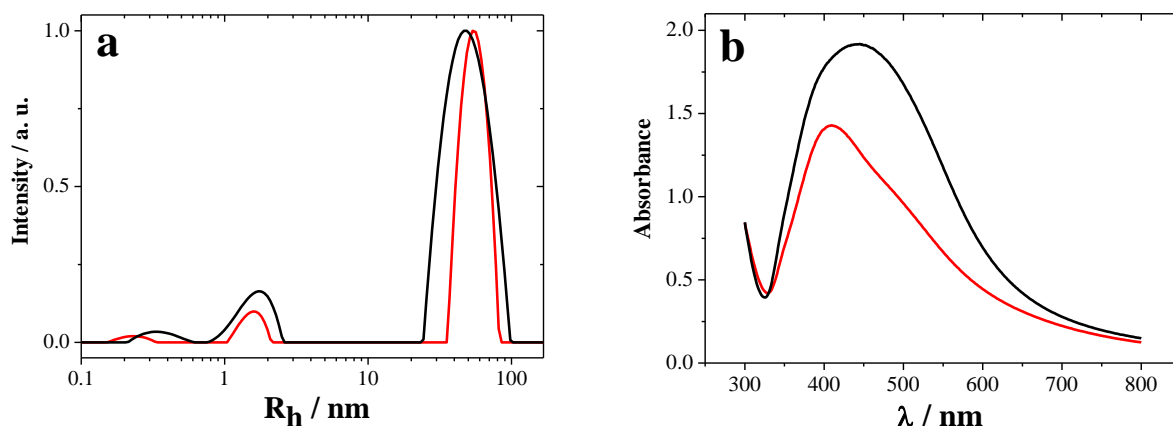
Figure 4.2.18 Size distribution (**a**) and UV-vis spectra (**b**) of two solutions containing [NaPA] = 2 mM: $[Ag^+]/[COO^-]$ = 0.40 (—) and 0.80 (—) exposed to UV-light for $t_{UV} = 4$ min. The distribution is calculated by means of the CONTIN analysis [133] of the field correlation functions measured at a scattering angle of $\theta = 30°$. Prior to the SLS/DLS analysis, solutions were diluted with aqueous 0.01 M $NaNO_3$ to [NaPA] = 0.7 mM and prior to analysis by UV-vis spectroscopy solutions were diluted with aqueous 0.01 M $NaNO_3$ to [NaPA] = 0.5 mM while the $[Ag^+]/[COO^-]$ ratio remained unchanged.

In order to clarify this issue TEM images were taken from both samples. Figure 4.2.19 shows representative TEM micrographs where the Ag-NPs are highly polydisperse for both systems. The size range of Ag-NPs is in agreement with SLS/DLS results. Although there are big particles with ca. 200 nm size, the main part consists of individual Ag-NPs of ca. 20-30 nm. The number of nanoparticles is clearly higher in case of $[Ag^+]/[COO^-] = 0.8$ (Figure 4.2.19b) which is in agreement with the higher absorbance of the respective SPR band in the UV-vis spectrum (Figure 4.2.18b).

It should be emphasized that in order to make a TEM image the sample has to be dried beforehand since the recording of TEM requires a high vacuum, whereas SLS/DLS and UV-vis spectroscopy are applied to the liquid state and characterize the situation in solution. Therefore, the large agglomerates of 2 μm size cannot be identified as assemblies of Ag-NPs since neither a slow mode, which might be correlated to such a size, was detected by DLS nor did UV-vis spectroscopy reveal a broad absorbance for such size of Ag-NPs [164]. Finally the SPR band at 443 nm refers to particles of a maximum size of 60 nm [153], which is by far smaller than a few micrometres.

For the sake of clarity reference TEM experiments were done using aqueous 1.6 mM $AgNO_3$ in 8.4 mM of $NaNO_3$ solution, which has the same Ag^+ concentration as the system with $[Ag^+]/[COO^-] = 0.8$ at $[NaPA] = 2$ mM. The stock solution of $AgNO_3$ and sample preparation were the same as in the previously described TEM experiments. Figure 4.2.20 shows a beautiful dendritic particle of several micrometres in size. The structure has a central point which might be a nucleation center of crystallisation. The similarity of the particle from Figure 4.2.20 with the large μm particle in Figure 4.2.19(b4) with respect to their morphology is striking and they are very likely to be of the same nature. As it was mentioned before, the excess of Ag^+ ions in the system with $[Ag^+]/[COO^-] = 0.8$ should be higher than in the system with $[Ag^+]/[COO^-] = 0.4$ (Figures 4.2.16 and 4.2.18b). Excessive Ag^+ ions, non-consumed in Ag-NP formation, are crystallising to micrometer size $AgNO_3$ crystals, whilst in the solution they are modifying the optical properties of Ag-NPs via chemisorption.
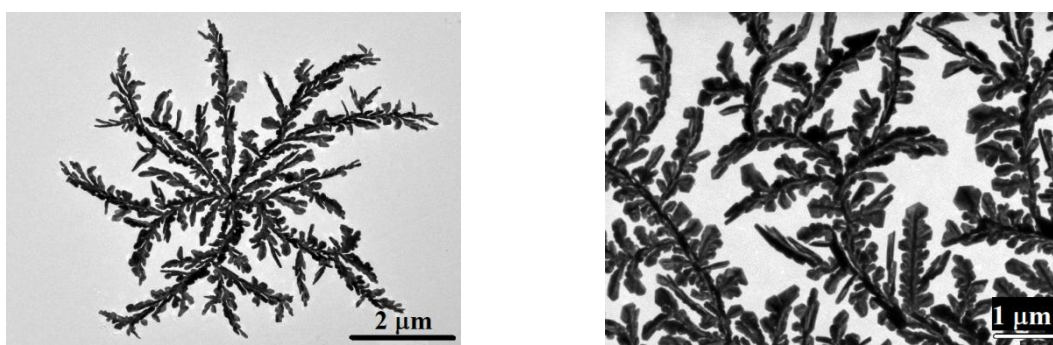
Figure 4.2.20 TEM micrographs of aqueous 1.6 mM $AgNO_3$ in 8.4 mM of $NaNO_3$ solution without exposure to UV-light.
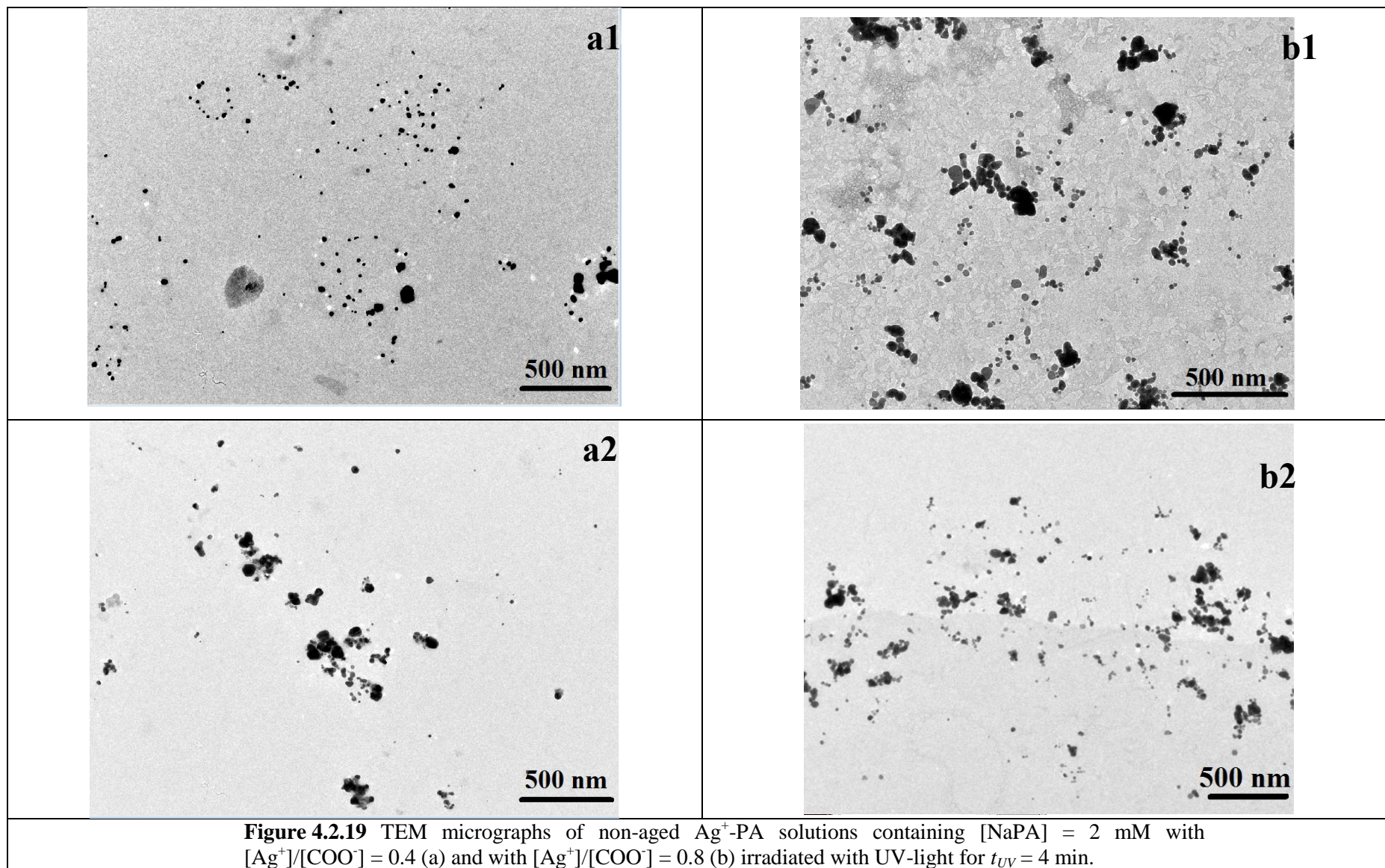
Figure 4.2.19 TEM micrographs of non-aged Ag^+-PA solutions containing [NaPA] = 2 mM with $[Ag^+]/[COO^-]$ = 0.4 (a) and with $[Ag^+]/[COO^-]$ = 0.8 (b) irradiated with UV-light for t_{UV} = 4 min.

Figure 4.2.19 TEM micrographs of non-aged Ag^+-PA solutions containing [NaPA] = 2 mM with $[Ag^+]/[COO^-]$ = 0.4 (a) and with $[Ag^+]/[COO^-]$ = 0.8 (b) irradiated with UV-light for t_{UV} = 4 min.
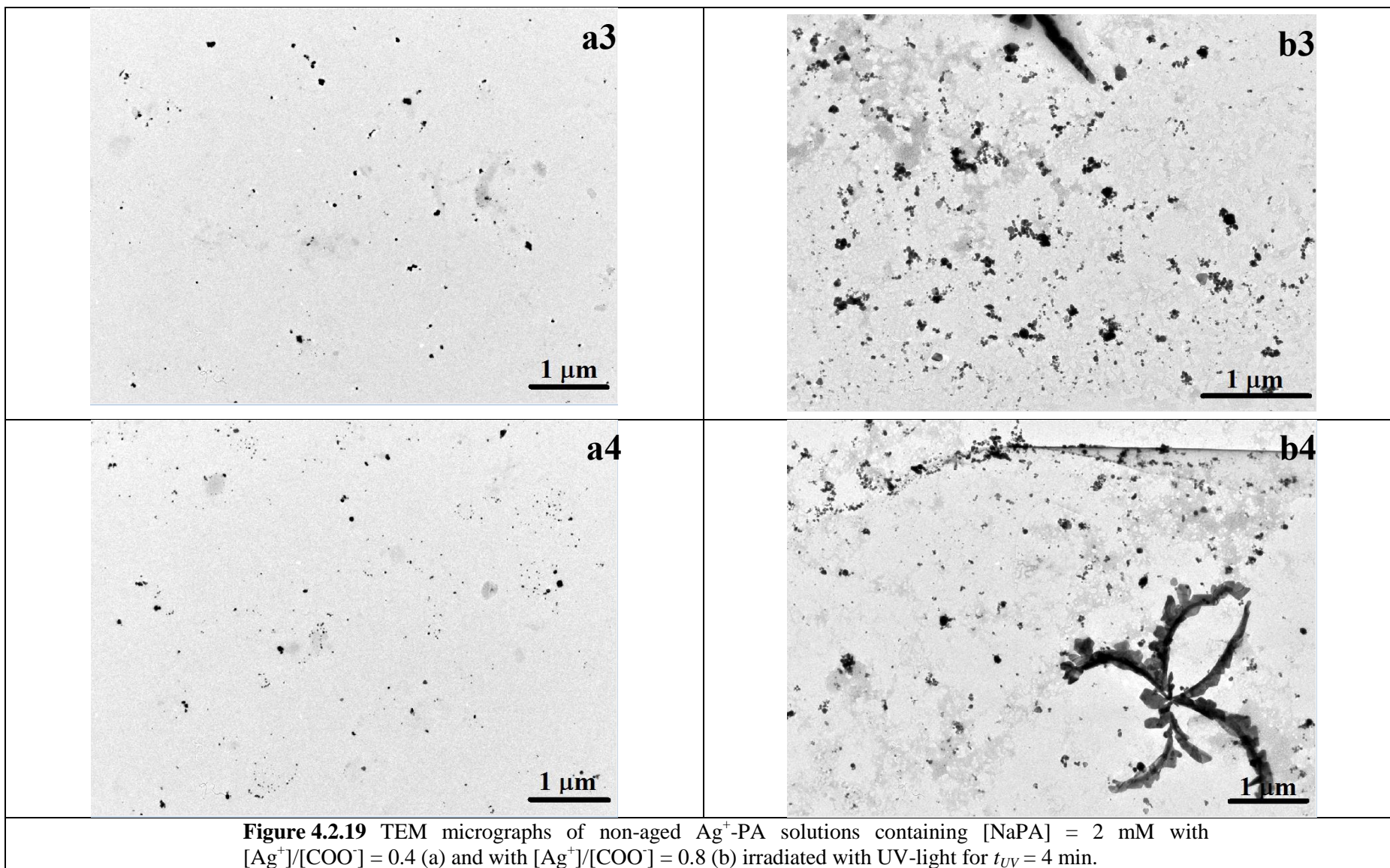
4.2.6 Impact of UV-exposure Time on Ag-NP Formation

The impact of exposure time of Ag^+-PA solutions to UV-light on the formation of Ag-NPs is an important parameter to be considered, especially in the case of dense unstable Ag^+-PA aggregates, where the photoreduction of Ag^+ leads to assemblies of Ag-NPs. Whereas the size of the assemblies in terms of R_g after UV-illumination for 7 min decreases from 135 nm to 55 nm (Figure 4.2.1), UV-exposure of Ag^+-PA aggregates for only 4 min did not give a significant change of the final size (Figures 4.2.8).

In order to analyse how the duration of the UV-light exposure time t_{UV} changes the size and properties of Ag-NPs, the following experiments were performed. Two systems with $[Ag^+]/[COO^-] = 0.16$ and 0.8 were chosen as representative examples for dense unstable and dense stable Ag^+-PA aggregates, respectively. Since the aggregation of Ag^+-PA before UV-illumination leads to the formation of Ag-NP assemblies in the successive UV-exposure, the system with $[Ag^+]/[COO^-] = 0.16$ was analysed at two sample histories: three solutions were illuminated for $t_{UV} = 2$ min, 4.5 min and 7 min without aging and the other three solutions were aged for 2 h and then exposed to UV-light for the same set of t_{UV}. Ag^+-PA solutions with $[Ag^+]/[COO^-] = 0.8$ were exposed to UV-light for 2 min, 4.5 min and 7 min only without aging. Figure 4.2.21 shows the results from SLS/DLS characterization, where the size parameters R_g and R_h along with the shape-sensitive parameter ρ are plotted versus the UV-exposure time t_{UV}. Figures 4.2.22-4.2.23 show UV-vis spectra for the same solutions.
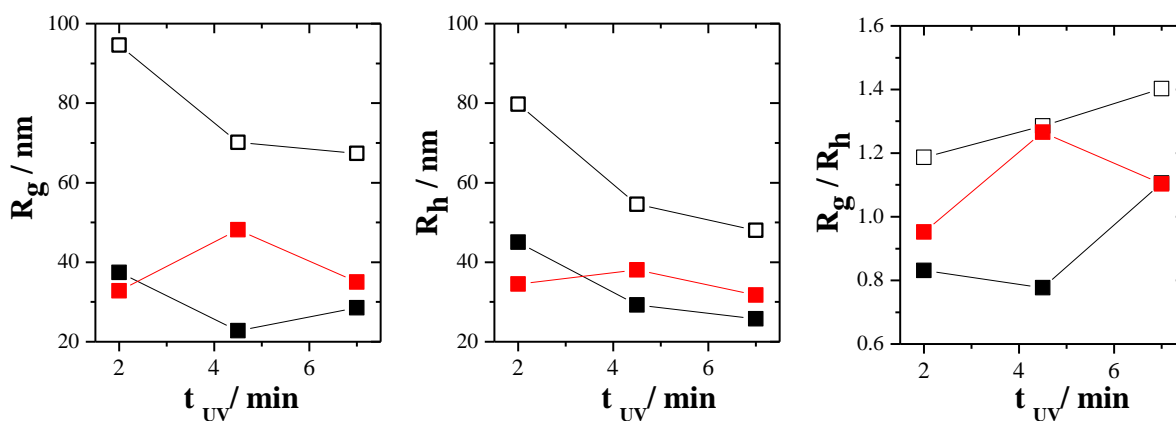
Figure 4.2.21 Radius of gyration R_g, hydrodynamic radius R_h and $\rho = R_g/R_h$ versus time of UV-illumination t_{UV} for solutions containing [NaPA] = 2 mM. The symbols denote $[Ag^+]/[COO^-] = 0.16$ without aging before exposure to UV-light (■) and with an aging time of 2 h before exposure to UV-light (□); $[Ag^+]/[COO^-] = 0.80$ without aging before exposure to UV-light for 2 h (■). Prior to SLS/DLS analysis, solutions were diluted with aqueous 0.01 M $NaNO_3$ to [NaPA] = 1 mM in case of $[Ag^+]/[COO^-] = 0.16$ and to [NaPA] = 0.7 mM in case of $[Ag^+]/[COO^-] = 0.80$.

As can be seen from Figure 4.2.21 (full symbols) the size of Ag-NPs keeps below 50 nm for both non-aged series. As it was mentioned in Chapter 4.2.2, solutions had been diluted with aqueous 0.01 M NaNO$_3$ in order to avoid multiple scattering during light scattering experiments. Hence, the apparent R_g values may increase upon dilution and the shape-sensitive parameter ρ may not be significant enough for a definition of the shape of Ag-NPs. The most reliable parameter from light scattering experiments is R_h. The net effect in the trends of R_g and R_h vs t_{UV} is significant only for $[Ag^+]/[COO^-] = 0.16$ after an aging time of 2 h where the longer UV-illumination time leads to a smaller size of hybrid entities (Ag-NPs embedded into PA-matrix). The decrease of the Ag-NP assembly size with longer UV-illumination may indicate that more Ag$^+$ ions are reduced and therefore cannot participate anymore in the interconnecting of PA-coils which host the Ag-NPs. Remarkably, that no significant changes could be observed for any of the samples once exposure times longer than $t_{UV} = 4$ min had been applied. These results are in line with experiments described in the Appendix 6.4 (Figure 6.12).

UV-vis spectra of solutions exposed to UV-light without aging (Figures 4.2.22-4.2.23) show an increase in the absorbance along with t_{UV} which indicates an increase of the total number of Ag-NPs. However, most of the absorbance increase has been accomplished already by increasing the exposure time from 2 min to 4.5 min. The absorbance maximums of the SPR bands remain at the same position independent of t_{UV} with $\lambda_{max} = 413$ nm for $[Ag^+]/[COO^-] = 0.16$ and $\lambda_{max} = 424$ nm for $[Ag^+]/[COO^-] = 0.8$, suggesting comparable size values of Ag-NPs.
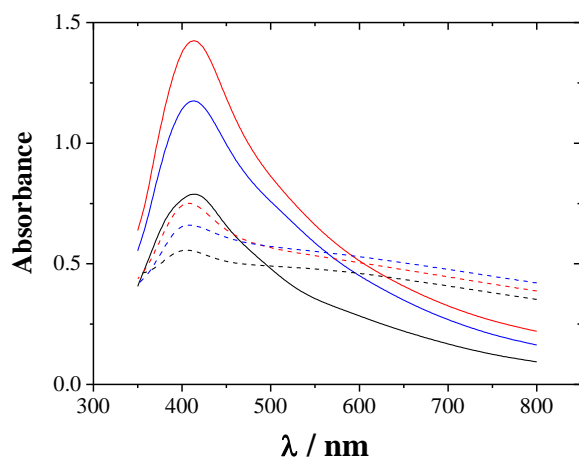
Figure 4.2.22 UV-vis absorption spectra of Ag$^+$-PA solutions after UV-illumination containing [NaPA] = 2 mM and $[Ag^+]/[COO^-]$ = 0.16 at variable UV-exposure time t_{UV}: 2 (━), 4.5 (━) and 7 (━) min. Dashed lines correspond to samples aged for 1 h before UV-exposure. Prior to the analysis by UV-vis spectroscopy, solutions were diluted with aqueous 0.01 M NaNO$_3$ to [NaPA] = 1 mM while $[Ag^+]/[COO^-]$ ratio was kept unchanged.
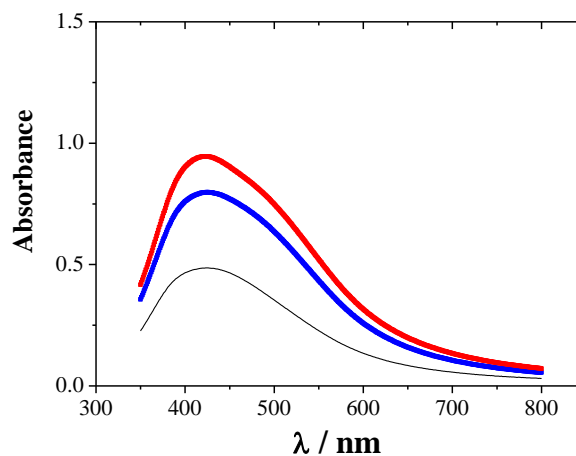
Figure 4.2.23 UV-vis absorption spectra of Ag$^+$-PA solutions exposed to UV-light without aging, containing [NaPA] = 2 mM and $[Ag^+]/[COO^-]$ = 0.80 at variable UV-exposure time t_{UV}: 2 (━), 4.5 (━) and 7 (━) min. Prior to the analysis by UV-vis spectroscopy, solutions were diluted with aqueous 0.01 M NaNO$_3$ to [NaPA] = 0.5 mM while $[Ag^+]/[COO^-]$ ratio was kept unchanged.

For the aged system with $[Ag^+]/[COO^-] = 0.16$ the position of the SPR band does not significantly depend on t_{UV} too (λ_{max} = 405-409 nm), while the absorbance of the SPR band rises when t_{UV} is increasing (Figure 5.2.22). A slight increase of the absorbance in the red region of aged Ag^+-PA aggregates exposed to UV-light at all t_{UV} indicates the presence of Ag-NP assemblies as it has been also suggested in the previous Chapters 4.2.3-4.2.4). We can assume that the number of these assemblies is growing along with a total number of individual Ag-NPs. However, it is not clear whether the number of Ag-NPs per assembly is increasing since the absorbance depends on several factors including shape, size and surrounding media of Ag-NPs in assembly [84, 152, 153] and SLS/DLS data show decrease in sizes of the overall hybrid particles (Figure 4.2.21).

4.2.7 Local Distribution of Ag$^+$ and Ag-NPs in PA-chains

ASAXS experiments were designed to investigate the distribution of the Ag^+ ions adsorbed onto the anionic PA coils and of Ag-NPs generated thereof after exposure to UV-light. It is expected to reveal a deeper insight into the evolution of size and local distribution of the Ag^+/Ag-NPs within the stabilizing PA coils.

Preparation of NaPA solutions with Ag^+ in aqueous 0.01 M $NaNO_3$ was performed at one concentration of [NaPA] = 2 mM with two different ratios $[Ag^+]/[COO^-]$ = 0.16 mM (system A from dense unstable aggregates regime) and 0.32 mM (system B from dense stable aggregates regime). The system A was analysed only after exposure to UV-light (t_{UV} = 7 min) since it is unstable before illumination. System B was analysed before and after exposure to UV-light. Results are shown in Figures 4.2.24 – 4.2.26.

An additional SAXS curve of the system B at a lower energy 12.000 keV made possible to investigate the general scattering from Ag^+-COO^- toward lower q demonstrating that Ag^+ ions assemble into small nodule-like structures (Figure 4.2.25). The solid lines of the Figures 4.2.24 and 4.2.26 represent a Porod law [165]. All scattering curves are parallel to this power law. Therefore the q^{-4}-decay indicates a smooth interface of dense Ag^+-COO^- nodules in case of the sample without UV-illumination (Figure 4.2.24) and of Ag-NPs in case of dense aggregates exposed to UV-light (Figure 4.2.26). Due to the limited q-range, of those curves which establish the energy dependent ASAXS analysis to be discussed in the following paragraphs, the size of Ag^+-COO^- nodules can be calculated only from the Kratky plot of the SAXS curve measured at 12.000 keV for system B (Figure 4.2.25) by means of the "Pseudo-Guinier Radius" R_{max} = $3^{1/2}/q_{max}$ [166], which is approximately 21 nm.
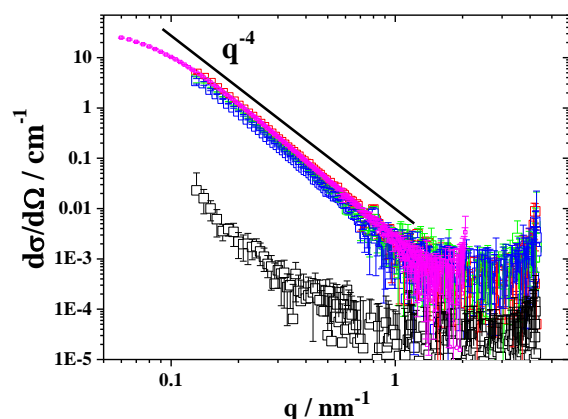
Figure 4.2.24 System B before exposure to UV-light measured at three different energies of 24.637 keV (□), 25.500 keV (□), 25.521 keV (□) and at a separate lower energy of 12.000 keV (□). The pure resonant scattering from Ag^+ cations (□) is extracted from the three SAXS curves measured at 24.637 keV, 25.500 keV and 25.521 keV.
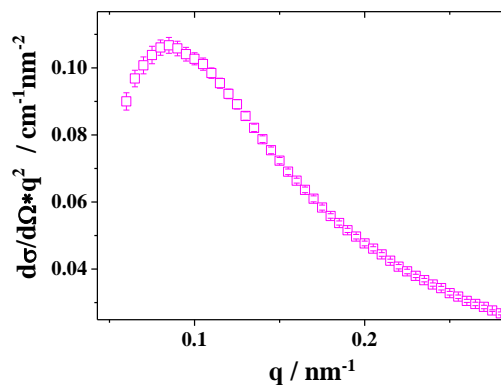
Figure 4.2.25 Kratky plot of SAXS curve at 12.000 keV of system B before exposure to UV-light.

Since ASAXS experiments showed sufficient differences in the intensities of scattering curves at three energies (Figures 4.2.24 and 4.2.26), it was possible to extract the pure resonant scattering from Ag entities (see Chapter 2.2, eq(2.38-2.40)). This will be used to analyse the distribution of the Ag^+ cations adsorbed onto the anionic PA coils prior to the exposure to UV-light and Ag-NPs generated in the domains of aggregated PA coils after the exposure to UV-light. The successful extraction of a pure resonant contribution of Ag from ASAXS can be further used to calculate the integral of the resonant invariant via eq(2.48). This resulting invariant enabled an estimation of the amount of bound Ag^+ ions and Ag-NPs within the polymer (Figure 4.2.27). Due to a restricted q-range of the ASAXS experiments, the calculation of the integral at $0 < q < 0.12$ nm was approximated as an area of a triangle. Such an approximation leads to a lower limit of the number density of the Ag^+ ions/Ag-NPs, since the maximum of the resonant invariant with respect to q is at a q-value lower than 0.12 nm (Table 4.2.4).

Table 4.2.4 Quantitative parameters of three solutions with different $[Ag^+]/[COO^-]$ ratios. $\langle v \rangle$ represents the concentration of Ag atoms in the condensed phase deduced from the experimentally accessible section of the resonant invariant (eq(2.48)).

System	[NaPA] / mM	$[Ag^+]$ / mM	$[Ag^+]/[COO^-]$	$\langle v \rangle$ / mM
B – before UV-exposure	2	0.64	0.32	0.350 ± 0.193
B – after UV-exposure	2	0.64	0.32	0.286 ± 0.129
A – after UV-exposure	2	0.32	0.16	0.228 ± 0.104
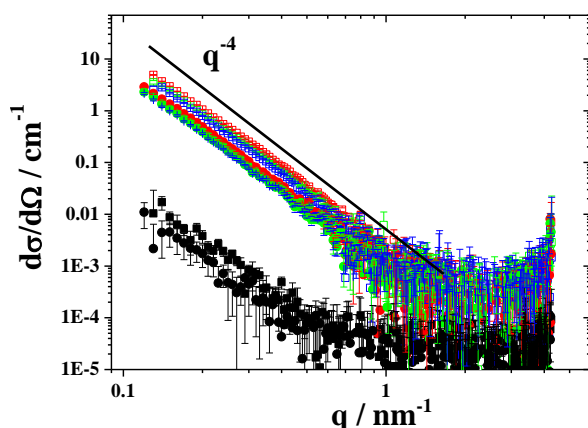
Figure 4.2.26 System A (circles) and B (squares) after exposure to UV-light measured at three different energies of 24.637 keV (●,□), 25.500 keV (●,□) and 25.521 keV (●,□). The pure resonant scattering from Ag (●,□) is extracted from the three SAXS curves measured at 24.637 keV, 25.500 keV and 25.521 keV.
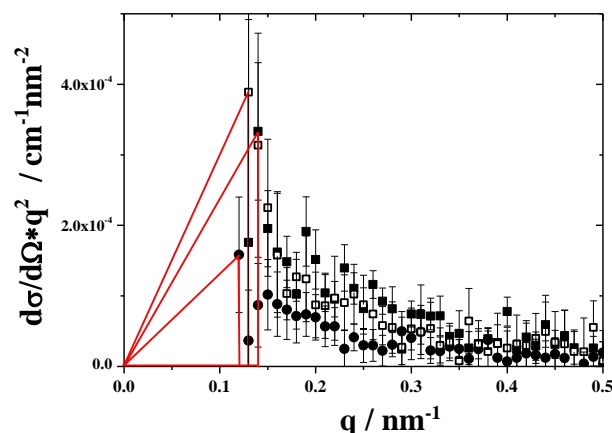
Figure 4.2.27 Kratky plots of the pure resonant scattering contribution of systems A (●) and B (□, ■). Full symbols correspond to systems exposed to UV-light, empty symbols indicate non-illuminated system B.

The concentration ⟨v⟩ of Ag sticking to PA coils for all samples is close to the averaged value of 0.29 mM, which corresponds to $[Ag^+]/[COO^-] = 0.145$. Although the standard deviation of the calculated ⟨v⟩ is ±50% and thus very high (Table 4.2.4), it may indicate that the increase of the Ag content in Ag^+-PA solutions by a factor of two does not significantly change the content of Ag-NPs in the PA matrix. The resonant invariants for system B before and after exposure to UV-light (Figure 4.2.27) overlay. Therefore we can assume that Ag-NPs are indeed formed from Ag^+ ions "arrested" by PA-coils. This supports the hypothesis of a limited capacity provided by the PA-coils in the process of the photoreduction of Ag^+ ions and probable absorption of non-consumed Ag^+ ions on the surface of Ag-NPs and thus modifying the optical response from Ag-NPs (Chapters 4.2.4-4.2.6).

4.2.8 Conclusion

The present Chapter 4.2 establishes the correlation between the state of Ag^+-PA solutions corresponding to a certain location in the phase diagram and properties of Ag-NPs formed by means of UV-exposure of the respective Ag^+-PA solutions. Two phase states have been considered: dense unstable (with $[Ag^+]/[COO^-] < 0.3$) and dense stable (with $0.3 < [Ag^+]/[COO^-] < 2.5$) Ag^+-PA aggregates. The size of hybrid particles containing both Ag-NPs and PA-coils were characterized by SLS/DLS. The Ag-NPs were analysed by UV-vis spectroscopy and TEM.

In case of dense unstable Ag+-PA aggregates ([Ag+]/[COO-] <0.3), individual Ag-NPs of the average size of ca. 25 nm were generated from non-aged Ag+-PA solutions by means of photoreduction of Ag+ ions under the UV-light. If the samples were aged before being UV-exposed, the system exhibited continuous aggregation and Ag-NPs were formed in assemblies. The size of Ag-NP assemblies depends on the aging time t_{AG} and time of UV-exposure t_{UV}. It can be assumed that the size of Ag-NP assemblies is proportional to the size of the hosting Ag+-PA aggregates, namely a longer aging time t_{AG} will lead to larger aggregates and thus to a formation of bigger Ag-NP assemblies. However, if the Ag+-PA aggregates are UV-exposed at increasingly longer time t_{UV}, more Ag+ ions will be reduced and hence the aggregated PA-coils will lose more bridging Ag+ ions. In such circumstances Ag-NP assemblies may disassemble into smaller ones. As a main result t_{AG} and t_{UV} can be considered as tools to control Ag-NP formation (Figure 4.2.28).
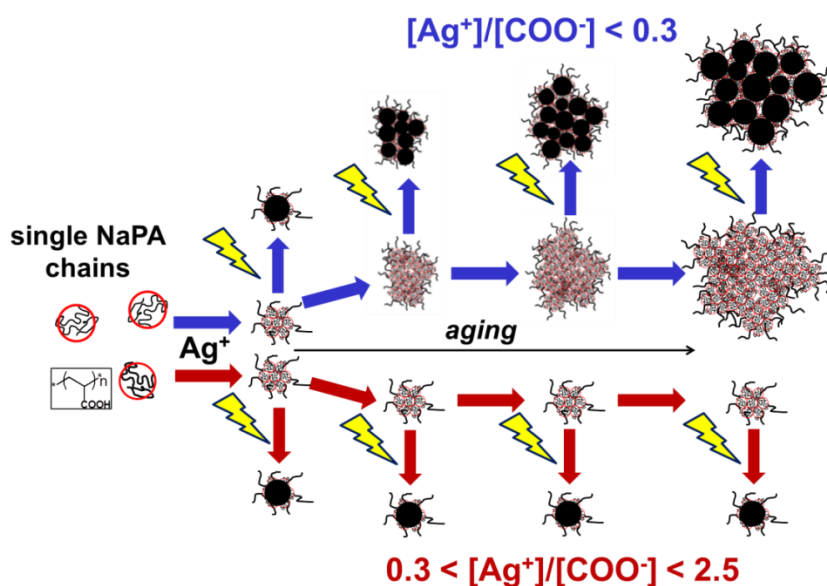
Figure 4.2.28 Illustration of the Ag-NP formation under UV-exposure to UV-light of Ag+-PA solutions belonging to dense unstable Ag+-PA aggregates ([Ag+]/[COO-] < 0.3) and dense stable Ag+-PA aggregates (0.3 < [Ag+]/[COO-] < 2.5).

Stable dense aggregates (0.3 < [Ag+]/[COO-] < 2.5) provide less options to vary the nature of Ag-NPs. The aging of Ag+-PA solutions before UV-exposure does not influence the final result. Independent of the sample history, predominantly individual Ag-NPs of ca. 25 nm in size are obtained (Figure 4.2.28). Variations of UV-exposure time increase slightly the number of Ag-NPs.

Increasing the ratio [Ag+]/[COO-] within the same phase state leads to a higher number of Ag-NPs without significant changes in their size and morphology. Since the concentration of NaPA has been kept constant along the increase of [Ag+]/[COO-], the

fixed source of electrons from carboxylic groups leads to an accumulation of excess Ag^+ ions on the surface of Ag-NPs modifying the optical properties thereof.

SAXS and ASAXS experiments reveal also a limiting capacity of PA-coils in reducing Ag^+ and successively hosting the Ag-NPs. Increasing the $[Ag^+]/[COO^-]$ ratio twice does not significantly vary the content of Ag. The size of Ag^+-COO^- nodules before UV-illumination is of comparable size to the Ag-NPs being formed thereof by means of the UV-exposure. This observation once again emphasises the essential role of polyacrylate in Ag-NP formation and demonstrates the correlation between the size of Ag^+-PA aggregate and the size of the individual/assembled Ag-NPs.

4.3 Specific Interactions between Ag^+, Ca^{2+}, Mg^{2+} Ions and Spherical Polyacrylate Brushes

Specific interactions between linear PA-coils and Ag^+ ions (Chapter 4.1) resulted in a rich diversity of entities described by a phase diagram (Figure 4.1.22). The latter one turned out to serve as a tool to control formation of Ag-NPs (Chapter 4.2). As a next step we decided to modify the PA-matrix by attaching PA-coils to a solid PS-core forming spherical polyacrylate brushes (SPB) thereof. This may extend our knowledge on the interaction pattern between COO^--groups and monovalent Ag^+ ions by looking at a morphologically different polyacrylate system such as SPB, which can also be used in Ag-NP formation (Chapter 4.4).

Figure 4.3.1 shows the comparison of the PA-shell shrinking in $AgNO_3$ and $NaNO_3$ aqueous solutions. In both cases the thickness of the PA-layer L was calculated via eq(3.5) with data from DLS measurements. In spite of the fact that the Ag^+ ions like Na^+ ions are monovalent, the shrinking of the PA-shell occurs at a much lower Ag^+ concentration. The trends are shifted by a factor of 10^{-3} if Na^+ ions are exchanged by Ag^+.
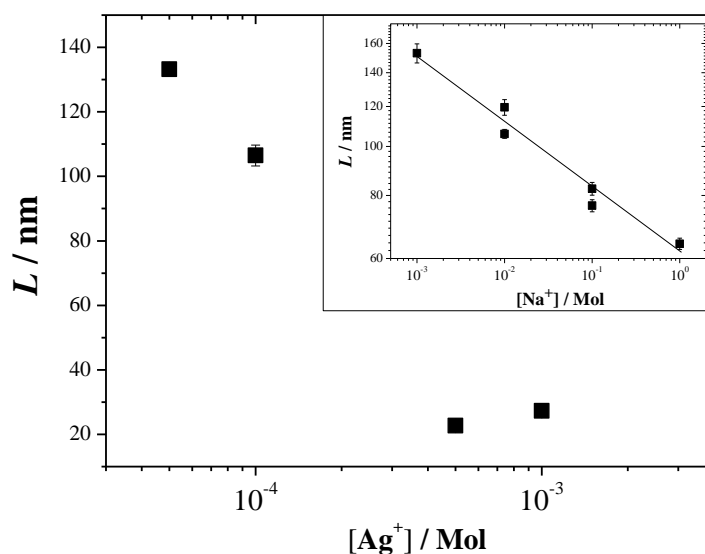
Figure 4.3.1 Thickness L of the PA-layer in SPB(HMEM) solutions at a pH of 7 as a function of $AgNO_3$ concentration. The inlet represents the thickness L of the PA-layer of SPB(HMEM) as a function of $NaNO_3$ concentration at a pH of 11.

Such a significant effect of Ag^+ ions on the PA-layer invokes further experiments and a clarification of the following aspects. (i) Since SPBs are very sensitive to pH and ionic strength, analyses of Ag^+-SPB solutions at variable pH and inert salt level may provide more information about the driving force for the shrinking of PA-shells in the presence of monovalent Ag^+ ions. (ii) As has been outlined in Chapter 4.1 the ratio between COO^--

groups and Ag$^+$ ions is a crucial factor in the formation of Ag$^+$-PA aggregates of a certain nature. It could be interesting to compare [Ag$^+$] at which the phase separations occur in Ag$^+$-PA and Ag$^+$-SPB systems. (iii) Since the length and grafting density of PA-chains chemically attached to the PS-cores can be varied (Table 3.7), three systems differing by these parameters will be tested with respect to their PA-shell shrinking in the presence of Ag$^+$. In order to enable a systematic study more than three types of SPB should be investigated. However, we believe that the comparison of three systems at least can give a general qualitative analysis of Ag$^+$-SPB systems. (iv) It is also worthwhile to compare the shrinking of the PA-shells induced by Ag$^+$ ions with the shrinking of the PA-layer induced by divalent metal ions such as Ca^{2+} and Mg^{2+}. (v) The phase behaviour of SPB in the presence of Ag$^+$ and Ca^{2+} can be compared to the respective phase behaviour of linear PA-chains.

The synthetic route toward SPB and their characterisation are described in detail in the Chapters 3.5-3.7.

4.3.1 Ag$^+$ induced Shell Shrinking at variable Ionic Strength

To consider the effect of Ag$^+$ ions on the shrinking of the PA-shell at variable ionic strength, two SPB(HMEM) stock solutions were used to prepare two series of the Ag$^+$-SPB solutions at fixed [COO$^-$] and variable [Ag$^+$]. One SPB(HMEM) stock solution was prepared using aqueous 0.01 M NaNO$_3$ as a solvent and the other one was based on salt free water. Details of the Ag$^+$-SPB solution preparation and of the light scattering measurements thereof are given in Chapter 3.8. Results of the DLS analysis are shown in Figure 4.3.2, where the thickness L of the PA-shell is plotted versus [Ag$^+$].

The threshold value, denoted as [Ag$^+$]$_{shr}$ at which the collapse of the PA-layer is completed, was estimated in the following way: at first we averaged all L values lie on the plateau in order to establish the corresponding L_{pl} (see Figure 4.3.2). After that we denote the lowest concentration of Ag$^+$ ions as [Ag$^+$]$_{pl}$ at which measured L still belongs to the plateau regime with ±6 nm. The closest concentration of Ag$^+$ ions to [Ag$^+$]$_{pl}$ where the value of L did not reach L_{pl} was denoted as [Ag$^+$]*. The mean value between [Ag$^+$]* and [Ag$^+$]$_{pl}$ was established as the concentration of Ag$^+$ ions at which the collapse of PA-shell can be completed ([Ag$^+$]$_{shr}$). The difference between [Ag$^+$]* and [Ag$^+$]$_{pl}$ was taken as the estimated uncertainty of [Ag$^+$]$_{shr}$ (Figure 4.3.2).

Full shrinking of the PA-layer of SPB occurs at [Ag$^+$]$_{shr}$ = 0.25 mM in both series. Even when the electrostatic interactions are screened by the inert salt (0.01 M NaNO$_3$), the amount of the Ag$^+$ ions inducing the shell shrinking is the same as in the salt free SPB solution, where only a few percent of the counterions are osmotically active (can leave the brush layer). We assume that in both cases as soon as Ag$^+$ ions are in the SPB solution they

are immediately "trapped" within the flexible PA-coils due to the strong complexation and inter-coil bridging, which causes the PA-shell shrinking at such a low $[Ag^+]_{shr}$.
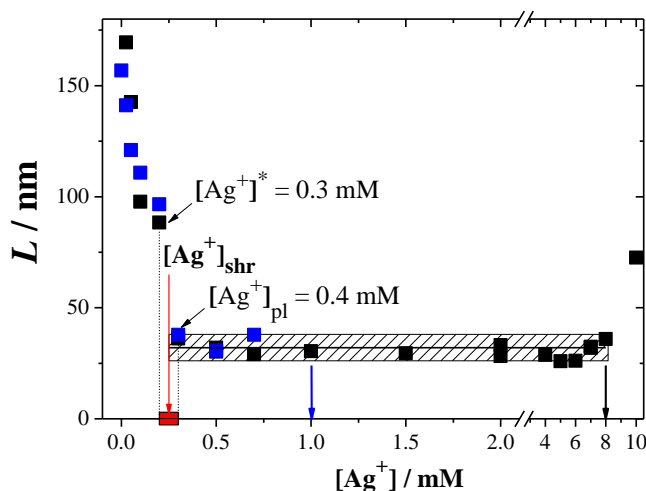
Figure 4.3.2. Thickness L of the PA-layer of SPB(HMEM) in Ag^+-SPB solutions at a pH of 6.5 as a function of $AgNO_3$ concentration in salt free solution (■) and in 0.01 M $NaNO_3$ (■). The concentration of $[COO^-]$ is 0.1 mM. The black horizontal line corresponds to the plateau value $L_{pl} = 32$ nm of the collapsed PA-layer. The shaded area indicates the standard deviation of L_{pl} which is ±6 nm. Blue and black arrows pointing down denote $[Ag^+]_c$ in salt free and in 0.01 M $NaNO_3$, respectively. The red arrow shows the $[Ag^+]_{shr}$ where the collapse of the PA-layer is completed, the red area on the x-axis indicates an experimental uncertainty of $[Ag^+]_{shr}$.

Coagulation of latex particles in the absence of inert salt, we call this situation as salt free solution, sets in at $[Ag^+] \approx 1$ mM, whereas the Ag^+-SPB solutions in 0.01 M $NaNO_3$ remain stable up to $[Ag^+] \approx 8$ mM. The DLS characterisation of Ag^+-SPB solutions in 0.01 M $NaNO_3$ at $[Ag^+] = 8$ mM identified a slight increase of R_h and which indicates the onset of aggregation of SPB. In fact, Ag^+-SPB solutions with $[Ag^+] \geq 8$ mM precipitated after a few hours. Since coagulation points to an effective attraction between the latex particles [167] one of the possible explanation for better stability of Ag^+-SPB solutions in 0.01 M $NaNO_3$ is the exchange pressure of Na^+ ions, which liberates a certain fraction of Ag^+ ions from the PA-layer preventing the coagulation to easily set it.

From these results we can conclude that additional salt in Ag^+-SPB solutions leads to a considerable shift of the coagulation threshold ($[Ag^+]_c$) but has no effect on the minimal Ag^+ concentration ($[Ag^+]_{shr}$) which induces full shrinking of the PA-shell.

4.3.2 Ag$^+$ induced Shell Shrinking at variable pH

The behaviour of SPBs consisting of PA-chains strongly depends on the pH value and ionic strength [46, 49, 51]. Considering the PA-layer of the brush in the presence of the inert salts (NaCl) at variable pH we have the following situation. At low pH the carboxyl groups of the PA-chains are virtually uncharged and the chains are only partially stretched. With increasing the pH, charges are gradually introduced and the osmotic pressure of the condensed counterions together with the electrostatic repulsions within the PA-chains swells the brush. At the same time with increasing the concentration of monovalent metal ions, as for example Na$^+$, the SPB shrinks due to a screening of charged carboxyl groups by these cations. At high pH, where the degree of dissociation of carboxylic groups is higher, this effect in terms of the change in L is more pronounced [51].

In order to see how a very low pH, where anionic PA-chains are hardly dissociated, may influence the Ag$^+$ induced shrinking of the PA-shell, we performed DLS measurements of the Ag$^+$-SPB solutions where the pH of SPB(HMEM) solutions was carefully adjusted to 4.4 and 6.5 before mixing with Ag$^+$ ions. The concentration of positive charges in Ag$^+$-SPB solutions was set to 0.01 M. The Ag$^+$-SPB solutions contained 0.05 mM of carboxylic residues were analysed by DLS. Details on the solution preparation and on the DLS characterisation are given in Chapter 3.8. Results of two experimental series are shown in Figure 4.3.3.

In Figure 4.3.3 a shrinking of the PA-layer was observed at $[Ag^+]_{shr} = 0.25$ mM when the pH of the solution was 6.5 and at $[Ag^+]_{shr} = 0.625$ mM in the solution with a pH of 4.4. The $[Ag^+]_{shr}$ values were estimated in the same way as in Chapter 4.3.1. The reason why at lower pH the shell shrinking in SPB solutions occurs at higher Ag-content may be the following: at high pH the PA-coils are almost fully dissociated and provide more "activated" carboxylic groups, which can be involved into the inter-particular bridging with Ag$^+$ ions immediately as the latter ones are in the solutions. Whereas when the pH is low and there are less neutralized carboxylic groups, Ag$^+$ ions sticking to PA-coils have to compete with protons within the PA-shell.

All Ag$^+$-SPB solutions were monitored by DLS for four days in order to check the stability of the Ag$^+$-SPB solutions in terms of their size. Figure 4.3.4 shows that the thickness of the PA-layer L does not vary with sample age and latices are stable over a long time.
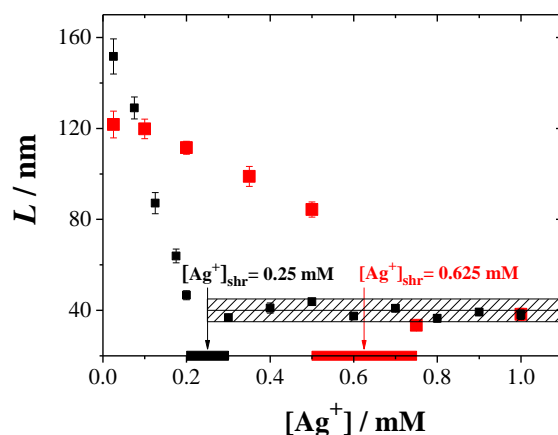
Figure 4.3.3. Thickness *L* of the PA-layer of SPB(HMEM) in solutions at a pH of 4.4 (■) and of 6.5 (■) as a function of $AgNO_3$ concentration in 0.01 M $NaNO_3$. The concentration of $[COO^-]$ is 0.05 mM. The black horizontal line corresponds to the plateau value $L_{pl} = 40$ nm of the collapsed PA-layer. The shaded area indicates the standard deviation of L_{pl} which is ±5 nm. Black and red arrows indicate $[Ag^+]_{shr}$ at a pH of 6.5 and at a pH of 4.4, respectively. The red and black area on the x-axis shows the $[Ag^+]_{shr}$ range where collapse of the PA-layer is completed.
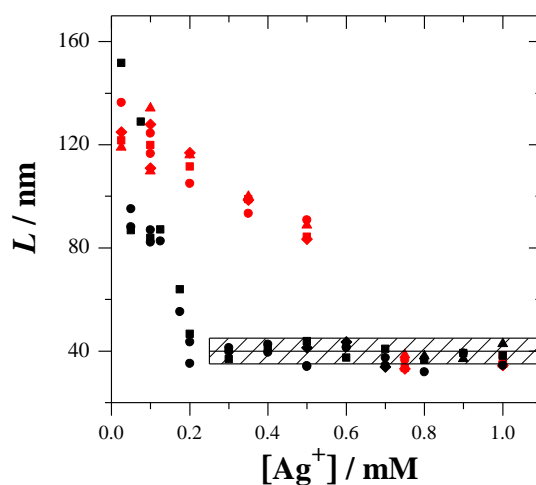
Figure 4.3.4. Thickness *L* of the PA-layer of SPB(HMEM) in solutions at a pH of 4.4 (■) and of 6.5 (■) as a function of $AgNO_3$ concentration in 0.01 M $NaNO_3$. The concentration of $[COO^-]$ is 0.05 mM. The black horizontal line corresponds to the plateau value $L_{pl} = 40$ nm of the collapsed PA-layers. The shaded area indicates the standard deviation of L_{pl} which is ±5 nm. Symbols indicate that DLS analysis was performed on the 1st (■), 2nd (●), 3rd (▲) and 4th (◆) day after the solution had been prepared.

126

4.3.3 Ag⁺ induced Shell Shrinking in Three SPB Types and Comparison of the Solubility Behaviour in Ag⁺-SPB and Ag⁺-PA Solutions

The PA-shell shrinking in the presence of Ag^+ was analysed with three types of SPB, which differ by the counter length of the grafted PA-chains L_c and by the grafting density σ (Table 3.7). Each of the SPB solutions was prepared by diluting a small amount of latices with aqueous 0.01 M $NaNO_3$ to the final concentrations of $[COO^-]$ = 0.05, 0.15 and 0.25 mM (see Chapter 3.8). The pH of the SPB solutions was adjusted in each case to 6.5. In these series of experiments we want to find out whether the brush parameters and concentrations can influence on $[Ag^+]$ range at which a full shrinking of the PA-shell is induced.

Figure 4.3.5 shows three graphs one for each SPB, where the thickness L of the PA-shell analysed by DLS is plotted versus the Ag^+ concentration. Each graph shows plots for three colloid concentrations $[COO^-]$. As expected, in all Ag^+-SPB solutions the minimal concentration of Ag^+ ions ($[Ag^+]_{shr}$) where the shrinking of PA-layer is completed, is shifted to higher values with increasing the monomer concentration or, in other words, with increasing number density of the SPB [167].

Figure 4.3.5 Thickness L of the PA-layer in Ag^+-SPB solutions at a pH of 6.5 as a function of $AgNO_3$ concentration in 0.01 M $NaNO_3$. Three types of SPB in the presence of Ag^+ ions are analysed: SPB(HMEM) – graph **a**, SPB(ABP) – graph **b**, SPB(BA) – graph **c**. The concentration of $[COO^-]$ is 0.05 mM (squares), 0.15 mM (circles) and 0.25 mM (triangles). The black horizontal lines correspond to the plateau values L_{pl} of the collapsed PA-layers: 40 nm (**a**), 17 nm (**b**) and 29 nm (**c**). The shaded area indicates the standard deviation of L_{pl} which is ±5 nm.

The absolute thickness of the collapsed PA-layer of SPB(BA) is ca. 29 nm (Figure 4.3.5(c)) which is smaller than the thickness $L_{pl} = 40$ nm of the collapsed PA-shell of SPB(HMEM) (Figure 4.3.5(a)). Since SPB(HMEM) and SPB(BA) have PA-chains similar in their contour length (L_c), the difference is probably caused by the size of the PS-core, which is bigger in case of SPB(BA), and by the grafting density of the PA-chains, which is higher for SPB(HMEM) (Table 3.7). Accordingly, the shrunk PA-shell should be thinner in case of Ag$^+$-SPB(BA) solutions compared to Ag$^+$-SPB(HMEM) solutions.

In case of the SPB(ABP) the thickness of the fully collapsed PA-layer induced by Ag$^+$ ions is $L_{pl} = 17$ nm (Figure 4.3.5(b)) and hence even smaller than that of the two others collapsed shells. This effect should be due to the length of PA-chains L_c (Table 3.7), which is shorter than in SPB(HMEM) and SPB(BA). At the same time, the size of the PS-core of SPB(ABP) is equal to the size of the PS-core of SPB(BA) and bigger than the size of the PS-core of SPB(HMEM). Hence, we can conclude that the thickness L of the PA-shell collapsed by Ag$^+$ ions is influenced by the brush parameters such as L_c, σ and $R_{h,PS}$ (Table 3.7).

In order to estimate the [Ag$^+$]$_{shr}$ values, at which the collapse of the PA-layer begins at variable [COO$^-$] and to further compare these values among the three SPBs the same procedure as in Chapter 4.3.1 was carried out. Table 4.3.1 summarises the results of the calculations made from the data presented in Figures 4.3.5.

Table 4.3.1 Parameters defining the thresholds of shell shrinking in Ag$^+$-SPB solutions in 0.01 M NaNO$_3$ at a pH of 6.5.

SPB type	[COO$^-$] / mM	[Ag$^+$]$_{pl}$ / mM	[Ag$^+$]* / mM	[Ag$^+$]$_{shr}$ / mM	Estimated uncertainty of [Ag$^+$]$_{shr}$
SPB(HMEM)	0.05	0.2	0.175	0.1875	0.025
	0.15	0.4	0.3	0.35	0.1
	0.25	0.6	0.4	0.5	0.2
SPB(ABP)	0.05	0.25	0.175	0.2125	0.075
	0.15	0.4	0.3	0.35	0.1
	0.25	0.5	0.25	0.375	0.25
SPB(BA)	0.05	0.4	0.25	0.325	0.15
	0.15	0.6	0.45	0.525	0.15
	0.25	0.75	0.5	0.625	0.25

Figure 4.3.6(a) shows the resulting diagram where the minimal threshold concentration of Ag$^+$ ions at which the collapse of PA-shell is considered to be completed [Ag$^+$]$_{shr}$ are plotted versus [COO$^-$]. The estimated uncertainties of [Ag$^+$]$_{shr}$ values are comparably high due to the broad increments (steps) of [Ag$^+$] in comparison to their absolute values. Nevertheless, there is a slight dependence of [Ag$^+$]$_{shr}$ on [COO$^-$] which agrees in all three

types of Ag^+-SPB solutions: in order to complete the shrinking of the PA-layer at higher SPB concentration more Ag^+ ions should be added. The difference between the threshold values among three different SPB types is within the experimental uncertainties and can be considered as negligible. Figure 4.3.6(b) shows the same data as in Figure 4.3.6(a) with the $[Ag^+]_{shr}$ exchanged by the $[Ag^+]_{shr}/[COO^-]$ ratio, calculated in according to used $[COO^-]$ in each series of experiments. For all Ag^+-SPB solutions the trend of the PA-shell shrinking with respect to $[Ag^+]/[COO^-]$ ratio is reversed: the shrinking of PA-layer is shifted to smaller $[Ag^+]/[COO^-]$ ratios with increasing the monomer concentration reaching a constant value of ca. 2-3.
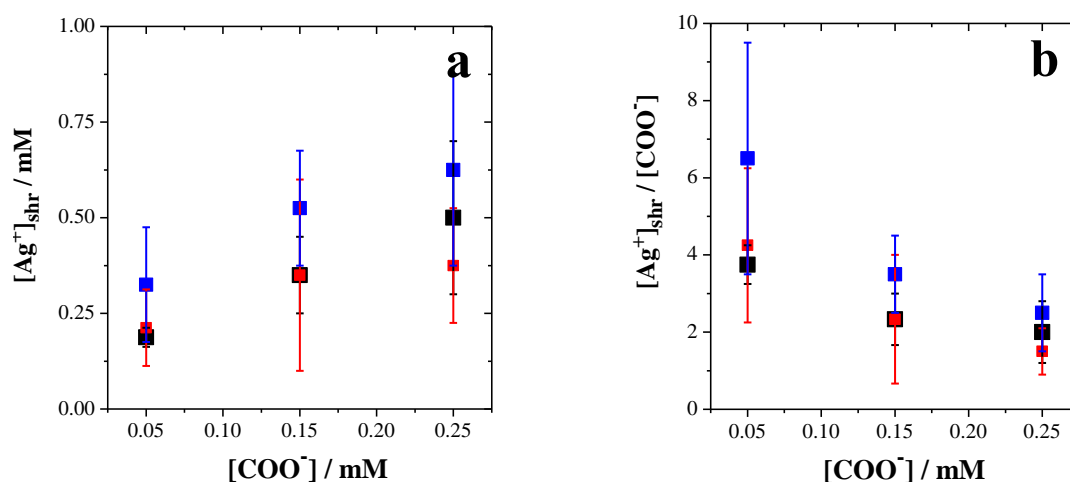
Figure 4.3.6 The Ag^+-SPB diagrams where $[Ag^+]_{shr}$ (graph **a**) and $[Ag^+]_{shr}/[COO^-]$ (graph **b**) is plotted versus the SPB concentration $[COO^-]$ for Ag^+-SPB solutions in 0.01 M $NaNO_3$ at a pH of 6.5 for three types of SPBs: SPB(HMEM) (■), SPB(ABP) (■) and SPB(BA) (■).

All Ag^+-SPB solutions were stable over days. Figure 4.3.7 shows the results from DLS measurements of Ag^+-SPB solutions at $[COO^-] = 0.25$ mM monitored for three days. The thicknesses of PA-layers at a certain value of $[Ag^+]$ remain constant.

From the data presented in Figure 4.3.2 we know that Ag^+-SPB solutions in 0.01 M $NaNO_3$ precipitate at $[Ag^+]_c \approx 8$ mM and the PA-shell is fully shrunk already at $[Ag^+]_{shr} = 0.25$ mM. The coagulation threshold was determined only for the Ag^+-SPB solutions with $[COO^-] = 0.1$ mM, however, from Figures 4.3.6, we learned that $[Ag^+]_{shr}$ at different $[COO^-]$ concentrations and types of SPB shift only slightly. Thus, we can assume that in the range of $0.05 \leq [COO^-] \leq 0.25$ mM the coagulation threshold will be located at a similar Ag^+ concentration (ca. 8 mM). Hence, the concentration range of $0.25 < [Ag^+] < 8$ mM corresponds to the regime of stable Ag^+-SPB solutions, where the PA-layer of SPB is fully shrunk but the latex particles are still separated and do not coagulate.
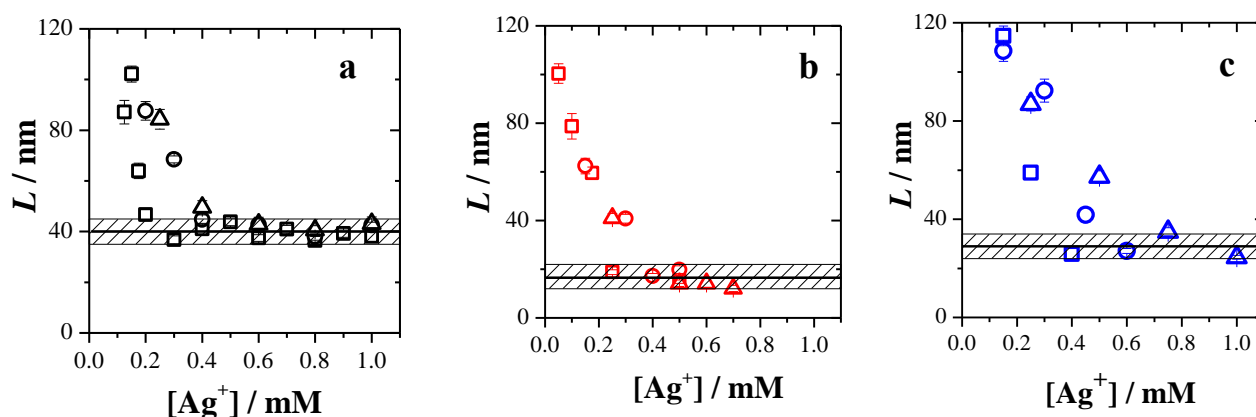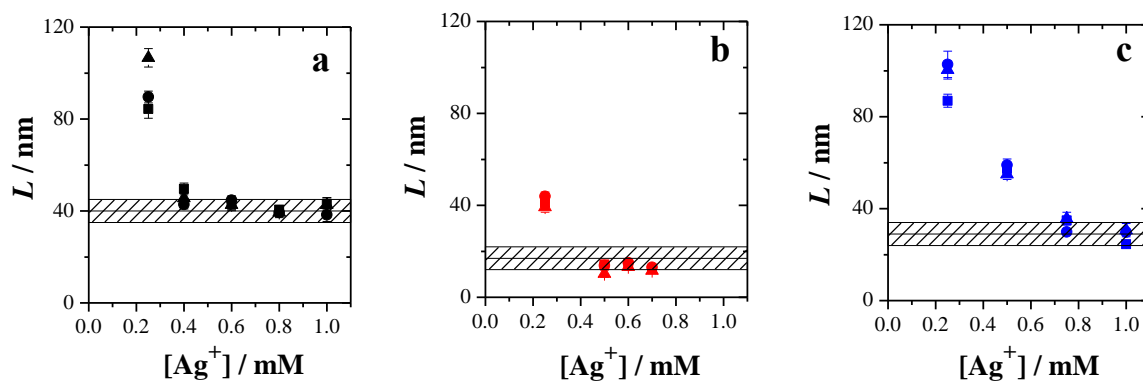
Figure 4.3.7 Thickness L of the PA-layer in Ag^+-SPB solutions at a pH of 6.5 as a function of $AgNO_3$ concentration in 0.01 M $NaNO_3$. Three types of SPB in the presence of Ag^+ ions are analysed: SPB(HMEM) – graph **a**, SPB(ABP) – graph **b**, SPB(BA) – graph **c**. The concentration of $[COO^-]$ is 0.25 mM. The black horizontal lines correspond to the plateau values L_{pl} of the collapsed PA-layers: 40 nm (a), 17 nm (b) and 29 nm (c). The shaded area indicates the standard deviation of L_{pl} which is ±5 nm. Symbols indicate that DLS analysis was performed on the 1st (squares), 2nd (circles), 3rd (triangles) day after the solution preparation.

It is not possible to characterize Ag^+-SPB solutions at $[COO^-] > 0.25$ because of the high turbidity. Therefore, we could not perform DLS experiments in the same range of $[COO^-]$ as we have done with linear Ag^+-PA solutions (Chapter 4.1), where it was varied between 0.64 mM and 5.12 mM. However, we established a coagulation threshold by visibility study, which further can be compared to the precipitation threshold of linear PA-chains in the presence of Ag^+.

Figure 4.3.8 shows the results from visual observations of Ag^+-SPB solutions, scrutinized in the range of the monomer concentrations of $1 \leq [COO^-] \leq 4$ mM and in the range of Ag-content of $8 \leq [Ag^+] \leq 15$ mM, presented as a phase diagram. Vials with 2 mL of Ag^+-SPB solutions were monitored during one month. In order to estimate the coagulation concentration $[Ag^+]_c$ we took the mean value between highest concentration of Ag^+ ions at which solutions are still stable ($[Ag^+]_1$) and lowest concentration of Ag^+ ions at which the latex coagulates ($[Ag^+]_2$). The difference between these two values is taken as the estimated uncertainty of $[Ag^+]_c$. Table 4.3.2 summarises parameters defining $[Ag^+]_c$ for Ag^+-SPB solutions from Figure 4.3.8. From this set of data we see that the coagulation threshold at higher SPB concentration is shifted toward higher Ag^+ concentration and is defined in the range of $7.5 \leq [Ag^+]_c \leq 9.5$ mM.

Table 4.3.2 Parameters defining coagulation of Ag^+-SPB(HMEM) solutions in 0.01 M $NaNO_3$ at a pH of 6.5.

[COO$^-$] / mM	[Ag$^+$]$_1$ / mM	[Ag$^+$]$_2$ / mM	[Ag$^+$]$_c$ / mM	Estimated uncertainty of [Ag$^+$]$_c$
1	7	8	7.5	1
2	8	9	8.5	1
3	8	9	8.5	1
4	9	10	9.5	1
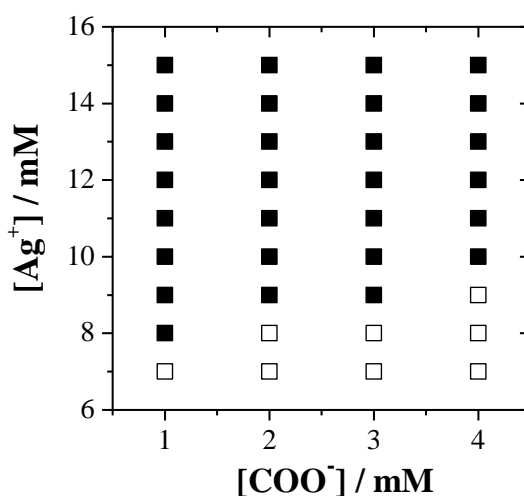
Figure 4.3.8 Results from visual observations on Ag^+-SPB solutions in 0.01 M $NaNO_3$ at a pH of ca. 6.5. Full squares denote a coagulation of latex in Ag^+-SPB solutions, whereas empty squares correspond to stable Ag^+-SPB solutions.

We can compare the obtained shrinking and coagulation thresholds of Ag^+-SPB solutions with the respective boundaries of solutions with linear Ag^+-PA thereof. Figure 4.3.9 shows a [Ag$^+$]-[COO$^-$] phase diagram where the phase behaviour of two PA-systems in the presence of Ag^+ ions are presented. Both of them have PA-chains, however in one case they are homogeneously distributed (linear PA-chains) and in the other case they are first of all much shorter and, secondly, chemically attached to a solid PS-core (SPB).
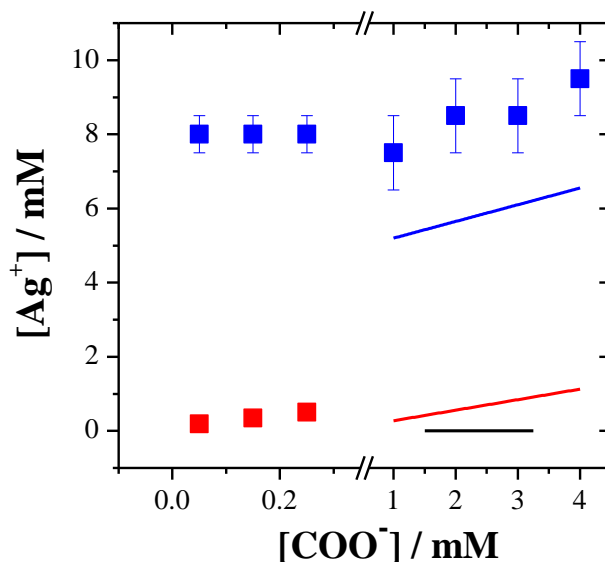
Figure 4.3.9 Results from the visual observations and the DLS experiments on Ag^+-SPB(HMEM) solutions in 0.01 M $NaNO_3$ at a pH of 6.5: PA-shell shrinking threshold (■) with data from Figure 4.3.6a and coagulation threshold (■) with data from Figure 4.3.8. Solid lines indicate phase boundaries of solutions of linear Ag^+-PA in 0.01 M $NaNO_3$ (Figure 4.1.22): precipitation threshold (—), separation line between dense unstable and dense stable aggregates (—), aggregation threshold (—).

The coagulation concentration of SPB was compared to the precipitation threshold of linear PA-chains and gave following results: Two thresholds differ by ca. 3 mM (Figure 4.3.9). The phase boundaries do not overlay but have a similar stoichiometric number of silver cations with respect to the number of negative monomer units required to precipitate the PA-chains: ca. 0.45 in case of Ag^+-PA solutions and ca. 0.6 in case of Ag^+-SPB solutions. In both polyacrylate systems there is a large range of $[Ag^+]$ where solutions are stable: a regime of dense stable aggregates with linear Ag^+-PA and a phase state when the PA-shell of SPB is shrunk but latices do not coagulate remaining homogeneously dispersed in water solution (the areas between red and blue symbols in Figure 4.3.9). The Ag^+ ions in case of Ag^+-SPB solutions are certainly located in the PA-shell, whereas in the core-shell Ag^+-PA dense stable aggregates it is not clear what part (shell or core) are dominantly enriched by Ag^+.

Since the distance between two neighbouring grafted PA-coils in SPB is smaller than two times R_g of PA-chains (Table 3.7), PA-layer represents highly concentrated solution of PA-chains. From this point of view the shrinking of PA-layer in Ag^+-SPB may be compared with the shrinking of the homogeneous low density aggregates to dense unstable aggregates observed in linear Ag^+-PA solutions. In conclusion of all these common properties of Ag^+-SPB and Ag^+-PA systems we can refer to a very strong binding of Ag^+ ions to PA-chains, independently of a PA morphology.

4.3.4 Ca²⁺ induced Shell Shrinking and Comparison of the Solubility Behaviour of Ca²⁺-SPB and Ca²⁺-PA Solutions

In order to compare the effect of monovalent Ag^+ ions on the shrinking of the PA-layer with the corresponding effect of divalent ions, we performed four series of DLS experiments on SPB(HMEM) latices at four different [COO⁻] in the presence of Ca^{2+} ions. The details of the solution preparation are given in Chapter 3.8.

Figure 4.3.10(a) shows the dependence of the brush thickness L on $[Ca^{2+}]$ for the SPB(HMEM) solutions. From these data we estimated the minimal concentration of Ca^{2+} ions ($[Ca^{2+}]_{shr}$) at which L reaches the plateau value L_{pl} within ±5 nm in an analogous way as it is described in Chapter 4.3.1. Table 4.3.3 summarises the results of the calculations made from the data presented in Figures 4.3.10(a), while Figures 4.3.10(b,c) represent two plots where $[Ca^{2+}]_{shr}$ and $[Ca^{2+}]_{shr}/[COO^-]$ are plotted versus the concentration of carboxylate groups.
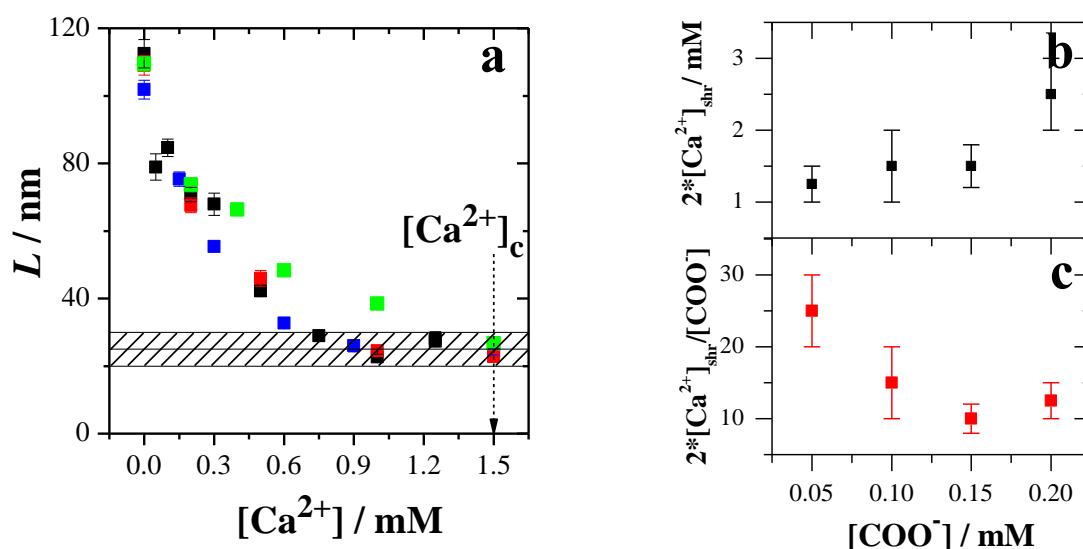
Figure 4.3.10 Graph **a**: thickness L of the PA-layer in Ca^{2+}-SPB(HMEM) solutions a pH of 6.5 as a function of $CaCl_2$ in 0.01 M NaCl. The concentration of [COO⁻] is 0.05 (■), 0.1 (■), 0.15 (■) and 0.2 (■) mM. The black horizontal line corresponds to the plateau value of the collapsed PA-layers $L_{pl} = 25$ nm. The shaded area indicates the standard deviation of L_{pl} which is ±5 nm. Black arrow shows $[Ca^{2+}]_c$. Graphs **b** and **c**: the Ca^{2+}-SPB diagrams where $[Ca^{2+}]_{shr}$ and $[Ca^{2+}]_{shr}/[COO^-]$ plotted versus the SPB(HMEM) concentration in terms of [COO⁻], respectively.

Full shrinking of the PA-layer was observed in the range of $0.6 \leq [Ca^{2+}] \leq 1.25$ mM and with increasing number density of SPB it was shifted to higher $[Ca^{2+}]_{shr}$ (Figure 4.3.10(b)) similar to the shrinking of PA-layer in Ag^+-SPB solutions (Figure 4.3.6). The initially strong decay of $[Ca^{2+}]_{shr}/[COO^-]$ in Figure 4.3.10(c) can be attributed to the fact that the

trend in Figure 4.3.10(b) has a finite intercept. The thickness of the shrunk PA-layer is about $L_{pl} = 30$ nm at all monomer concentrations. Coagulation of Ca^{2+}-SPB solutions sets in at $[Ca^{2+}]_c \approx 1.5$ mM, however an aggregation process at this Ca^{2+} concentration is comparably slow. The respective Ca^{2+}-SPB solution had been characterized by DLS, where we observe an increase of R_h. After a few hours this Ca^{2+}-SPB solution precipitates. The DLS measurements at $[Ca^{2+}] > 1.5$ were not possible to perform due to a fast coagulation process.

Table 4.3.3 Parameters defining the thresholds of shell shrinking in Ca^{2+}-SPB(HMEM) solutions at a pH of 6.5 in 0.01 M $NaNO_3$.

$[COO^-]$ / mM	$[Ca^{2+}]_{pl}$ / mM	$[Ca^{2+}]^*$ / mM	$[Ca^{2+}]_{shr}$ / mM	Estimated uncertainty of $[Ca^{2+}]_{shr}$
0.05	0.75	0.5	0.625	0.25
0.1	1	0.5	0.75	0.5
0.15	0.9	0.6	0.75	0.3
0.2	1.5	1	1.25	0.5

The shrinking of the PA-layer in the Ca^{2+}-SPB solutions was also compared at variable ionic strengths in analogy to Chapter 4.3.1. In one case Na^+ ions were exchanged by Ca^{2+} keeping the overall concentration of the positive charges at 0.01 M and in the other case Ca^{2+}-SPB solutions were prepared using a salt free SPB solution. Results of these experiments are depicted in Figure 4.3.11. The shrinking of PA-shells in the presence of exclusively Ca^{2+} begins at lower $[Ca^{2+}]_{shr} = 0.35$ mM than in the case where Ca^{2+} ions are introduced into the Na^+-SPB solution ($[Ca^{2+}]_{shr} = 0.85$ mM). The difference between these values is not significant. However, we can assume that in a saline SPB solution there is a slight competition between Na^+ and Ca^{2+} ions in inducing a shell shrinking unlike to Ag^+-SPB solutions (Chapter 4.3.1).

Stabilisation of colloids was also observed in Ca^{2+}-SPB solutions, however ranges of $[Ca^{2+}]$, at which Ca^{2+}-SPB are not coagulating after complete shrinkage of the PA-shell, are much narrow than in case of Ag^+-SPB solutions (Chapter 4.3.1). The coagulation of Ca^{2+}-SPB solutions at both conditions was observed at a similar $[Ca^{2+}]_c$ of ca. 1.5 mM. However, the concentration range of Ca^{2+} ions between $[Ca^{2+}]_{shr}$ and $[Ca^{2+}]_c$ is slightly broader in salt free SPB solutions.

It is interesting to compare the thresholds in Ca^{2+}-SPB solutions with the precipitation threshold of linear PA-chains in presence of Ca^{2+} ions. The solutions of latices were prepared in 0.01 M NaCl solution. Therefore the Ca^{2+} induced precipitation threshold of linear PA-chains was compared at this level of an inert salt. The concentration range of the monomer units in the analysis of the precipitation threshold in Ca^{2+}-PA solutions in reference [11] was $0.5 \leq [COO^-] \leq 1.5$ mM. Since the Ca^{2+}-SPB solutions at $[COO^-] > 0.3$ are unsuited for the analysis by light scattering because of the high turbidity, Ca^{2+}-SPB solutions in the range of $0.5 \leq [COO^-] \leq 1.5$ mM were tested only for the visual appearance of coagulation.
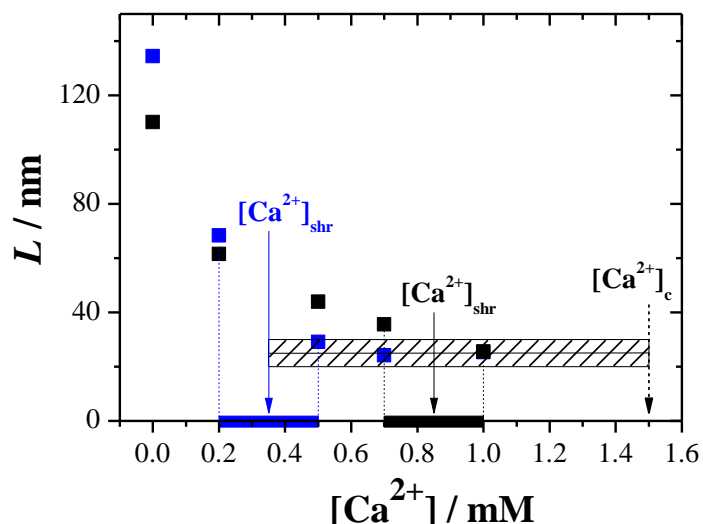
Figure 4.3.11 Thickness L of the PA-layer on SPB(HMEM) in Ca^{2+}-SPB solutions at a pH of 6.5 as a function of $CaCl_2$ concentration in a salt free solution (■) and in 0.01 M NaCl (■).The concentration of [COO⁻] is 0.1 mM. The experiments in 0.01 M NaCl are the reproductions of the respective experiments shown in Figure 4.3.10(a). The black horizontal line corresponds to the plateau value $L_{pl} = 25$ nm of the collapsed PA-layers. The shaded area indicates the standard deviation of L_{pl} which is ±5 nm. Arrows denote estimated $[Ca^{2+}]_{shr}$ and $[Ca^{2+}]_c$. The blue and black areas on the x-axis show where collapse of PA-layer is completed (the experimental uncertainty of $[Ca^{2+}]_{shr}$) in salt free SPB and in Na^+-SPB solutions, respectively.
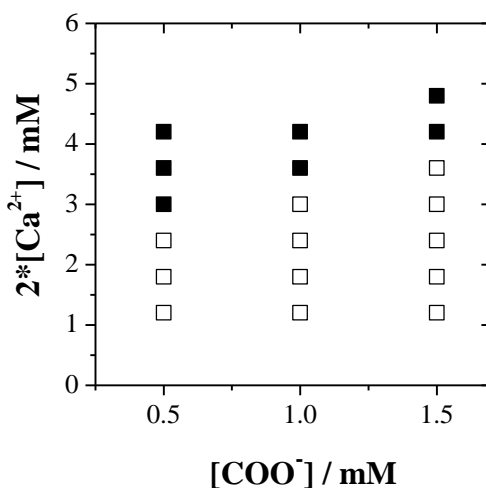
Figure 4.3.12 Results from the visual observation of the Ca^{2+}-SPB solutions in 0.01 M NaCl at a pH of 6.5. Full squares indicate coagulation in Ca^{2+}-SPB solutions and empty squares correspond to stable Ca^{2+}-SPB solutions.

135

Figure 4.3.12 shows the results from visual observations of Ca^{2+}-SPB solutions presented as a phase diagram. Vials with 2 mL of Ca^{2+}-SPB solutions were monitored during one month. Identification of the coagulation concentration [Ca^{2+}]$_c$ is achieved in the same way as in the case of [Ag$^+$]$_c$ in Chapter 4.3.3. Table 4.3.4 summarises the parameters defining [Ca^{2+}]$_c$. As we see the coagulation threshold at higher SPB concentration is shifted toward higher Ca^{2+} concentration and occurs in the range of $3 \leq$ [Ag$^+$]$_c \leq 3.9$ mM.

Table 4.3.4 Parameters describing the coagulation of Ca^{2+}-SPB(HMEM) solutions at a pH of 6.5 in 0.01 M NaNO$_3$.

[COO$^-$] / mM	[Ca^{2+}]$_1$ / mM	[Ca^{2+}]$_2$ / mM	[Ca^{2+}]$_c$ / mM	Estimated uncertainty of [Ca^{2+}]$_c$
0.5	3.6	4.2	3.9	0.6
1.0	3	3.6	3.3	0.6
1.5	2.4	3	3	0.6

Figure 4.3.13 shows a phase diagram with the coagulation and shell shrinking thresholds of Ca^{2+}-SPB solutions. Comparison of these phase transitions with the corresponding behaviour of linear Ca^{2+}-PA chains reveals a close similarity of the [Ca^{2+}] ranges at which precipitation/coagulation occurs. Although these concentrations are higher in case of Ca^{2+}-SPB, the nature of these processes is the same: PA-coils are aggregating and ultimately precipitating due to the interaction between PA-coils and Ca^{2+} ions. Interestingly, the shrinking threshold is directed towards the coagulation threshold which may indicate that the Ca^{2+}-SPB solutions with shrunk PA-layers directly precipitate at high concentration of brushes and the range of stable solutions disappears. It is important to emphasize at this point, that in the phase diagram of solutions with linear Ca^{2+}-PA chains there is no other separation than the phase boundary separating single PA-chains and precipitates.
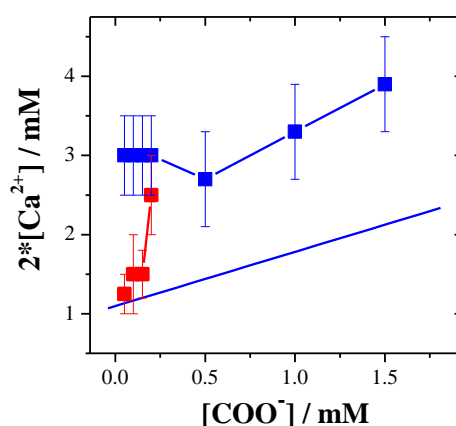
Figure 4.3.13 Results from the visual observations and the DLS experiments on Ca^{2+}-SPB solutions in 0.01 M NaCl at a pH of 6.5: PA-shell shrinking threshold (■) with data from Figure 4.3.10(b) and coagulation threshold (■) with data from Figure 4.3.12. The blue line indicates the precipitation threshold of Ca^{2+}-PA solutions in 0.01 M NaCl from reference [11].

4.3.5 Mg^{2+} induced Shell Shrinking

Two series of DLS experiments on SPB(HMEM) latices dissolved in 0.01 M NaCl solution were performed in order to analyse Mg^{2+} induced shell shrinking. Magnesium ions are also divalent, however its atomic number is smaller than the atomic number of the calcium ion. In case of M^{n+}-PA systems the precipitation threshold was shifted toward smaller metal ion concentrations with increasing atomic numbers [16], indicating the significance of not only electrostatic interactions but also of the complexation and of the inter-chain bridging via these metal ions. Analyses of the Mg^{2+}-SPB solutions by DLS is expected to yield information about one more M^{n+}-SPB system thereby helping to find general trends in the shrinking of PA-layer and in the coagulation thresholds of brushes in the presence of Ag^+, Ca^{2+} and Mg^{2+}.
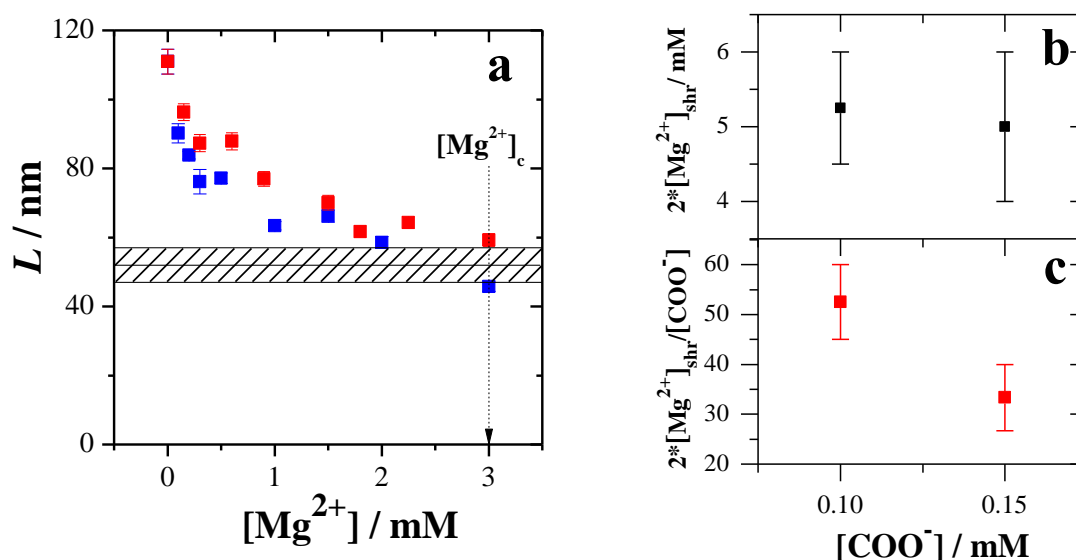
Figure 4.3.14 Graph **a**: thickness L of the PA-layer in Mg^{2+}-SPB(HMEM) solutions at a pH of 6.5 as a function of $MgCl_2$ in 0.01 M NaCl. The concentration of [COO⁻] is 0.1 (■) and 0.15 (■) mM. The black horizontal line corresponds to the plateau value of the collapsed PA-layers $L_{pl} = 52$ nm. The shaded area indicates the standard deviation of L_{pl} which is ±5 nm. Graphs **b** and **c** show the Mg^{2+}-SPB diagrams where $[Mg^{2+}]_{shr}$ and $[Mg^{2+}]_{shr}/[COO^-]$ plotted versus the SPB(HMEM) concentration in terms of [COO⁻], respectively.

Here, a certain amount of Na^+ ions were exchanged by Mg^{2+} ions. The solution preparation procedure is similar to the one for the Ag^+-SPB solutions (Chapter 4.3.1) with the exception that the monomer concentration of SPB was set to [COO⁻] = 0.1 and 0.15 mM. Figure 4.3.14 shows the change of the shell thickness L, calculated by eq(3.5) with DLS data, and plotted versus $[Mg^{2+}]$. The full shrinking of PA-layers occurs at around $[Mg^{2+}]_{shr} = 3$ mM for both [COO⁻]. The estimation of the minimal concentrations of Mg^{2+}

ions at which the shrinking of the PA-layer begins, $[Mg^{2+}]_{shr}$ values, was performed in the same way as in Chapter 4.3.1. The parameters defining $[Mg^{2+}]_{shr}$ are summarized in Table 4.3.5.

Table 4.3.5 Parameters defining the thresholds of shell shrinking in Mg^{2+}-SPB(HMEM) solutions in 0.01 M $NaNO_3$ at a pH of 6.5.

$[COO^-]$ / mM	$[Mg^{2+}]_{pl}$ / mM	$[Mg^{2+}]^*$ / mM	$[Mg^{2+}]_{shr}$ / mM	Estimated uncertainty of $[Mg^{2+}]_{shr}$ / mM
0.1	3	2.25	2.625	0.75
0.15	3	2	2.5	1

After a few hours the Mg^{2+}-SPB solutions at $[Mg^{2+}]_c = 3$ mM coagulate. At higher Mg^{2+} concentration the coagulation proceeds much faster, which prevents to analyse them by DLS. The coagulation concentration of Mg^{2+}-SPB established in our experiments is less than 0.01 M reported by Guo [48], which may be caused by the differing brush parameters. Since we did not extend the experiments to a broader range of $[COO^-]$ in Mg^{2+}-SPB solutions, we only can assume that with increasing number density of SPB, the threshold of shrinking and of coagulation is shifted toward higher concentration of $[Mg^{2+}]_{shr}$ and lower $[Mg^{2+}]_{shr}/[COO^-]$ (Figure 4.3.13(b,c)) similar to Ag^+- and Ca^{2+}-SPB (Figures 4.3.6 and 4.3.10(b,c)).

4.3.6 Comparison of the PA-shell shrinking induced by Ag^+, Ca^{2+} and Mg^{2+} Ions

After a detailed look at the behaviour of SPB solutions in the presence of Ag^+, Ca^{2+} and Mg^{2+} ions separately and after drawing the parallels in their behaviour with the linear PA-chains once possible, we shall compare the shell shrinking and the coagulation threshold among Ag^+-, Ca^{2+}- and Mg^{2+}-SPB solutions.

Figure 4.3.15 illustrates the comparison of the size change of the thickness L in Ag^+-, Ca^{2+}- and Mg^{2+}-SPB(HMEM) solutions, using the concentration of carboxylic groups of $[COO^-] = 0.15$ mM. Shrinking of the PA-layer in the presence of Ag^+ ions occurs at a very low concentration of $[Ag^+] = 0.4$ mM. This concentration range is much lower than for $[Na^+]$, where the salt concentration had to exceed a few moles (Figure 3.13). Divalent ions tested in our work also showed that PA-layers do not undergo a drastic shrinking at 0.4 mM. In terms of the total amount of the added positive charges, where $n[M^{n+}] = 2*[Ca^{2+}]$ or $n[M^{n+}] = 2*[Mg^{2+}]$, PA-layers begin to shrink at 2 mM and 6 mM in the presence of Ca^{2+} and Mg^{2+}, respectively (Figures 4.3.10 and 4.3.14). The thicknesses of the shrunk PA-layers differ between 25 nm and 52 nm, which may indicate the different interaction patterns between PA-chains and metal ions. A more reasonable explanation requires more research on this question.
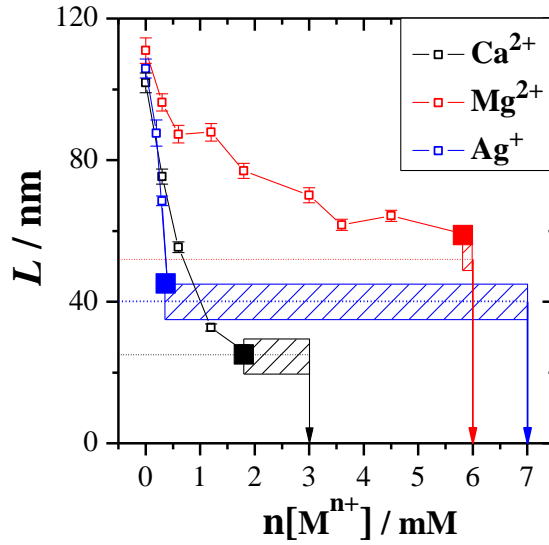
Figure 4.3.15 Thickness L of the PA-layer in M^{n+}-SPB(HMEM) solutions at a pH of 6.5 in 0.01 M NaNO$_3$/NaCl as a function of positive charges n[M^{n+}], where n[M^{n+}] = 2*[Ca^{2+}] (□), 2*[Mg^{2+}] (□) and [Ag^+] (□). The concentration of [COO^-] is 0.15 mM. The horizontal dash lines of the respective colour correspond to the plateau values of the collapsed PA-layers L_{pl}: 25 nm (▬), 40 nm (▬) and 52 nm (▬). The shaded areas indicate the standard deviation of L_{pl} which is ±5 nm. The n[M^{n+}] range of these areas correspond to the stable non-coagulated M^{n+}-SPB solutions. The full symbols indicate n[M^{n+}]$_{shr}$, the arrows show the n[M^{n+}]$_c$ value.

The most significant ion specific effect we can see in the n[M^{n+}] ranges between n[M^{n+}]$_{shr}$ and n[M^{n+}]$_c$ which correspond to a brush state with a fully shrunk PA-layer by Ag^+, Ca^{2+} and Mg^{2+} ions and M^{n+}-SPB solutions do not coagulate and remain stable. In Figure 4.3.15 this range is represented by shaded areas around the L_{pl}. The coagulation of latex particles in the presence of Ag^+ occurs at [Ag^+]$_c$ ≈ 8 mM, which is much higher than in the presence of Ca^{2+} (≈ 1.5 mM) and Mg^{2+} (≈ 3 mM). In Figure 4.3.16 these data from the variable [COO^-] transferred into M^{n+}-SPB phase diagram. The estimated stability regime over the whole range of analysed [COO^-] in Ag^+-SPB solutions is much broader than in Ca^{2+}-SPB solutions and in the case of Mg^{2+}-SPB solutions.
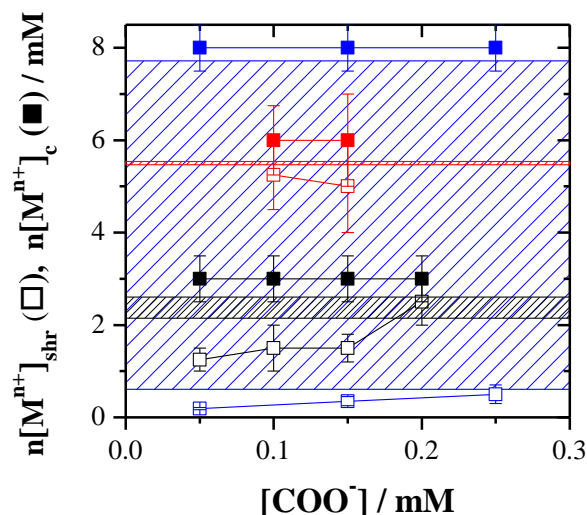
Figure 4.3.16 Results from the visual observations and the DLS experiments on M^{n+}-SPB solutions in 0.01 M NaNO$_3$ at a pH of 6.5: PA-shell shrinking threshold (empty squares) and coagulation threshold (full squares), where $n[M^{n+}] = 2*[Ca^{2+}]$ (black), $2*[Mg^{2+}]$ (red) and $[Ag^+]$ (blue). The sparse areas between $n[M^{n+}]_{shr}$ and $n[M^{n+}]$ correspond to the estimated range of stable M^{n+}-SPB solutions.

4.3.7 Conclusion

Detailed analysis of the numerous M^{n+}-SPB solution series, where M^{n+} is Ag^+, Ca^{2+} or Mg^{2+}, was aiming at a comparison of intra- and interparticle processes: the full collapse of the PA-chains constituting the shell of the brush (shell shrinking) and the coagulation of the M^{n+}-SPB particles. The present study revealed that both processes are closely related to the nature of the used counterion.

Comparison of the PA-shell shrinking induced by Ag^+ ions with shrinking induced by the divalent ions Ca^{2+} and Mg^{2+} showed that the $[Ag^+]_{shr}$ values, corresponding to the complete shrinking of the PA-shell of SPB, were significantly lower than $[Ca^{2+}]_{shr}$ and $[Mg^{2+}]_{shr}$ (Figure 4.3.15). Hence, similar to the Ag^+-PA system (Chapter 4.1), where PA was in the form of linear chains with a high molecular weight, carboxylate groups of PA-chains forming the PA-shell tended to be intra- or/and interconnected (complexed) by monovalent Ag^+ ions stronger than by divalent cations.

The thickness L of the PA-shell collapsed by the selected counterions within a particular SPB type decreases in the following row: $Mg^{2+} > Ag^+ > Ca^{2+}$ (Figure 4.3.15). This should be connected to an interaction pattern between PA-chains and corresponding metal cation. In order to give a justification for this trend, more research on this issue should be done. We meanwhile can assume that the thickness of a fully collapsed PA-shell induced by a specific cation should be related to the amount of water molecules released from the PA-layer during its shrinking and to the dominating either intra- or interchain bridging between M^{n+} and PA-chains.

The established counterion concentrations where the shrinking of PA-shell is completed $[M^{n+}]_{shr}$ were increasing with increasing the SPB concentrations (Figure 4.3.16). However, in terms of $[M^{n+}]/[COO^-]$ ratios it showed that at higher COO^- concentration less counterions per COO^- residue are needed to complete the collapse of PA-chains of the shell (Figures 4.3.6, 4.3.10 and 4.3.14). All trends had relatively high uncertainty and less pronounced for Ag^+ than for the other two cations.

Varying the ionic strength in Ag^+-SPB solutions (Figure 4.3.2) we found that an exchange pressure of Na^+ ions did not play any role in the shrinking of the PA-shell induced by Ag^+. However, similar experiments with Ca^{2+}-SPB solutions (Figure 4.3.11) indicated a slight competition between Ca^{2+} and Na^+ which led to smaller $[Ca^{2+}]_{shr}$ values when a salt free SPB solutions was used. The analysis made at variable pH in Ag^+-SPB solutions revealed that protons, representing probably the most specifically interacted cations, could compete significantly with Ag^+ in the shrinking of PA-shells (Figure 4.3.3) thus leading to higher $[Ag^+]_{shr}$ values at lower pH.

Analysis of Ag^+-SPB solutions prepared with latices differing by their brush parameters such as a counter length of PA-chains L_c, a grafting density σ and a hydrodynamic radius of the PS-cores $R_{h,PS}$ showed that the threshold values, i.e. $[Ag^+]_{shr}$ and $[Ag^+]_c$, are barely influenced by these parameters, whereas the absolute thickness of the collapse PA-layer L may vary between 17 nm and 40 nm (Figure 4.3.5).

We compared the phase diagrams of systems belonging to different polyacrylate morphologies in the presence of Ag^+ and Ca^{2+}. The study showed that the precipitation thresholds established for Ag^+-SPB/Ag^+-PA and for Ca^{2+}-SPB/Ca^{2+}-PA solutions were located at a similar counterion concentrations and corresponded to comparable stoichiometric amounts of silver or calcium ions per anionic groups (Figures 4.3.9 and 4.3.13). At the same time the solubility behaviour of Ag^+-PA and Ag^+-SPB systems turned out to be more rich and complex than corresponding Ca^{2+}-PA and Ca^{2+}-SPB ones. For Ag^+-SPB solutions the regime of stable SPB solutions with completely collapsed PA-chains can be compared to dense stable aggregates formed in Ag^+-PA solutions. Accordingly, the process of the PA-shell shrinking in Ag^+-SPB resembles the transition from homogenous low density to dense unstable Ag^+-PA aggregates.

The empirical study presented in Chapter 4.3 showed the importance to consider not only the valency of the counterions and electrostatic effect between PA-coils and these counterions [52] but also its nature, i.e., tendency to form complexes. With respect to Ag^+-SPB solutions these results give an opportunity to vary the ratio of $[Ag^+]/[COO^-]$ in a broad range, being secure that the latices do not precipitate, and thus test them as reactor systems in Ag-NP formation (see Chapter 4.4).

4.4 Ag-NP Formation in Spherical Polyacrylate Brushes

In Chapter 4.3 it has been demonstrated that PA-chains serve as reducing and as stabilizing agents in Ag-NP formation induced under the exposure of Ag^+-PA solutions to UV-light. The most decisive factor in the morphology of generated Ag-NPs was the state of the precursory Ag^+-PA solutions ($[Ag^+]/[COO^-]$ ratio) defined by the phase diagram (Figure 4.1.22). In case of SPBs the consisting PA-chains forming the PA-layer around the solid PS-core have less degree of freedom and the effects of Ag^+ ions on such morphologically different PA-systems induce shell shrinking at $0.4 < [Ag^+] < 8$ mM and coagulation of latex particles at $[Ag^+] \geq 8$ mM. The Ag^+ concentration range, where Ag^+-SPB solutions exhibit stability, is fairly broad (Figure 4.4.1). Thus the $[Ag^+]/[COO^-]$ ratio can be varied in a very broad range too.
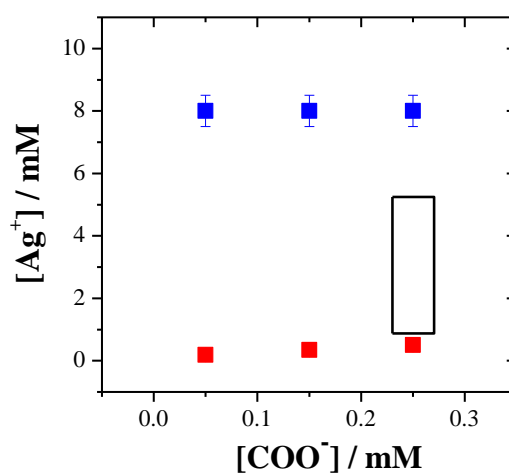
Figure 4.4.1 Results from the visual observations and the DLS experiments on Ag^+-SPB(HMEM) solutions in 0.01 M $NaNO_3$ at a pH of 6.5: PA-shell shrinking threshold (■) with data from Figure 4.3.6(a) and coagulation threshold (■) with data from Figure 4.3.8. The black frame indicates a regime of performed experiments in the present Chapter 4.4.

The reduction of Ag^+ ions in Ag^+-SPB solutions under UV-illumination is expected to be similar to the reduction of Ag^+ in Ag^+-PA solutions. In the present Chapter 4.4 we want to see whether the control under the generation of Ag-NPs can be also established through such parameters as $[Ag^+]/[COO^-]$ and time of UV-exposure (t_{UV}). As an alternative way to modify the protocol toward a higher yield of Ag-NPs we will use chemical reduction agent ($NaBH_4$).

Due to a high interest in the field of metamaterials we also want to verify whether the size and the amount of Ag-NPs formed under reduction processes in Ag^+-SPB solutions are appropriate enough in order to consider these hybrid Ag-SPBs particles as ones exhibiting artificial magnetism.

4.4.1 Ag-NP Formation induced by the Exposure to UV-light of Ag$^+$-SPB

The value of PA-coils for the Ag$^+$ reduction is unique and formation of Ag-NPs was repeatedly investigated with Ag$^+$-PA solutions exposed to daylight and, in order to accelerate the photoreduction process, to UV-light (see discussions of Chapter 1.1.2). The simplicity and convenience of such a method was already applied in Chapter 4.2 where individual Ag-NPs and assemblies thereof were formed in Ag$^+$-PA solutions via exposure to UV-light. The same strategy is implemented with Ag$^+$-SPB solutions and discussed in the present Chapter 4.4.1.

In the following experiments we scrutinized several Ag$^+$-SPB solutions which are varied by its composition. By means of exposing them to UV-light for variable times (t_{UV}) we tried to analyse the size and relative number of formed Ag-NPs by UV-vis spectroscopy and SEM.

Five Ag$^+$-SPB solutions based on a SPB(HMEM) stock solution were prepared in 0.01 M NaNO$_3$ at a pH of 5. The monomer concentration of the carboxylate groups [COO$^-$] was fixed to 0.25 mM and the concentration of Ag$^+$ ions was varied in the range of $0.75 \leq [Ag^+] \leq 5$ mM. This SPB concentration insures that latex solutions are transparent thus stirring of the latex suspensions during exposure to UV-light is not necessary. Since the aging of Ag$^+$-SPB solutions in this [Ag$^+$] range does not cause an aggregation or a coagulation, they were exposed to UV-light for $t_{UV} = 1.5$ min only in the non-aged condition. All solutions contained 0.01 M of positive charges and were prepared in an analogous way as it is described in the Chapter 3.8. Table 4.4.1 summarises the information about the composition of Ag$^+$-SPB solutions and Figures 4.4.2 and 4.4.3 represent a photo and UV-vis characterisation, respectively, thereof.

Table 4.4.1 Composition of Ag$^+$-SPB solutions exposed to UV-light.

Sample Code	[Ag$^+$] / mM	[Ag$^+$]/[COO$^-$]	t_{UV} / min
A	0.75	3	1.5
B	1.50	6	1.5
C	2.50	10	1.5
D	3.75	15	1.5
E	5.00	20	1.5
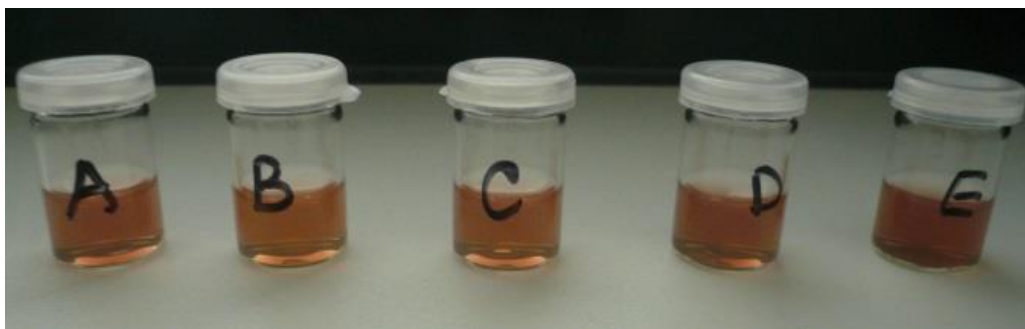
Figure 4.4.2 Ag$^+$-SPB solutions with [COO$^-$] = 0.25 mM and with [Ag$^+$] increasing from A to E in a range of $0.75 \leq$ [Ag$^+$] ≤ 5 mM (Table 4.4.1) after exposure to UV-light for $t_{UV} = 1.5$ min without aging.
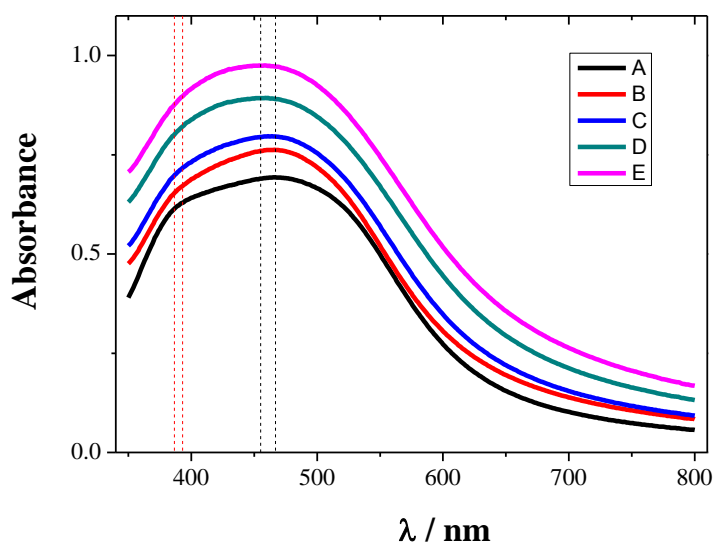
Figure 4.4.3 UV-vis spectra of Ag$^+$-SPB solutions with [COO$^-$] = 0.25 mM and [Ag$^+$]/[COO$^-$]: 3 (━), 6(━), 10 (━), 15 (━) and 20 (━) after their exposure to UV-light for $t_{UV} = 1.5$ min without aging.

From Figure 4.4.2 we see that all solutions are equally brownish although the concentration of Ag$^+$ varies in a very significant range. UV-vis spectra in Figure 4.4.3 show a slight increase in the absorbance with increasing the Ag-content, which means that the amount of Ag-NPs should also slightly increase from sample A to sample E with increase of the Ag$^+$ concentration. The position of broad maximums is located in a regime of $455 \leq \lambda \leq 467$ nm (black dashed lines in Figure 4.4.2) and slightly shifts to a blue range going from sample E to sample A. The position of the SPR, which can be correlated with the size of single Ag-NP, is difficult to identify. For all spectra we see a broadening of the peak, which is very similar to the one, observed in Figure 4.2.14 and can be explained by absorption of non-consumed Ag$^+$ ions onto the surface of Ag-NPs or by agglomeration of

144

Ag-NPs. A hardly recognized shoulder in the range of $386 \leq \lambda \leq 392$ nm (red dashed lines in Figure 4.4.2) may indicate the existence of smaller Ag-NPs (under 10 nm).

In order to see whether an extension of the duration of the UV-exposure leads to substantial changes in terms of size and number of Ag-NPs two Ag^+-SPB solutions (B and E) after variable t_{UV} were analysed by UV-vis spectroscopy. Ten additional solutions, five with the composition identical to B and five with the composition identical to E, were exposed to UV-light for $t_{UV} = 2$, 3, 4, 5 and 7.5 min directly after their preparation. Table 4.4.2 presents the characteristics of these solutions and Figures 4.4.4 shows UV-vis spectra thereof.

Table 4.4.2 Composition of two series of Ag^+-SPB solutions (B and E) exposed to UV-light for variable t_{UV}.

Sample Code	$[Ag^+]$ / mM	$[Ag^+]/[COO^-]$	t_{UV} / min
B1			2
B2			3
B3	1.50	6	4
B4			5
B5			7.5
E1			2
E2			3
E3	5	20	4
E4			5
E5			7.5

As we see from the UV-vis spectra (Figure 4.4.4) a longer UV-exposure time in both series leads to an increase of the absorbance only up to a certain t_{UV} limit: in the B-series this limit is at $t_{UV} = 5$ min and in the E-series it is at $t_{UV} = 4$ min. Samples exposed to UV for longer t_{UV} exhibit a decrease of absorbance at λ_{max} and an increase of the absorbance in the red region.

The shape of spectra within the same series is comparable. In the case of the E-series we have a smooth almost symmetrical peak at λ_{max}, which shifts from 456 nm to 475 nm. All spectra with an increase of t_{UV} steadily broaden at $\lambda > 550$ nm. For the B-series we observe an increase of the absorbance in the region of $390 \leq \lambda \leq 415$ nm, which may indicate that the number of fairly small Ag-NPs grows, at the same time the maxima of spectra in the range of $460 \leq \lambda \leq 480$ nm turn to a more plateau-like shape. In general all these signatures indicate an increase of generated Ag-NPs when time of UV-exposure gets longer. However, it is difficult to draw exact conclusions about the size of individual Ag-NPs.
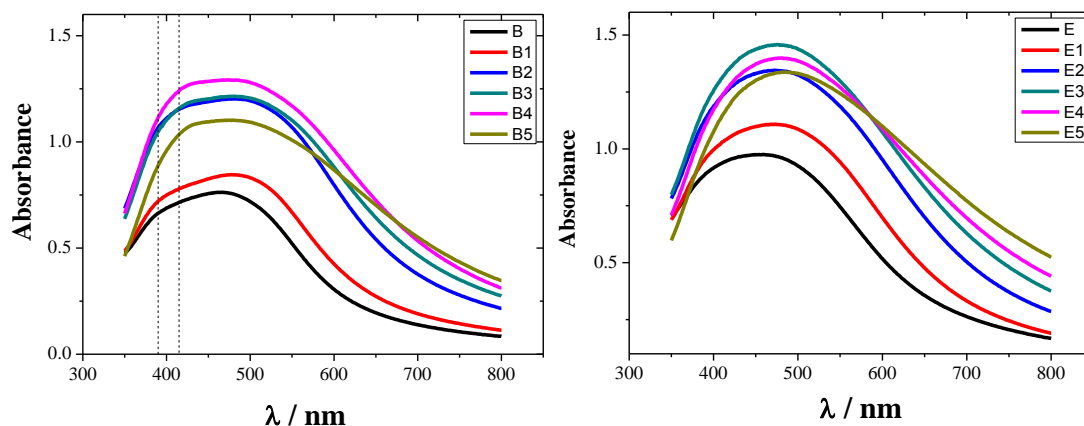
Figure 4.4.4 UV-vis spectra of Ag$^+$-SPB solutions with [COO$^-$] = 0.25 mM and [Ag$^+$]/[COO$^-$] = 6 (of B-series – left graph) and [Ag$^+$]/[COO$^-$] = 20 (of E-series – right graph) after the exposure to UV-light for variable t_{UV}: 1.5 min (━), 2 min (━), 3 min (━), 4 min (━), 5 min (━) and 7.5 min (━).

Figures 4.4.5 represent two photos made after all UV-spectra had been registered. The time interval between the preparation of all solutions and completion of all UV-spectra corresponds to ca. 2 h. Here we can clearly see that in case of the B-series solutions exposed to UV for $t_{UV} \geq 3$ min precipitate whereas in the E-series precipitation gets visible at $t_{UV} \geq 4$ min.
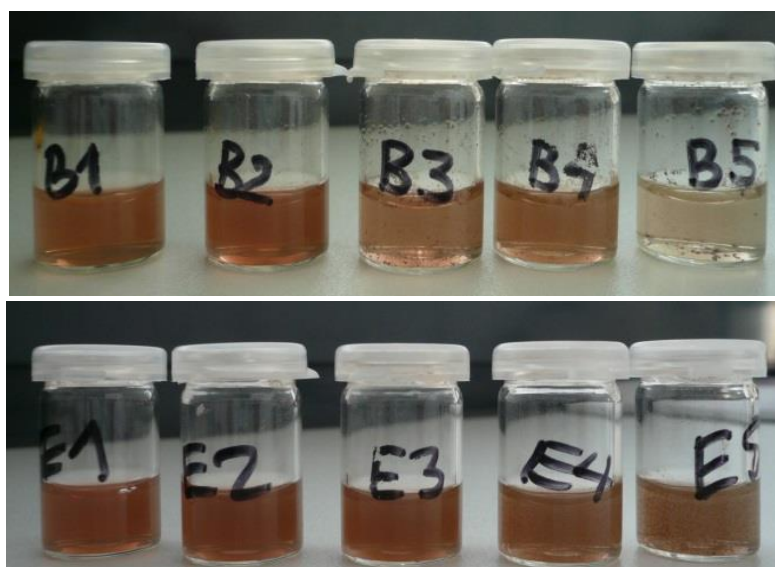
Figure 4.4.5 Ag$^+$-SPB solutions with [COO$^-$] = 0.25 mM and with [Ag$^+$] of 1.5 mM and of 5 mM in series B and E, respectively, after exposure to UV-light for $2 \leq t_{UV} \leq 7.5$ min (Table 4.4.2).

In order to learn more about the Ag-NPs formed via exposure to UV-light in Ag^+-SPB solutions we prepared four solutions, the compositions of which are indicated in Table 4.4.3, and analysed them by SEM. Two types of SPB were used: SPB(BA) and SPB(HMEM) corresponding to BA-1,2 and HMEM-1,2 series, respectively. The concentration of $[COO^-]$ was 0.25 mM, similar to previously discussed solutions. The pH of solutions were also very similar: 5.6 (BA-1,2) and 4.8 (HMEM-1,2). The concentration of $[Ag^+]$ was taken quite different in its value: 0.75 and 2.5 mM for the sake of a possible distinction in the number of formed Ag-NPs. These two $[Ag^+]/[COO^-]$ ratios set to 3 and 10 are by a factor of two smaller than in B- and E-series, however the relation between these two values is similar (3.33). The reason to use smaller absolute $[Ag^+]/[COO^-]$ ratios was to ensure that no processes of agglomeration or precipitation of Ag-SPBs can occur during ca. 14 h, while solutions are drying on the aluminium stub prior to SEM analysis. Wherefore the time of UV-illumination was set to $t_{UV} = 3$ min, which is smaller than those limiting t_{UV} values, identified for series B and E in the previously described experiments.

Table 4.4.3 Composition of two series of Ag^+-SPB solutions (BA and HMEM) exposed to UV-light.

Sample Code	pH	$[Ag^+]$ / mM	$[Ag^+]/[COO^-]$	t_{UV} / min
BA-1	5.6	0.75	3	
BA-2	5.6	2.50	10	3
HMEM-1	4.8	0.75	3	
HMEM-2	4.8	2.50	10	

Figure 4.4.6 shows four representative SEM-micrographs where we can distinguish big spheres, corresponding to SPBs, and considerably smaller particles clearly located on the surface of the bigger ones, corresponding to Ag-NPs. Figures 6.13 of the Appendix show the SEM-images of the same samples at a smaller magnification. Since solutions were dried before analysing them by SEM, big spheres represent the PS-cores which are covered by a thin layer of collapsed PA-chains. Since the SEM-images of pure SPBs do not exhibit an existence of any small particles on their surface (Figure 3.11), we can unambiguously identify the last ones as Ag-NPs. The average size of these Ag-NPs is ca. 10-20 nm in diameter.

The difference in type of used SPB and concentration of Ag^+ concentration do not increase significantly the number or size of generated Ag-NPs (Figure 4.4.6). In case of HMEM-1,2 the coverage of SPBs by Ag-NPs appears to be slightly lower than in case of BA-1,2, at least in the latter ones there are less completely "bare" spheres. This feature might be connected to the difference in pH of SPB solutions. In case of the higher amount of neutralised COO^--functions the reduction of Ag^+ is supported by a higher number of electrons leading to a higher amount of Ag-NPs at the end. However, comparing the samples belonging to the same SPB-type and pH, an increase of Ag-content by a factor of

ca. 3 does not amplify the photoreduction process. The reason for that might be the same like the one mentioned for Ag$^+$-PA solutions (Chapter 4.2): due to a given [COO$^-$] the number of electrons, which are probably come from COO$^-$-groups, for the photoreduction of Ag$^+$ is limited.
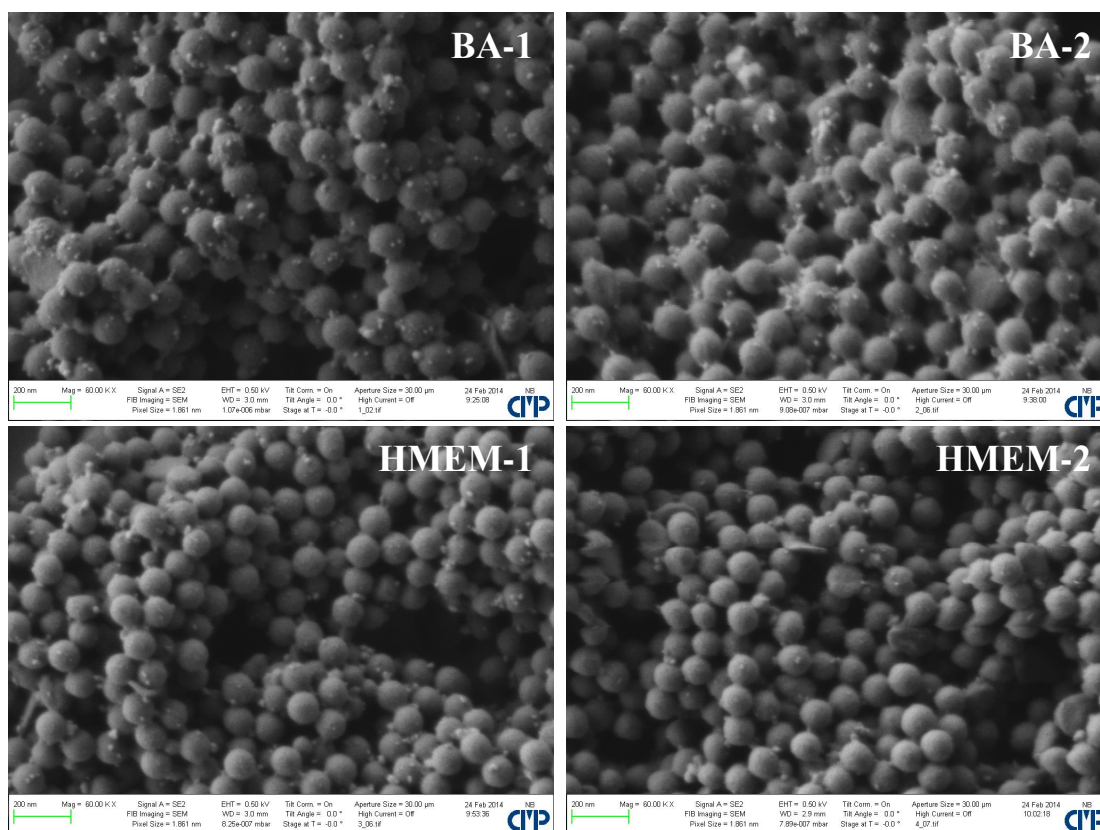
Figure 4.4.6 SEM images of Ag$^+$-SPB solution containing [COO$^-$] = 0.25 mM and [Ag$^+$]/[COO$^-$] = 3 (BA-1 and HMEM-1) and [Ag$^+$]/[COO$^-$] = 10 (BA-2 and HMEM-2) exposed to UV-light for t_{UV} = 3 min.

In order to develop the idea about an approximate amount of Ag-NPs, which can be generated via one-electron transfer from carboxylic groups (see Figure 1.2), we estimated the number of Ag-NPs with a size of 20 nm and 10 nm in diameter formed per one SPB(HMEM), under the assumption that all COO$^-$ groups are involved in the reduction process of Ag$^+$, in the following way:

1.   The grafting density of SPB(HMEM) is $\sigma = 0.055$ nm^{-2} (the number of PA-chains per 1 nm^2), the molecular weight of NaPA measured by using an Ubblohde viscometer is $M_\eta = 61642$ g/mol. The size of the PS cores is 59.2 nm (Table 3.7).

2.   The area of the PS surface is $4\pi R^2$ ➜ $4\pi(59.2)^2 = 3504.64$ (nm^2).

3.   The area per one chain is 1/0.055 (nm^{-2}) = 18.182 nm^2 therefore the number of chains per one PS core is 3504.64 (nm^2) / 18.182 (nm^2) = 192.75 chains.

4.   The amount of COO$^-$-groups is equal to a degree of the polymerization of NaPA. The molecular weight of the monomer is 94 g/mol ➜ (61642 (g/mol) /94 (g/mol) · 192.75 = 126399 anionic groups per one SPB.

5.   With the assumption that all COO$^-$-groups were neutralized by silver ions, we have 126399 silver ions per one SPB.

6.   With respect to the atomic radius of one silver atom (0.144 nm) and assuming that each silver atom occupies the volume of a cube with an edge of 0.30 nm we can calculate the number of silver atoms in a sphere with 20 nm in its diameter. The volume of that nanoparticle is $4/3\pi R^3$ ➜ $4/3\pi$ (10(nm))^3 = 4188.8 nm^3. The number of atoms in such a nanoparticle is 4188.8/0.027 ≈ 155141 atoms. For an Ag-NP 10 nm in diameter the volume is $4/3\pi$ (5(nm))^3 = 523.3 nm^3, thus the number of atoms in such nanoparticle is 523.3/0.027 ≈ 19383 atoms.

From these calculations we see that if all anionic groups donate their electrons to Ag$^+$ ions for their reduction, as a limiting case, we have about one Ag-NP 20 nm size in diameter or eight of Ag-NPs of 10 nm size in diameter. Applying the same calculations, we can get two Ag-NPs of 15 nm in diameter. Hence, the results on UV-light assisted Ag-NP formation which we see in SEM-micrographs of Figure 4.4.6 are in agreement with these calculations, representing theoretically possible cases with respect to amount of generated Ag-NPs by means of electron-transfer to Ag$^+$ from carboxylic functions of PA-coils, despite the fact that the concentration of Ag$^+$ ions in those experiments is higher than the concentration of COO$^-$-groups (Table 4.4.2).

Figure 4.4.7 shows the TEM-micrographs corresponding to Ag$^+$-SPB solution with [COO$^-$] = 0.25 mM and [Ag$^+$] = 0.25 mM exposed to UV-light for t_{UV} = 4 min. The [Ag$^+$]/[COO$^-$] = 1 represents a case which can be used as a reference to all others, since this SPB-content should be enough to reduce all Ag$^+$ ions in Ag$^+$-SPB solutions via photoreduction and amount of Ag-NPs should be comparable to that one observed in Figure 4.4.6. The pH of SPB solution was adjusted to 5, which is comparable to solutions analysed before.

In TEM-micrograph we do not see where Ag-NPs are located, however, due to a higher contrast of metal particles in comparison to polymer spheres we can better estimate the overall amount of Ag-NPs per one SPB. In Figure 4.4.7 we can observe a very inhomogeneous distribution of Ag-NPs on the polymer particles. In some areas there are a lot of Ag-NPs and in others there are no Ag-NPs at all. Interestingly, the size of individual

Ag-NPs is in the range of 10-20 nm which is the same as in the four other systems those SEM-images presented in Figures 4.4.6.
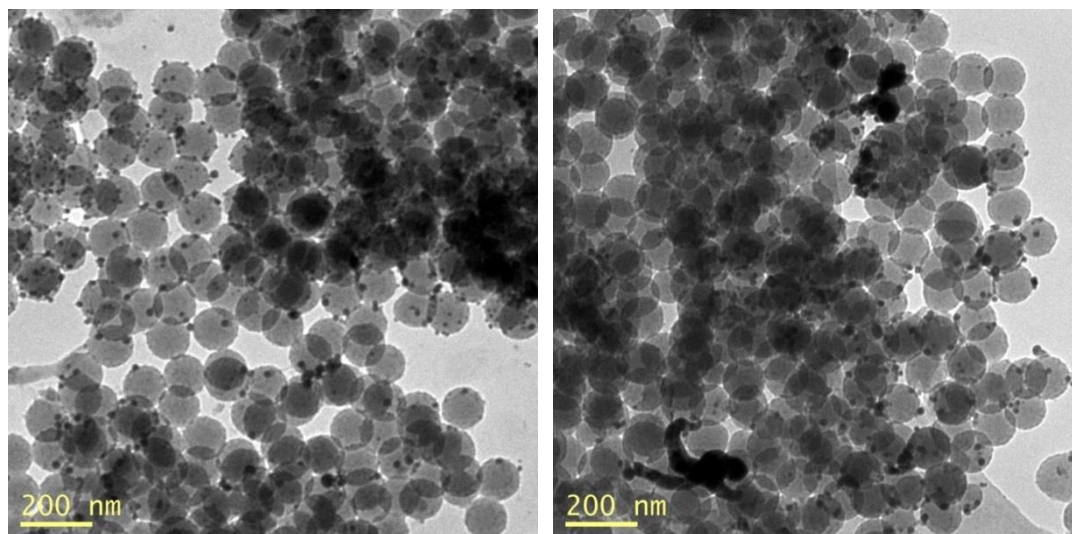
Figure 4.4.6 TEM images of Ag$^+$-SPB(HMEM) solution containing [COO$^-$] = 0.25 mM and [Ag$^+$]/[COO$^-$] = 1 exposed to UV-light for t_{UV} = 4 min.

The obtained results in this Chapter showed that the size of individual Ag-NPs, which was established by microscopic methods (SEM and TEM), lays in the range of 10-20 nm (Figures 4.4.6 and 4.4.7). On UV-vis spectra the broad absorption peak in the wavelength regime of $380 \leq \lambda \leq 470$ nm does not allow to correlate the exact position of SPR of Ag-NPs to their size. Probably, the characterisation by UV-vis spectroscopy could be more efficient if solutions would be washed out by pure water in the ultrafiltration cell removing not reacted AgNO$_3$. This procedure of cleaning will be applied in the further experiments (see Chapter 4.4.2).

From all performed experiments on the UV-light assisted Ag-NP formation in Ag$^+$-SPB solutions we can conclude that among such parameters as the type of SPB, the pH of the SPB solutions. Ag$^+$ ion concentration and the exposure time (t_{UV}), which may have an influence on the photoreduction process, probably the most important parameter is the concentration of COO$^-$-groups or in other words the grafting density of PA-chains. The higher grafting density should increase the amount of neighboured carboxyl groups and consequently the amount of reduced Ag atoms which will be concentrated in a high enough density in order to form Ag-NP.

In the next Chapter 4.4.2 we will analyse the ability of SPBs to act as the containers for Ag-NPs which can be formed via chemical reduction of Ag$^+$ ions. Performing a large series of experiments we want to find a favourable synthetic protocol which can increase a coverage of PS-cores by Ag-NPs.

4.4.2 Ag-NP Formation induced by Chemical Reducing Agent (NaBH$_4$) in Ag$^+$-SPB

In the present Chapter 4.4.2 we try to find suitable protocols in order to achieve first of all densely packing Ag-NPs covering the dielectric PS-cores of SPBs, where additionally PA-coils can act as a dielectric material preventing individual Ag-NPs to be in a direct contact. Such a feature of SPBs coincides with the prerequisite condition in the formation of a raspberry-like metamolecules (Chapter 1.1.4), where only when the plasmon resonance of each adjacent Ag-NP is coupled, it can give rise to a strong optical-frequency circulating displacement current and hence a magnetic dipole [75, 76, 78]. In our approach, as a potential receipt toward raspberry-like metamolecules, we focus on the efficient coverage of PA-core by Ag-NPs.

As a reducing agent we selected commonly used inorganic salt NaBH$_4$. This substance dissolves well in water and its excess can easy be removed by the ultrafiltration method. Since Ag-NPs are suitable candidates for catalytic reduction, for example of *4*-nitrophenol, there are a few works where Ag-NPs, embedded into the SPBs or "nano-tree" type of SPBs, were synthesized via chemical reduction of Ag$^+$ ions using NaBH$_4$ as a reducing agent too [57, 59, 62, 64]. For the catalytic purposes they were aiming at, it was desirable to obtain as smaller size of individual Ag-NPs as possible, thus synthetic procedures mentioned in those works were designed in a way which led to formation of Ag-NPs in the size range of $3-8$ nm in diameter. This small size was usually achieved by using a small portion of Ag$^+$ ions, via replacing Na$^+$ ions in the PA-layers and washing out the rest of Ag$^+$ by the ultrafiltration method. Contrariwise, in our method we will try to reduce as much Ag$^+$ ions as possible in order to get more Ag-NPs being at the same time embedded into PA-layer.

There are a lot of parameters, which can be varied and needed to be kept under control in order to obtain desired results in Ag-NP formation from Ag$^+$-SPB solutions using NaBH$_4$. Therefore this piece of study can be considered as a good starting point for further optimisation of conditions. We performed a lot of experiments to synthesize Ag-NPs from Ag$^+$-SPB solutions using NaBH$_4$ and found distinctive requirements which should be fulfilled. Later on one series of experiments, where the following conditions had been used, will be discussed in detail.

(i) In order to achieve a high coverage of the PS-cores with Ag-NPs, the ratio of [Ag$^+$]/[COO$^-$] is selected to be at least 15. Such a choice also results from the calculations made in Chapter 4.4.1 in terms of the size of single Ag-NP and brush parameters. (ii) Ag$^+$-SPB solutions (in 0.01 M NaNO$_3$) should be added into an aqueous solution of NaBH$_4$ cooled to ca. 0-4 °C. Such temperature prevents NaBH$_4$ to react violently and quickly with water at room temperature. Very cold water sufficiently slows this reaction to allow the reduction of silver ions. And such order of mixing ensures that Ag$^+$ ions are in the PA-layer and and the resulting Ag-NPs can be directly stabilized by an excess of BH$_4^-$ ions.

(iii) Addition of an Ag^+-SPB solution to the $NaBH_4$ solution should be done under starved conditions (0.05 mL per 2 sec), because of fast mixing leads to an agglomeration of Ag-NPs which eventually precipitate. (iv) The stirring of the solution with Ag-NPs being formed should be set to 500 rpm and stopped after the final addition of Ag^+-SPB to $NaBH_4$. Continuation of the stirring of the reactive mixture leads to a loss of Ag-NPs from the surface of SPB. (v) An excess ratio of $[NaBH_4]/[Ag^+]$ of 5 - 7 was examined as the most favourable in both the reduction process and the stabilisation of Ag-NPs. (vi) As it has been mentioned in the Chapter 3.8, the pH of SPB solutions should not be higher than 7 in order to avoid the precipitation of Ag_2O.

Here we present a final series of experiments, where all mentioned aspects of the synthesis were adequately considered. Only the two parameters $[Ag^+]/[COO^-]$ and $[NaBH_4]/[Ag^+]$ ratios were varied in a very narrow range. Table 4.4.3 summarises compositions of the solutions in the experiments on Ag-NPs formation in Ag^+-SPB solutions where Ag^+ ions were reduced by means of $NaBH_4$ as a reducing agent. Details of the synthesis are given in Chapter 3.9.

Table 4.4.3 Composition of Ag^+-SPB solutions and the amount of $NaBH_4$ used in the reduction process toward formation of Ag-NPs.

Sample Code	$[Ag^+]$ / mM	$[Ag^+]/[COO-]$	$[NaBH_4]/[Ag^+]$
2	2.5	10	3
4	2.5	10	7
5	3.75	15	3
6	3.75	15	5

Figures 4.4.8 and 4.4.9 show the UV-vis spectra and SEM-micrographs of four samples, respectively. On the SEM-images we can clearly see that in samples 2 and 4 the amount of small particles (Ag-NPs) on the big spheres (SPB) is smaller than in case of samples 5 and 6. In order to see a distinguished difference between 2 or 4 and 5 or 6 in terms of the amount of Ag-NPs per SPB as well as to derive a size distribution of Ag-NPs a higher magnification of SEM is needed.

In all SEM-micrographs we observe some big spheres which are completely deprived of Ag-NPs. This fact can be explained by the process of purification by ultrafiltration. A small portion of latex particles were used to check the effectiveness of the ultrafiltration cell. Since the apparatus was built at the university workshop (Figure 3.10), the diameter of the PVC tube is slightly bigger than the diameter of the membrane and quite often the purified solution is leaking through the small gaps. In such cases the whole apparatus should be disassembled and brought into action again. This readjustment in some cases may be repeated up to 4 times, which also led to inevitable losses of purified solution. In our case these losses are highly undesirable, because the total amount of the synthesis

samples was just 12 mL. However another reason is even more crucial. Since in all these series the colour of the solutions were yellow-brown and due to a low [COO⁻] the samples were only slightly turbid, it is hard to distinguish between the eluent and eluate. The washing process inevitably removes Ag-NPs which are not embedded into the shell of SPB. Therefore in the beginning the eluate is also yellow and only after some time gets colourless.

In order to see whether the membrane passes only water and other impurities under 100 nm in size, we used a small portion of pure latex particles SPB(HMEM) dissolved in water which had a high turbidity. Only when the liquid leaving the cell was transparent and not "milky", the cell was assigned to be ready for the sample purification process. Accordingly, the same membrane which was finally adjusted on the metal grid, gasket and PVS tube was also used for sample cleaning. Although the cell was washed with pure water several times before injecting the sample with hybrid SPB/Ag-NPs, probably a small portion of pure SPB(HMEM) was still left and on SEM we see these left latex particles as the "bold/naked" ones.

The process of the purification is very important to the characterization of samples by SEM. Without performing it we cannot see anything due to a high amount of inorganic salt, which is predominantly $NaBH_4$. One example of a non-washed case is given in Figure 6.14 of the Appendix, where a thick layer of $NaBH_4$ does not allow to see even polymer spheres.
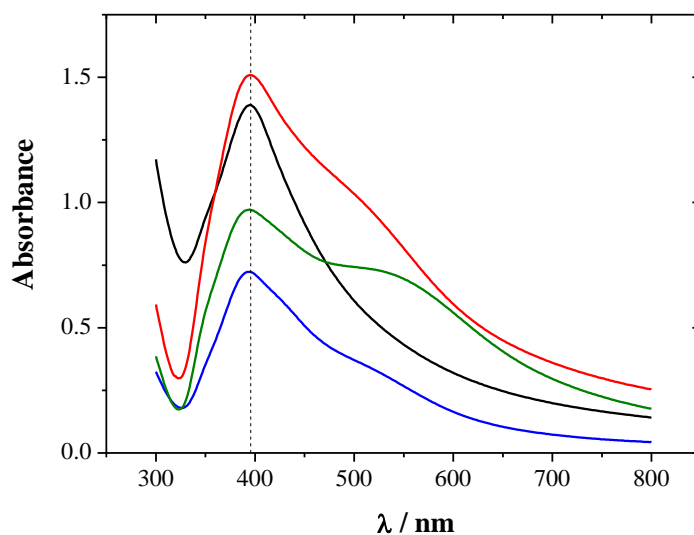
Figure 4.4.8 UV-vis spectra of Ag-SPB solutions. Compositions of samples are indicated in Table 5.4.3. The coloured lines indicate samples as: 2 (━), 4 (━), 5 (━) and 6 (━).
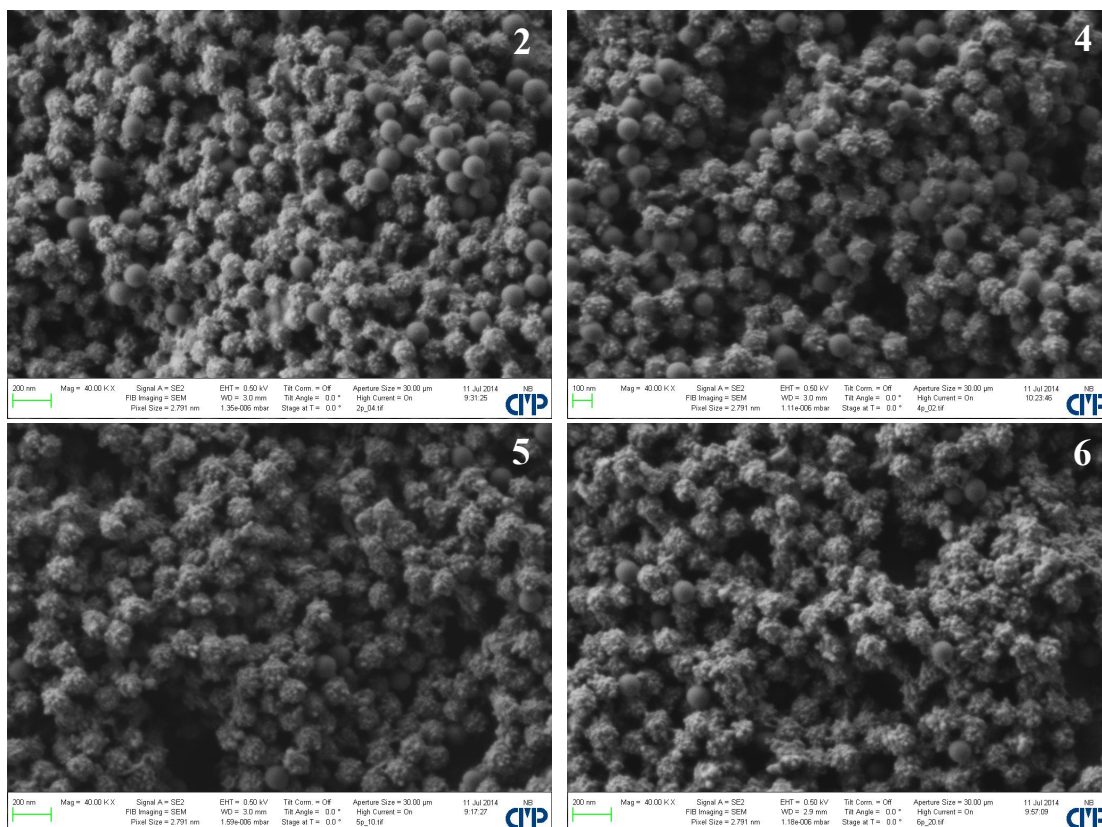
Figure 4.4.9 UV-vis spectra of Ag-SPB(HMEM) solutions. The numbers on the images correspond to sample code which is given in Table 4.4.3.

In Figure 4.4.8 there are four UV-vis spectra of solutions. Due to a different dilution extent during the cleaning process (ultrafiltration) it is difficult to compare the absolute values of their absorbances. For example in case of sample 6 it is smaller than in case of sample 2, however as it is seen on the SEM-micrographs (Figure 4.4.9) the amount of Ag-NPs per SPB is significantly higher for sample 6. Therefore we will discuss the peaks and their characteristics. We see for all UV-vis spectra well pronounced and relatively narrow peaks at $\lambda \approx 400$ nm (Figure 4.4.8). For all four samples these peaks, which come from the surface plasmon resonance of single Ag-NPs, appear at the same energy and thus indicate a similar size of presented Ag-NPs among all samples. In accordance with literature [154, 155] the SPR band at $\lambda \approx 400$ nm could be related to Ag-NPs under 10 nm in size. This estimation is in agreement with results obtained by SEM (Figure 4.4.9).

The peak (or shoulder) in the red region usually indicates an agglomeration of the particles and the optical response from an Ag-NP assembly [154, 155]. Since on the SEM-micrographs (Figure 4.4.9) pure Ag-NP agglomerates are not seen, we can suggest that the additional peaks (or shoulders) come from the collective oscillations of Ag-NPs located on the PS-cores. In case of sample 6 the packing of Ag-NPs on the PS-cores appears higher than in other samples and such peak at ca. $\lambda = 550$ nm appears with a higher intensity than for samples 4 and 5. For the latter ones we see a slight shoulder at approximately the same

λ. For raspberry-like (or core-satellite) metamolecules similar to ours these low energy signals can be also assigned to a magnetic plasmon mode [78, 80, 81], however to prove it further analytical and theoretical analyses are necessary.

In summarizing the results presented in this Chapter 4.4.2 we conclude that specific interactions of Ag^+ ions with PA-chains of the brush lead to *in-situ* formation of Ag-NPs which are embedded into the PA-shell thus giving raspberry-like hybrid Ag-SPB particles. The size of the Ag-NPs and its size distribution can be further optimized. In order to obtain an even higher coverage of the SPBs by Ag-NPs a ratio of $[Ag^+]/[COO^-] = 15$ can be used or even increased while the ratio of $[NaBH_4]/[Ag^+]$ should be ca. 6. Since Ag^+-SPB solutions precipitate at $[Ag^+] \approx 8$ mM, this Ag^+ concentration can be used as the maximal one.

The hybrid Ag-SPB particles can be further analysed with respect to artificial magnetism. A first indication seems to be reflected by the red-shifted peak on the UV-vis spectra (Figure 4.4.8), which may be related to a dipole magnetic response [78].

4.4.3 Conclusion

In Chapter 4.4 we investigated Ag^+-SPB solutions applied for the generation of Ag-NPs induced by exposure to UV-light and by the chemical reducing agent $NaBH_4$. The following results are obtained:

(i) Our experiments showed that the amount of generated Ag-NPs under UV-illumination of Ag^+-SPB solutions is limited and is not influenced by varying such parameters as used $[Ag^+]$ and t_{UV}. Since we believe that the photoreduction process under exposure to UV-light is supported by the electron source coming from the anionic groups of PA chains, where the latter ones serve also as the stabilizing agent, the Ag-NP formation can be enhanced by preparing SPB with a higher grafting density. The justification of this hypothesis need more research.

(ii) In order to significantly increase the number of Ag-NPs, the reduction process of Ag^+ ions can be amplified by using a chemical reducing agent, e.g. $NaBH_4$. In the synthetic protocol of the reduction we revealed some requirements which must be fulfilled in order to obtain satisfactory results (Chapter 4.4.2). The Ag-NPs are generated *in situ* and are embedded in the PA-shell. They remain there even under the force of the pressure applied during the purification process (ultrafiltration) of latices. The high coverage of the PS-core by Ag-NPs leads to the appearance of a red-shifted peak due to densely packed Ag-NPs on the PS-core which can be related to a magnetic dipole resonance and thus be considered as a sign of the artificial magnetism in these Ag-SPB particles.

In both synthetic paths the reduction of Ag^+ in SPB leads to a formation of small Ag-NPs of the size of 10-20 nm. In order to see more details in their size distribution TEM experiments are required.

5 Conclusions and Outlook

The present work investigated two polyacrylate (PA) systems in dilute aqueous solutions, commercially available long linear PA-chains and spherical polyacrylate brushes (SPBs) composed of polystyrene (PS) cores and PA-shells, which have been synthesized as part of the thesis. Investigation of these two systems addressed their specific interactions with Ag^+ ions and was compared to the corresponding interactions the two systems exhibited with alkaline earth cations. In order to reveal inter- and intraparticular changes induced by Ag^+ ions PA of each type was mixed at variable ratios of $[Ag^+]/[COO^-]$, where $[COO^-]$ indicates the monomer concentration of PA, and scrutinized by light scattering methods (SLS, DLS, combined SLS/DLS, TR-SLS/DLS). Results on the solubility behavior of these two morphologically different silver acrylate solutions turned out to be a crucial tool for a controlled formation of silver nanoparticles (Ag-NPs) supported by PA. For this purpose photoreduction of Ag^+ ions embedded into PA-matrices was induced by UV-illumination without additional reducing or stabilizing agents. Ag-NP formation in Ag^+-PA solutions, i. e., solutions of long linear PA-chains mixed with $AgNO_3$ in saline aqueous solution, were predominantly studied with SLS/DLS, SAXS/ASAXS and UV-vis spectroscopy and complemented by TEM experiments. In the case of SPBs, by means of SEM and TEM we estimated the coverage of SPBs by Ag-NPs whereas UV-vis spectroscopy was applied to register their optical response.

Highly interesting results were obtained from the study of solutions of linear Ag^+-PA at variable composition. In comparison with the phase diagrams of linear PA systems with divalent alkaline earth or transition metal cations, the interaction pattern with monovalent Ag^+ ions disclosed a rich solubility behavior resulting in a diverse set of Ag^+-PA entities. Thus, a carefully established aggregation threshold at extremely low $[Ag^+]$ preceded the formation of **homogeneous low density aggregates** formed at slightly higher $[Ag^+]$, where the ratio of $0.001 < [Ag^+]/[COO^-] < 0.05$). Although these aggregates exhibited the form factor of a homogeneous sphere as obtained from the analysis of the SLS data, the structures being formed are not compact due to a very low amount of bridging agents, i.e., Ag^+ ions.

Ag^+-PA solutions at a higher Ag-content underwent an aggregation process, which was proposed to begin with a collapse of homogeneous low density aggregates and to continue with immediate aggregation. Due to the high molecular weight and comparatively small size we named those Ag^+-PA entities as **dense unstable aggregates**. Their form factor from the SLS data corresponded to coil-like structures. However, the structure-sensitive factor ρ obtained from combined TR-SLS/DLS measurements had a value characteristic for core-shell particles. Thus, the morphology of growing aggregates is not yet well understood and needs more research.

Beyond the ratio of $[Ag^+]/[COO^-] = 0.3$ Ag^+-PA solutions remained stable. Their molecular parameters turned out to be very similar to the ones observed in the beginning of the formation of dense unstable aggregates. Apparently, a certain excess of Ag^+ ions led not only to a very fast formation of small dense aggregates, similar or equal to the initial intermediates formed in the regime of dense unstable aggregates, but also to a stabilization thereof. Small size values in terms of R_g and R_h and high M_w values gave a reason to call these particles **dense stable aggregates**. The proposed model for these dense stable aggregates includes a dense non-draining core surrounded by a drainable shell of dangling PA-chains.

Further increase of $[Ag^+]$ in Ag^+-PA solutions finally resulted in aggregation and precipitation. Systematically organised experiments at different concentrations of NaPA and Ag^+ ions allowed us to identify conditions in terms of $[Ag^+]/[COO^-]$ ratios necessary to selectively address any of the aggregate types. All results were summarised as a phase diagram.

Such a rich set of structures formed in Ag^+-PA solutions established a base for the Ag-NP formation induced by UV-illumination thereof. We focused on two regimes corresponding to dense unstable and dense stable Ag^+-PA aggregates. Here the crucial role of Ag^+ ions as the inter-particular bridging agents was revealed in the experiments where the aggregation, i.e. formation of unstable dense aggregates, could be stopped due to the exposure of these solutions to UV-light. Exposure to UV-light was applied at different aging times where in each case the halt of aggregation was accompanied by the appearance of a surface plasmon resonance registered by UV-vis spectroscopy. The peak corresponded to Ag-NPs with a size of ca. 20-30 nm, whereas an additional shoulder in the red region indicated the formation Ag-NP assemblies of these Ag-NPs. A longer aging time of Ag^+-PA solution prior to the UV-exposure led to formation of bigger Ag-NP assemblies, where the size of the constituting Ag-NPs invariably corresponded to ca. 20-30 nm. Thus, the number of Ag-NPs per assembly could be controlled by means of aging the Ag^+-PA solutions prior of being illuminated with UV-light. Predominantly individual Ag-NPs were formed from dense unstable Ag^+-PA aggregates if the UV-exposure was applied to non-aged Ag^+-PA solutions. Dense stable aggregates lead to entities with mainly single Ag-NPs independent of the solution history before UV-illumination. Hence, the solution properties of Ag^+-PA in saline water enabled us not only to specifically form single Ag-NPs or their assemblies but also to control the size of these Ag-NP assemblies.

Numerous experiments on Ag^+-SPB solutions were aiming at an analysis of the shrinking of the PA-shell and coagulation of latices induced by these monovalent ions. Based on three SPB types which varied by the counter length of the PA-chains (L_c), the grafting density (σ) and the size of the PS-core ($R_{h,PS}$), SPB solutions at different $[Ag^+]$ were scrutinized by DLS. It was revealed that those brush parameters influence only the thickness L of the shrunk PA-shell, whereas the Ag^+ concentration range where shrinking of the PA-layer was completed ($[Ag^+]_{shr}$) remained unchanged. The experiments made at

different pH in Ag^+-SPB solutions indicated that Ag^+ ions only competed with protons and not with Na^+ ions while inducing the shrinking process of the PA-layer. By varying the ionic strength in SPB solutions before mixing it with Ag^+ we showed that no exchange pressure of Na^+ ions became noticeable during the collapse of PA-chains of the shell, whereas the coagulation threshold ($[Ag^+]_c$) was significantly shifted toward lower Ag^+ concentration.

SPB solutions in saline water were also analysed with respect to a shrinking of the PA-shell and successive coagulation of latices in the presence of Ca^{2+} and Mg^{2+} ions. The concentrations of divalent Ca^{2+} and Mg^{2+} ions where the collapse of PA-shells occurred ($[M^{2+}]_{shr}$) were much higher than the corresponding concentration of Ag^+ ions, while $[M^{n+}]_c$ at which latices coagulate increased in the following row: $[Ca^{2+}]_c < [Mg^{2+}]_c < [Ag^+]_c$. Unlike to Ca^{2+} or Mg^{2+}, the phase behaviour of Ag^+-SPB solutions showed a broad range of $[Ag^+]$ where the PA-layer was fully shrunk but Ag^+-SPB did not yet coagulate. This phase state of stable Ag^+-SPB solutions resembles dense stable aggregates of Ag^+-PA solutions. In extending analogies between linear PA chains and SPBs we hypothesize that the collapse of PA-chains constituting the brush shell can be compared to the shrinking of the homogeneous low density aggregates, which are assumed to act as primary entities in the growth of dense unstable aggregates. Hence, the impact of Ag^+ ions inducing intra- and interparticular changes by means of two polyacrylate morphologies was confirmed and supplemented.

Ag-NP formation generated in SPB solutions by the same routine as applied to the solutions of linear Ag^+-PA showed that independent of the brush parameters or Ag^+ concentration a few similar sized Ag-NPs per SPB were generated. In order to increase the number of Ag-NPs per SPB particle the decoration of SPB with Ag-NPs has also been performed by applying an additional chemical reducing agent. We have chosen $NaBH_4$ as commonly used reducing agent in aqueous media. With this alternative way the number of Ag-NPs could significantly be increased. By carefully adjusting conditions we achieved a high coverage of PS-cores by Ag-NPs, located within the PA-shell. Registration of the UV-vis spectra of solutions containing hybrid raspberry-like Ag-SPB particles indicated an appearance of an additional peak at a wavelength longer than the one corresponding to single Ag-NPs. This peak in the red region can be related to an occurrence of a magnetic dipole resonance caused by Ag-NPs arranged on a dielectric PS-core. These results can be considered as a starting point to further develop raspberry-like metamolecules based on the synthetic route proposed in this work.

Despite of our progress, there are plenty of issues which still remain unsolved. (i) The small size of dense stable aggregates requires SANS experiments in order to make accessible form factors thereof. It may turn out that the high values of apparent molar mass from light scattering were affected by a high refractivity of Ag^+ ions. This fact forced us to wonder whether these dense stable entities were indeed dense aggregates or just single coils heavily loaded with highly refracting Ag^+ ions. (ii) Interesting results may also be

expected from a specifically designed procedure where dense unstable entities aggregating in solution will be loaded by additional Ag^+ ions. If the resulting Ag^+-PA aggregates will be stabilized similar to dense stable aggregates, addition of the further Ag^+ ions at variable aging times and successive exposure of them to UV-light may offer a further interesting route to control formation of Ag-NP assemblies. (iii) The origin causing the stability of dense aggregates once the ratio of $[Ag^+]/[COO^-]$ in Ag^+-PA solutions exceeded a value of 0.3 is still unknown. It may be connected to a change in the coordination shell established by the carboxylate ligands around Ag^+ ions. Additional IR spectra of Ag^+-PA solutions of different composition, i.e. from regimes of dense unstable and dense stable Ag^+-PA aggregates, could probably shed light on this issue. (vi) In this work only one additional NaPA1300 sample was studied in order to prove the general phenomena of the existence of dense stable aggregates next to dense unstable aggregates in the phase diagram. Use of other molecular weight samples of long linear PA-chains could extend our knowledge. We can also assume that exposing Ag^+-PA solutions consisting of shorter or longer PA-chains to UV-light either may better stabilize single Ag-NPs or rather lead to a certain shape of Ag-NP assemblies. (v) It would be also interesting to investigate microgels equipped with COO^--residues with respect to conformational changes induced by Ag^+ ions and to Ag-NP formation.

6 Appendix

6.1 Determination of the Aggregation Threshold for NaPA800

Figures 6.1 – 6.5 show changes in coil dimensions for five dilution series, which have been performed in an Ag^+ concentration range of $0.001 < [Ag^+] < 0.003$ mM. The evaluation of aggregation thresholds was made in a way described in Chapter 4.1.1.2. Results are summarized in Table 4.1.1. In Figure 6.1 – 6.5 the red arrow indicates the molecular weight of single coils (Table 3.3), which are included in order to illustrate that the apparent M_w data established in the presence of Ag^+ ions only cross this limit toward larger values once the threshold has been approached, i. e. once $[NaPA] < [NaPA]_{agg}$.

Figure 6.1 Radii of gyration R_g, hydrodynamic radii R_h, $\rho = R_g/R_h$ and apparent molar mass values M_w plotted versus [NaPA] for sample NaPA800 at $[Ag^+] = 0.001$ mM. Symbols (■) and (■) denote two dilution series to prove the reproducibility of the aggregation threshold. Upper black/green and lower black/green lines correspond to ρ_1 and ρ_2, respectively. Inclined vertical black/green line depicts the drop of the ρ ratio from ρ_1 to ρ_2. Blue squares and blue bars represent the $[NaPA]_{agg}$ with the respective estimated uncertainty of $[NaPA]_{agg}$. Red line indicates the trend of M_w calculated with Zimm's approximation using established $A_2 = 4.55*10^6$ molLg^{-2}, whereas the red arrow indicates $M_{w,c=0}$ (Table 3.3).

Figure 6.2 Radii of gyration R_g, hydrodynamic radii R_h, $\rho = R_g/R_h$ and apparent molar mass values M_w plotted versus [NaPA] for sample NaPA800 at $[Ag^+] = 0.00125$ mM. Upper and lower black lines correspond to ρ_1 and ρ_2, respectively. Inclined vertical black line depicts the drop of the ρ ratio from ρ_1 to ρ_2. Blue square and blue bar represent the $[NaPA]_{agg}$ with the respective estimated uncertainty of $[NaPA]_{agg}$. Red line indicates the trend of M_w calculated with Zimm's approximation using established $A_2 = 4.55*10^6$ molLg^{-2}, whereas the red arrow indicates $M_{w,c=0}$ (Table 3.3).

Figure 6.3 Radii of gyration R_g, hydrodynamic radii R_h, $\rho = R_g/R_h$ and apparent molar mass values M_w plotted versus [NaPA] for sample NaPA800 at $[Ag^+] = 0.002$ mM. Upper and lower black lines correspond to ρ_1 and ρ_2, respectively. Inclined vertical black line depicts the drop of the ρ ratio from ρ_1 to ρ_2. Blue square and blue bar represent the $[NaPA]_{agg}$ with the respective estimated uncertainty of $[NaPA]_{agg}$. Red line indicates the trend of M_w calculated with Zimm's approximation using established $A_2 = 4.55*10^6$ molLg^{-2}, whereas the red arrow indicates $M_{w,c=0}$ (Table 3.3).

Figure 6.4 Radii of gyration R_g, hydrodynamic radii R_h, $\rho = R_g/R_h$ and apparent molar mass values M_w plotted versus [NaPA] for sample NaPA800 at $[Ag^+] = 0.0025$ mM. Upper and lower black lines correspond to ρ_1 and ρ_2, respectively. Inclined vertical black line depicts the drop of the ρ ratio from ρ_1 to ρ_2. Blue square and blue bar represent the $[NaPA]_{agg}$ with the respective estimated uncertainty of $[NaPA]_{agg}$. Red line indicates the trend of M_w calculated with Zimm's approximation using established $A_2 = 4.55*10^6$ molLg^{-2}, whereas the red arrow indicates $M_{w,c=0}$ (Table 3.3).

Figure 6.5 Radii of gyration R_g, hydrodynamic radii R_h, $\rho = R_g/R_h$ and apparent molar mass values M_w plotted versus [NaPA] for sample NaPA800 at $[Ag^+] = 0.003$ mM. Upper and lower black lines correspond to ρ_1 and ρ_2, respectively. Inclined vertical black line depicts the drop of the ρ ratio from ρ_1 to ρ_2. Blue square and blue bar represent the [NaPA]$_{agg}$ with the respective estimated uncertainty of [NaPA]$_{agg.}$ Red line indicates the trend of M_w calculated with Zimm's approximation using established $A_2 = 4.55*10^6$ molLg^{-2}, whereas the red arrow indicates $M_{w,c=0}$ (Table 3.3).

6.2 Determination of the Aggregation Threshold for NaPA1300

Figures 6.6 – 6.10 show changes in coil dimensions for five dilution series, which have been performed in an Ag^+ concentration range of $0.003 < [Ag^+] < 0.005$ mM. The evaluation of aggregation thresholds was made in the same way as described for sample NaPA800 (Chapter 4.1.1.2). Results are summarized in Table 4.1.2. In Figures 6.6 – 6.10 the red arrow indicates the molecular weight of single coils (Table 3.4), which are included in order to illustrate that the apparent M_w data established in the presence of Ag^+ ions only cross this limit toward larger values once the threshold has been approached, i. e. once $[NaPA] < [NaPA]_{agg}$.

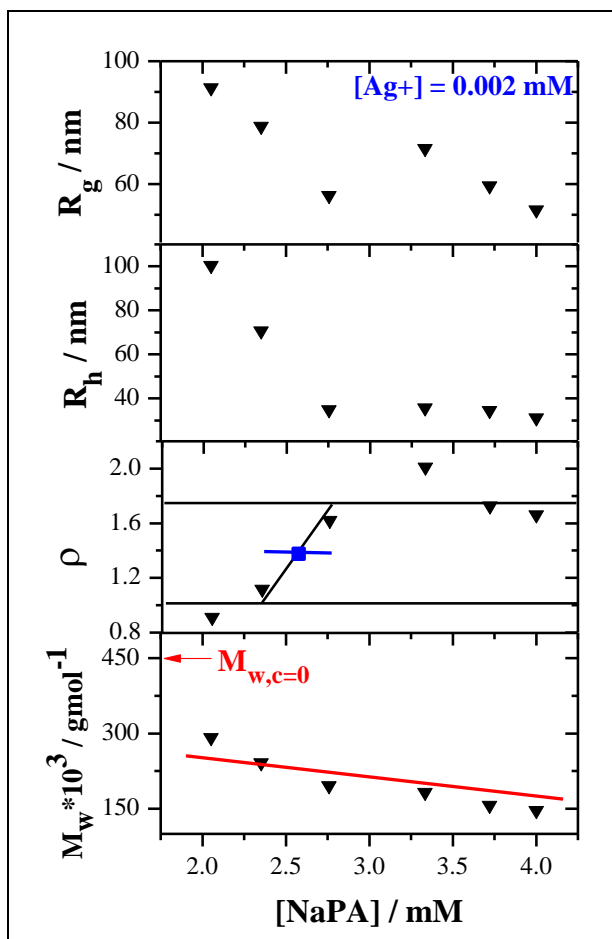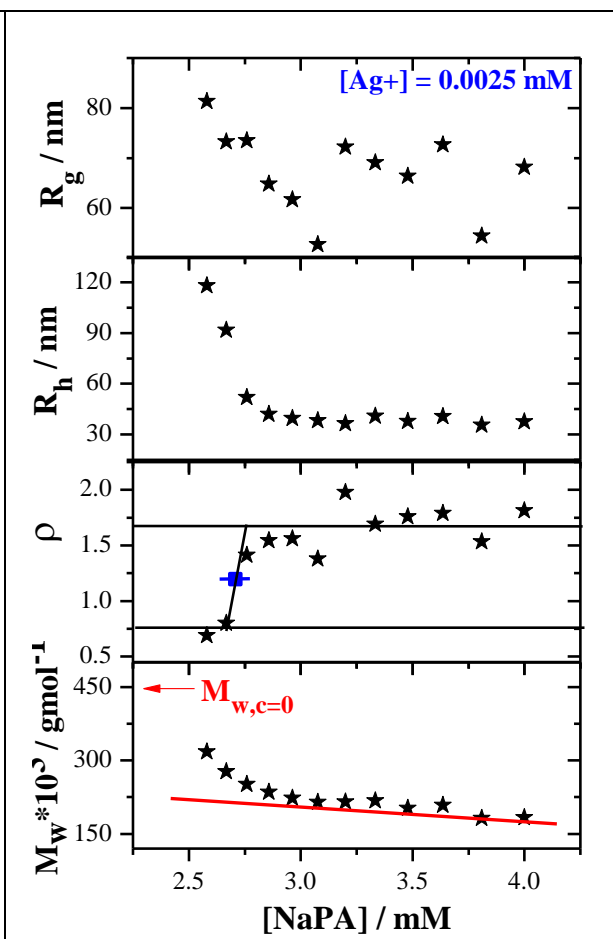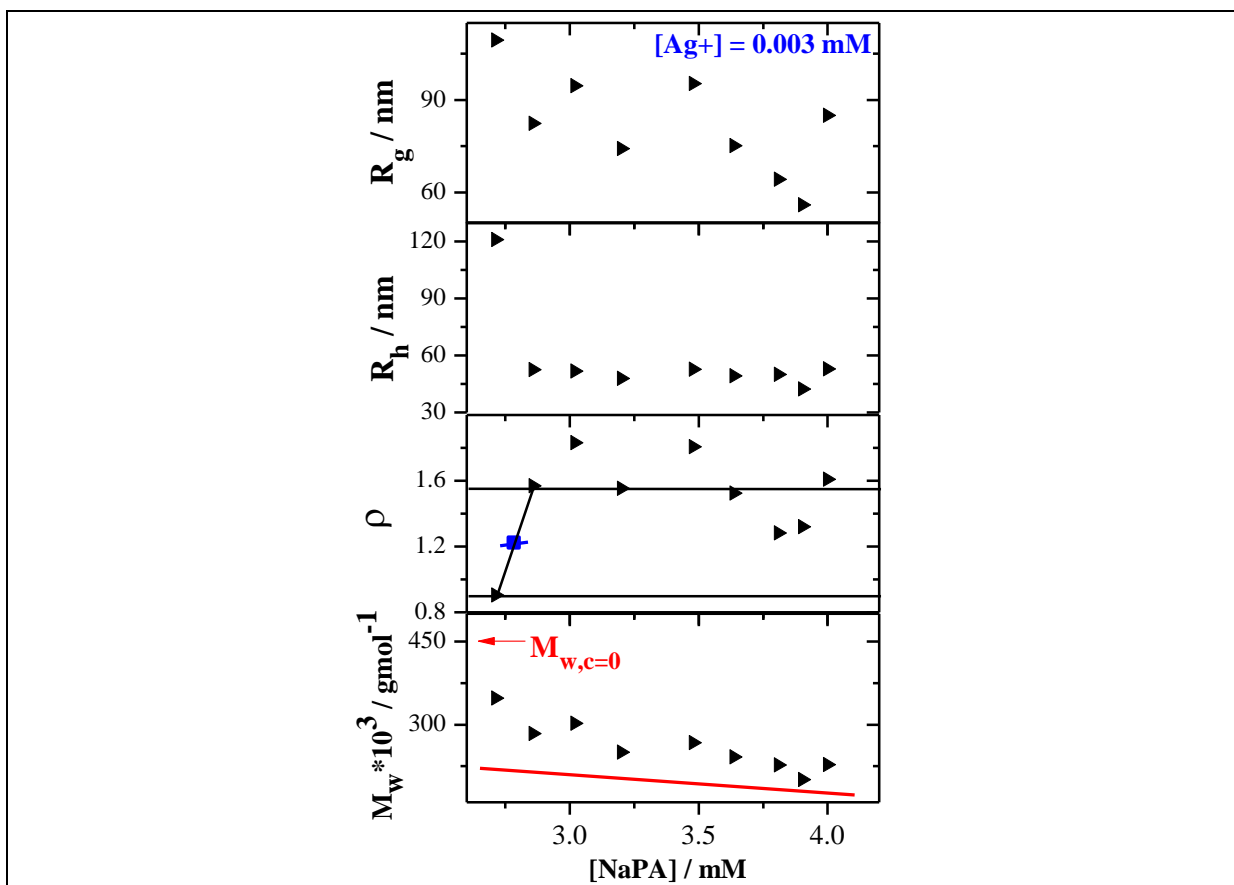|	
Figure 6.6 Radii of gyration R_g, hydrodynamic radii R_h, $\rho = R_g/R_h$ and apparent molar mass values M_w plotted versus [NaPA] for sample NaPA1300 at $[Ag^+] = 0.003125$ mM. Upper and lower black lines correspond to ρ_1 and ρ_2, respectively. Inclined vertical black line depicts the drop of the ρ ratio from ρ_1 to ρ_2. Blue square and blue bar represent the $[NaPA]_{agg}$ with the respective estimated uncertainty of $[NaPA]_{agg}$. Red arrow indicates $M_{w,c=0}$ (Table 3.4).	**Figure 6.7** Radii of gyration R_g, hydrodynamic radii R_h, $\rho = R_g/R_h$ and apparent molar mass values M_w plotted versus [NaPA] for sample NaPA1300 at $[Ag^+] = 0.0035$ mM. Symbols ($\blacksquare$) and ($\blacksquare$) denote two dilution series to prove the reproducibility of the aggregation threshold. Upper black/green and lower black/green lines correspond to ρ_1 and ρ_2, respectively. Inclined vertical black/green line depicts the drop of the ρ ratio from ρ_1 to ρ_2. Blue squares and blue bars represent the $[NaPA]_{agg}$ with the respective estimated uncertainty of $[NaPA]_{agg}$. Red arrow indicates $M_{w,c=0}$ (Table 3.4).

Figure 6.8 Radii of gyration R_g, hydrodynamic radii R_h, $\rho = R_g/R_h$ and apparent molar mass values M_w plotted versus [NaPA] for sample NaPA1300 at [Ag$^+$] = 0.004 mM. Upper and lower black lines correspond to ρ_1 and ρ_2, respectively. Inclined vertical black line depicts the drop of the ρ ratio from ρ_1 to ρ_2. Blue square and blue bar represent the [NaPA]$_{agg}$ with the respective estimated uncertainty of [NaPA]$_{agg}$. Red arrow indicates $M_{w,c=0}$ (Table 3.4).
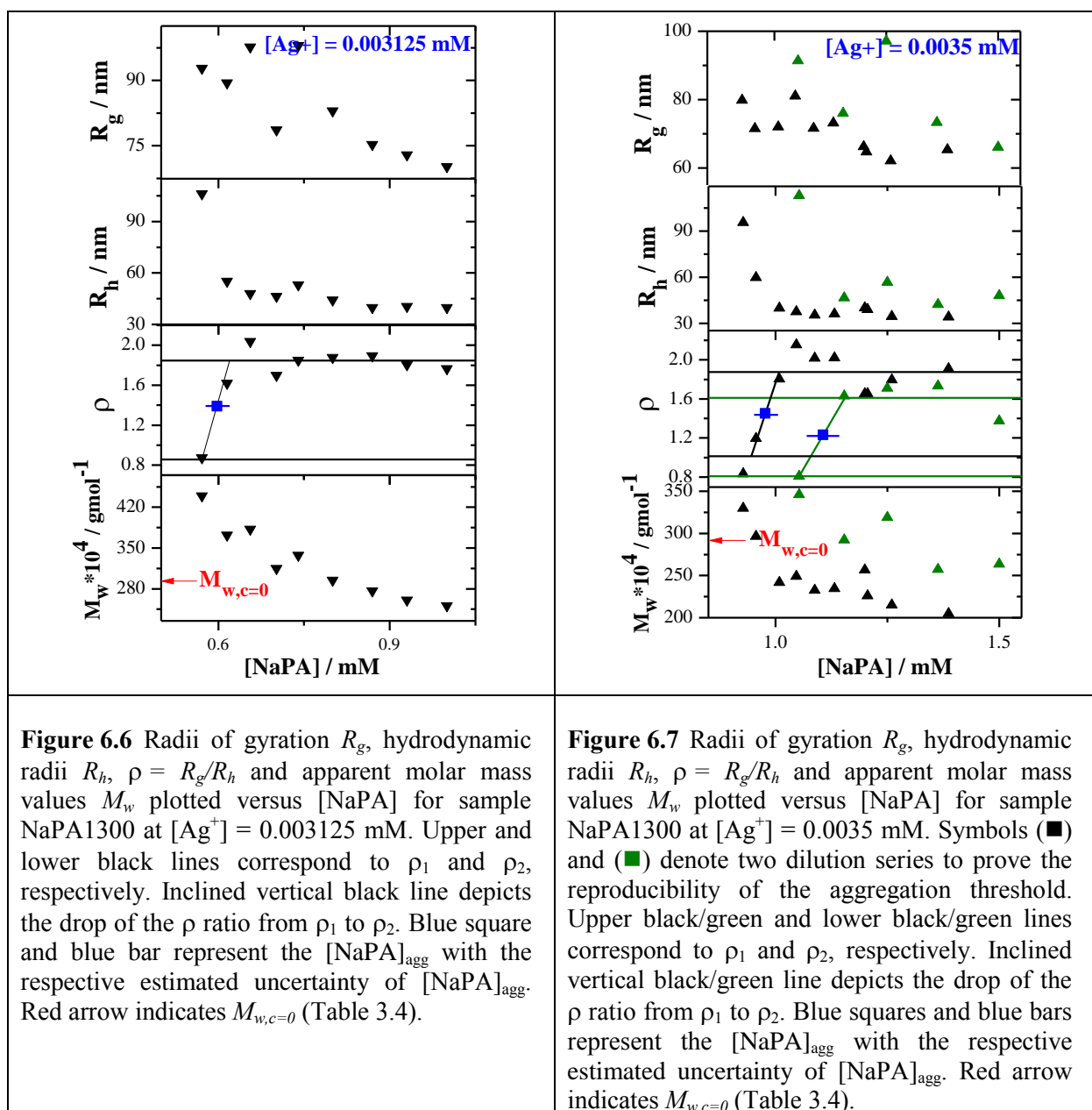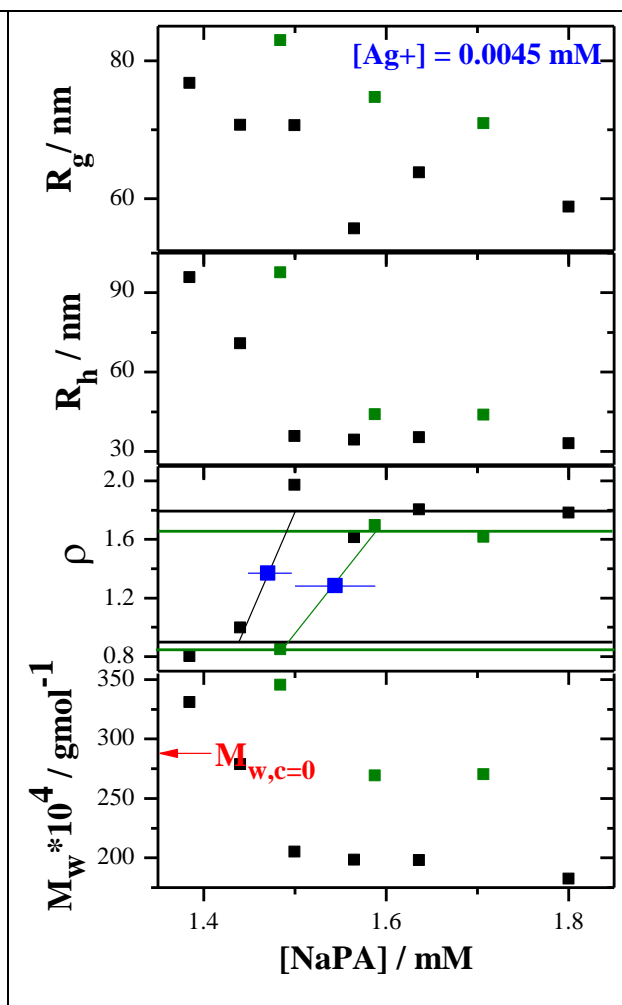
Figure 6.9 Radii of gyration R_g, hydrodynamic radii R_h, $\rho = R_g/R_h$ and apparent molar mass values M_w plotted versus [NaPA] for sample NaPA1300 at [Ag$^+$] = 0.0045 mM. Symbols (■) and (■) denote two dilution series to prove the reproducibility of the aggregation threshold. Upper black/green and lower black/green lines correspond to ρ_1 and ρ_2, respectively. Inclined vertical black/green line depicts the drop of the ρ ratio from ρ_1 to ρ_2. Blue squares and blue bars represent the [NaPA]$_{agg}$ with the respective estimated uncertainty of [NaPA]$_{agg}$. Red arrow indicates $M_{w,c=0}$ (Table 3.4).
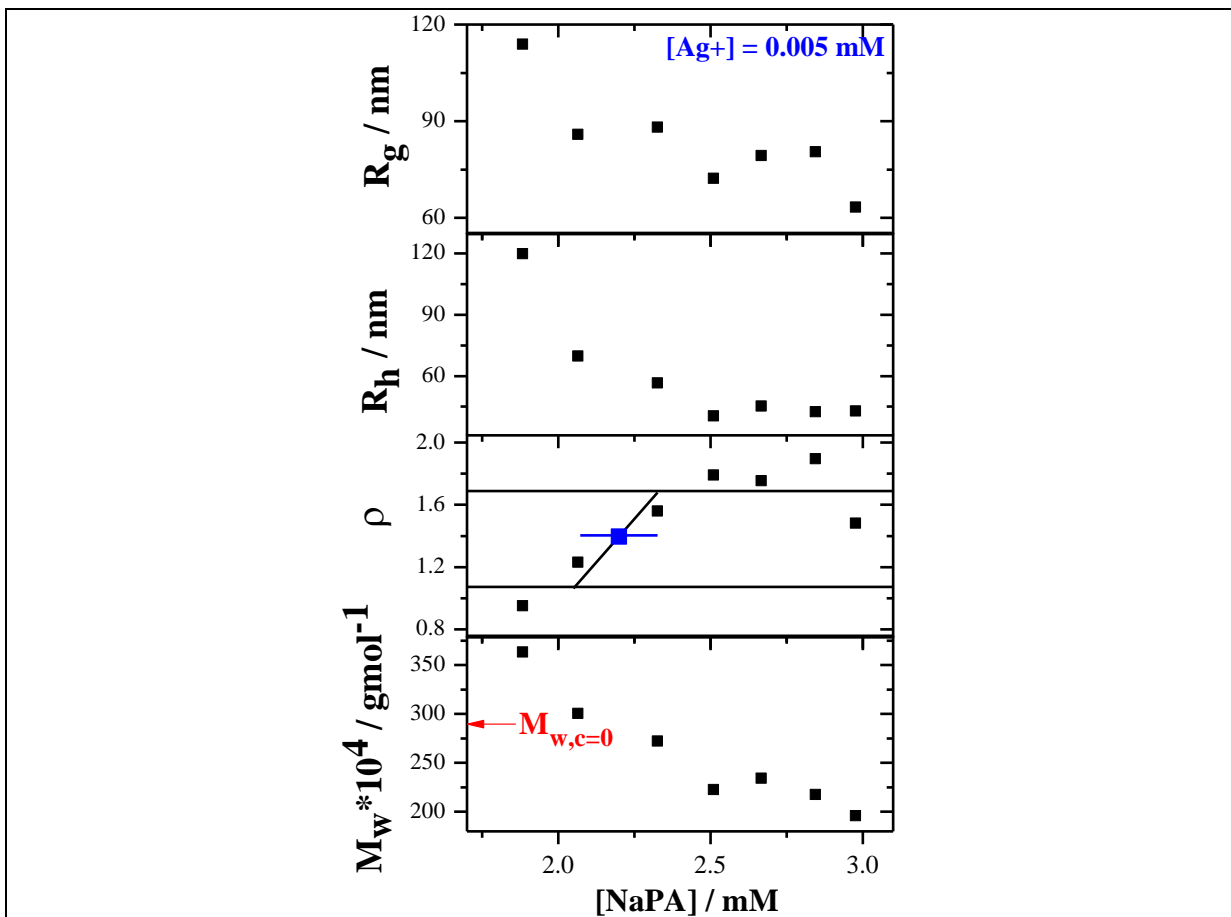
Figure 6.10 Radii of gyration R_g, hydrodynamic radii R_h, $\rho = R_g/R_h$ and apparent molar mass values M_w plotted versus [NaPA] for sample NaPA1300 at $[Ag^+] = 0.005$ mM. Upper and lower black lines correspond to ρ_1 and ρ_2, respectively. Inclined vertical black line depicts the drop of the ρ ratio from ρ_1 to ρ_2. Blue square and blue bar represent the $[NaPA]_{agg}$ with the respective estimated uncertainty of $[NaPA]_{agg}$. Red arrow indicates $M_{w,c=0}$ (Table 3.4).

6.3 Ag-NPs formed Under Exposure to UV-light of Non-aged Dense Unstable Ag⁺-PA aggregates

Figures 6.11 show additional TEM results performed with a higher resolution TEM-microscope of the solution containing $[NaPA] = 2$ mM and $[Ag^+]/[COO^-] = 0.16$. This TEM experiment was made on a different day with different stock solutions, but with the same sample history as applied for the series presented in Figure 4.2.12a. On these TEM-micrographs mono- and polycrystalline structure of Ag-NPs can be recognized by parallel stripes. On Figure 6.11a the particle on the very left side contains rows of parallel stripes with the different directions demonstrating an example of the polycrystalline structure, whereas the biggest Ag-NP of the Figure 6.11b with stripes of the same geometry is a representative example of the monocrystalline structure.
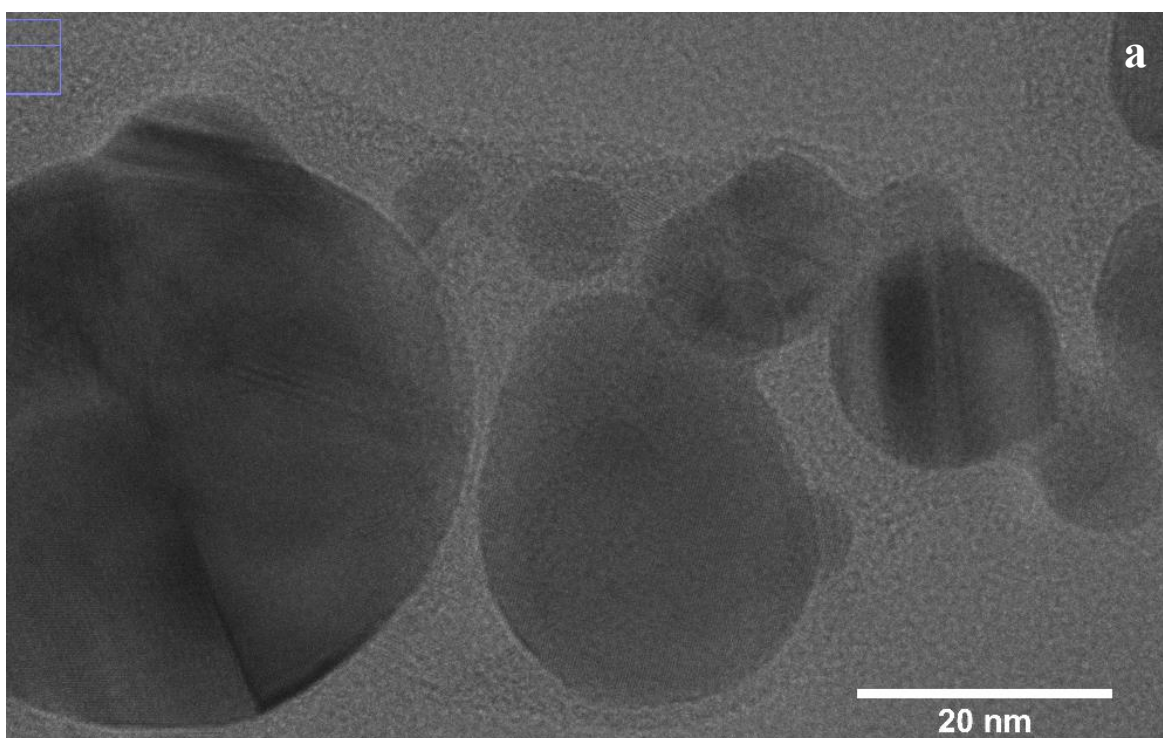
Figure 6.11a TEM images from Ag⁺-PA solution containing $[NaPA] = 2$ mM and $[Ag^+]/[COO^-] = 0.16$ exposed to UV-light for $t_{UV} = 4$ min without aging.
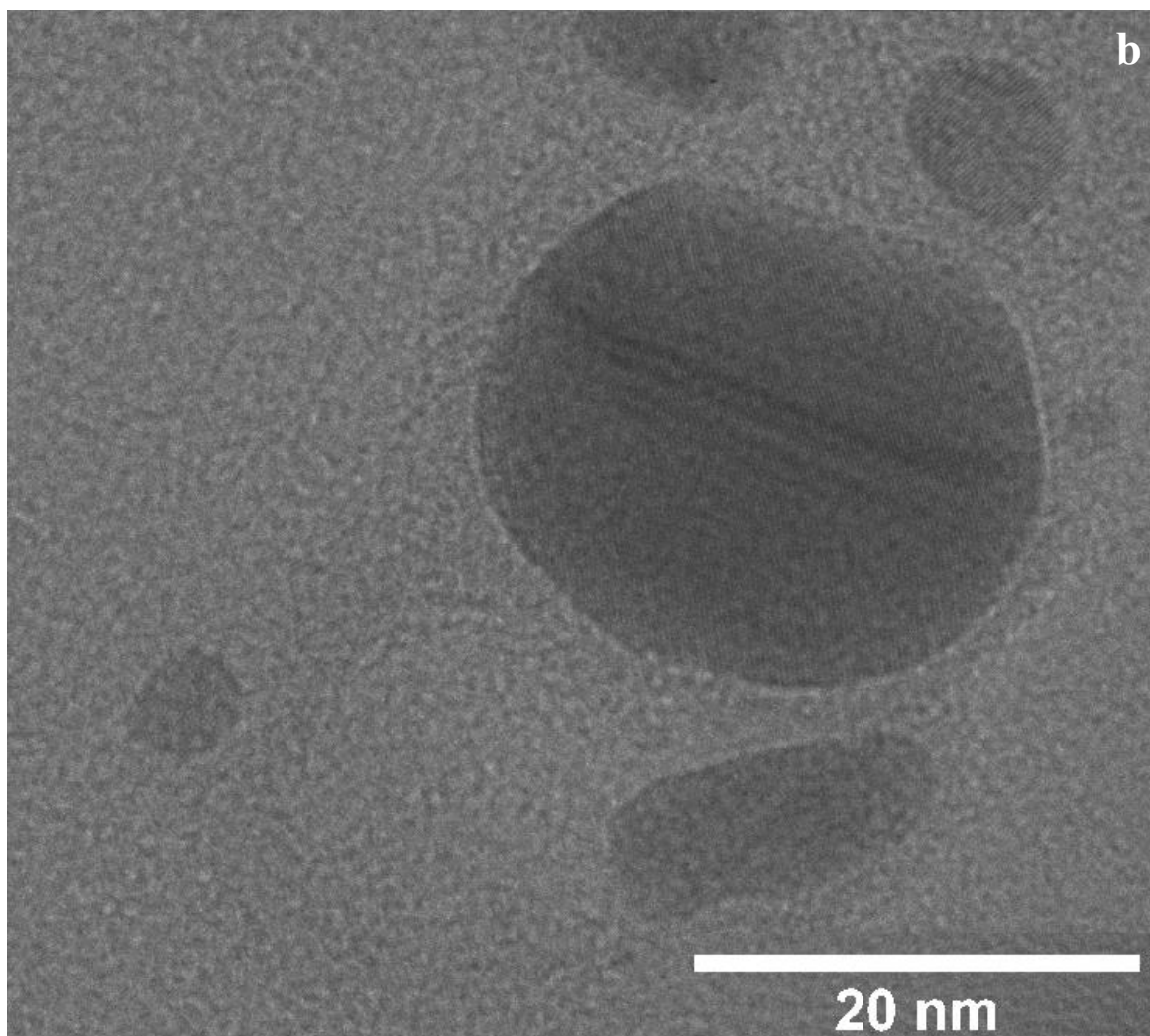
Figure 6.11b TEM images from Ag$^+$-PA solution containing [NaPA] = 2 mM and [Ag$^+$]/[COO$^-$] = 0.16 exposed to UV-light for t_{UV} = 4 min without aging.

167

6.4 Influence of UV-exposure Time on the Size of Ag-NP assemblies

The influence of the exposure time of UV-illumination on the size of entities containing Ag-NPs from aged samples is addressed in the following experiment. Three Ag^+-PA solutions with [NaPA] = 2 mM and $[Ag^+]/[COO^-]$ = 0.16 were analysed in time-resolved mode by SLS/DLS before and after UV-illumination. Aging time was varied between 35 min to 56 min. Duration of UV-exposure was set to t_{UV} = 2, 3 and 4 min.

Figure 6.12 shows the results from the TR-SLS/DLS measurements of this experimental series. The aggregation stops after UV-illumination and the solution gets stable in accordance to Figure 4.2.1. The discrepancy between the size of Ag^+-PA aggregates immediately before UV-exposure and the size of Ag-NP assemblies formed by means of UV-exposure is getting smaller with decreasing t_{UV}. A similar trend is observed in Figure 4.2.1 and Figure 4.2.21 where UV-exposure for 7 min caused the formation of smaller entities than the sample which was exposed to 2.5 min after being aged. Also, the R_g values in Figure 6.12 seem to be less affected than R_h values in agreement with Figure 4.2.6. However, the more significant insight can be expected from a comparison of the R_h values, because they are less affected by the dilution of the UV-illuminated solutions before light scattering characterisation.
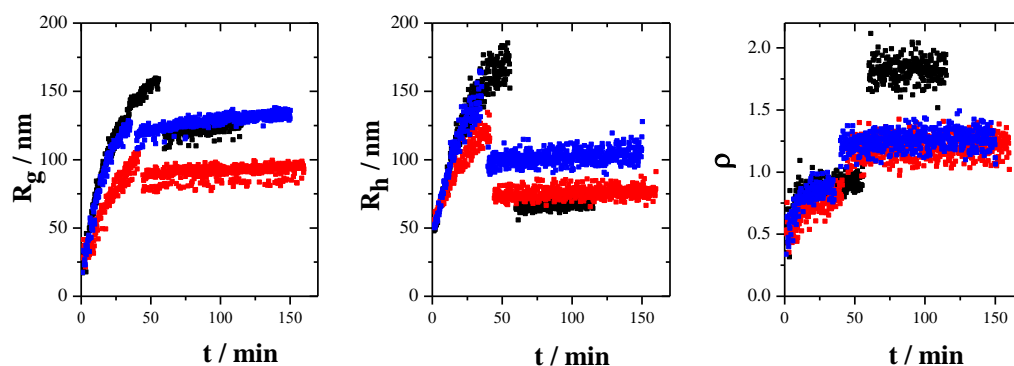
Figure 6.12 Evolution of the radius of gyration R_g, hydrodynamic radius R_h and $\rho = R_g/R_h$ with time t for solutions containing [NaPA] = 2 mM and $[Ag^+]/[COO^-]$ = 0.16 exposed to UV-light for different exposure times t_{UV}: 2 (■), 3 (■) and 4 (■) min at t_{AG} = 56 (■), 41 (■) and 35 (■) min. Prior to the SLS/DLS analysis solutions exposed to UV-light were diluted with aqueous 0.01 M NaNO$_3$ to [NaPA] = 1 mM while the $[Ag^+]/[COO^-]$ ratio was kept unchanged.

Since the aging time t_{AG} in this series of experiments is not identical (35 min, 41 min and 56 min) and the rate of aggregation slightly varies, it is difficult to quantitatively deduce the trends between t_{UV} and the size of Ag-NP assemblies formed under UV-illumination from Ag^+-PA aggregates (Figure 6.12). However, on a qualitative base it is clearly visible that the size of Ag-NP assemblies is tuneable not only by means of the aging time t_{AG} before UV-exposure (Figures 4.2.8-4.2.9), but also by the time of the UV-exposure t_{UV}. The reason for the decrease of the size of the Ag-NP assemblies can be explained by a larger amount of Ag^+ ions reduced to silver atoms at longer UV-exposure, which may lead to decrease of bridging in PA-aggregates and along with it to a partial disassembling of the "containers" for the Ag-NPs.

6.5 Ag-NP Formation induced by the Exposure to UV-light of Ag$^+$-SPB

Figure 6.13a SEM image of Ag-SPB(BA) solution containing [COO$^-$] = 0.25 mM and [Ag$^+$]/[COO$^-$] = 3 exposed to UV-light for t_{UV} = 3 min.

Figure 6.13b SEM images of Ag-SPB(BA) solution containing [COO$^-$] = 0.25 mM and [Ag$^+$]/[COO$^-$] = 10 exposed to UV-light for t_{UV} = 3 min.

| 1 µm | Mag = 15.00 K X | Signal A = SE2
FIB Imaging = SEM
Pixel Size = 7.443 nm | EHT = 0.50 kV
WD = 2.1 mm
8.30e-007 mbar | Tilt Corr. = On
Tilt Angle = 0.0 °
Stage at T = -0.0 ° | Aperture Size = 30.00 µm
High Current = Off
3_04.tif | 24 Feb 2014
9:50:36 | NB |

Figure 6.13c SEM images of Ag-SPB(HMEM) solution containing $[COO^-]$ = 0.25 mM and $[Ag^+]/[COO^-]$ = 3 exposed to UV-light for t_{UV} = 3 min.

| 1 µm | Mag = 15.00 K X | Signal A = SE2
FIB Imaging = SEM
Pixel Size = 7.443 nm | EHT = 0.50 kV
WD = 2.9 mm
8.16e-007 mbar | Tilt Corr. = On
Tilt Angle = 0.0 °
Stage at T = -0.0 ° | Aperture Size = 30.00 µm
High Current = Off
4_04.tif | 24 Feb 2014
10:00:20 | NB |

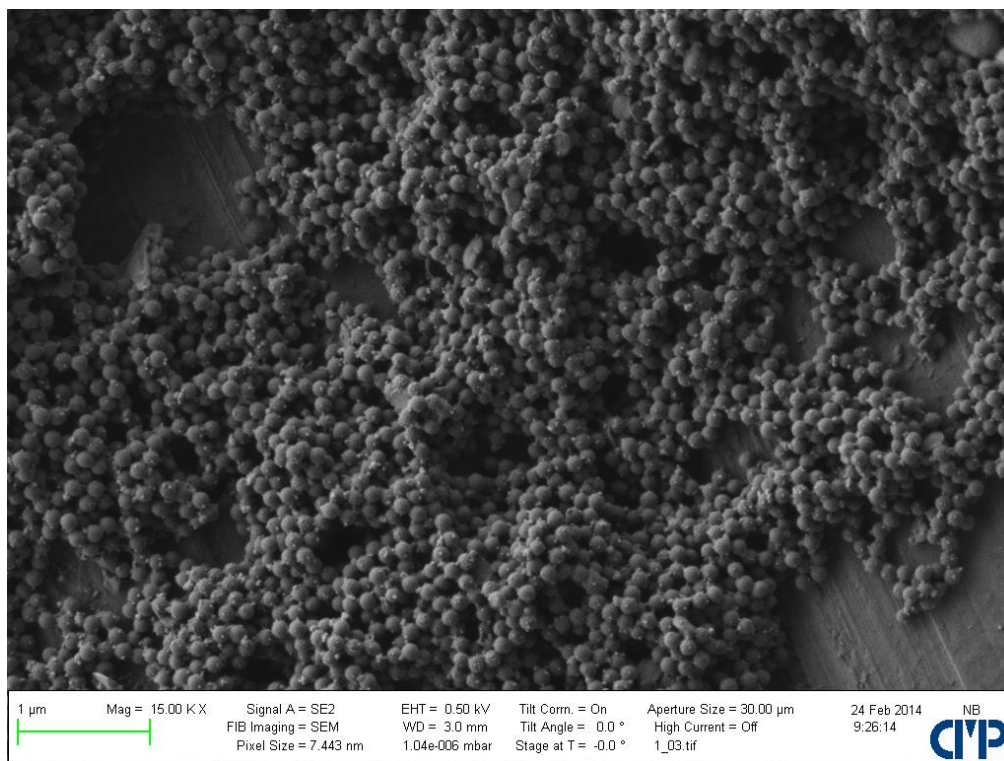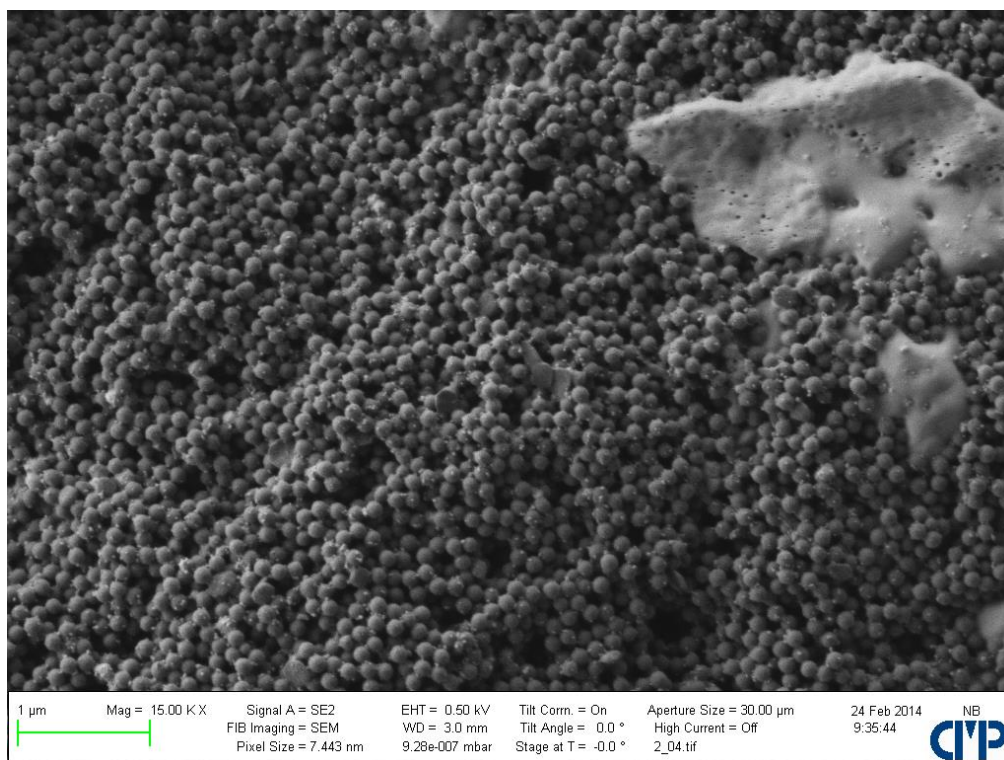**Figure 6.13d** SEM images of Ag-SPB(HMEM) solution containing $[COO^-]$ = 0.25 mM and $[Ag^+]/[COO^-]$ = 10 exposed to UV-light for t_{UV} = 3 min.

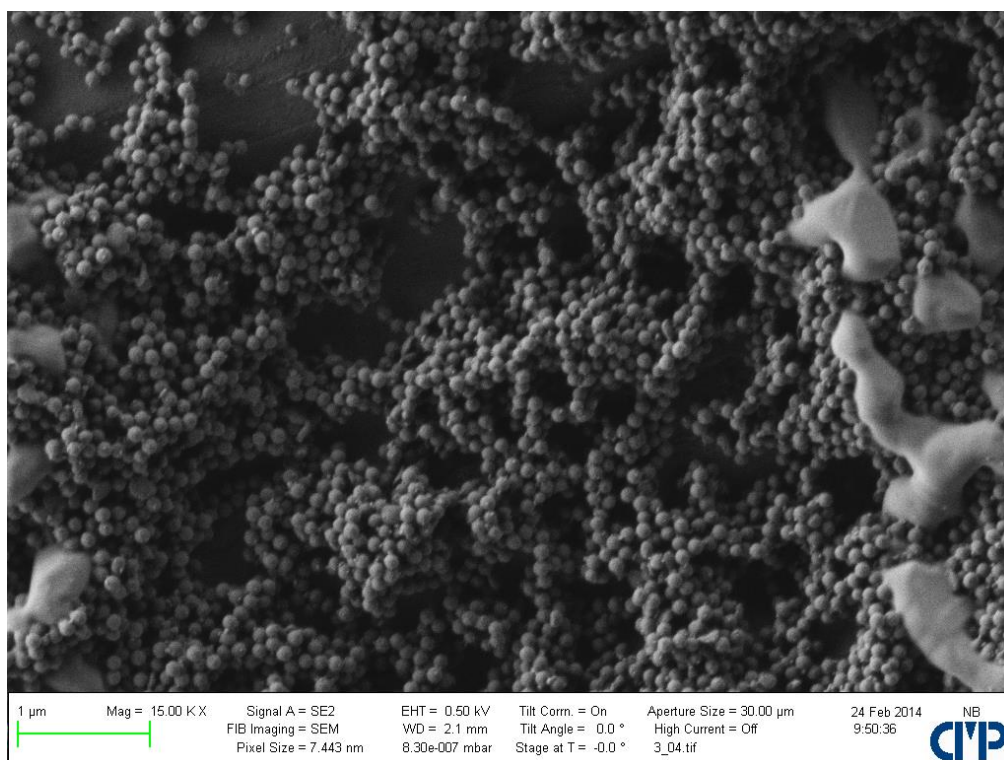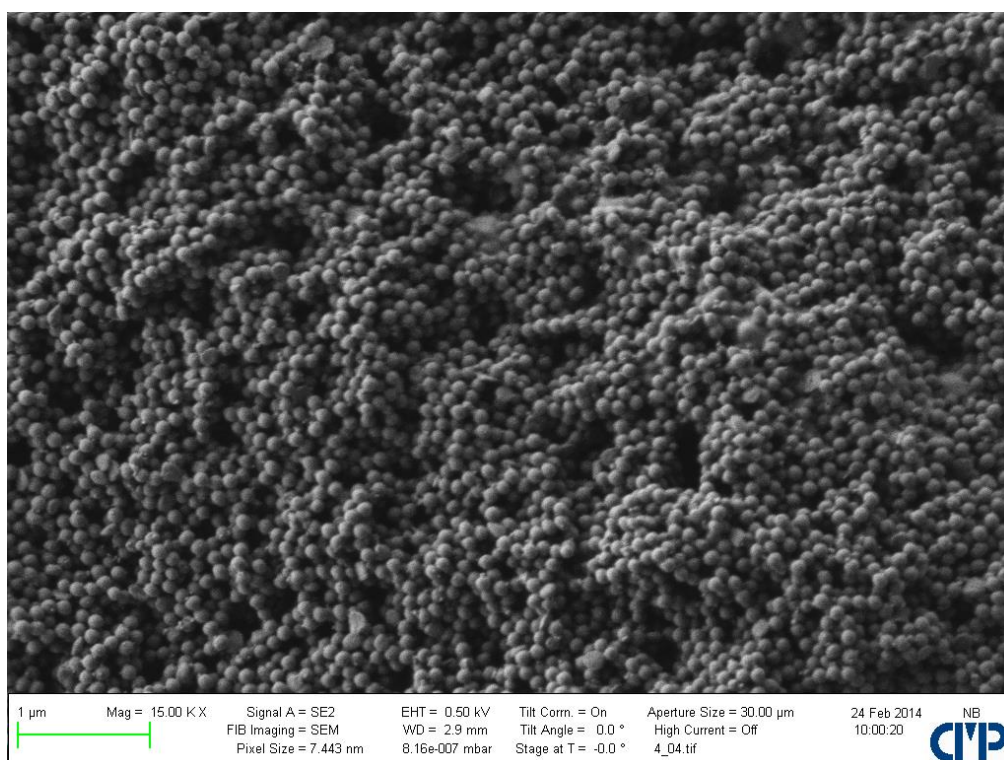# 6.6 Ag-NP Formation induced by
Chemical Reducing Agent (NaBH$_4$) in Ag$^+$-SPB
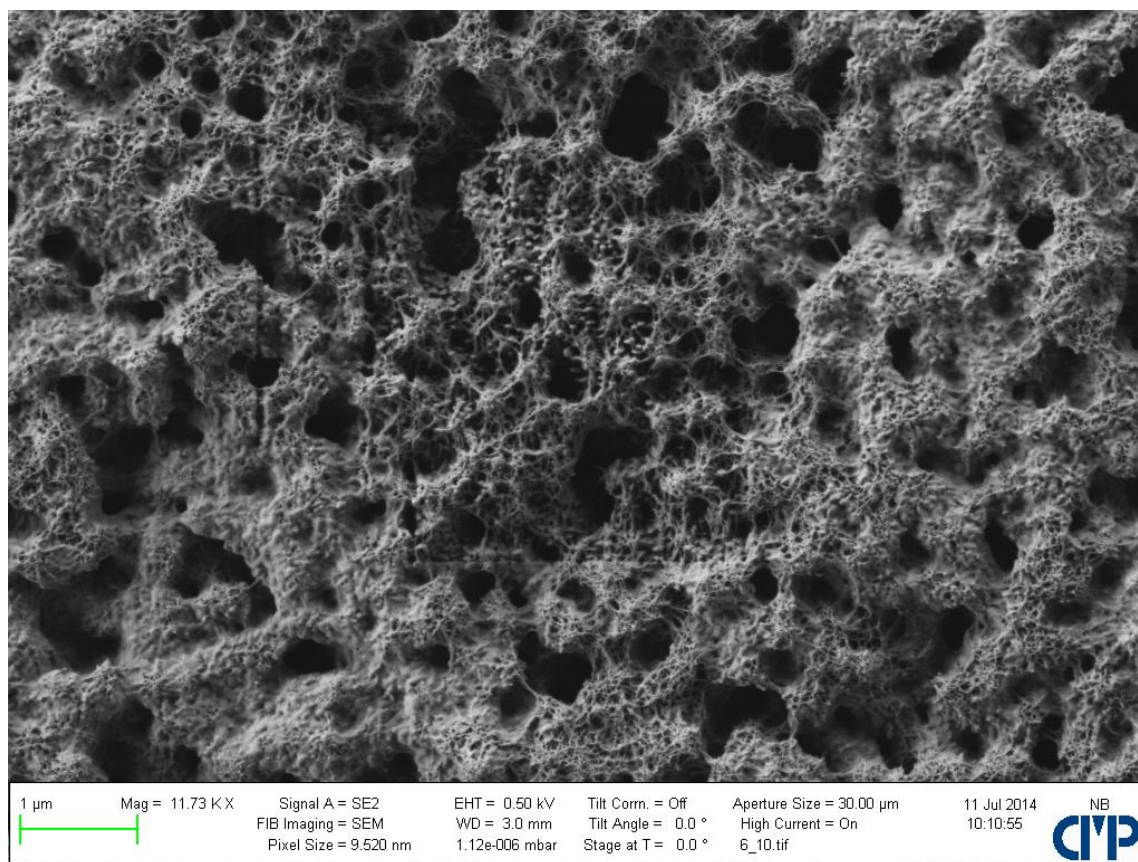
Figure 6.14 SEM images of Ag-SPB(HMEM) solution containing [COO$^-$] = 0.25 mM, [Ag$^+$]/[COO$^-$] = 15 and [NaBH$_4$]/[Ag$^+$] = 5 before ultrafiltration.

References

[1]   Manning, G.S. *Acc. Chem. Res.* **1979**, *12,* 443

[2]   Kitano, T.; Taguchi, A.; Noda, I.; Nagasawa, M. *Macromolecules* **1980**, *13*, 57

[3]   Takahashi, A; Nagasawa, M. *J. Am. Chem. Soc.* **1964**, *86,* 543

[4]   Wang, L.; Yu, H. *Macromolecules* **1988**, *21,* 3498

[5]   Schweins, R.; Hollmann, J.; Huber, K. *Polymer* **2003**, *44,* 7131

[6]   Ikegami, A.; Imai, N. *J. Polym. Sci.* **1962**, *56,* 133

[7]   Volk, N.; Vollmer, D.; Schmidt, M.; Oppermann, W.; Huber, K. *Adv. Polym. Sci.* **2004**, *166,* 29

[8]   Eisenberg, H.; Mohan, G.R. *J. Phys. Chem.* **1959**, *63*, 671; Eisenberg, H.; Casassa, E.F. *J. Polym. Sci.* **1960**, *47*, 29

[9]   Wall, F.T.; Drenan, J.W. *J. Polym. Sci.* **1951**, *7*, 83

[10]   Michaeli, I. *J. Polym. Sci.* **1960**, *48,* 291

[11]   Schweins, R; Huber, K. *Eur. Phys. J E* **2001**, *5,* 117

[12]   Schweins, R.; Lindner, P.; Huber, K. *Macromolecules* **2003**, *36,* 9564

[13]   Lages, S.; Lindner, P.; Sinha, P.; Kiriy, A.; Stamm, M.; Huber, K. *Macromolecules* **2009**, *42*, 9564

[14]   Goerigk, G.; Schweins, R.; Huber, K.; Ballauff, M. *Europhys. Lett.* **2004**, *66*, 331

[15]   Lages, S.; Michels, R.; Huber, K. *Macromolecules* **2010**, *43,* 3027

[16]   Schweins, R.; Goerigk, G.; Huber, K. *Eur. Phys. J E* **2006**, *21,* 99

[17]   Lages, S.; Goerigk, G.; Huber, K. *Macromolecules* **2013**, *46,* 3570

[18]   Ikeda, Y.; Beer, M.; Schmidt, M.; Huber, K. *Macromolecules* **1998**, *31*, 728

[19]   Huber, K.; Witte, T.; Hollmann, J.; Keuker-Baumann, S. *J. Am. Chem. Soc.* **2007**, *129*, 1089

[20]   Olvera de la Cruz, M.; Belloni, L.; Delsanti, M.; Dalbiez, J.P.; Spalla, O.; Drifford, M. *J. Chem. Phys.* **1995**, *103*, 5781

[21]   Wittmer, J.; Johner, A.; Joanny, J.F. *J. Phys. (Paris) II* **1995**, *5*, 635

[22]   Kubal, J. *Nature* **1962**, *4821*, 1175

[23]   Kubal, J. Silver hydrosols, CS 108244, 19630815, **1963**

[24]   Konishi, Y.; Saijo, H.; Hada, H.; Tamura, M. *Nature* **1977**, *268*, 709

[25]   Taush-Treml, R.; Henglein. A.; Lilie, J. *Ber. Bunsen-Ges. Phys. Chem.* **1978**, *82*, 1335; Hada, H.; Yonezawa, Y.; Yoshida, A.; Kurakake, A. *J. Phys. Chem.* **1976**, *80*, 2728; Yonezawa, Y.; Sato, T.; Ohno, M.; Hada, H. *J. Chem. Soc. Faraday Trans. 1.* **1987**, *83*, 1559; Yonezawa, Y.; Sato, T.; Kuroda, S.; Kuge, K. *J. Chem. Soc. Faraday Trans.* **1991**, *87*, 1905

[26]   Henglein, A. *Chem. Phys. Lett.* **1989**, *154*, 473; Mulvaney, P.; Henglein, A. *J. Phys. Chem.* **1990**, *94*, 4182

[27]   Henglein, A.; Linnert, T.; Mulvaney, P. *Ber. Bunsen-Ges. Phys. Chem.* **1990**, *94*, 1449

[28]   Mostafavi, M.; Keghouche, N.; Delcourt, M.O.; Belloni, J. *Chem. Phys. Lett*. **1990**, *167*, 193

[29]   Yonezawa, Y.; Takami, A.; Sato, T.; Yamamoto, K.; Sasanuma, T.; Ishida, H.; Ishitani, A. *J. Appl. Phys.* **1990**, *68*, 1297; Yonezawa, Y.; Kijima, M.; Sato, S. *Ber. Bunsen-Ges. Phys. Chem.* **1992**, *96*, 1828

[30]   Sato, T.; Yonezawa, Y.; Hada, H. *J. Soc. Photogr. Sci. Technol. Jpn.* **1988**, *51*, 122; Sato, T.; Ichikawa, T.; Ito, T.; Yonezawa, Y.; Kadono, K.; Sakaguchi, T.; Miya, M. *Chem. Phys. Lett.* **1995**, *242*, 310

[31]   Ershov, B.G.; Henglein, A. *J. Phys. Chem. B* **1998**, *102*, 10663

[32]   Ershov, B.G.; Henglein, A. *J. Phys. Chem. B* **1998**, *102*, 10667

[33]   Remita, S.; Orts, J.M.; Feliu, J.M.; Mostafavi, M.; Delcourt, M.O. *Chem. Phys. Lett.* **1994**, *218*, 115

[34]   Shiraishi, Y.; Toshima, N. *Colloids and Surfaces A: Physicochem. Eng. Aspects* **2000**, *169*, 59

[35]   Sergeev, B.M.; Kiryukhin, M.V.; Prusov, A.N.; Sergeev, V.G. *Vestn. Mosk. Un-ta. Ser. 2* **1999**, *40*, 129

[36]   Sergeev, B.M.; Sergeev, G.B. *Colloid Journal* **2007**, *69*, 639

[37]   Falletta, E.; Bonini, M.; Fratini, E.; Lo Nostro, A.; Pesavento, G.; Becheri, A.; Lo Nostro, P.; Canton, P.; Baglioni, P. *J. Phys. Chem. C* **2008**, *112*, 11758

[38]   Zhang, Z.; Patel, R.C.; Kothari, R.; Johnson, C.P.; Friberg, S.E.; Aikens, P.A. *J. Phys. Chem. B* **2000**, *104*, 1176

[39]   Lee, G.J.; Shin, S.-II.; Oh, S.G. *Chemistry Letters (The Chemical Society of Japan)* **2004**, *33*, 118

[40]   Mitra, A.; Bhaumik, A. *Materials Letters* **2007**, *61*, 659

[41]   Balan, L.; Schneider, R.; Lougnot, D. J. *Progress in Organic Coatings* **2008**, *62*, 351

[42] Guzmán, M.G.; Dille, J.; Godet, S. *International Journal of Chemical and Biological Engineering* **2009**, *2*, 104

[43] Panáček, A.; Prucek, R.; Hrbáč, J.; Nevečná, T.; Šteffková, J.; Zbořil, R.; Kvítek, L. *Chem. Materials* **2014**, *26*, 1332

[44] Rühe, J.; Ballauff, M.; Biesalski, M.; Dziezok, P.; Gröhn, F.; Johannsmann, D.; Houbenov, N.; Hugenberg, N.; Konradi, R.; Minko, S.; Motornov, M.; Netz, R.R.; Schmidt, M.; Seidel, C.; Stamm, M.; Stephan, T.; Usov, D.; Zhang, H. *Adv. Polym. Sci.*, **2004**, *165*, 79

[45] Belder, G.F.; ten Brinke, G.; Hadziioannou, G., *Langmuir*, **1997**, *13*, 4102; Hariharan, R.; Biver, C.; Mays, J.; Russel, W.B., *Macromolecules*, **1998**, *31*, 7506; Wittmer, J.; Joanny, J.F., *Macromolecules*, **1993**, 26, 2691

[46] Guo, X.; Weiss, A.; Ballauff, M. *Macromolecules* **1999**, *32*, 6043

[47] Wang, X.; Wu, S.; Li, L.; Zhang, R.; Zhu, Y.; Ballauff, M.; Lu, Y.; Guo, X.H. *Ind. Eng. Chem. Res.* **2011**, *50*, 3564

[48] Guo, X. *Synthesis and Study of the Colloidal Polyelectrolyte Brushes Prepared by Photo-emulsion Polymerisation* **2001**, Logos Verlag, Berlin

[49] Guo, X.; Ballauff, M. *Langmuir* **2000**, *16*, 8719

[50] Zhulina, E.B.; Borisov, O.V.; Birshtein, T.M. *Macromolecules* **1999**, *32*, 8189; Borisov, O.V.; Birshtein, T.M.; Zhulina, E.B. *J. Phys. II (France)* **1991**, *1*, 521

[51] Guo, X.; Ballauff, M. *Physical Review E* **2001**, *64*, 051406

[52] Jusufi, A.; Borisov, O.; Ballauff, M. *Polymer* **2013**, *54*, 2028

[53] Biesalski, M.; Jonannsmann, D.; Rühe, J. *J. Chem. Phys.* **2004**, *120*, 8807

[54] Konradi, R.; Rühe, J. *Macromolecules* **2005**, *38,* 4345

[55] Mei, Y.; Ballauff, M. *Eur. Phys. J. E* **2005**, *16*, 341

[56] Scott, R.W.J.; Wilson, O.M.; Crooks, R.M.; *J. Phys. Chem. B* **2005**, *109*, 692

[57] Lu, Y.; Mei, Y.; Drechsler, M.; Ballauff, M. *J. Phys. Chem. B* **2006**, *110*, 3930

[58] Sun, Q.; Deng, Y. *Langmuir* **2005**, *21*, 5812

[59] Lu, Y.; Mei, Y.; Walker, R., Ballauff, M.; Drechsler, M. *Polymer* **2006**, *47*, 4985

[60] Lu, Y.; Mei, Y.; Schrinner, M.; Ballauff, M.; Möller, M.W.; Breu, J. *J. Phys. Chem. C* **2007**, *111*, 7676

[61] Gupta, S.; Uhlmann, P.; Agrawal, M.; Chapuis, S.; Oertel, U.; Stamm, M. *Macromolecules* **2008**, *41*, 2874

[62] Li, G.S.; Xu, J.; Zhao, S.F.; Zhu, Y.Q.; Li, L.; Guo, X.H. *Z. Phys. Chem.* **2012**, *226*, 613

[63]   Liu, J.; Wang, J.; Zhu, Z.; Li, Li; Guo, X.; Lincoln, S.F.; Prud'homme, R.K. *AlChE Journal* **2014**, *60*, 1977

[64]   Veselago, V.G. *Sov. Phys. Uspekhi* **1968**, *10*, 509

[65]   Zheludev, N.I. *Science* **2010**, *328*, 582

[66]   Soukoulis, C.M.; Wegener, M. *Nature Photonics* **2011**, *5*, 523

[67]   Schurig, D.; Mock, J.J.; Justice, B.J.; Cummer, S.A.; Pendry, J.B.; Starr, A.F.; Smith, D.R. *Science* **2006**, *314*, 977

[68]   Valentine, J.; Li, J.; Zentgraf, T.; Bartal, G.; Zhang, X. *Nat. Mater.* **2009**, *8*, 568

[69]   Chen, P.Y.; Soric, J.; Alù, A. *Adv. Mater.* **2012**, *24*, 281

[70]   Liu, Z.; Lee, H.; Xiong, Y.; Sun, C.; Zhang, X. *Science* **2007**, *315*, 1686; Smolyaninov, I.I.; Hung, Y.-J.; Davis, C. C. *Science* **2007**, *315*, 1699

[71]   Alù, A.; Engheta, N. *Optics Express* **2009**, *17*, 5723

[72]   Enkrich, C.; Wegener, M.; Linden, S.; Burger, S.; Zschiedrich, L.; Schmidt, F.; Zhou, J.F.; Koschny, T.; Soukoulis, C.M. *Phys. Rev. Lett.* **2005**, *95*, 203901

[73]   Valentine, J.; Zhang, S.; Zentgraf, T.; Ulin-Avila, E.; Genov, D.A.; Bartal, G.; Zhang, X. *Nature* **2008**, *455*, 376

[74]   Rockstuhl, C.; Lederer, F.; Etrich, C.; Pertsch, T.; Scharf, T. *Phys. Rev. Lett.* **2007**, *99*, 017401

[75]   Simovski, C. R.; Tretyakov, S.A. *Phys. Rev. B* **2009**, *79*, 045111

[76]   Vallecchi, A.; Albani, M.; Capolino, F. *Opt. Express* **2011**, *19*, 2754

[77]   Alù, A.; Salandrino, A.; Engheta, N. *Opt. Express* **2006**, *14*, 1557

[78]   Mühlig, S.; Cunningham, A.; Scheeler, S.; Pacholski, C.; Burgi, T.; Rockstuhl, C.; Lederer, F. *ACS Nano* **2011**, *5*, 6586

[79]   Mühlig, S.; Rockstuhl, C.; Yannopapas, V.; Bürgi, T.; Shalkevich, N.; Lederer, F. *Opt. Express* **2011**, *19*, 9607

[80]   Sheikholeslami, S.N.; Alaeian, H.; Koh, A.L.; Dionne J.A. *Nano Lett.* **2013**, *13*, 4137

[81]   Qian. Z.; Hastings, S.P.; Li, C.; Edward, B.; McGinn, C.K.; Engheta, N.; Fakhraai, Z.; Park, So-Jung. *ACS Nano* **2015**, *9*, 1263

[82]   Urban, A.S.; Shen, X.; Wang, Y.; Large, N.; Wang, H.; Knight, M.W.; Nordlander, P.; Chen, H.; Halas, N.J. *Nano Lett.* **2013**, *13*, 4399

[83]   Wheeler, M.S.; Aitchison, J.S.; Mojahedi, M. *Phys. Rev. B* **2005**, *72*, 193103

[84]   Kelly, K.L.; Coronado, E.; Zhao, L.L.; Schatz, G.C. *J. Phys. Chem. B* **2003**, *107*, 668

[85]   Riikonen, S.; Romero, I.; Garca de Abajo, F.J. *Phys. Rev. B* **2005**, *71*, 235104

[86]   Lu, Y.; Mei, Yu; Drechsler, M.; Ballauff, M. *Angew. Chem. In. Ed.* **2006**, *45*, 813

[87]   Ahamed, M.; Karns, M.; Goodson, M.; Rowe, J.; Hussain, S.M.; Schlager, J.J.; Hong, Y. *Toxicology and Applied Pharmacology* **2008**, *233*, 404

[88]   Sondi, I.; Salopek-Sondi, B. *Journal of Colloid and Interface Science* **2004**, *275*, 177

[89]   Sun, Y.; Xia, Y. *Science* **2002**, *298*, 2176

[90]   Callegari, A.; Tonti, D.; Chergui, M. *Nano Lett.* **2003**, *3*, 1565

[91]   Taleb, A.; Petit, C.; Pileni, M.P. *Chem. Mater.* **1997**, *9*, 950

[92]   Brust, M.; Kiely, C.J. *Colloids and Surfaces A*: *Physicochem. Eng. Aspects* **2002**, *202*, 175

[93]   Falletta, E.; Bonini, M.; Fratini E.; Lo Nostro, A.; Pesavento, G.; Becheri, A.; Lo Nostro, P.; Canton, P.; Baglioni, P. *J. Phys. Chem. C* **2008**, *112*, 11758

[94]   Evans, D.F.; Wennerström, H. *The colloidal domain: where physics, chemistry, biology and technology meet* **1999**, Willey-VCH, 2nd ed., New York

[95]   Huber, K. *J. Phys. Chem.* **1993**, *97,* 9825

[96]   Sharma, G.; Ballauff, M. *Macromol. Rapid. Commun.* **2004**, *25*, 547

[97]   Zhu, Z.; Guo, X.H.; Wu, S.; Zhang, R.; Wang, J.; Li, L. *Ind. Eng. Chem. Rev.* **2011**, *50*, 13848

[98]   Wu, S.; Kaiser, J.; Guo, X.H.; Li, L.; Lu, Y.; Ballauff, M. *Ind. Eng. Chem. Rev.* **2011**, *51*, 5608

[99]   Lindner, P.; Zemb, T. *Neutrons, X-rays and Light: Scattering Methods Applied to Soft Condensed Metter* **2002**, Elsevier Science, Amsterdam

[100]   Berne, B.J.; Pecora, R. *Dynamic Light Scattering with Applications to Chemistry, Biology and Physics* **2000**, Dover Publications Inc., New York

[101]   Chu, B. *Laser Light Scattering* **2007**, Dover Publications Inc., New York

[102]   Schärtl, W. *Light Scattering from Polymer Solutions and Nanoparticle Dispersions* **2007**, Springer Verlag, Heidelberg

[103]   Teraoka, I. *Polymer Solutions* **2002**, Wiley Interscience, New York

[104]   Colby, R.H.; Rubinstein, M. *Polymer Physics* **2003**, Oxford University Press

[105]   Rayleigh, L. *Proc. R. Soc. London* **1914**, *A90*, 219

[106]   Yamakawa, H. *Modern Theory of Polymer Solutions* **2001**, Electronic Edition

[107] Øgendal, L. *Light Scattering Demystified. Theory and Practice* **2013**, University of Copenhagen

[108] ALV / CGS-3 *A Guide to perform simultaneous Dynamic & Static Light Scattering Measurements using the ALV-5000 & 60X0 Software*

[109] Zimm, B. *J. Chem. Phys.* **1948**, *16*, 1099

[110] Guinier, A.; Fournet, G. *Small Angle Scattering of X-rays* **1955**, Wiley, New York

[111] Siegert, A.J.F. *MIT Radiation Lab* **1943**, Report No.465

[112] Mandel, L. *Prog. Opt.* **1963**, *2*, 181

[113] Provencher, S.W. *Comput. Phys.* **1982**, *27*, 213. *Comput. Phys.* **1982**, *27*, 229

[114] Koppel, D.E. *J. Chem. Phys.* **1972**, *57*, 4814

[115] Brown, J.C.; Pusey, P.N.; Dietz, R. *J. Chem. Phys.***1975**, *62*, 1136

[116] Stockmayer, W.H. *Pure Appl. Chem.* **1982**, *54*, 407; *Macromolecules* **1984**, *17*, 509

[117] Burchard, W.; Schmidt, M.; Stockmayer, W.H. *Macromolecules* **1980**, *13*, 580; *Macromolecules* **1980**, *13*, 1265

[118] Akcasu, A.Z.; Benmouna, M.; Han, C.C. *Polymer* **1980**, *21*, 866

[119] Einstein, A. *Ann. Physik Leipzig* **1905**, *17*, 549

[120] Huber, K.; Bantle, S.; Lutz, P.; Burchard, W. *Macromolecules* **1985**, *18*, 1461

[121] Schmidt, M. *Simultaneous Static and Dynamic Light Scattering: Application to Polymer Structure Analysis in Dynamic Light Scattering: The Method and Some Applications* W. Brown (Hrsg.)*,* **1993**, Clarendon Press, Oxford

[122] Burchard, W. *Adv. Polym. Sci.* **1983**, *48*, 1-124 (see chapter D therein)

[123] Schweins, R.; Hollmann, J.; Huber, K. *Polymer* **2003**, *44,* 7131

[124] Akcasu, A.Z.; Benmouna, M. *Macromolecules* **1978**, *11*, 1193

[125] Kunz, D.; Thurn, A.; Burchard, W. *Colloid Polym. Sci.* **1983**, 261, 635

[126] Becker, A.; Schmidt, M. *Macromol. Chem. Macromol. Symp.* **1991**, *50*, 249

[127] Glatter, O.; Kratky, O. *Small Angle X-Ray Scattering* **1982**, Academic Press, London

[128] Stribeck, N. *X-Ray Scattering of Soft Matter* **2008**, Springer Verlag, Heidelberg

[129] Huber, K.; Scheler, U. *Current Opinion in Colloid & Interface Science* **2012**, *17*, 64

[130] Goerigk, G.; Huber, K.; Schweins, R. *J. Chem. Phys.* **2007**, *127*, 154908

[131] Stuhrmann, H.B. *Adv. Polym. Sci.* **1985**, *67*, 123

[132] Debye, P. *Ann. Physik Leipzig* **1915**, *46***, 809

[133] Cromer, D.T.; Liberman, D. *J. Chem. Phys.* **1970**, *53*, 1891

[134] Cromer, D.T.; Liberman, D. *Acta Crystallogr., Sect. A: Cryst. Phys., Diffr., Theor. Gen. Crystallogr.* **1981**, *A37*, 267

[135] Porod, G. *Kolloid Z.* **1951**, *124*, 83

[136] Shannon, R. D. *Acta Crystallogr.* **1976**, *A32*, 751

[137] Goerigk, G. Electronic and Computer Upgrade at ASAXS Beamline JUSIFA. HASYLAB *Annual Report* **2006**, 77

[138] Haubold, H.G.; Gruenhagen, K.; Wagener, M.; Jungbluth, H.; Heer, H.; Pfeil, A.; Rongen, H.; Brandenburg, G.; Moeller, R.; Matzerath, J.; Hiller, P.; Halling, H. *Rev. Sci. Instrum.* **1989**, *60*, 1943

[139] Lages, S. *Dissertation zur Erlanung des Grades eines Doktors der Naturwissenschaften* **2009**, Paderborn

[140] Goerigk, G.; Huber, K.; Mattern, N.; Williamson, D. L. *Eur. Phys. J. Spec. Top.* **2012**, *208*, 259

[141] McNaught, A. D.; Wilkinson, A. *IUPAC. Compendium of Chemical Terminology, (the "Gold Book")* **1997**, Blackwell Scientific Publications, Oxford; *Green Book: IUPAC Quantities, Units and Symbols in Physical Chemistry*, **1993**, Blackwell Scientific Publications, Oxford

[142] Burda, C.; Chen, X.; Narayanan, R.; El-Sayed, M.A. *Chem. Rev.* **2005**, *105*, 1025

[143] Han, Z.; Bozhevolnyi, S.I. *Rep. Prog. Phys.* **2013**, *76*, 016402

[144] Berry, G.C. *J. Chem. Phys.* **1966**, *44*, 4550

[145] Ahmed, S.M.; El-Aasser, M.S.; Pauli, G.H.; Poehlein, G.W.; Vanderhoff, J.W. *Journal of Colloid and Interface Science* **1980**, *73*, 388; Wilkinson, M.C.; Hearn, J.; Cope, P.; Chainey, M. *The British Polymer Journal* **1981**, *13*, 82

[146] Brandrup, J.; Immergut, E. *Polymer Handbook*, 3rd ed. **1989**, Wiley, New York

[147] Hariharan, R.; Biver, C.; Mays, J.; Russel, W.B. *Macromolecules* **1998**, *31*, 7506

[148] Guptha, V.S.; Hsiao, P.Y. *Polymer* **2014**, *55*, 2900

[149] Liu, J.; Rieger, J.; Huber, K. *Langmuir* **2008**, *24*, 8262

[150] Debye, P. *J. Colloid Chem.* **1947**, *51*, 18

[151] Greschner, G.S. *Makromol. Chem.* **1973**, *170*, 203

[152] Mock, J.J.; Barbic, M.; Smith, D.R.; Schultz, D. A.; Schultz, S. *J. Chem. Phys.* **2002**, *116*, 6755

[153] Skillman, D. C.; Berry, C. R. *J. Chem. Phys.* **1968**, *48*, 3297

[154] Abargues, R.; Albert, S.; Valdes, J.L.; Abderrafi, K.; Martınez-Pastor, J.P. *J. Mater. Chem.* **2012**, *22*, 22204

[155] Zhang, Z.; Wu, Y. *Langmuir* **2010**, 26, 9214

[156] McGill W.J.; Ackerman L. *J. Appl. Polym. Sci.* **1975**, *19*, 2773

[157] Rånby B. *J.M.C. – Pure Appl. Chem.* **1993**, *A30*, 583

[158] Saita T. *JJAP* **1980**, *19(12)*, 2501

[159] Saita T.; Matumura On. *JJAP* **1983**, *22*, 1310

[160] Ishikawa M. *Journal of Polymer Science: Part A-2* **1969**, *7*, 993

[161] Grassie N.; Davis T. I. *Die Makromolekulare Chemie* **1974**, *175*, 2657

[162] Amendola, V.; Bakr, O.M.; Stellacci, F. *Plasmonics* **2010**, *5*, 85

[163] Henglein, A. *Chem. Mater.* **1998**, *10*, 444

[164] Widoniak, J.; Eiden-Assmann, S.; Maret, G. *Colloids and Surfaces A: Physicochemical and Engineering Aspects* **2005**, *270/271*, 340

[165] Porod, G. *Kolloid-Z.* **1951**, *124*, 83

[166] Deschamps, A.; De Geuser, F. *J. Appl. Cryst.* **2001**, *44*, 343

[167] Mei, Yu.; Lauterbach, K.; Hoffmann, M.; Borisov, O.V.; Ballauff, M.; Jusufi, A. *PRL* **2006**, *97*, 158301

Curriculum Vitae

Anna Ezhova, Chem.-Dipl.

PERSONAL INFORMATION

Date and place of birth   March 31st 1989 in Malmyzh, Russia
E-mail   annezhova@gmail.com

QUALIFICATIONS

06/2015   **Ph.D. in Natural Science**
                             in Physical Chemistry,
                             Faculty of Science,
                             University of Paderborn, Germany

06/2011   **Diploma (with honours)**
                             in Chemistry,
                             Alexander Butlerov Institute of Chemistry,
                             Kazan Federal University, Russia

WORK EXPERIENCE

08/2011   **Research Associate**
                             Dr. Prof. Klaus Huber's group at the University of Paderborn
                             <u>Main activities:</u>
                             - Research on polyelectrolyte conformations in dilute solutions,
                               silver nanoparticle formation in polyacrylate matrix (polyacrylate
                               chains and spherical polyacrylate brushes), synthesis of spherical
                               polyacrylate brushes and raspberry-like metamolecules
                             - Used analytical techniques: SLS, DLS, SAXS, ASAXS, UV/VIS,
                               SEM, TEM
                             - Supervision of Bachelor theses
                             - Supervision of Master course "Small Angle Neutron Scattering
                               (SANS) experiments" at Forschungs-Neutronenquelle Heinz
                               Maier-Leibnitz (FRM II), Munich
                             - Teaching in Bachelor- and Master-courses in physical and
                               macromolecular Chemistry
                             - Oral and poster presentations at the scientific seminars and
                               conferences

EDUCATION AND TRAINING

08/2011 - Present Day   **Interdisciplinary Ph.D. program**
                             Micro- and Nanostructures in Optoelectronics and Photonics
                             Research Training Group 1464 (Deutsche Forschungsgemeinschaft),
                             University of Paderborn, Germany

09/2006 - 06/2011   **Specialist Diploma program**
                             in Fundamental and Applied Chemistry
                             with focus on Organic Synthesis,
                             Alexander Butlerov Institute of Chemistry,
                             Kazan Federal University, Russia

09/1995 - 06/2006	**Secondary School (equivalent to A level)**
	with focus on Mathematics,
	Municipal educational institution "Secondary school №1",
	Malmyzh, Russia

JOB-RELATED EXPERIENCE

10/2010 - 06/2011	**Laboratory assistant**
	Synthesis and characterisation of 2($5H$)-furanones
	with *S,S´*-binucleophilic reagents
	A. Arbuzov Institute of Organic and Physical Chemistry,
	Russian Academy of Science, Kazan, Russia

12/2010 - 06/2011	**Laboratory assistant**
	Mutation assay (Ames Test) of 2($5H$)-furanones on different mediums
	Genetics Department, Biology Faculty,
	Kazan Federal University, Russia

ORGANIZATIONAL AND MANAGERIAL EXPERIENCE

11/2008 - 11/2009	**Board Member and Representative of Institute of Chemistry**
	Providing social securities to students,
	organisation and promotion of cultural and sport events
	Kazan Federal University, Russia

SCIENTIFIC AWARDS

12/2014	**PACE Best Presentation Award**
	11th Convention of the Doctoral Research Training Group GRK1464
	Paderborn, Germany

LANGUAGE SKILLS

Russian	Mother tongue (C2)
English	Proficient user (C2)
German	Independent user (B1.2)

COMPUTER SKILLS

Text processing / presentation	Word, PowerPoint (Microsoft)
Calculation software	Excel (Microsoft)
	Origin 8G (Originlab)
	HDRC
	MestRec
	ChemDraw Ultra 7.0

FURTHER INTERESTS

Jogging, Swimming, Travelling, Visiting Art Exhibitions and Museums, Playing Piano

LIST OF PUBLICATIONS IN PEER-REVIEWED JOURNALS

[1]   A. Ezhova, Y. Hertle, T. Hellweg, F. Polzner and K. Huber: "Tailoring of Ag-Nanoparticle Assemblies by means of the Solution State of Silver Polyacrylate",
Langmuir (2015), submitted.

[2]   A. Ezhova and K. Huber: "Specific Interactions of Ag^+ Ions with Anionic Polyacrylate Chains in Dilute Solution",
Macromolecules 47, 8002-8011 (2014), DOI: 10.1021/ma501146m

ORAL PRESENTATIONS

[1]   A. Ezhova, G. Goerigk, T. Zentgraf and K. Huber: "Comparison study of Ag-NPs formation within PA-coils and spherical PA-brushes",
11th Convention of the Doctoral Research Training Group GRK1464, Paderborn, Germany, 2014.

[2]   A. Ezhova, R. Michels, T. Hikov, G. Goerigk and K. Huber: "Specific binding of Ag^+ ions to polyacrylate in dilute solution - a combined SAXS and ASAXS study",
Makromolekulares Kolloquium, Freiburg, Germany, 2013.

[3]   A. Ezhova, G. Goerigk and K. Huber: "Silver nanoparticles in polyacrylate template",
7th Convention of the Doctoral Research Training Group GRK1464, Paderborn, Germany, 2012.

POSTER PRESENTATIONS

[1]   A. Ezhova and K. Huber: "Tailoring of Ag-nanoparticles in polyacrylate solutions",
4th Europhotonics Spring School, Paderborn, Germany, 2015

[2]   M. Bürger, A. Ezhova and K. Huber: "Preparation of core-shell colloids enabling controlled nucleation of Ag-nanoparticles in the shell",
11th Convention of the Doctoral Research Training Group GRK1464, Paderborn, Germany, 2014.

[3]   A. Ezhova, J.K.N. Lindner, M. Muldarisnur, T. Zentgraf and K. Huber: "Silver nanoparticle formation in spherical polyelectrolyte brushes",
3rd Europhotonics Spring School, Île de Porquerolles, France, 2014.

[4]   M. Hansch, A. Ezhova and K. Huber: "Specific interactions of cations with polyelectrolytes in dilute solution",
International Simposium of Polyelectrolytes, Ein Gedi, Israel, 2014.

[5]   A. Ezhova, M. Muldarisnur, T. Zentgraf and K. Huber: "Formation of Ag-nanoparticles in PA-templates",
9th Convention of the Doctoral Research Training Group GRK1464, Paderborn, Germany, 2013.

[6]   A. Ezhova, R. Michels, T. Hikov, G. Goerigk and K. Huber: "Specific binding of Ag^+ ions to polyacrylate in dilute solution",
46th Biennial Meeting of the German Colloid Society, Paderborn, Germany, 2013.

[7]   A. Ezhova, R. Michels, T. Hikov, G. Goerigk and K. Huber: "Specific binding of Ag^+ ions to polyacrylate in dilute solution - a combined SAXS and ASAXS study",
Makromolekulares Kolloquium, Freiburg, Germany, 2013.